

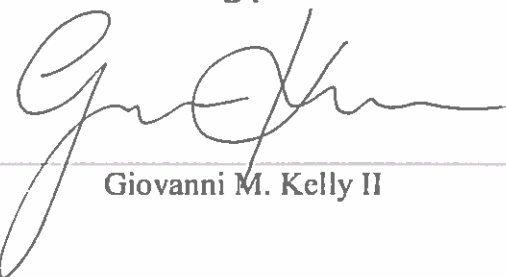
**THIN FILM CRYSTALLIZATION OF LINEAR AND CYCLIC  
POLYCAPROLACTONE**

AN ABSTRACT

SUBMITTED ON THE 14TH DAY OF JUNE 2018  
TO THE DEPARTMENT OF CHEMICAL AND BIOMOLECULAR  
ENGINEERING

IN PARTIAL FULFILLMENT OF THE REQUIREMENTS  
OF THE SCHOOL OF SCIENCE AND ENGINEERING  
OF TULANE UNIVERSITY  
FOR THE DEGREE OF  
DOCTOR OF PHILOSOPHY

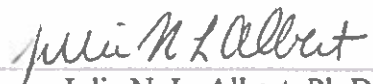
BY



---

Giovanni M. Kelly II

APPROVED:



---

Julie N. L. Albert, Ph.D.  
Director



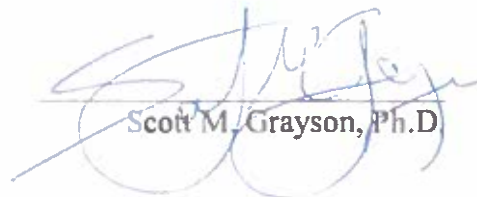
---

Vijay T. John, D.Eng.Sci.



---

Brian S. Mitchell, Ph.D.



---

Scott M. Grayson, Ph.D.

## **Abstract**

Semi-crystalline polymers are a class of polymeric materials that have been heavily studied and used in both consumer products and high-tech applications for decades. This is due to the many beneficial characteristics that semi-crystalline polymers exhibit, including attractive mechanical properties, solvent resistance, optical opacity, as well as biodegradability and biocompatibility. These properties are due to and dictated by the semi-crystalline state of the macromolecules, or the way in which these polymers are able to form varying amounts of well-ordered domains. It is this interplay between completely crystalline and completely amorphous regions that drive physical properties that in turn allow these materials to be used in so many applications.

More specifically, much research has been done to study the way that the geometry in which these polymers exist affects these factors, such as degree of crystallinity, chain orientation, morphology, and other characteristics. Whereas semi-crystalline polymers in the bulk have no driving force leading to preferred chain orientations, the substrate and the confined geometry encountered in thin films have a wide variety of effects on the semi-crystalline state, both in homopolymer systems and in polymer blends. This confined geometry is further complicated when studying new, non-linear architectures such as cyclic and star polymers. While synthetic challenges have caused the comparison of linear and cyclic PCL in thin films to lag behind bulk studies, advances in synthetic methods has allowed us to begin to better understand the interplay of confinement and chain architecture on the phenomena exhibited in these systems.

In this dissertation, I discuss a few research areas where we have tried to better understand semi-crystalline polymers confined in thin films. This work focuses most often

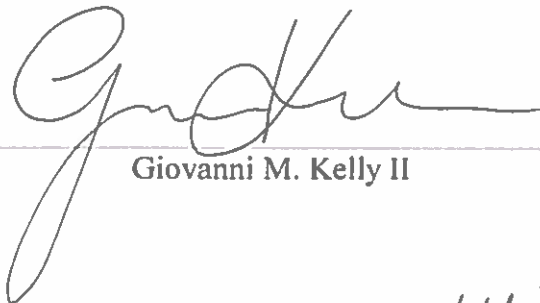
on linear and cyclic polycaprolactone, but some work has compared polycaprolactone to other semi-crystalline polymers like polyethylene glycol. This dissertation has three main focus areas. First are the phenomena exhibited by semi-crystalline polymers when blended with a second, non-crystalline component. The cooperativity of phase separation, interfacial effects, and crystallization cause interesting and insightful morphologies to form. I also discuss the discovery that spectral reflectance, a method typically used to measure film thickness, can be used to detect thermal transitions in semi-crystalline thin films and furthermore for isothermal crystallization studies that used to require more complicated calorimetry or X-ray scattering techniques. Finally, this dissertation discusses the work done so far in comparing linear and cyclic polycaprolactone confined to thin film geometries. Our first major observation is the enhanced stability exhibited by cyclic polycaprolactone, but there are many additional differences, such as the orientation assumed by the polymer chains, crystallization kinetics, and morphology.

Overall, this work aims to further some of the unexplored areas of semi-crystalline polymer research, especially as it pertains to thin films. As the techniques for characterizing and monitoring crystallization improve, we will find ourselves with an enhanced insight into the fundamentals of polymer crystallization, which will in turn allow us to tune polymer crystallinity and enhance the many applications that rely on semi-crystalline materials.

**THIN FILM CRYSTALLIZATION OF LINEAR AND CYCLIC  
POLYCAPROLACTONE**

A DISSERTATION  
SUBMITTED ON THE 14TH DAY OF JUNE 2018  
TO THE DEPARTMENT OF CHEMICAL AND BIOMOLECULAR  
ENGINEERING  
IN PARTIAL FULFILLMENT OF THE REQUIREMENTS  
OF THE SCHOOL OF SCIENCE AND ENGINEERING  
OF TULANE UNIVERSITY  
FOR THE DEGREE OF  
DOCTOR OF PHILOSOPHY

BY



---

Giovanni M. Kelly II

APPROVED:   
Julie N. L. Albert, Ph.D.  
Director



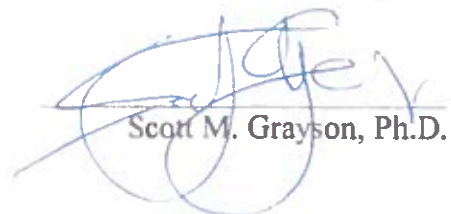
---

Vijay T. John, D.Eng.Sci.



---

Brian S. Mitchell, Ph.D.



---

Scott M. Grayson, Ph.D.



## Acknowledgments

To give the proper thanks to the people that have helped me get to where I am at this moment would take up many more pages than the rest of this work.

First, I'd like to thank Dr. Julie Albert for taking me on as her first graduate student. The two of us fought through our own "starting out" uncertainties together as we built a lab and, in my humble opinion, did some great science that will lead to even greater science in the future. You always held me to a standard that was exceptionally high, but in the end, I realized that standard helped me grow as a scientist and engineer more than I could have ever imagined, and for that I am sincerely thankful.

To my committee, Dr. Vijay John, Dr. Brian Mitchell, and Dr. Scott Grayson, your collective wisdom is truly incredible, and something I will never forget. I especially kept with me Dr. John's advice the *first* time I took the qualifying exam and received feedback: "Go deep into understanding the 'why' of everything you do in research." Dr. Mitchell, thank you for brainstorming with me about crystallization kinetics on multiple occasions. Your explanations at those times and in class really helped me to better appreciate the complexity of polymer physics. Dr. Grayson, I especially enjoyed our discussions on the future of cyclic polymers, because it expanded my understanding and conceptualization of the topic and helped me see things from a chemist's perspective, which was incredibly helpful. I can't wait to see the knowledge in this area that you and Julie will contribute to in the near future.

Dr. Dan Shantz, you have been a true mentor to me both in terms of how to succeed in graduate school and how to take on the world as a young Ph.D. level engineer. Though our long conversations about golf, politics, and other topics during the day and on Sunday evenings probably delayed my finishing on the order of months, I very much enjoyed and appreciated them.

The Chemical Engineering department is full of wonderful people that have been a pleasure to work with and around. I have made life-long friendships here, and even though we will probably end up all over the map once we finish, I hope nothing changes.

Thank you to the staff that keep things running like a well-oiled machine, and to the faculty who make this department a really special place.

To my lab mates, thank you for dealing with me as I learned how to manage, mentor, and train you all in everything from keeping the fume hood clean(ish) to working on manuscripts. I am sure I learned as much from you all as you learned from me, if not more. Baraka, there is no one I would have rather started a lab with. Sam and Amy, thanks for always being a text away. You two are the best.

My family was there well before I made the crazy decision to go to graduate school. My Mom, who unfortunately wasn't around to see what I have accomplished these last five years, instilled in me an incredible work ethic and drive that I hope never leaves me, and showed me how to truly care for people. My Dad has always been there for me and has always made me feel like what I was doing was incredibly important. You'll always be one of my best friends. To my siblings, cousins, aunts, uncles, and grandparents, thank you for always making me feel proud of what I was doing. I would have never been able to do this without your support. Additionally, thank you for nodding your heads and going "ah" and "cool" and trying your best to understand the gibberish I was saying whenever I talked about my research. Thinking about it still makes me laugh. To Aunt Cathy and Uncle Paul, thank you for all of your support, especially over the last five years. You'll never comprehend how much it continues to mean to me. To Donna and Larry Crawford, I never thought I'd meet two people that make me feel as truly welcome as my own family, but you two do it, and are both wonderful people.

Finally, graduate school would have never been as special as it's been had I not met Lydia Crawford. Thank you for being my friend on campus and at home, and for dealing with the good days and the bad. You and Maddy have made life so much better. I'm incredibly proud of all that you've accomplished as a Marine Biologist, even though I still get a little jealous since most sane individuals find sharks cooler than polymers. This is the beginning of a great adventure for us.

Again, thank you all.

Giovanni M Kelly II

## Table of Contents

<b>ACKNOWLEDGMENTS .....</b>	<b>ii</b>
<b>LIST OF TABLES .....</b>	<b>vii</b>
<b>LIST OF FIGURES .....</b>	<b>viii</b>
<b>CHAPTER 1: INTRODUCTION.....</b>	<b>1</b>
1.1 CRYSTAL STRUCTURE AND UNIT CELL.....	2
1.2 CRYSTALLINE LAMELLAE .....	5
1.3 SPHERULITES.....	6
1.4 ULTRATHIN FILM STRUCTURES.....	10
1.5 CRYSTALLIZATION KINETICS .....	12
1.6 THESIS OVERVIEW .....	15
<b>CHAPTER 2: CHARACTERIZATION TECHNIQUES.....</b>	<b>19</b>
2.1 GEL PERMEATION CHROMATOGRAPHY (GPC).....	19
2.2 MATRIX ASSISTED LASER DESORPTION/IONIZATION (MALDI-TOF).....	21
2.3 DIFFERENTIAL SCANNING CALORIMETRY (DSC).....	23
2.4 SPECTRAL REFLECTANCE.....	25
2.5 OPTICAL MICROSCOPY/POLARIZED LIGHT OPTICAL MICROSCOPY (OM/PLOM).....	28
2.6 ATOMIC FORCE MICROSCOPY (AFM) .....	30
2.7 GRAZING INCIDENCE WIDE-ANGLE X-RAY SCATTERING (GIWAXS) .....	33
2.8 SPINCOATING .....	36
2.9 FLOWCOATING .....	38
<b>CHAPTER 3: ULTRATHIN FILM CRYSTALLIZATION OF POLY(<math>\epsilon</math>-</b>	
<b>CAPROLACTONE) IN BLENDS CONTAINING STYRENE-ISOPRENE BLOCK</b>	
<b>COPOLYMERS: THE NANO-ROSE MORPHOLOGY.....</b>	<b>40</b>
3.1 INTRODUCTION.....	41
3.2 EXPERIMENTAL SECTION .....	46
3.3 RESULTS AND DISCUSSION.....	48

3.4 CONCLUSIONS .....	69
<b>CHAPTER 4: THERMAL TRANSITIONS IN SEMI-CRYSTALLINE POLYMER THIN FILMS STUDIED VIA SPECTRAL REFLECTANCE .....</b>	<b>70</b>
4.1 INTRODUCTION.....	72
4.2 EXPERIMENTAL SECTION .....	75
4.3 DETERMINATION OF T <sub>m</sub> AND T <sub>c</sub> BY SR .....	79
4.4 TRACKING ISOTHERMAL RECRYSTALLIZATION BY SR.....	88
4.5 DETERMINING DEGREE OF CRYSTALLINITY FROM SPECTRAL REFLECTANCE DATA ..	94
4.6 CONCLUSIONS .....	102
<b>CHAPTER 5: SUPPRESSION OF MELT-INDUCED DEWETTING IN CYCLIC POLY(<math>\epsilon</math>-CAPROLACTONE) THIN FILMS .....</b>	<b>104</b>
5.1 INTRODUCTION.....	105
5.2 EXPERIMENTAL SECTION .....	106
5.3 RESULTS .....	109
5.4 DISCUSSION .....	114
5.5 CONCLUSIONS .....	117
<b>CHAPTER 6: MORPHOLOGY AND KINETICS OF CRYSTAL GROWTH IN LINEAR AND CYCLIC PCL.....</b>	<b>118</b>
6.1 THIN FILM MORPHOLOGY .....	119
6.2 CRYSTAL ORIENTATIONS VIA GIWAXS .....	122
6.3 CRYSTAL GROWTH KINETICS.....	127
6.4 CONCLUSIONS .....	134
<b>CHAPTER 7: CONCLUSIONS AND FUTURE WORK.....</b>	<b>136</b>
7.1 POLYMER CRYSTALLIZATION IN THIN AND ULTRATHIN FILM BLENDS .....	137
7.2 SPECTRAL REFLECTANCE TO EXAMINE THERMAL BEHAVIOR OF SEMI-CRYSTALLINE POLYMERS .....	139
7.3 THIN FILM STABILITY OF CYCLIC POLYCAPROLACTONE.....	141
7.4 THIN FILM MORPHOLOGY AND KINETICS OF CYCLIC POLYCAPROLACTONE.....	143
<b>APPENDIX A: SUPPORTING INFORMATION FOR ULTRATHIN FILM CRYSTALLIZATION OF POLY(<math>\epsilon</math>-CAPROLACTONE) IN BLENDS</b>	

<b>CONTAINING STYRENE-ISOPRENE BLOCK COPOLYMERS: THE NANO-ROSE MORPHOLOGY .....</b>	<b>145</b>
<b>APPENDIX B: SUPPORTING INFORMATION FOR “THERMAL TRANSITIONS IN SEMI-CRYSTALLINE POLYMER THIN FILMS STUDIED VIA SPECTRAL REFLECTANCE” .....</b>	<b>180</b>
<b>APPENDIX C: SUPPORTING INFORMATION FOR “SUPPRESSION OF MELT-INDUCED DEWETTING IN CYCLIC POLY(E-CAPROLACTONE) THIN FILMS” .....</b>	<b>193</b>
<b>APPENDIX D: ACQUIRING CRYSTAL ORIENTATION AND DEGREE OF CRYSTALLINITY FROM GIWAXS AND GIXSGUI .....</b>	<b>201</b>
<b>REFERENCES.....</b>	<b>214</b>
<b>BIOGRAPHY .....</b>	<b>239</b>

## **List of Tables**

5.1 Mass determination of l-PCL <sub>6k</sub> and c-PCL <sub>6k</sub> by GPC and MALDI-TOF MS.....	111
--	-----

## List of Figures

<b>Figure 1.1:</b> Unit cell diagram showing dimensions of polyethylene.....	3
<b>Figure 1.2:</b> Diagrams of the hypothesized structures of crystalline lamellae in the a) adjacent re-entry model; and b) “switchboard” model .....	5
<b>Figure 1.3:</b> a) Diagram of the hierarchy of polymer crystal structure from the basic unit cell to lamellae and finally to a polymer spherulite; and b) Spherulitic structure showing alternating layers of crystalline lamellae and amorphous regions. ....	7
<b>Figure 1.4:</b> Maltese cross extinction patterns exhibited by polymer spherulites when studied via polarized light optical microscopy (PLOM).....	8
<b>Figure 1.5:</b> Yield stress measured as a function of spherulite size in isotactic polystyrene.	9
<b>Figure 1.6:</b> Diagram illustrating the edge-on (left) to flat-on (right) transition in ultrathin semi-crystalline polymer films .....	11
<b>Figure 1.7:</b> Atomic force microscopy image of 12 nm 45 kDa PCL as cast from toluene. This film exhibits a dense branching morphology (DBM) .....	12
<b>Figure 1.8:</b> Diagram showing the three regimes of Lauritzen-Hoffman growth theory ..	14
<b>Figure 2.1:</b> GPC chromatogram showing the elution times of linear and cyclic polycaprolactone using a refractive index detector. “a.u.” is the absorbance intensity measured by the detector and $t_E$ is the elution time. Here, cyclic PCL exhibits a longer elution time due to the smaller hydrodynamic radius caused by the collapsed ring structure.....	20

**Figure 2.2:** Diagram showing the basic operation of MALDI-TOF. A high-power laser is directed onto the matrix containing the polymer and ion. This laser treatment causes the mixture to ablate, generating free-floating polymer in the gas phase that is then directed to the time-of-flight detector due to differential charge along the path to the detector.

Based on the mass to charge ratio (and therefore the molecular weight), the species will reach the detector at different time points.....22

**Figure 2.3:** Sample DSC data showing the three main thermal transitions determined by DSC when a semi-crystalline polymer is first rapidly cooled to below its  $T_g$  from the melt and then heated (temperature increased from left to right); one method for determining thermal transitions in semi-crystalline polymers via DSC: glass transition ( $T_g$ ), crystallization temperature ( $T_c$ ), and melting temperature ( $T_m$ ). .....24

**Figure 2.4:** Reflectance intensity vs. wavelength for 491 nm 45 kDa PCL studied via spectral reflectance .....27

**Figure 2.5:** 550 nm 12 kDa linear PCL studied via polarized light optical microscopy (PLOM). This film exhibits Maltese Cross extinction patterns, indicative of well-formed 2-dimensional spherulites .....29

**Figure 2.6:** Basic operation of PeakForce Tapping showing the generation of force curves and the steps (A-E) of tip interaction with the sample surface during operation ..32

**Figure 2.7:** Diagram showing the basic operation of grazing incidence wide-angle x-ray scattering. Coherent x-rays enter the surface of the film at an incident angle  $\alpha$  and are scattered into the two-dimensional detector .....34

**Figure 2.8:** Two-dimensional scattered x-ray intensity from a 500 nm 45 kDa PCL film studied at the Advanced Photon Source (APS) at Argonne National Laboratory. This  $q_z$

vs  $q_y$  representation of scattered intensity exhibits the anisotropy of crystals in different planes of the film, as well as the unit cell spacing.....35

**Figure 2.9:** Concurrent events during the spincoating process that cause the film to thin and dry .....37

**Figure 2.10:** Cartoon showing the basic setup and variables involved in the flowcoating of thin polymer films .....39

**Figure 3.1:** AFM height image of 12 nm thick blend film of 45 kDa PCL and SIS vector 4293A containing 50 wt % SIS, spin coated from toluene. This film exhibits the “nano-rose” morphology .....45

**Figure 3.2:** GIWAXS 2D spectra and intensity vs.  $q_y$  plots for samples of (a) pure PCL and (b) nano-rose, both exhibiting characteristic crystalline peaks at  $q_y$ -values of  $1.5 \text{ \AA}^{-1}$  and  $1.7 \text{ \AA}^{-1}$  corresponding to (110) and (200) growth faces, respectively.....51

**Figure 3.3:** AFM height images of 45 kDa PCL/SIS Vector 4293A blend exhibiting the nano-rose morphology (a) as cast from toluene and (b) after washing with cyclohexane to selectively remove the SIS component .....52

**Figure 3.4:** AFM height images of 45 kDa PCL/SIS vector 4293A blend containing 50 wt % SIS showing the development and disappearance of the nano-rose morphology as a function of film thickness: (a) 6 - 7 nm; (b) 7 - 8 nm; (c) 8 - 9 nm; (d) 9 - 14 nm; (e) 14 - 16 nm; and (f) 16 - 18 nm.....54

**Figure 3.5:** AFM height images of approximately 12 nm thick blend films containing 45 kDa PCL and 50 wt % amorphous polymer: (a) SIS vector 4211A; (b) SIS vector 4215A; (c) P2208 SI diblock; (d) P3868 SI diblock; (e) 35 kDa PI; and (f) 20 kDa PS.....56

**Figure 3.6:** AFM height images of 45 kDa PCL/SIS vector 4293A blends at 10 - 14 nm thickness. Inset for 100 wt % SIS shows the presence of block copolymer nanostructure

.....60

**Figure 3.7:** AFM height images of 45 kDa PCL/SIS vector 4293A blends at thicknesses of (a) 11 nm; and (b) 14 nm cast on substrates modified with benzyl silane .....61

**Figure 3.8:** AFM height images of blends of (a) 10 kDa PCL and SIS vector 4211A containing 50 wt % SIS and (b) 80 kDa PCL and SIS vector 4293A containing 50 wt % SIS .....52

**Figure 3.9:** 45 kDa PCL SIS vector 4293A blend containing 50 wt % SIS cast from (a) benzene at 12 nm; (b) 1,4-dioxane at 12 nm; (c) THF at 14 nm; and (d) chloroform at 14 nm .....63

**Figure 3.10:** *In situ* AFM study of nano-roses as they form: (a) initial lamella begins to curve up due to competing surface stresses; (b) the initial curved lamella grows into a full nano-rose; (b)-(c) existing lamellae give birth to subsequent lamellae that either continue curling into the original nano-rose or curve out to spawn new nano-roses; (c) new lamellar layers form at the edges of existing nano-roses; (d) sustained lamellar curvature continues, both filling in edges of nano-roses or continuing to crystallize out from the edges of formed nano-roses. Arrows show direction of crystal growth. Inset schematics depict dynamics of a single crystalline lamella; amorphous phase of PCL and SIS not shown .....66

**Figure 4.1:** Melting point determination for a 500 nm 45 kDa PCL thin film: a) Thickness vs. temperature (open diamond symbols) and degree of crystallinity vs. temperature as determined from GIWAXS (black X's). This film exhibits characteristic

expansion upon melting with a transition at approximately 61 °C. Blue, purple, and red shading indicate the semi-crystalline, melting transition, and melt state regions, respectively. b) Melting point studied via elevated temperature GIWAXS showing loss of crystalline order between 60 °C and 61 °C. c) Analysis of slope of the thickness versus temperature curve from (a) showing a primary peak value at 57 °C. This value corresponds to when the degree of crystallinity has decreased by half during melting and can be considered the midpoint of the melting transition region .....81

**Figure 4.2:** Film thickness vs. temperature for: a) “bulk” 1130 nm 20 kDa PEG film; and b) 147 nm 20 kDa PEG thin film. This comparison shows that SR can be used to detect  $T_m$  depression in PEG due to thin film confinement. Blue, purple, and red shading indicate the semi-crystalline, melting transition, and melt state regions, respectively .....85

**Figure 4.3:** Observed  $T_m$  vs film thickness for 45 kDa PCL (red open squares) and 20 kDa PEG (black open diamonds). This comparison illustrates the confinement driven melting point depression in these two materials. No appreciable  $T_m$  depression is observed in 45 kDa PCL, even in films as thin as 21 nm. In 20 kDa PEG films, the onset of  $T_m$  depression can be seen in the 659 nm film ( $T_m = 63$  °C) and becomes more dramatic as the film thickness decreases. Error bars represent the  $\pm 1$  °C window we report as the uncertainty associated with determining  $T_m$  from SR data .....86

**Figure 4.4:** Thickness vs. temperature of 500 nm 45 kDa PCL for a 1 °C/min recrystallization from 100 °C. This film exhibits a sharp decrease in film thickness starting at 47 °C, which is within a few degrees of the onset of crystallization in the DSC endotherm. Red, purple, and blue shading indicate the melt state, crystallization transition, and semi-crystalline regions, respectively .....87

<b>Figure 4.5:</b> Thickness vs. time of 96 nm 45 kDa PCL films measured during isothermal recrystallization at 30 °C (blue diamonds) and 40 °C (red squares).....	90
<b>Figure 4.6:</b> Thickness (measured via spectral reflectance) & degree of crystallinity (measured via GIWAXS) vs. temperature for 96 nm 45 kDa PCL isothermally crystallized at 30 °C .....	92
<b>Figure 4.7:</b> Thickness (measured via spectral reflectance) & degree of crystallinity (measured via GIWAXS) vs. temperature for 96 nm 45 kDa PCL isothermally crystallized at 40 °C .....	93
<b>Figure 4.8:</b> Degree of crystallinity vs. temperature calculated using both GIWAXS and the spectral reflectance method for 95 nm 45 kDa PCL .....	96
<b>Figure 4.9:</b> Degree of crystallinity via spectral reflectance vs. degree of crystallinity via GIWAXS for 95 nm 45 kDa PCL. Dotted line represents $y = x$ .....	97
<b>Figure 4.10:</b> Degree of crystallinity vs. time calculated using both spectral reflectance and GIWAXS for 96 nm 45 kDa PCL isothermally crystallized at 30 °C .....	98
<b>Figure 4.11:</b> Degree of crystallinity via spectral reflectance vs. degree of crystallinity via GIWAXS for 96 nm 45 kDa PCL isothermally recrystallized at 30 °C. Dotted line represents $y = x$ .....	99
<b>Figure 4.12:</b> Degree of crystallinity vs. time calculated using both spectral reflectance and GIWAXS for 96 nm 45 kDa PCL isothermally crystallized at 40 °C .....	100
<b>Figure 4.13:</b> Degree of crystallinity via spectral reflectance vs. degree of crystallinity via GIWAXS for 96 nm 45 kDa PCL isothermally recrystallized at 40 °C. Dotted line represents $y = x$ .....	101

**Figure 5.1:** Structures of *l*-PCL<sub>6k</sub> and *c*-PCL<sub>6k</sub>. The numbers (1) and (3) correspond to the synthetic identification of these polymers in the “Synthetic Protocols” section of the Appendix C .....107

**Figure 5.2:** Molecular weight characterization data for *l*-PCL<sub>6k</sub> and *c*-PCL<sub>6k</sub>. a) GPC chromatograms illustrate the longer elution time for the *c*-PCL<sub>6k</sub> due to its decreased hydrodynamic radius. b-c) MALDI-TOF MS spectra of *l*-PCL<sub>6k</sub> and *c*-PCL<sub>6k</sub> indicate exceptional uniformity in both species with respect to end group functionalities and architectural transformations .....110

**Figure 5.3:** Comparison of *l*-PCL<sub>6k</sub> and *c*-PCL<sub>6k</sub> before and after melting and recrystallization: a) optical image of *l*-PCL<sub>6k</sub> as cast; b) optical image of *l*-PCL<sub>6k</sub> melted and recrystallized; c) AFM height image of *l*-PCL<sub>6k</sub> melted and recrystallized showing a section taken across the dewet area (average depth: 104.6 ± 7.58 nm); d) optical image of *c*-PCL<sub>6k</sub> as cast; e) optical image of *c*-PCL<sub>6k</sub> melted and recrystallized; f) AFM height image of *c*-PCL<sub>6k</sub> melted and recrystallized showing a section across a grain boundary (average depth: 64.7 ± 6.46 nm) .....112

**Figure 5.4:** Chemical structures of the additional linear PCL controls. The numbers (2), (4), (5), and (6) correspond to the synthetic identification of these polymers in the “Synthetic Protocols” section of the Appendix C.....114

**Figure 6.1:** Bright field optical microscopy images of: a) 90 nm 1.2 kDa linear PCL as cast from toluene and b) 85 nm 1.2 kDa cyclic PCL as cast from toluene .....119

**Figure 6.2:** Bright field optical microscopy images of: a) 79 nm 4 kDa linear PCL as cast from toluene and b) 80 nm 4 kDa cyclic PCL as cast from toluene .....120

<b>Figure 6.3:</b> Bright field optical microscopy images of: a) 58 nm 6 kDa linear PCL as cast from toluene and b) 56 nm 6 kDa cyclic PCL as cast from toluene .....	120
<b>Figure 6.4:</b> Bright field optical microscopy images of: a) 117 nm 6 kDa linear PCL as cast from toluene and b) 106 nm 6 kDa cyclic PCL as cast from toluene .....	121
<b>Figure 6.5:</b> Two-dimensional scattering intensity measured via GIWAXS for a) 117 nm 6 kDa linear PCL as cast from toluene; and b) 106 nm 6 kDa cyclic PCL as cast from toluene .....	123
<b>Figure 6.6:</b> Two-dimensional scattering intensity measured via GIWAXS for a) 114 nm 6 kDa linear PCL melted and recrystallized at 25 C; and b) 113 nm 6 kDa cyclic PCL melted and recrystallized at 25 C. Note: as discussed in Chapter 4, the linear sample suffers slight dewetting, which contributes to the halos directly above the beam stop ..	124
<b>Figure 6.7:</b> Two-dimensional scattering intensity measured via GIWAXS for a) 58 nm 6 kDa linear PCL melted and recrystallized at 25 C; and b) 57 nm 6 kDa cyclic PCL melted and recrystallized at 25 C. Note: as discussed in Chapter 4, the linear sample suffers slight dewetting, which contributes to the halos directly above the beam stop .....	125
<b>Figure 6.8:</b> Two-dimensional scattering intensity measured via GIWAXS for a) 474 nm 6 kDa linear PCL melted and recrystallized at 25 C; and b) 502 nm 6 kDa cyclic PCL melted and recrystallized at 25 C .....	126
<b>Figure 6.9:</b> Radial growth rate at multiple isothermal recrystallization temperatures for 475 nm linear PCL; 502 nm cyclic PCL; and 350 nm 50-50 blend of linear and cyclic PCL .....	128
<b>Figure 6.10:</b> Increase in degree of crystallinity as a function of time during isothermal recrystallization as studied via GIWAXS for 475 nm linear PCL (red open triangles), 502	

nm cyclic PCL (blue open diamonds), and a 350 nm 50-50 linear-cyclic PCL blend film (purple open circles). Degree of crystallinity calculations are discussed more thoroughly in Chapter 4 and Appendix D .....129

**Figure 6.11:** Polarized optical microscopy images of a) 475 nm 6 kDa linear PCL isothermally crystallized at 30C; and b) 502 nm 6 kDa cyclic PCL isothermally crystallized at 30C. Scale bar equals 200  $\mu\text{m}$  .....131

**Figure 6.12:** Temperature dependence of crystal growth rate from the melt for a variety of polymers; rubber, Nylon6, PTMPS, PET, i-PS, PLLA, PESU. Solid and broken lines are best fitting by Arrhenius and WLF expressions, respectively .....133

## **Chapter 1**

### **INTRODUCTION**

Crystallinity forms the basis of and leads to most of the beneficial and unique properties of materials ranging from snowflakes to diamonds. In the simplest sense, crystallization refers to the process of a material's constituent parts forming an ordered structure. This ordered structure can range from simple cubic structures to more complicated hexagonal and other polygonal packings. Regardless of what order the form takes, that the material's constituent atoms can arrange themselves in an ordered structure or crystal lattice is what makes a material crystalline. Crystalline materials can be found in every facet of life. In addition to the well-known crystalline materials mentioned above, many plastics, the revolutionary class of materials that have transformed the world in the past century, are also capable of crystallization. Some of the most heavily used commodity plastics, such as polyethylene (PE), polypropylene (PP), and polyethylene terephthalate (PET), belong to a class of plastics known as semi-crystalline polymers<sup>1-3</sup>. Like the crystallization that differentiates diamond from coal, it is the crystallization in these plastics that leads to the favorable mechanical and optical properties that they exhibit and which have helped them become and remain multi-billion dollar commodities. Importantly, they are known as "semi-crystalline" because polymers are macromolecules and not small molecules, and as such are unable to form completely crystalline materials. However, the

degree of crystallinity ( $X_c$ ), defined as the mass or volume fraction of crystalline regions in the material, dictates most of the important properties of semi-crystalline materials<sup>4</sup>.

Because the crystallinity is what dictates the mechanical and optical properties of these materials, the basis for most research focusing on semi-crystalline polymers has focused on better understanding the fundamental crystal structure and morphology, ways to manipulate the crystal structure on an atomic scale and macrostructure morphology, and the effects that external factors have on crystallinity<sup>1,5-22</sup>. These external factors range from polymer architecture<sup>7, 9, 12, 17, 23-28</sup>, how the polymer is processed (such as extrusion or drawing processes)<sup>5, 8, 13, 19</sup>, blending with other crystalline and non-crystalline polymeric and non-polymeric components<sup>5, 11, 16, 20-21, 29-33</sup>, and the geometry in which the semi-crystalline polymer exists, such as thin films or spherical nanoparticles<sup>6, 10-11, 15, 20-21, 33-35</sup>. Fundamentally, if we can better understand what affects crystal structure and morphology, we can use that understanding to enhance and tune the properties of these materials that will in turn enhance the numerous applications that depend on semi-crystalline polymers.

### 1.1 Crystal Structure and Unit Cell

As alluded to above, polymer crystals have many similar characteristics to metallic and small molecule crystals. That is, polymer chains are able to form domains that exhibit positional and orientational order. However, the long-chain structure of a polymer complicates the crystal system. Unlike small molecules and metallic crystals, one polymer chain can participate in multiple crystal unit cells due to the size of unit cell and length of the chain (see Figure 1.1)<sup>1</sup>.

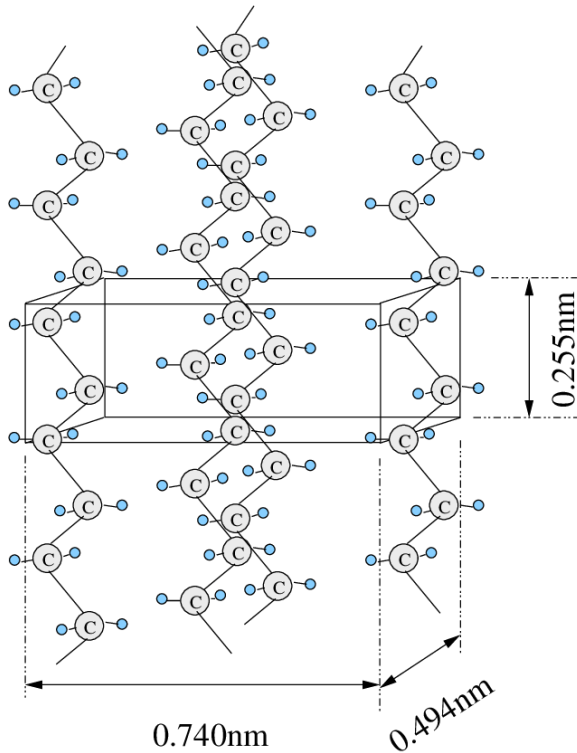


**Figure 1.1.** Unit cell diagram showing dimensions of polyethylene. Reproduced with permission from González-Viñas, Wenceslao, and Héctor L. Mancini. *An introduction to materials science*. Princeton University Press, 2015<sup>36</sup>

Related, the constituent parts of the unit cell (typically the monomer) are not independent of one another due to the covalent linkage between monomer units. These are the restrictions leading to the inability of complete crystallinity in polymers. For the polymer chain to assume a completely crystalline state, it has to have a perfectly regular structure, and be oriented in such a way that it can participate in constituent unit cells without discontinuities due to bulky groups leading to steric hindrances<sup>37</sup>. The flexibility of the chain itself also plays a significant role. Considering these factors, it becomes clear why certain polymers are able to crystallize while some cannot. Crystallizing polymers typically

have compact monomer units without bulky side chains<sup>38</sup>. This is why polymers such as polyethylene, polypropylene, polycaprolactone, and polyethylene glycol are able to crystallize. Their simple structure allows them to assume compact conformations much more easily. In the case of polymers with more bulky monomer units, crystallizability is typically only observed when there is sufficient stereoregularity. This can be observed in the difference between atactic polystyrene (amorphous) and isotactic polystyrene (semi-crystalline)<sup>39</sup>.

The determination of polymer crystallization at the molecular level is conducted via a number of techniques. The most fruitful of these techniques is X-ray scattering, where researchers can study the powder diffraction of polymers to resolve unit cell dimensions and orientations based on the scattering peak positions in  $Q$ <sup>12, 40-42</sup>.  $Q$  is called the “scattering vector” or the “wave vector transfer”, and is defined as:

$$Q = \frac{2\pi}{d}$$

Equation 1.1

where “d” is the real domain spacing of the ordered part of the material, such as a crystal lattice dimension. Grazing incidence (see Chapter 2) can be used to study the orientation and unit cell of semi-crystalline polymers confined in thin film geometries. Also used to study the degree of crystallinity as well as the enthalpies of melting is differential scanning calorimetry (DSC)<sup>22, 43-47</sup>. By measuring the heat flow into or out of the polymer in relation to a reference pan, these and other quantities like the heat capacity can be calculated, which are closely related to the crystal structure and chain packing. Finally, much work has using computational tools to model crystallization at the molecular level<sup>1, 8</sup>.

## 1.2 Crystalline Lamellae

The crystallization that occurs at the molecular level in turn leads to crystalline nano-structures called crystalline lamellae<sup>1, 34, 48</sup>. Several hypotheses claim that lamellae are formed by polymer chains that fold back on themselves to form closely packed stems (adjacent reentry) (see Figure 1.2a)<sup>1, 38</sup>. They can also form via many independent polymer chains stacking together, sometimes referred to as the “switchboard” model<sup>8</sup>. (see Figure 1.2b)

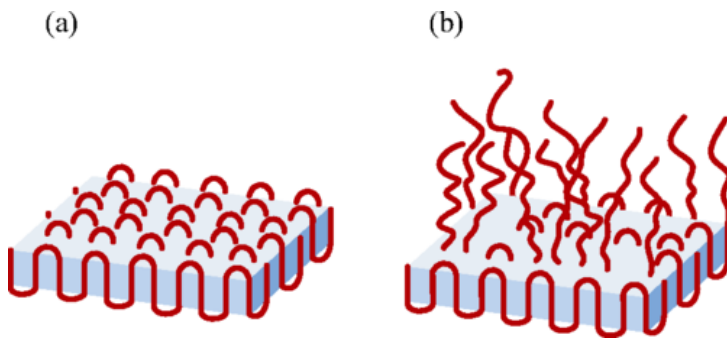


**Figure 1.2.** Diagrams of the hypothesized structures of crystalline lamellae in the a) adjacent re-entry model; and b) “switchboard” model. Reproduced with permission from Dargazany, Roozbeh, et al. "Constitutive modeling of strain-induced crystallization in filled rubbers." *Physical Review E* 89.2 (2014)<sup>8</sup>

Regardless, it has been established that these semi-crystalline lamellae are approximately 10 nm in thickness, depending on polymer, molecular weight, and crystallization conditions<sup>38</sup>. This has been found through multiple experiments over the years, such as etching away the amorphous regions with acids and studying the remaining crystalline material via AFM<sup>49</sup>, or via small angle X-ray scattering (SAXS) which reveals the domain sizes (and therefore thicknesses) of the lamellae<sup>1, 19, 40-41</sup>. Through thermodynamic study,

it was hypothesized that 10 nm corresponds to the smallest stable crystal that can nucleate, having a free energy slightly lower than the polymer melt<sup>38</sup>. The lamellar thickness can be most easily affected by the crystallization temperature, or rather, the degree of supercooling ( $\Delta T$ ). The degree of supercooling is the temperature difference between the experimental isothermal crystallization temperature ( $T_c$ ) and the equilibrium melting temperature ( $T_{m,0}$ )<sup>1</sup>.  $T_c$  is any temperature below the experimental melting temperature where crystallization is favored over the system remaining in the melt state. The equilibrium melting temperature is taken as the melting temperature of an infinite collection of extended chain crystals such that surface effects are negated<sup>50</sup>. The equilibrium melting temperature is not to be confused with the experimental melting temperature ( $T_m$ ), or the temperature at which the crystals melt under ambient conditions. At high supercooling, the speed of crystal growth creates lamellae that are relatively small. At low supercooling, the opposite has been found. Wunderlich et al. found that melt-crystallizing polyethylene at 110 °C vs 130 °C generated lamellar thicknesses of 10 nm and 20 nm, respectively<sup>51</sup>. Comparatively, the molecular weight of the polymer has only been shown to have an effect on lamellar thickness in oligomeric and very low molecular weight polymers<sup>4</sup>.

### 1.3 Spherulites

The crystalline lamellae, along with amorphous sections of the polymer chain existing alongside each other form semi-crystalline macrostructures called spherulites in bulk materials, especially at low crystallization temperatures<sup>1, 11, 48, 52-56</sup>. Figure 1.3a shows the progression of polymer crystals from the molecular scale to the final spherulite

structure. As the name suggests, spherulites are spherical macrostructures (see Figure 1.3b).

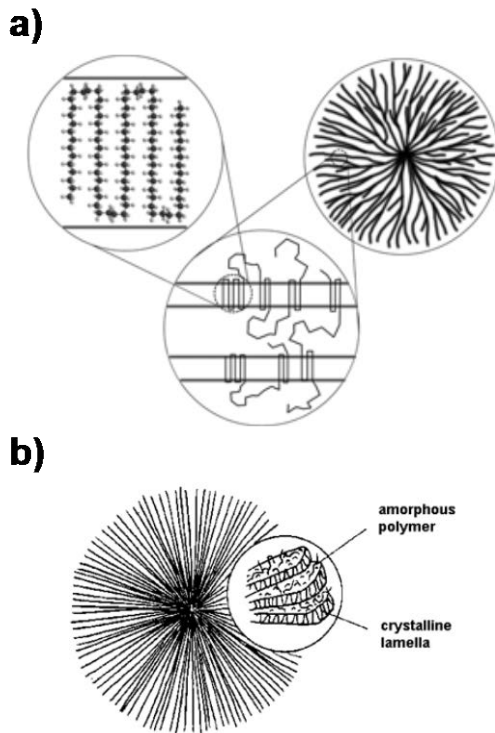


**Figure 1.3.** a) Diagram of the hierarchy of polymer crystal structure from the basic unit cell to lamellae and finally to a polymer spherulite. Reproduced with permission from Milner, Scott T. "Polymer crystal–melt interfaces and nucleation in polyethylene." *Soft Matter* 7.6 (2011): 2909-2917<sup>57</sup>; and b) Spherulitic structure showing alternating layers of crystalline lamellae and amorphous regions. Reproduced with permission from DoITPoMS, University of Cambridge

After a crystal nucleus forms, growth of the crystal face propagates in all three dimensions, and since the growth rate of polymer crystals is constant, spherical structures are formed. Spherulites are often tens of microns in diameter. While they are most often observed and

discussed in bulk materials, spherulites are also able to form in thin and ultrathin films at thicknesses greater than approximately 50 nm<sup>6, 11, 15, 33-34</sup>. Here, they are known as “two-dimensional” spherulites<sup>58-60</sup>, as their width is hundreds of times greater than their thickness. Spherulites can be observed via multiple microscopy techniques, including optical microscopy and atomic force microscopy. However, the greatest evidence of the existence of spherulites is found via polarized light optical microscopy, where the birefringence of polymer crystals creates what are commonly called Maltese Cross extinction patterns if spherulitic macrostructures are present (extended discussion of polarized light optical microscopy (PLOM) can be found in chapter 2)<sup>1, 48</sup>. Different Maltese Cross types are generated based on the direction of the chain axis in relation to the radial direction as well as the refractive index differences based on orientation.

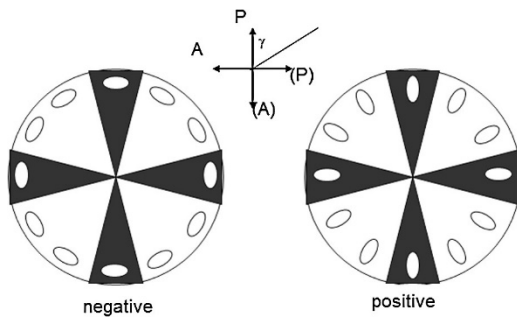


**Figure 1.4.** Maltese cross extinction patterns exhibited by polymer spherulites when studied via polarized light optical microscopy (PLOM). Reproduced with permission from Crist, Buckley, and Jerold M. Schultz. "Polymer spherulites: A critical review." *Progress in Polymer Science* 56 (2016): 1-63.<sup>48</sup>

Spherulites are important not only because they are the largest macrostructure that are able to be formed by semi-crystalline polymers, but also because their characteristics

define many of the mechanical and optical properties of the materials<sup>48</sup>. For example, it has been shown that changes in the size (and therefore density) of spherulites has a large effect on mechanical properties. Specifically, Atkinson and Nutting<sup>54</sup> found that the yield stress at failure for isotactic polypropylene decreased dramatically with an increase in spherulite size (see Figure 1.5).

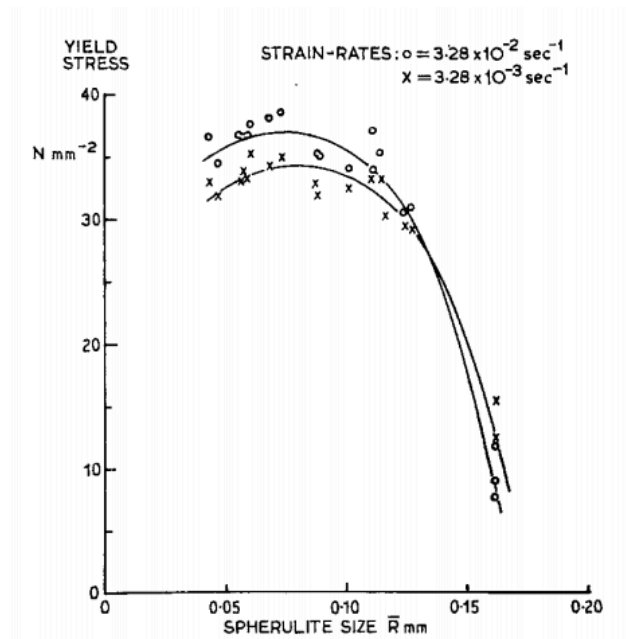


**Figure 1.5.** Yield stress measured as a function of spherulite size in isotactic polystyrene. Reproduced with permission from Way, J. L., J. R. Atkinson, and J. Nutting. "The effect of spherulite size on the fracture morphology of polypropylene." *Journal of Materials Science* 9.2 (1974): 293-299.

Similar effects have been found with tensile strength, toughness, and yield stress. These effects have to do with the surface area of interaction between the spherulites. As the volume of the spherulite increases, so too does the surface area of the spherulitic

boundaries. Thus, a large amount of work has been done to try and better understand the ways we can manipulate spherulite morphology<sup>11, 14, 48, 54</sup>. The two main methods of increasing or decreasing spherulite size has been either via crystallization kinetics<sup>22, 61-62</sup> (i.e. crystallization temperature) or via the use of additives known as nucleating agents that increases the density of nucleation sites, and therefore decreases the size of individual crystals<sup>1, 19</sup>.

Semi-crystalline polymers are also able to form other macrostructures such as hedrites grown at high temperatures<sup>14, 63-65</sup> and single multi-faceted crystals grown from dilute solutions. Hedrites are similarly spherical like spherulites, however the chain orientation of the crystals that comprise hedrites tend to be flat-on, and these structures lack the birefringence that spherulites exhibit<sup>1</sup>. Crystals grown from very dilute solutions (typically < 1 wt.%) are used to study lamellar thickness and the dimension and growth direction of specific growth faces<sup>27, 66-68</sup>. An extended discussion of those structures is beyond the scope of this thesis.

#### 1.4 Ultrathin Film Structures

As discussed above, spherulites can be found in films ranging from multiple millimeters down to approximately 50 nm<sup>11, 34, 69</sup>. Therefore, one might ask: what occurs in films thinner than this? Obviously, the film thickness eventually reaches a critical value such that spherulitic formation is no longer possible. At these film thicknesses, the system turns into a collection of randomly oriented lamellae and regions of amorphous polymer<sup>70-71</sup>. The lamellae have been shown to have a preferential orientation at certain film thicknesses<sup>34</sup>. For example, in sufficiently thick films ( $t_f > 100$  nm) the preferred

orientation is for the lamellae to orient “edge-on” to the substrate, i.e. with the chain axes normal to the surface of the substrate. When the film thickness drops below a critical value that is polymer, molecular weight, and crystallization condition dependent, the lamellae prefer to orient themselves “flat-on” to the substrate with the chain axis parallel to the surface of the substrate. A schematic of the edge-on to flat-on transition is shown in Figure 1.6. This confinement-driven transition is an important phenomenon that is the leading driver of morphology in thin and ultrathin films, as the chain orientation is a function of the direction of crystal growth and polymer chains as they attach to the growing crystal<sup>10-11, 13, 34, 71</sup>.

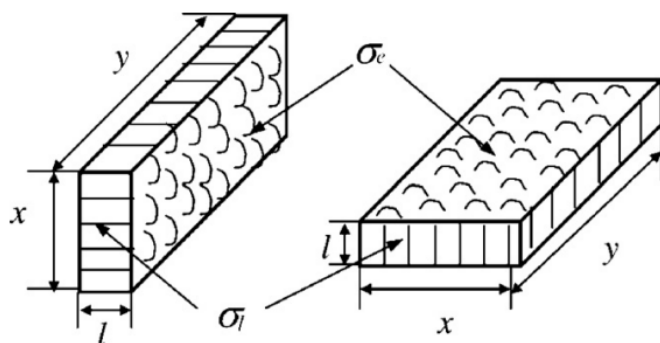


**Figure 1.6.** Diagram illustrating the edge-on (left) to flat-on (right) transition in ultrathin semi-crystalline polymer films. Reproduced with permission from Liu, Yi-Xin, and Er-Qiang Chen. "Polymer crystallization of ultrathin films on solid substrates." *Coordination chemistry reviews* 254.9-10 (2010): 1011-1037<sup>34</sup>.

In thin and ultrathin films where flat-on orientations are preferred, the system exhibits “diffusion-limited” growth where “dense branching,” “dendritic,” “seaweed,” and “fractal” crystals can form<sup>1</sup>. Because the film thickness is very near that of the lamellar thickness,

growth can *only* occur parallel to the substrate. Whereas in spherulitic structures where the crystal can grow by amorphous polymer chains attaching to the growing crystal in all three dimensions, growing crystalline nuclei in these ultrathin films rely on the diffusion of amorphous polymer chains to the growth front parallel to the substrate surface only, leading to flat, branching morphologies such as the one shown in Figure 1.7:

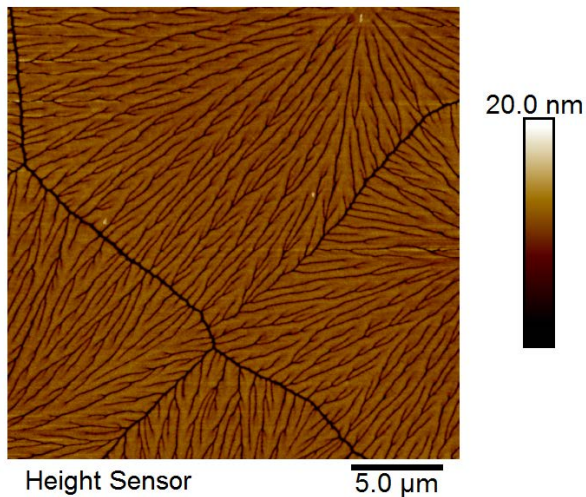


**Figure 1.7.** Atomic force microscopy image of 12 nm 45 kDa PCL as cast from toluene. This film exhibits a dense branching morphology (DBM).

This leads to two main phenomena: First, the speed of crystal growth in these ultrathin films is greatly reduced due to the longer time it takes the polymer chains to diffuse to the much smaller growth faces. Second, the morphology observed in these films are dendritic or fractal in nature, having multiple independent branches that are comprised of the growing two-dimensional crystals.

### 1.5 Crystallization Kinetics

Because the crystallization of semi-crystalline polymers is a continuous growth process, the kinetics of crystallization can be better understood on the basis of a few key steps. In fact, the overall crystallization process can be broken up to two main events: nucleation and growth<sup>1, 17, 38, 62, 72</sup>. Primary nucleation is the formation of the first seed of a domain where order is higher than the surrounding medium. In homogeneous nucleation, which is typically driven by temperature, the system reaches a point at which two polymer molecules are close enough together and oriented in such a way such that they are able to be attracted to each other and form a densely-packed initial nucleus. While temperature provides the energetic effects necessary such that forming a stable crystal is as likely as not (i.e. at the melting temperature,  $T_m$ ), the homogeneous process is very much stochastic<sup>38</sup>. That is, two systems at the same external conditions (temperature, pressure, etc.) will undergo nucleation at different times due in part to the entropy in the system and the necessity for there to be two polymer molecules in the right place and oriented in the right way. On the other hand, heterogeneous nucleation is the nucleation of ordered polymer domains driven in part by an external surface such as a dust particle or some other impurity. Heterogeneous nucleation is far more likely to occur due to the rarity of having a completely pure system. Secondary nucleation refers to crystal nucleation due to the presence of already-formed crystal nuclei that lower the driving force for crystallization and spur multiple nucleation sites.

Naturally, the secondary nucleation process is also a growth process. This growth process is controlled by two main albeit conflicting characteristics. The first is the change in free energy necessary to form a secondary nucleation event. The other is the energy barrier of chains diffusing to the nucleus so that the growth front may progress. The

prevailing theory of polymer crystallization kinetics was done by Lauritzen and Hoffman (hence why it is now known as Lauritzen-Hoffman growth theory)<sup>62, 72-74</sup>. Their main finding was that secondary nucleation and crystal growth can be described in terms of three main “regimes:”

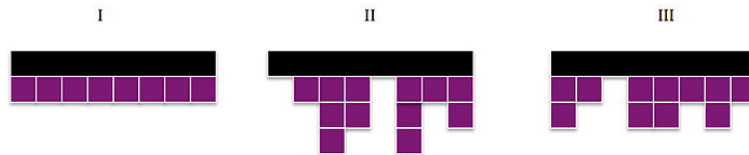


**Figure 1.8.** Diagram showing the three regimes of Lauritzen-Hoffman growth theory. Reproduced with permission from “Hoffman nucleation theory,” Creative Commons.

Regime I growth can be found at crystallization temperatures close to the melting point. At these temperatures, the dynamics of chain movement are very slow, and as such, chains are more likely to grow parallel to the growth face of the crystal to completely cover the crystal plane than continue nucleating outwards. Regime II can be found at temperatures farther away from Regime II growth. Here, the likelihood of growing laterally is approximately equal to nucleation and growth outwards. In Regime III, at temperatures significantly far away from the melting point, Nucleation is sporadic across the face of the crystal such that multiple new layers are formed before a complete plane is filled in. These findings form the basis of how crystal growth at different conditions is understood, especially on the foundation of different crystallization temperatures.

## 1.6 Thesis Significance & Overview

This work focuses on the unique characteristics exhibited by semi-crystalline polymers confined in thin film geometries. Specifically, polycaprolactone (PCL), a biocompatible and biodegradable polyester is used as a model system. This is due to several factors. For one, polycaprolactone is a semi-crystalline polyester with a simple chain structure like that of polyethylene, one of the most widely-used commodity semi-crystalline polymers<sup>10, 16, 19, 29, 31, 75-76</sup>. Additionally, polyethylene and polycaprolactone have similar crystal structures, having comparable *a* and *b* dimensions, but a larger *c* dimension due to the ester group in PCL<sup>29</sup>. However, PCL crystallizes orders of magnitude more slowly than polyethylene, which eases the study of crystallization kinetics, especially growth rate. Furthermore, PCL exhibits a melting point ( $T_m$ ) around 60 °C, which makes melting and crystallization experiments simple to conduct without a need for significant heating over ambient conditions. Finally, polycaprolactone exhibits better solubility in commonly used casting solvents such as toluene and THF, especially as compared to other semi-crystalline polymers like polyethylene, polypropylene, and polyethylene glycol. These favorable characteristics alongside the large body of research into PCL in bulk systems make PCL a very attractive model system for thin film studies.

Additionally, there is valid reasoning behind the study of the effects that thin film confinement has on polymer crystallization. Many studies in the past few decades have studied the phenomena exhibited in thin films because this geometry is advantageous for numerous applications, such as thin film transistors<sup>77-78</sup>, photovoltaics<sup>79-80</sup>, solar cells<sup>30, 81</sup>, and for surface-mediated drug delivery<sup>82-84</sup>. Additionally, the large body of research into semi-crystalline polymers in the bulk, including studies on thermal properties elucidated

via calorimetry or structure elucidated by X-ray scattering provide us a solid basis on which to compare our results and comment on the unique advantages of thin films. Studies in thin films allow us to more closely monitor the phenomena exhibited by individual crystals and lamellae, and when compared to the averaged information obtained in the bulk, provides us a clearer picture of crystallization. For example, these studies allow us to better understand the way that the orientation of crystals on a lamellar scale affects film stability, the direction and speed of crystal growth, nucleation density, crystal size, and thermal transitions, and other factors. Control over the extent of confinement means some level of control over the polymer characteristics. Taken one step further, this means we can enhance the applications that rely on semi-crystalline polymers, including electronics, optics, and solar cell technology, via control of the geometric confinement. While much of the work contained in this thesis leans towards the study of some of the more fundamental characteristics of semi-crystalline polymers, such as morphology, film stability, thermal transitions, and kinetics, the insight we gain from these studies is what is eventually used to tune applications since their characteristics rely on these fundamental factors.

This thesis is broken into seven sections. Chapter 2 focuses on the methods used to characterize the polymers both synthesized in our lab as well as once they are processed and confined in a thin film geometry. This is done from a fundamental viewpoint as well as through commentary on the useful information these techniques provide for thin film studies.

Chapter 3 discusses our discovery of a new nano-structured polymer blend morphology we named the “nano-rose” morphology for its resemblance to a bouquet of roses. This study illustrates that certain non-crystalline blend components allow us to affect

the direction of crystal growth under controlled confinement conditions. Therefore, it allows us to discuss the blend factors that affect crystal growth and those that do not.

Chapter 4 describes the discovery and development of a new, simple method for measuring thermal transitions in semi-crystalline polymer thin films. By studying film thickness, we can detect melting and crystallization temperatures as well as study crystal growth under isothermal conditions. Because many of the techniques used to study thermal transitions in thin films require removal of the film from the substrate, this technique allows study of substrate effects on thermal transitions in an accessible and simple manner.

Chapter 5 describes our first major observation in the study of the significant differences between linear and cyclic PCL confined in thin and ultrathin films, specifically that cyclic PCL exhibits a resistance to dewetting compared to its exact linear analogs. Despite the expectation that cyclic should be less stable than the linear architecture, we find the opposite to be true. This study brings into question, among other things, the effects that chain orientation and chemistry have on film stability. Furthermore, the possibility that the cyclic architecture affords significantly enhanced stability over the linear has significant implications on applications using polymers confined in thin films, especially those involving lithography or some thermal treatments where dewetting is likely and a barrier to using certain materials.

Chapter 6 discusses further observations of the differences in morphology and especially the kinetics of crystal growth in linear and cyclic PCL. Specifically, it is shown that linear and cyclic PCL exhibit different crystallization kinetics in thin and ultrathin films. Furthermore, blending the two architectures together allows modulation of both the crystal growth rate as well as nucleation density and crystal size. Thus, we can affect these

factors without introducing non-polymer additives, which is attractive for drug delivery and cell studies where the purest material possible is extremely attractive.

Finally, Chapter 7 concludes the work described in this thesis with an outlook to the future of semi-crystalline thin film studies, both in the short and long term. This chapter includes commentary on each of the five project areas. Specifically, we would like to have a better understanding of how transferable the findings we have made on PCL are to other semi-crystalline polymers. This is especially important in areas where we find very intriguing properties, such as unique crystal growth and blend phenomena, enhanced film stability due to different architectures, and control over crystal growth kinetics. In the end, these studies must be taken one step further to additional semi-crystalline systems since that will allow us to comment further on PCL itself as well as semi-crystalline phenomena due to thin film confinement. Because of the decades of work that have been done already and the continuing use of semi-crystalline polymers in various applications, this body of research will continue to be an exciting and important one, especially as the techniques used to monitor and study crystallization improve.

## Chapter 2

### CHARACTERIZATION TECHNIQUES

The chemical and physical characterization methods available for polymers confined in thin film geometries can be divided into a few focus areas. First are the methods for characterizing synthesis, such as molecular weight, dispersity, and end-group modifications as done by gel permeation chromatography (GPC) and matrix-assisted laser desorption/ionization (MALDI). Next are the methods for characterizing thermal behavior, such as the glass transition temperature and melting point, which is typically done via differential scanning calorimetry (DSC). Finally, thin-film specific characterization techniques aim to quantify film thickness, morphology, and molecular-scale crystal structure, including spectral reflectance, optical and atomic force microscopy, and X-ray scattering. This chapter will also discuss spincoating and flowcoating, the two film casting techniques used in this work.

#### 2.1 Gel Permeation Chromatography (GPC)

One of the most important characteristics of a polymer is its molecular weight distribution or dispersity. In fact, the molecular weight of the polymer will dictate virtually every important characteristic of the final material, especially how it behaves in thin films. Namely, molecular weight affects casting solution viscosity, diffusion, crystal growth rate, film stability, annealing kinetics, degradation rate, and phase separation behavior, to name

a few. Therefore, measuring and reporting the molecular weight of every synthesized polymer is vital. One of the favored techniques for characterizing the molecular weight of polymers is gel permeation chromatography (GPC), part of the characterization techniques that falls under the umbrella of size exclusion chromatography (SEC)<sup>12, 85-89</sup>. In a typical GPC setup, there is a collection of columns in series filled with beads of a porous gel with varying pore geometry. The polymer sample, dissolved in a carrier solvent (typically tetrahydrofuran or toluene for hydrophobic polymers), is injected into the columns. The dispersity in the molecular weight of the individual polymer molecules leads to a range of hydrodynamic radii in solution. The porous gel beads are able to trap and slow down material with smaller hydrodynamic radii<sup>90-91</sup>. Therefore, the higher the hydrodynamic radius (and therefore molecular weight), the quicker it will complete the path through and out of the column(s). Once the molecule leaves the column, their concentration can be measured via several techniques, typically through a refractive index detector (as was used in these studies) (see Figure 2.1) or via other techniques such as UV absorption.

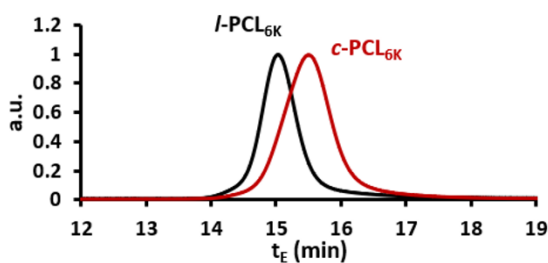


**Figure 2.1.** GPC chromatogram showing the elution times of linear and cyclic polycaprolactone using a refractive index detector. “a.u.” is the absorbance intensity measured by the detector and  $t_E$  is the elution time. Here, cyclic PCL exhibits a longer elution time due to the smaller hydrodynamic radius caused by the collapsed ring structure.

By measuring the differential refractive index of the polymer solution leaving the column and comparing it to the refractive index of the pure solvent, we can determine a concentration distribution which is directly related to the molecular weight of the polymer in the solution. This observed concentration distribution is compared to a set of monodisperse polystyrene standards that are also run through the columns. For many polymer systems, there are calibration equations relating the elution times of the polymer with the unknown dispersity with that of the polystyrene standards. Furthermore, in studying the concentration distribution, if we find that the concentration distribution is broad, it is indicative that there is a broad distribution of molecular weights in the sample tested<sup>92</sup>. Additionally, the ability to detect differences in hydrodynamic radius also provides us a tool to confirm the synthesis of non-linear architectures such as cyclic polymers (as shown above). For example, cyclizing a polymer will significantly decrease its hydrodynamic radius, which can be detected using GPC. Since the goal is to synthesize polymers with the lowest dispersity possible, the narrowest distribution possible is ideal.

## 2.2 Matrix Assisted Laser Desorption/Ionization (MALDI-TOF)

One of the pitfalls of GPC is its reliance on the porous crosslinked polystyrene gel or surface treated silica gel as a packing material, as well as the use of polystyrene standards to compare elution times of the polymer studied. Because the hydrodynamic phenomena exhibited by every polymer is unique, this creates a non-negligible amount of error in the reported molecular weight. To combat this, polymer scientists and engineers have studied and developed the use of mass spectroscopy for measuring the molecular weight of polymers and other macromolecules. Specifically, the discovery and commercialization of

matrix-assisted laser desorption/ionization – time of flight (MALDI-TOF) has enhanced the ability to measure molecular weight in low to mid-molecular weight materials (<50 kDa)<sup>93-97</sup>. A diagram of the general operation of MALDI-TOF is shown in Figure 2.2:

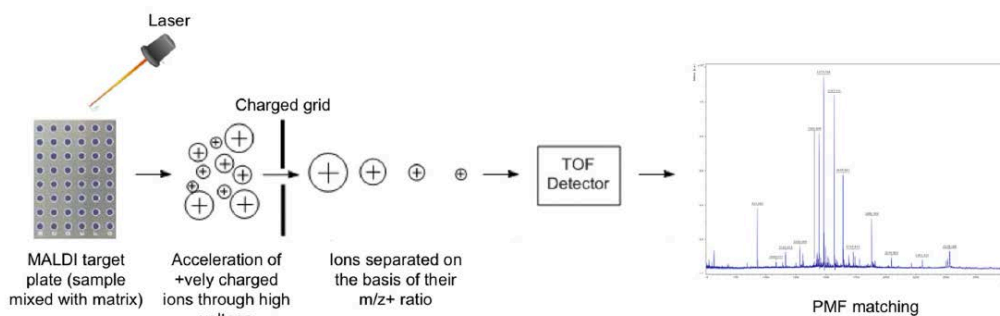


**Figure 2.2.** Diagram showing the basic operation of MALDI-TOF. A high-power laser is directed onto the matrix containing the polymer and ion. This laser treatment causes the mixture to ablate, generating free-floating polymer in the gas phase that is then directed to the time-of-flight detector due to differential charge along the path to the detector. Based on the mass to charge ratio (and therefore the molecular weight), the species will reach the detector at different time points. Reproduced with permission from *Singhal N, Kumar M, Kanaujia PK and Viridi JS (2015) MALDI-TOF mass spectrometry: an emerging technology for microbial identification and diagnosis. Front. Microbiol. 6:791*<sup>98</sup>

Polymer sample is mixed in very dilute conditions with a metal ion in a low molar mass crystalline material (the matrix). When this solid mixture is exposed to short pulses of a high energy laser in vacuum, the matrix ablates, and the polymer enters the vapor phase. Concurrently, the polymer complexes with the metal ions that were part of the matrix. The path length between the matrix and the detector contains an ion accelerator and a system

for modulating electric and magnetic fields. Because the extent of ionic charge is directly related to the number of molecules available for ionization, different molecular weights will have different mass-to-charge ratios, and when under constant magnetic/electric fields, the polymer molecules will move through the flight path at different velocities, and therefore encounter the detector at different time points. Thus, the molecular weight distribution of a polymer sample can be detected. However, because MALDI operates behind the principle of mass-to-charge ratios, it offers exceptional resolution in terms of molar masses. Therefore, not only can MALDI-TOF offer molecular weight and dispersity information, but it can resolve repeat unit molar masses and confirmation of end group modification due to unique molar masses of these chemical functionalities.

### 2.3 Differential Scanning Calorimetry (DSC)

Similar in importance to the molecular weight of the polymer are the thermal transitions the polymer exhibits. For amorphous polymers, the key thermal transition is the glass transition temperature ( $T_g$ ). The glass transition temperature is the temperature at which polymer goes from a “glassy” or thermally trapped state where motion is minimized to a “rubbery” state where segmental motion is greatly enhanced. This is the point at which thermal annealing can occur as is used in block copolymer thin film work. For semi-crystalline polymers, the more pertinent thermal transitions are usually the crystalline melting point ( $T_m$ ) and equilibrium crystallization temperature ( $T_{c,0}$ ). The melting point is the temperature at which the crystalline domains melt, and the entire system becomes amorphous. Correspondingly, the equilibrium crystallization temperature ( $T_{c,0}$ ) is the temperature at which the chains overcome thermal motion and begin to form locked-in

ordered domains during the temperature ramp. These values have been shown to be dependent on the heating or cooling rate<sup>99</sup>. Of course, as is observed in isothermal crystallization experiments, the system can crystallize at any isothermal crystallization temperature ( $T_c$ ) below the melting point given sufficient time.

The preferred method for measuring these thermal transitions is differential scanning calorimetry (DSC)<sup>43-45, 100</sup>. This technique works by measuring the heat flow required to maintain the sample at a predetermined temperature ramp, either up or down and comparing it to a reference sample (typically an empty sample pan). When the system reaches a thermal transition, the material requires a greater heat flow in or out to maintain the temperature, which is different than that of the reference cell. Thus, the thermal transitions can be easily measured and reported.

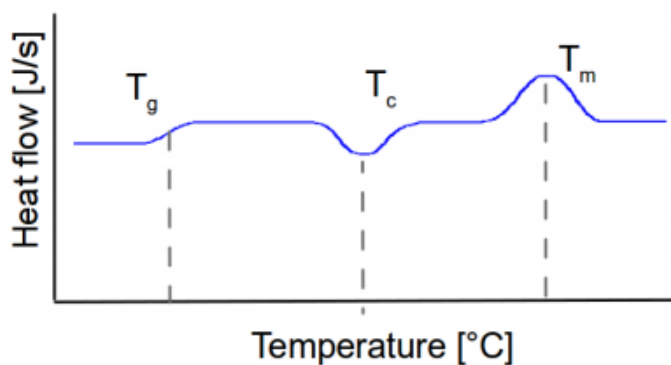


**Figure 2.3.** Sample DSC data showing the three main thermal transitions determined by DSC when a semi-crystalline polymer is first rapidly cooled to below its  $T_g$  from the melt and then heated (temperature increased from left to right); one method for determining thermal transitions in semi-crystalline polymers via DSC: glass transition ( $T_g$ ), crystallization temperature ( $T_c$ ), and melting temperature ( $T_m$ ). Reproduced from a DSC

operation manual, “Investigation of Polymers with Differential Scanning Calorimetry.”  
Humboldt Universitat Zu Berlin

As shown in Figure 2.3, the data generated by a DSC experiment can be interpreted by studying the heat flow in our out and the characteristic transitions at the glass transition ( $T_g$ ), crystallization ( $T_c$ ), and melting ( $T_m$ ) temperatures, because each one has a well-defined increase or decrease in the amount of heat flow needed to keep the polymer at the same temperature ramp as the sample cell. For semi-crystalline polymers, DSC has also been used to determine enthalpies of melting, crystallization kinetics, and degree of crystallinity<sup>22, 27, 47, 101-102</sup>, however the methods for those analyses are not applicable to thin and ultrathin films. This is because DSC study requires milligrams of material, and in any case, would require complete removal of the polymer from the substrate.

#### 2.4 Spectral Reflectance

Any studies which aim to describe the effect of thin film confinement on any polymer phenomena are dependent on a very precise technique for measuring the film thickness. Generally, this is accomplished via a few techniques, ranging from generating a hole in the film and measuring its depth using atomic force microscopy (the so called “scratch test”) to X-ray reflectivity (XRR) as part of small angle X-ray scattering experiments. Less destructive techniques rely on the refractive index and reflectivity of light, which is material-dependent. Such is the basis behind techniques such as ellipsometry<sup>103-107</sup> and spectral reflectance<sup>108-109</sup>. Based on the refractive index and reflectivity of the substrate, reflected light can be measured and compared to an optical

model to determine a very precise film thickness. Because it was the most widely used film thickness measurement technique used in this thesis, the discussion will focus on the background of spectral reflectance.

Spectral reflectance is a method used to measure the film thickness of both polymeric and non-polymeric materials ranging from a few nanometers all the way up to tens of microns. Unlike ellipsometry, where the reflectance of light is measured at a pre-determined low incident angle, spectral reflectance measures the intensity of reflected light normal to the substrate. With knowledge of the substrate material and refractive index of the material(s) present in the film, spectral reflectance can resolve film thicknesses accurate to 1 nm or  $\pm 0.2\%$ , whichever is greater. Additionally, the ability to use light ranging from 200 nm to 1100 nm paired with measurement times in the millisecond range allows users a relatively non-destructive technique depending on the UV-sensitivity of the material. Spectral reflectance can also be used to measure the wavelength dependence of refractive index ( $n_D$ ) and the extinction coefficient ( $k$ ). It has been used in countless studies to very precisely measure film thicknesses in a wide variety of materials, and in Chapter 4, a method is discussed using spectral reflectance to measure thermal transitions in crystalline polymer thin films.

The concept of spectral reflectance and how it is used to measure film thickness is relatively simple. Light is reflected at some magnitude whenever it crosses the boundary between two materials. In a typical experiment, reflection intensity of a polymer thin film sample is measured as a function of wavelength (see Figure 2.4).

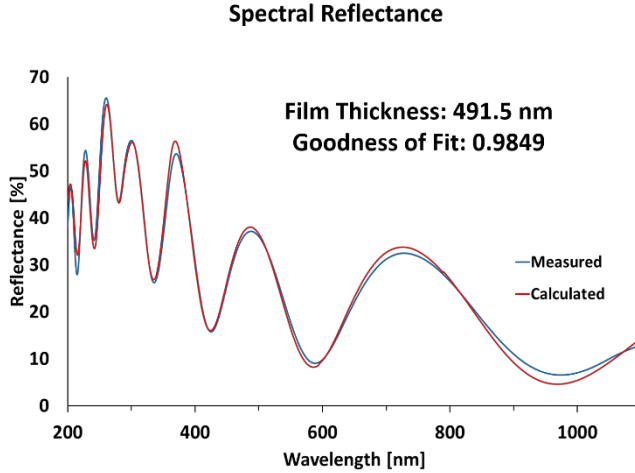


**Figure 2.4.** Reflectance intensity vs. Wavelength for 491 nm 45 kDa PCL studied via spectral reflectance. The blue and red curves represent the measured and calculated spectra, respectively.

The magnitude of the reflection is directly related to the optical constants  $n$  and  $k$ , and the film thickness:

$$R \approx A + B \cos\left(\frac{4\pi}{\lambda} nd\right)$$

Equation 2.1

where  $A$  and  $B$  are constants that include  $k$ ,  $d$  is the thickness of the film,  $n$  is the refractive index, and  $\lambda$  is the wavelength of light. Since the user typically knows what material they are measuring the film thickness of, the only unknown is the intensity of reflected light. It is important to note that  $n$  and  $k$  show some wavelength dependence (for  $k$ , only if the material is absorbing;  $k \neq 0$ ). However, since the measured spectral reflectance is taken at multiple wavelengths, the  $n$  and  $k$  can be resolved as a function of wavelength as well.

## 2.5 Optical Microscopy/Polarized Light Optical Microscopy (OM/PLOM)

Optical microscopy is one of the key techniques used to observe the surface structure and morphology of various materials, both polymeric and non-polymeric. This technique allows for magnification of surface features between 2.5x and 100x, which is adequate to study the micron-sized spherulites in thin polymer films. Because the films described in this study are confined to silicon wafers, reflection mode is used since the substrate does not allow the transmission of light. Therefore, reflection allows the study of the topography of the surface of polymer films, and since thin polymer films are semi-transparent, offer the ability to probe somewhat beyond the surface and into the film. Optical microscopy is also used to study the existence of defects in polymer films due to impurities on the substrate surface or in the polymer/polymer solution. Overall, optical microscopy is an excellent technique for studying the global morphology of thin polymer films.

Additionally, optical microscopy can be modified with the use of several in-line polarization filters, which is referred to as polarized light optical microscopy (PLOM)<sup>1</sup>. This technique uses the normal microscope reflection mode setup, however adds two additional polarizing filters: a polarizer situated after the condenser and analyzer situated after the objective lens<sup>1</sup>. This filter allows only light that is polarized in a specific plane to enter the lens. Thus, it blocks light polarized in the other planes. If an amorphous sample is studied, i.e. one that is unable to shift the polarization plane of light entering and returning, no features can be observed. However, for a semi-crystalline sample with anisotropic crystals that exhibit birefringence, the reflected light can be rotated in such a way that it is in the correct plane to pass through the polarizer and analyzer<sup>48</sup>. Most

importantly, polarized light optical microscopy allows us to verify the existence of spherulitic crystalline macrostructures. This is because spherulitic crystals in polymer thin films exhibit a characteristic Maltese Cross extinction pattern (see Figure 2.5) when observed by cross polarizers<sup>48, 53, 55</sup>.

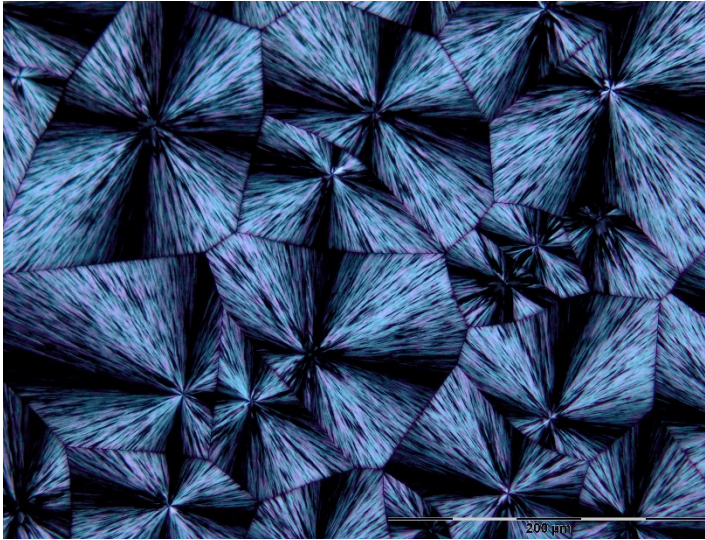


**Figure 2.5.** 550 nm 12 kDa linear PCL studied via polarized light optical microscopy (PLOM). This film exhibits Maltese Cross extinction patterns, indicative of well-formed 2-dimensional spherulites. Scale bar equals 200  $\mu\text{m}$ .

The ability to quantify the global morphology of a polymer thin film and the existence of spherulites is a powerful one. Optical and polarized light microscopy can also be used in *in situ* studies of crystal growth. By affixing a well-controlled heating stage to the microscope, microscopy can be used to observe melting and crystallization, and quantify crystal growth kinetics.

## 2.6 Atomic Force Microscopy (AFM)

As described above, for films in the hundreds of nanometers to tens of microns on reflective surfaces such as silicon, there is enough material in the film such that morphology can be studied optically. However, as the film thickness goes below approximately 50 nm, there is a negligible optical contrast due to the small amount of material present in the film. In film thickness regimes below this critical value, typically termed “ultra-thin” films, AFM is the favored technique due to its ability to resolve surface morphology in films as thin as polymer brushes (tens of angstroms)<sup>1, 4, 11, 13-14, 20, 33, 110-113</sup>. Generally, AFM operates by the interaction between the material surface with a tip that is rapidly scanning back and forth across the surface. A red laser is focused onto the apex of the tip which is calibrated to reflect into a photodetector. As the tip scans across the surface, its movement is tracked via the movement of this laser reflection in the photodetector, thus creating an “image” of the substrate. The fundamentals of how the tip interacts with the surface can be chosen and dictates the scanning mode, the most commonly used being contact mode, tapping mode, and PeakForce tapping mode (pioneered by Bruker).

Contact mode, typically reserved for more mechanically robust materials like metals, works via the tip remaining in close contact with the surface and therefore directly tracking the materials surface features. This method is not commonly used for polymeric materials due to the likelihood of damage to the polymer surface.

In TappingMode, the tip is driven by a piezo element in the AFM unit at or near its resonance frequency. “Tapping” refers to the fact that this mode requires only intermittent interactions between the tip and the surface. As the tip gets closer to the surface, the amplitude of the cantilever oscillations decreases, which can be measured by the AFM

software. Thus, the feedback control in TappingMode is based on a determined amplitude set point from which deviations are calculated and corrected for through movement of the piezo element. This serves two purposes that make TappingMode advantageous: First, because sample topography will mean that this amplitude will change at different points in the up-and-down motion, TappingMode is able to precisely record sample topography and surface features. Second, different materials will affect the tip oscillation to different degrees. In the case of phase separated polymer blends or nanostructured block copolymers, this allows AFM to resolve different domains based on mechanical properties which helps resolve the phase-separated morphology.

In PeakForce Tapping, the probe similarly encounters the surface only intermittently in a “tapping” fashion. However, in PeakForce Tapping, the tip is not oscillating at its resonance frequency as in TappingMode. This minimizes the effect of a resonating system. Additionally, the system can resolve a force curve at every interaction point. This is because the tip, in its up and down motion, goes through several distinct events (see Figure 2.6).

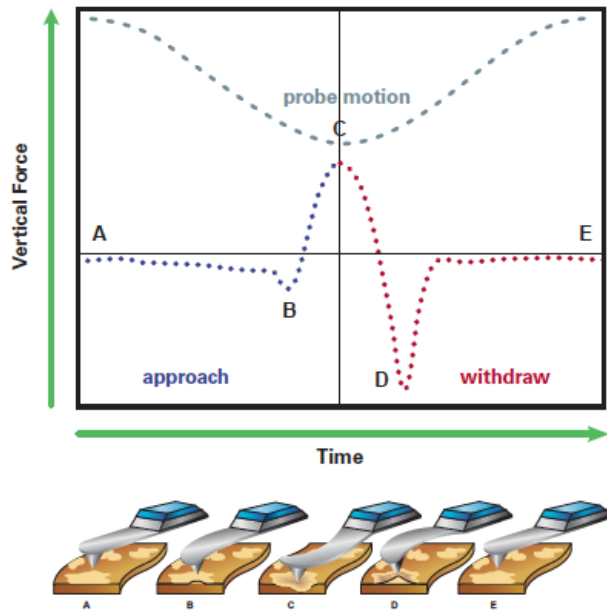


**Figure 2.6.** Basic operation of PeakForce Tapping showing the generation of force curves and the steps (A-E) of tip interaction with the sample surface during operation. From Bruker Application Notes: “Introduction to Bruker’s ScanAsyst and PeakForce Tapping AFM Technology” by Stefan B. Kaemmer.

First, as the tip approaches the surface (A), it will feel the attraction due to the long-range Van der Waals forces. This will cause the tip to “snap on” to the surface (B). Force will then be applied and either the sample or the tip will deform (C), thus reaching the “peak force” in that spot. Upon retraction, the tip will again feel the adhesion force between the surface and the oscillating tip (D). Finally, the tip retracts from the surface and is free to complete another oscillation (E). Here, feedback control is instead based on the peak force set point and deviations from this setpoint are mapped as differences in height, mechanical, adhesion, etc. This mode carries with it several benefits. Like TappingMode, it can very precisely measure the topography of the surface, down to atomic level

resolution. Because of the intermittent nature of the interaction, sample damage is exceptionally minimized. Finally, when operated in PeakForce Quantitative Nanomechanical Mapping (QNM) mode, the program algorithm can use the force curves generated during contact along with a calibrated probe to not only resolve differences in the mechanical properties of one or more components, but it can quantify the mechanical properties, such as modulus, extent of deformation, and adhesion force. Thus, PeakForce Tapping and PeakForce QNM offer researchers studying thin film materials the best resource to fully characterize the surface morphology and other characteristics of their films.

### 2.7 Grazing-Incidence Wide Angle X-Ray Scattering (GIWAXS)

The aforementioned techniques excel at studying the morphology of the films on a local (nm to  $\mu\text{m}$ ) and global ( $\mu\text{m}$  to mm) scale, especially structure at the free surface of the film. These methods, however, do a poor job of probing the molecular-level structure and overall crystal organization of the film. For these studies, we require a technique that can probe both deep into the film, and measure features at a size scale in the angstrom range. To this end, researchers have developed and used wide angle X-ray scattering (WAXS) to study the crystal structure and orientation of crystalline materials, both polymeric and non-polymeric<sup>19, 41-42, 114</sup>. By studying the scattering of coherent X-rays, users can resolve very important crystal characteristics, namely the orientation and dimensions of the material crystal faces. However, WAXS is used for bulk materials such as powder samples or thick, free standing films<sup>39</sup>. WAXS cannot be used for substrate supported thin films due to the impermeability of the silicon substrate and smaller amounts

of material present in these thin films. Thus, grazing incidence wide-angle X-ray scattering was developed (see Figure 2.7).

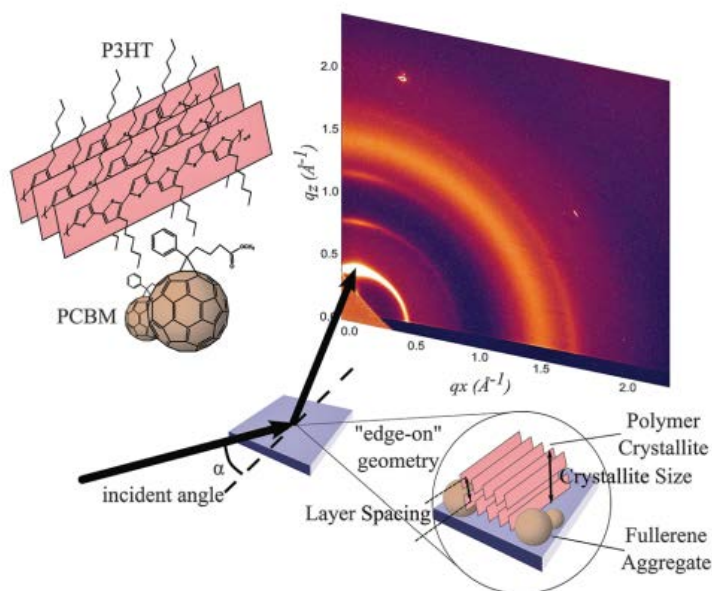


**Figure 2.7.** Diagram showing the basic operation of grazing incidence wide-angle X-ray scattering. Coherent X-rays enter the surface of the film at an incident angle  $\alpha$  and are scattered into the two-dimensional detector. Reproduced with permission from Ashraf, A., D. M. N. M. Dissanayake, and M. D. Eisaman. "The effect of confinement on the crystalline microstructure of polymer: fullerene bulk heterojunctions." *Physical Chemistry Chemical Physics* 17.36 (2015): 23326-23331<sup>115</sup>

Here, the scattering of X-rays is measured at very low incident angles. By tuning to the correct incident angle such that the X-rays permeate far enough into the film, the crystal structure and orientation in thin films can be resolved. This is done by studying the scattered intensity captured by the two-dimensional detector. If there are no crystalline domains in the film, there will be effectively no discernible scattering patterns except for an "amorphous halo" that is seen in completely amorphous materials. However, if

crystallization is present, this will manifest itself as scattering spots or more commonly, scattering bands (see Figure 2.8).

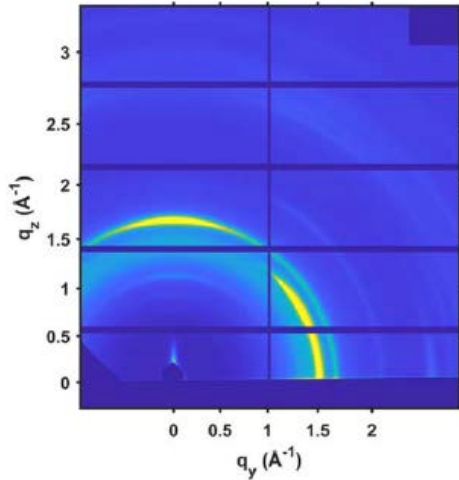


**Figure 2.8.** Two-dimensional scattered X-ray intensity from a 500 nm 45 kDa PCL film studied at the Advanced Photon Source (APS) at Argonne National Laboratory. This  $q_z$  vs  $q_y$  representation of scattered intensity exhibits the anisotropy of crystals in different planes of the film, as well as the unit cell spacing.

Most often seen in thicker films, these scattering bands are indicative of the range of orientations of the crystalline lamellae due to their radial distribution in the spherulites that comprise the material (see Chapter 1). In materials with a single or perfect orientation (more commonly seen in small molecules) the bands would instead be discrete scattering spots. The location of these bands in  $q$  are characteristic to the polymer and are directly related to the different crystal indices and unit cell dimensions. Furthermore, the relative intensity of these bands is indicative of the ratio of crystal indices as well as the orientations

of the crystal groups in the planes of the film. Thus, GIWAXS offers a multitude of information regarding the crystal structure and orientation in thin and ultrathin films.

One of the main shortcomings of the grazing incidence technique is its inability to calculate an exact degree of crystallinity due to the lack of a full 360-degree scattering pattern. However, we are still able to calculate a qualitative degree of crystallinity. This is done by integration of the two-dimensional scattering data to generate a one-dimensional intensity vs.  $q$  plot of the entire scattering data. This plot can then be used to fit the individual crystalline and amorphous peaks that comprise the scattering data. The degree of crystallinity is then the ratio of the crystalline peak area to the entire peak area.

## 2.8 Spincoating

Spincoating is one of the most widely-used film casting techniques due to the commercial availability of spincoating systems and their ease of use<sup>11, 20-21, 32-33, 105, 111</sup>. Spincoating has been used for decades in academic and industrial research areas ranging from polymer thin film study to nano-templating and photolithography. As the name implies, spincoating is the process of casting a thin film via a circular, spinning motion of the substrate<sup>116-118</sup>. After a liquid is deposited onto the substrate surface, the spinning motion of the substrate generates centrifugal force that thins the liquid, both through the centrifugal force acting on the liquid, as well as the through a fraction of the liquid leaving the substrate altogether (see Figure 2.9).

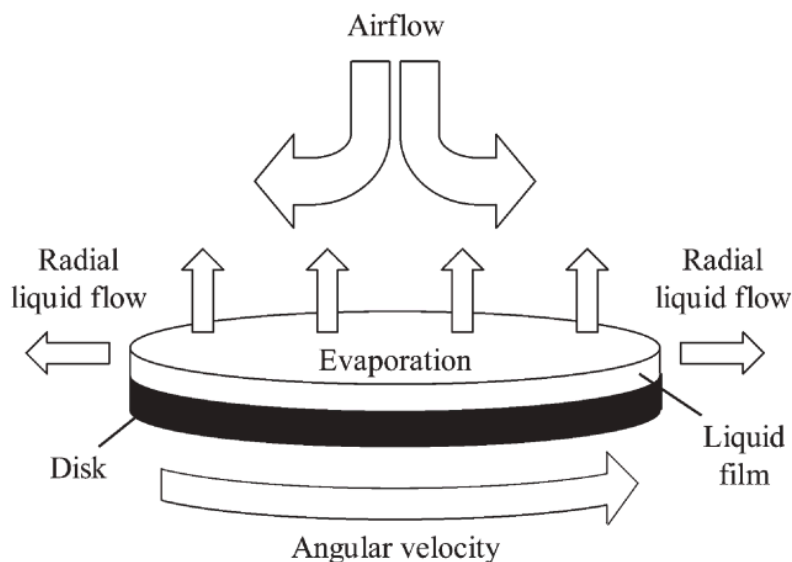


**Figure 2.9.** Concurrent events during the spincoating process that cause the film to thin and dry. Reproduced with permission from Norrman, K., A. Ghanbari-Siahkali, and N. B. Larsen. "6 Studies of spin-coated polymer films." Annual Reports Section "C"(Physical Chemistry) 101 (2005): 174-201<sup>118</sup>

In most polymer thin film studies, this liquid is an organic solution of polymer dissolved in some chosen solvent. Thus, this thinning will be combined with and followed by the evaporation of the solvent and formation of a solid polymer layer. Following from the above, there are a few main variables that dictate the spincoating process.

The motion of the substrate can be broken down into three factors: the rotation speed [rpm], rotational acceleration to that constant rotation speed [rpm/s], and the amount of time that the substrate is rotated in total [s]. Obviously, the film thickness is going to be inversely proportional to the rotation speed, as a higher rotation speed generates more centrifugal force, and therefore a greater extent of thinning. This speed is the most important and most easily tunable variable in the spincoating process. The acceleration

dictates how quickly the substrate goes from immobile to the chosen final rotation speed. Generally, the acceleration is set such that the film reaches its final rotation speed in 5-10 seconds. Tuning this value is mostly dependent on the viscosity of the solution, i.e. a more viscous solution should be accelerated more quickly than a less viscous one, so as to minimize initial non-uniformities that are more likely to occur with a viscous solution that has more resistance to thinning. If these non-uniformities are not resolved early in the spincoating process, and the solvent has a sufficiently high vapor pressure, these non-uniformities can be locked-in to the final film structure. Finally, the amount of time that the substrate is rotated should be dictated solely by the vapor pressure of the solvent so as to ensure a solid final film. In other words, the amount of time the substrate is rotated should be sufficiently long such that it has no effect on the final film thickness.

## 2.9 Flowcoating

Flowcoating is a relatively new film coating technique that has gained traction in the last decade<sup>21, 119-123</sup>. In a typical flowcoating system, a coating blade, usually a glass slide, is positioned at a predetermined angle ( $\alpha$ ) above a mobile substrate stage. The gap height of the blade (G) (the distance between the coating blade and the substrate) is usually held at 200 microns. Because of this small gap height, a polymer solution deposited between the blade and substrate wicks and is confined between the two surfaces. When the substrate is then moved, capillary and friction forces leave a layer of polymer solution that subsequently dries into a uniform polymer thin film (see Figure 2.10).

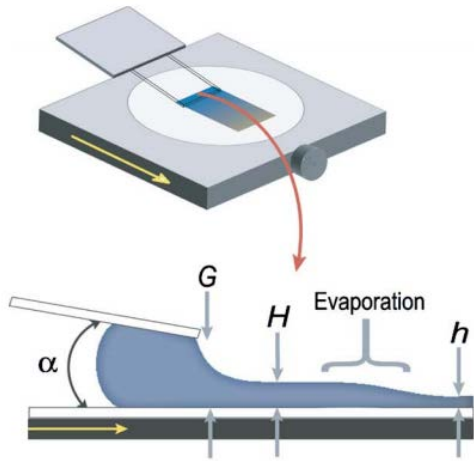


**Figure 2.10.** Cartoon showing the basic setup and variables involved in the flowcoating of thin polymer films. Reproduced with permission from Stafford, Christopher M., et al. "Generating thickness gradients of thin polymer films via flow coating." *Review of scientific instruments* 77.2 (2006): 023908<sup>121</sup>.

The most important factor in this coating process is the speed at which the stage moves. It is the instantaneous velocity of the substrate that dictates the thickness of the wet film coated ( $H$ ), and therefore the thickness of the final dry film ( $h$ ). Thus, moving the stage at a constant velocity will generate a uniform film of a constant thickness. This factor also leads to one of the well-known benefits of flowcoating over spincoating: the ability to create gradient thickness films by moving the substrate with a constant acceleration instead of a constant velocity. Thus, flowcoating adds another powerful tool to generate uniform or gradient thickness films which, in the case of the gradient thickness films, allows for high-throughput studies on the effect of film thickness driven confinement.

## **Chapter 3**

# **ULTRATHIN FILM CRYSTALLIZATION OF POLY( $\epsilon$ - CAPROLACTONE) IN BLENDS CONTAINING STYRENE- ISOPRENE BLOCK COPOLYMERS: THE NANO-ROSE MORPHOLOGY**

We report the discovery of a new nanostructured morphology in ultrathin blend films of semi-crystalline poly( $\epsilon$ -caprolactone) (PCL) and various styrene-isoprene block copolymers. The nano-rose morphology is visualized by atomic force microscopy as a monolayer of approximately 500 nm diameter crystalline spirals. Our finding that the nano-rose morphology occurs in a narrow film thickness window commensurate with the crystalline lamellar thickness suggests that this distinctive morphology results from redirection of growing PCL crystalline lamellae due to confinement effects during film casting. The nano-rose morphology was located in blends with several block copolymers of various architecture but was absent in blends with the individual homopolymer components. PCL molecular weight did not affect nano-rose size or film thickness window. However, solvent choice was an important factor, with nano-rose formation favored in non-polar and weakly polar solvents. This work supports theories that unbalanced surface stresses and impurity exclusion cause polymer crystals to grow unconventionally.

This chapter is based on published work: Kelly, Giovanni M., and Julie NL Albert. "Ultrathin film crystallization of poly ( $\epsilon$ -caprolactone) in blends containing styrene-isoprene block copolymers: The nano-rose morphology." *Polymer* 117 (2017): 295-305.

### 3.1 Introduction

A “polymer blend” refers to any system where two (or more) unique polymers are mixed together. Blends can be comprised of semi-crystalline, amorphous, copolymers, or any combination of these different polymer types. What is most important about these systems is the immiscibility of the two polymers. The thermodynamics of mixing can be described rather simply:

$$\Delta G_m = \Delta H_m - T\Delta S_m$$

(Equation 3.1)

Where  $\Delta G_m$ ,  $\Delta H_m$ , and  $\Delta S_m$  are the free energy, enthalpy, and entropy of mixing, respectively. In some cases, due to chemistry and other factors, and if the free energy of mixing ( $\Delta G_m$ ) is negative, the polymers are called miscible with each other. In this case, the polymer blend exhibits a single phase and a combination of the characteristics of the components (such as combined thermal transitions). More often though, the two components in the polymer blend are immiscible ( $\Delta G_m$  is positive), that is that they undergo phase separation from each other. This leads to a polymer blend that contains independent, phase separated domains of the polymer components.

Similar to the treatment done with polymer-solvent systems, Flory-Huggins theory can be applied to polymer blends to describe their thermodynamic behavior. Instead of

having a polymer-solvent lattice system, both polymer chains can be considered on the same lattice. Thus, a polymer molecule can either interact with itself, or a molecule of the other component of the polymer blend.

Polymer blending has benefitted society for many years, allowing the advantageous properties of multiple materials to be combined into a single product. Much work has been done on the theoretical and experimental aspects of miscibility and phase separation in polymer blends and the synergistic benefits of polymer blending for a wide variety of consumer applications. In thin films, research has focused on specialty coatings and the effect of substrate and free surface interfaces and film thickness on polymer blend and block copolymer phase behavior<sup>20, 30, 124-127</sup>. These variables may lead to thin film phase behavior that differs significantly from the bulk. Additional factors like crystallization, chain architecture, and copolymer sequence may complicate phase behavior but offer opportunities for tuning material properties and discovering new morphologies.

Polymer crystallization is especially interesting since the kinetics of crystal growth often lead to unique morphological phenomena. Within this field, several studies have documented unconventional crystal growth in single-component polymer systems<sup>10, 53, 55, 128-129</sup>. For example, Keith and Padden observed that polyethylene crystals can undergo non-uniform lamellar twisting in spherulites, creating s- and c-shaped crystals and banded spherulites<sup>52, 130-131</sup>. In these studies, the authors found that polyethylene crystals grown from the melt experience asymmetric surface stresses exacerbated by chain tilt in the growing half-lamellae that make up the full crystal. These studies led to what is known as Keith and Padden theory<sup>52, 130-132</sup>, which states that lamellar twisting arises from half lamellae curving in opposite directions whereas s- and c- shaped crystals result from half

lamellae curving in the same direction. Kikkawa et al. studied melt-grown poly(L-lactide) (PLLA) in 70 nm and 300 nm films and observed s-shaped crystals in the former and s- and c-shaped crystals in the latter via atomic force microscopy (AFM)<sup>129</sup>. They reasoned that the origin of curved lamellae was either inclination of molecular chains inside the crystal as it grew or chain shift along the crystallographic c-axis that exacerbated screw dislocations during crystal growth, but that this effect was not a consequence of the film thickness. Mareau and Prud'homme observed that 6 nm poly( $\epsilon$ -caprolactone) (PCL) films isothermally crystallized at 30 °C for 20 hours showed c-shaped crystal growth<sup>10</sup>. The authors connected their results to Keith and Padden theory, attributing c-shaped crystal growth to curvature in half PCL lamellae during growth from the melt. Additionally, the studies by Kikkawa et al.<sup>129</sup> and Mareau and Prud'homme<sup>10</sup> as well as results from Vancso et al.<sup>14</sup> show that the forces applied during *in situ* AFM measurement can alter the dynamics and direction of crystal growth. Another cause of non-linear crystal growth observed by Bassett and coworkers<sup>133-135</sup> and modeled by Schultz<sup>56</sup> is the presence of “impurities” in the form of non-crystallizable material. In polyethylene systems, the growing polymer crystal reorients itself to avoid a high concentration of non-crystallizable material, which would serve as an impediment to crystal growth. In the work by Bassett and coworkers, the growing crystalline lamellae avoided impurities by branching or nucleating crystals with slightly altered directions<sup>134-135</sup>. In contrast, Schultz's model predicted lamellar twisting due to the impurity effect, and these model results were consistent with other experimental data<sup>56</sup>. An indispensable and exhaustive review of the causes and observations of lamellar twisting and other unconventional crystal growth phenomena was written by Lotz and Cheng<sup>132</sup>. Analyzing and describing the origin of

lamellar twisting and non-linear crystal growth remains challenging due to difficulties in observing crystal growth at the molecular level. To the best of our knowledge, there is still no widely accepted cause for these growth phenomena, but they are instead thought to be a complex interplay of surface stresses, crystal structure, chirality, non-crystallizable impurities, and crystal growth characteristics<sup>132</sup>.

Herein we report the discovery of a new semi-crystalline polymer morphology, which we refer to as the “nano-rose” morphology for its resemblance to a bouquet of roses. This morphology occurs in thin film blends of poly(caprolactone) (PCL) with various block copolymers containing polystyrene and polyisoprene (SIS) (Figure 3.1). The nano-rose morphology contains features that curl outward and upward in a regular manner, creating a relatively monodisperse collection of 500 nm diameter spirals. Correlation length analysis of Figure 3.1 using the program GTFiber<sup>136</sup> provided additional verification of the nano-rose diameter (see Appendix A, Figure A1). Selectively removing the SIS component by washing the films with cyclohexane showed no change in the morphology (see Appendix A, Figures A2 and A3). Therefore, we attribute nano-rose formation to PCL crystallization after film casting. Line cuts across the nano-rose features of the washed sample showed that the lamellar spirals have a height of  $7.65 \pm 0.31$  nm, which is close to the lamellar thickness of PCL<sup>10,27</sup>. We find the nano-rose morphology remarkable not only for its novelty, but also for its potential to add to our understanding of crystallization in thin films.

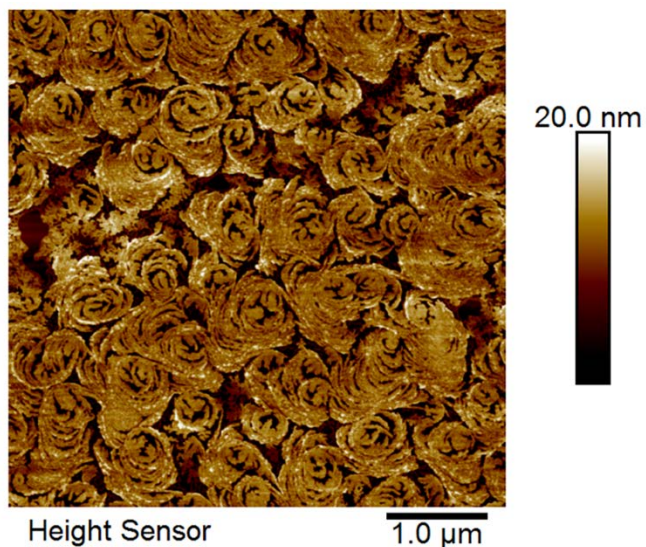


**Figure 3.1.** AFM height image of 12 nm thick blend film of 45 kDa PCL and SIS vector 4293A containing 50 wt % SIS, spin coated from toluene. This film exhibits the “nano-rose” morphology.

Ours is the first blend system that we know of to exhibit this form of crystal growth, and it does so in the ultrathin film regime commensurate with the crystalline lamellar thickness of PCL. Compared to prior studies, we have a two-component blend instead of a single component system, we observe extensive lamellar spiraling rather than twisting or scrolling, and we find that curved crystals form during film casting as opposed to recrystallization from the melt state. The PCL/SIS system forms features with more regular and much smaller radii than previously reported curved morphologies<sup>131, 137-138</sup>, and because the films are fully crystallized prior to imaging by AFM, the morphology cannot be attributed to shear forces imparted on the sample during AFM. In the current study, we focus on identifying the crystallization environment that gives rise to deviating lamellar growth directions. Specifically, we investigated the dependence of the nano-rose morphology on film thickness, block copolymer architecture, blend ratio, substrate surface

energy/chemistry, PCL molecular weight, and casting solvent. Our results show that confinement effects may give rise to unbalanced surface stresses that form the foundation for curving of lamellar crystals.

### 3.2 Experimental Section

**Materials.** Three commercially available hydroxyl-terminated linear poly( $\epsilon$ -caprolactones) (Sigma Aldrich,  $M_n = 10$  kDa,  $\mathcal{D} = 1.4$ ;  $M_n = 45$  kDa,  $\mathcal{D} = 1.5$ ;  $M_n = 80$  kDa,  $\mathcal{D} = <2$ ) were used as received. Three block copolymers containing polystyrene and polyisoprene blocks (collectively referred to as “SIS”) of various architectures were kindly supplied by TSRC Dexco, and also used as received. Vector 4211A is a linear SIS triblock; vector 4215A is a linear SIS triblock/SI diblock blend; and vector 4293A is a 4-arm star/SI diblock blend in which the arms of the star contain polyisoprene midblocks (core) and polystyrene endblocks. All three SIS species have a 30 wt % polystyrene fraction and a molecular weight slightly above 100 kDa. Comparable linear SI diblocks were purchased from Polymer Source (P2208-Sip,  $M_n = 117$  kDa,  $\mathcal{D} = 1.07$ ; P3868-Sip,  $M_n = 47$  kDa,  $\mathcal{D} = 1.08$ ). Polystyrene and poly(*cis*-isoprene) homopolymers ( $M_w = 20$  kDa and 35 kDa, respectively) were purchased from Sigma Aldrich and used as received. Benzyltrimethylchlorosilane (benzyl silane) was purchased from Gelest, Inc. and used as received.

**Film Preparation.** All ultra-thin films were cast via spin coating or flow coating. Briefly, spin coating is a method of film casting where the rotation of the substrate is used to thin and dry a deposited polymer solution. Flow coating uses the capillary forces of the polymer solution entrenched between the substrate and a coating blade paired with drag forces induced by a moving substrate to coat a thin polymer film<sup>119, 121</sup>. While both film

casting methods are excellent for creating polymer films at a discrete film thickness, flow coating is beneficial for creating gradient thickness films to facilitate high throughput studies on thin film confinement effects<sup>6, 122-123, 139-143</sup>. Spin coated films were cast using 0.5 wt % solutions at speeds of 10,000 RPM and an acceleration of 2,500 RPM/s. Flow coated films were cast using 1 wt % solutions at a stage velocity of 10 mm/s and acceleration of 1.67 mm/s<sup>2</sup>. For substrate modifications prior to film casting, benzyl silane was pipetted directly onto clean, UV-ozone treated silicon wafers and left to react for 2 hours to form a monolayer. Excess silane was rinsed off with toluene, and the sample was blown dry with nitrogen.

**Characterization.** Film thicknesses were quantified by spectral reflectance over a wavelength range of 400 nm to 1100 nm (Filmetrics F20). Spin coated samples were characterized by taking the average of five film thickness measurements from different spots on the sample. Gradients were characterized by taking the average of five film thicknesses measurements perpendicular to the flow coating direction. This data was used to create film thickness [nm] vs. position [mm] maps to assign film thicknesses to images acquired by AFM (see Appendix A, Figure A4). Static water contact angles in air were quantified using a Ramé-Hart goniometer to verify successful substrate modification with benzyl silane.

Thin film morphology was characterized via atomic force microscopy (AFM) (Bruker Dimension ICON AFM) operating in PeakForce Quantitative Nanomechanical Mapping (PF-QNM) mode and using ScanAsyst-Air tips ( $k = 0.4$  N/m; resonant frequency = 70 kHz). All films were fully crystallized prior to AFM characterization except in the case of the *in situ* temperature and growth studies. In the *in situ* temperature study, thin

films were placed on a heating stage, and the temperature was increased in 5 °C increments from 25 °C up to the temperature at which melting or motion was observed. These samples were allowed time to equilibrate for at least 3 minutes at each temperature before images were acquired. The *in situ* growth study was conducted by taking AFM images immediately after flow coating to capture images of nano-rose growth. To probe the molecular-level structure of the nano-rose morphology, as-cast thin film samples of pure PCL and a blend exhibiting the nano-rose morphology were studied via grazing incidence wide-angle X-ray scattering (GIWAXS). GIWAXS measurements were performed at beamline 8-ID-E of the Advanced Photon Source at Argonne National Laboratory<sup>42</sup>. An X-ray wavelength of  $\lambda = 1.1417 \text{ \AA}$  (energy 10.86 keV) was used. The sample was measured under vacuum and the scattering measured for an incident angle  $\theta = 0.14^\circ$  and exposure time of 5 s. To quantify the domain spacing ( $L_0$ ) of the block copolymers used, pure block copolymer films (thicknesses  $\approx 125 \text{ nm}$ ) were studied via grazing incidence small-angle X-ray scattering (GISAXS). GISAXS measurements were performed at beamline 8-ID-E of the Advanced Photon Source at Argonne National Laboratory<sup>42</sup>. An X-ray wavelength of  $\lambda = 1.1364 \text{ \AA}$  (energy 10.91 keV) was used. The sample was measured under vacuum and the scattering measured for an incident angle  $\theta = 0.14^\circ$  and exposure time of 1 s. The acquired GIWAXS and GISAXS data (as two-dimensional images) were further treated and analyzed using *GIXSGUI* software package<sup>144</sup>.

### 3.3 Results and Discussion

Our first discovery of the nano-rose morphology occurred in a blend of 45 kDa PCL and SIS vector 4293A (4-arm star/SI diblock blend, TSRC Dexco) containing 50 wt % SIS

spin coated from toluene solution to produce a film 12 nm in thickness (Figure 3.1). This morphology presents itself as a monolayer of circular crystalline structures that bears no resemblance to the thin film morphologies of the individual components. PCL homopolymer films exhibit crystalline dendrites or dense branches that grow parallel to the substrate and radially outwards from the nucleation point (see Appendix A, Figure A5). SIS vector 4293A exhibits a poorly ordered cylinder nanostructure with a domain spacing of  $\approx 30$  nm (see Appendix A, Figure A6). Traces of the morphologies associated with typical polymer-polymer phase separation via nucleation and growth or spinodal decomposition are also absent. Instead, the growing crystals appear to be impeded by the block copolymer component causing crystalline lamellae to curl and grow upwards instead of laterally outwards. The chains curl both clockwise and counterclockwise, and the nanoroses are relatively monodisperse, with an average diameter of approximately 500 nm. In the context of polymer crystallization, this narrow feature size distribution and symmetry of features is intriguing given the polydispersity and anisotropy of crystal grains typically seen in bulk and in thin films.

## Molecular Structure

Although AFM is the primary technique used to characterize thin and ultrathin film morphologies, we aimed to better understand the molecular level structure of this morphology using grazing incidence wide-angle X-ray scattering (GIWAXS). The 2D spectra as well as the scattering profiles along the  $q_y$  axis for thin film samples of pure PCL and the nano-rose morphology are compared in Figure 3.2. Both films exhibit peaks corresponding to (110) and (200) growth faces at  $q_y$ -values of  $1.5 \text{ \AA}^{-1}$  and  $1.7 \text{ \AA}^{-1}$ , respectively. These growth faces are characteristic to PCL<sup>41</sup> and verified that while the nano-rose morphology exhibits a curling morphology, crystal organization at the molecular level is unchanged. However, the 2D GIWAXS images indicate a difference in lamellar orientations between the pure PCL and nano-rose films. While the 2D GIWAXS pattern from the pure PCL film has distinct diffraction spots that can be interpreted as near-perfect alignment of lamellae flat-on with respect to the substrate, the banding present in the pattern from the nano-rose film shows that this film has a broader distribution of lamellar orientations. Thus, our GIWAXS data analysis supports the idea that confinement effects in the nano-rose system cause reorientation of the growing crystalline lamellae.

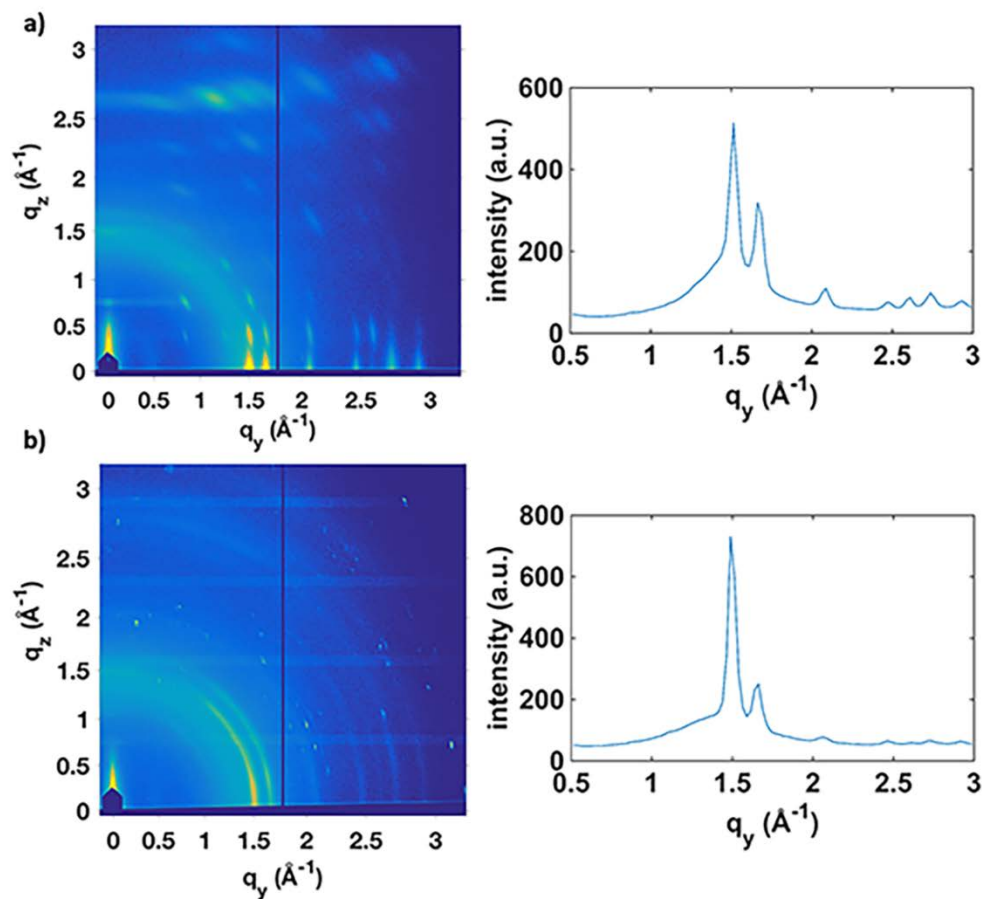


**Figure 3.2.** GIWAXS 2D spectra and intensity vs.  $q_y$  plots for samples of (a) pure PCL and (b) nano-rose, both exhibiting characteristic crystalline peaks at  $q_y$ -values of 1.5  $\text{\AA}^{-1}$  and 1.7  $\text{\AA}^{-1}$  corresponding to (110) and (200) growth faces, respectively.

To locate each of the two components in the nano-rose morphology, 1  $\mu\text{m}$  scan size AFM images were taken of the nano-rose morphology before and after washing with cyclohexane to remove the SIS component (Figure 3.3). Comparison of these images revealed that the majority of the nano-rose spiral consists of crystalline material (PCL), with some of the amorphous SIS integrated into the rose “petals” but the majority segregating to the areas in between individual nano-roses. This lateral segregation is

similar to what was described by Bassett and coworkers, who postulated that impurities and other non-crystallizable materials would be laterally displaced by growing crystalline lamellae<sup>134-135</sup>. The SIS component within the nano-rose showed no evidence of nanoscale order, unlike 14 nm thick films of pure SIS, which exhibit a poorly-ordered nanostructure (see Appendix A, Figure A6).

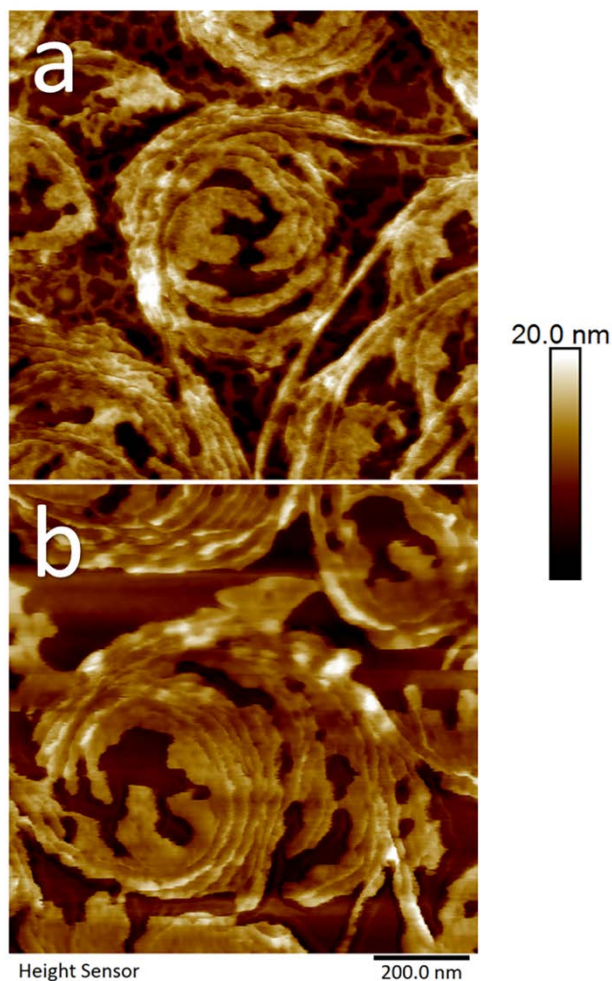


**Figure 3.3.** AFM height images of 45 kDa PCL/SIS Vector 4293A blend exhibiting the nano-rose morphology (a) as cast from toluene and (b) after washing with cyclohexane to selectively remove the SIS component.

## **Melting and Recrystallization**

We suspected that the nano-rose morphology was non-equilibrium so we conducted melting and recrystallization experiments to test this hypothesis. Upon melting a film exhibiting nano-roses at 75 °C and recrystallizing the film at 25 °C, the nano-roses completely disappeared (see Appendix A, Figure A7). This result was surprising; we had expected that at this temperature the SIS component (highest  $T_{g, \text{bulk}} \approx 100$  °C due to the polystyrene block) would be able to lock in the blend structure and force PCL ( $T_{m, \text{bulk}} \approx 65$  °C) to recrystallize in the form of nano-roses. However, the thermal transition temperatures of both components are significantly depressed due to the ultrathin film geometry<sup>145-147</sup>. In studying morphology as a function of temperature in nano-rose, pure PCL, and pure SIS films, we observed that nano-roses began melting at approximately 45 °C. Pure PCL and pure SIS films exhibited an onset of thermal transition around 55°C (see Appendix A, Figures A8-A10). These results highlight both the vertical and lateral confinement effects in this blend.

## **Effect of Film Thickness on Morphology**

Because the nano-rose morphology was discovered in spin coated films, we first verified that its formation is independent of casting method (compare Figure 3.1 (spin coated) and Figure 3.4d (flow coated)). This result allowed us to cast gradient thickness films via flow coating to study the effect of film thickness on the nano-rose morphology. Gradients were flow coated in the thickness range of 5 nm to 20 nm. At 6 to 7 nm, the system has a dendritic morphology (Figure 3.4a). Increasing slightly in film thickness

revealed that the roses first appear at the crystal nucleation points (Figure 3.4b and Appendix A, Figure A11) and then increasingly cover the surface until they occur over the entirety of the film from 9 to 14 nm (Figure 3.4c-3.4d). Increasing film thickness further causes the roses to fill in, and the morphology evolves into a larger dense branching structure (Figure 3.4e-3.4f).

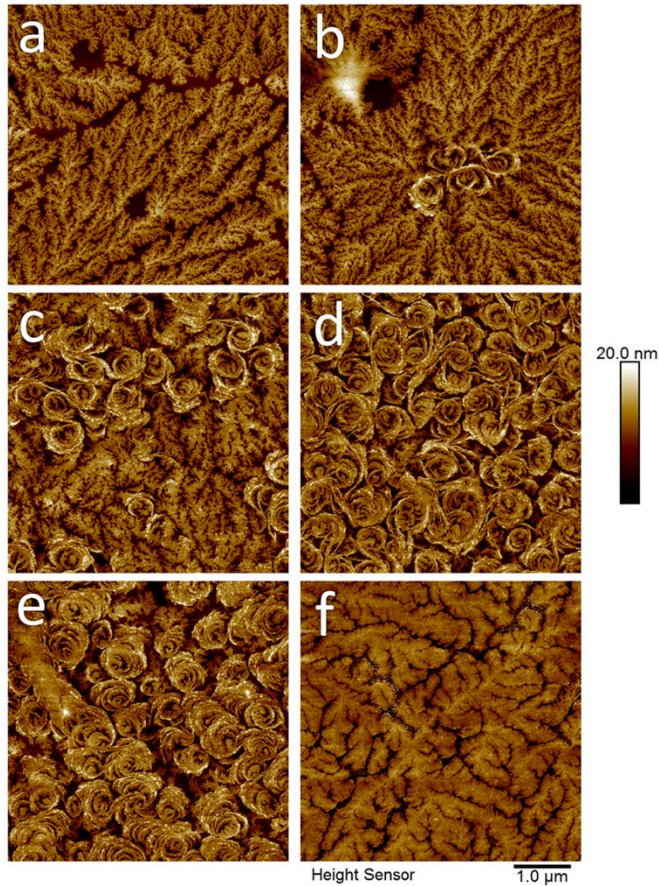


**Figure 3.4.** AFM height images of 45 kDa PCL/SIS vector 4293A blend containing 50 wt % SIS showing the development and disappearance of the nano-rose morphology as a function of film thickness: (a) 6 - 7 nm; (b) 7 - 8 nm; (c) 8 - 9 nm; (d) 9 - 14 nm; (e) 14 - 16 nm; and (f) 16 - 18 nm.

Both the dendritic (6 – 8 nm) and dense branching (16 – 18 nm) morphologies are associated with lamellae oriented flat-on to the substrate. Unlike the flat-on to edge-on transition in homopolymer films, the lamellar re-orientation in our blends appears to be transient and occurs over a thickness range close to the lamellar thickness.

### **Effect of Block Architecture on Morphology**

Prior research by others has shown that block copolymer architecture affects morphology in asymmetric diblock copolymers, star-branched block copolymers, and single and double-crystalline block copolymers<sup>23, 148-151</sup>. Thus, we wanted to understand whether the star or block architecture of SIS vector 4293A was necessary for the formation of the nano-rose morphology, or if PCL would crystallize in this form in other polymer blends as well. TSRC Dexco kindly supplied us with two additional SIS block copolymers of differing architectures: vector 4211A (linear SIS) and vector 4215A (triblock SIS/diblock SI blend). Comparable 118 kDa SI diblock (40k-b-77.5k) (P2208) and 47 kDa SI diblock (16.5k-b-30.5k) (P3868) were purchased from Polymer Source. We observed that blends of PCL with each of the four additional block copolymers exhibited the nano-rose morphology in a thickness window comparable to that of the original PCL/SIS vector 4293 blend (Figure 3.5a-3.5d). However, the nano-rose morphology did not form in blends of PCL with polyisoprene (PI) or polystyrene (PS) at 50 wt % PI or PS (Figure 3.5e-3.5f). The PCL/PI blend exhibited a branching morphology. These branches form an incomplete layer at low thicknesses (6 - 9 nm) but gradually cover the substrate as film thickness increases (Figure 3.3d); however, no evidence of curling crystalline features was observed. The PCL/PS blend exhibited a thick bi-continuous phase separated morphology with PS at

the free surface and PCL at the substrate, consistent with previous reports<sup>20, 124</sup>. Thus, the nano-rose morphology could not be attributed to the polymer architecture (star, diblock, linear triblock) or molecular weight of the amorphous component, but blending with a block copolymer rather than another homopolymer was necessary for its formation. Furthermore, these results show that the nano-rose size as quantified using GTFiber is not strongly dependent on the block copolymer molecular weight or domain spacing (see Appendix A, Figure A12; domain spacings from GISAXS:  $L_{0,SIS4211A} = 28.5$  nm;  $L_{0,SIS4215A} = 30.3$  nm;  $L_{0,SIS4293A} = 28.5$  nm;  $L_{0,P2208 SI} = 52.5$  nm;  $L_{0,P3868 SI} = 36.9$  nm). The average nano-rose diameter calculated across all 45 kDa PCL/block copolymer blends is  $498.9 \pm 34.3$  nm.

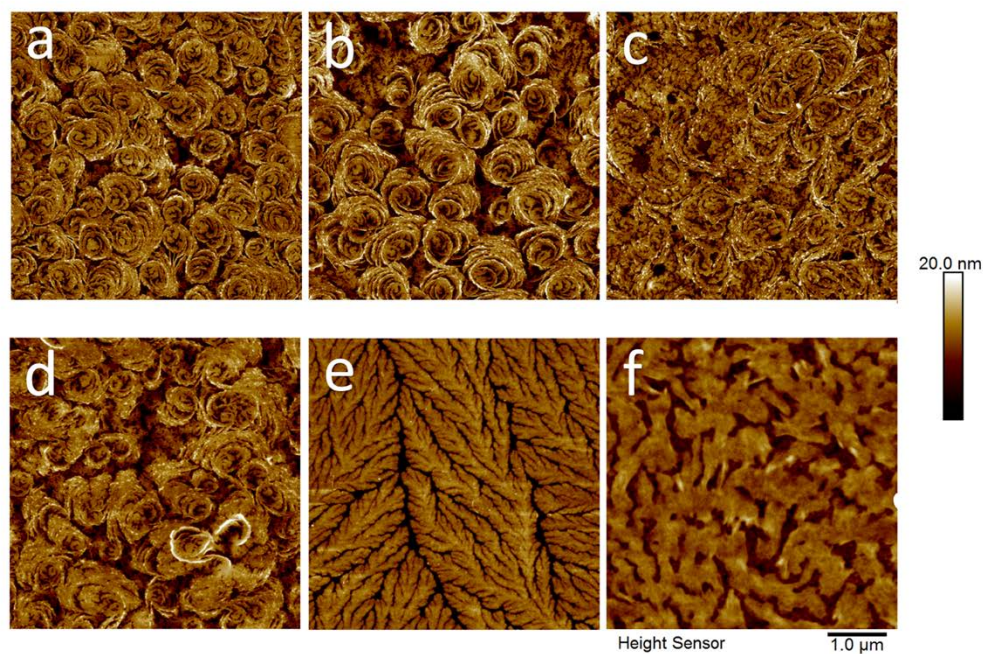


**Figure 3.5.** AFM height images of approximately 12 nm thick blend films containing 45 kDa PCL and 50 wt % amorphous polymer: (a) SIS vector 4211A; (b) SIS vector 4215A; (c) P2208 SI diblock; (d) P3868 SI diblock; (e) 35 kDa PI; and (f) 20 kDa PS.

Chemical and physical differences between PS, PI, and SIS may lead to nano-rose development in blends with block copolymers but not homopolymers. First, PS is glassy whereas PI is rubbery at ambient conditions. The styrene-isoprene block copolymers combine these attributes making them stiffer than PI due to the PS block(s) and more pliable than PS due to the PI block. Structural rigidity, or lack thereof, in the non-crystalline component will dictate how quickly and in what direction crystals can grow<sup>19</sup>. Second, PCL, PS, and PI have surface energies of 43 mJ/m<sup>2</sup>, 41 mJ/m<sup>2</sup>, and 32 mJ/m<sup>2</sup><sup>3,33</sup>, respectively, and the surface energy of SIS is estimated as 33.4 mJ/m<sup>2</sup> (volume-fraction weighted average of block components assuming 10% toluene as residual solvent), so the differences in interfacial interactions between these components and the growing PCL crystal are non-negligible. Being the lowest surface energy component, PI or SIS is expected to segregate to the free surface, while PCL is expected to favor the polar silica substrate surface. Finally, the mobility of block copolymer chains at different solvent evaporation conditions may have synergistic effects on PCL crystallization in this blend system. These factors highlight important differences between homopolymer and block copolymer blends.

### **Effect of Blend Composition on Morphology**

Just as the magnitudes of surface interactions between polymer components and between the polymers and the substrate are principle considerations in morphology development, the surface area of interaction is equally important. Experimentally, the interfacial area between blend components is determined by blend composition through its influence on domain sizes<sup>32, 111, 124, 148</sup>. To study and quantify the blend compositions where nano-rose formation is possible, film thickness gradients of 45 kDa PCL/SIS vector 4293A blends with compositions ranging from pure PCL (0% SIS) to pure SIS (100% SIS) were flow coated from toluene. The results for films cast within the original nano-rose film thickness window are shown in Figure 3.6. Pure PCL at this film thickness exhibits a dense branching morphology. At 25 wt % SIS, crystal growth parallel to the surface is disrupted and propagation perpendicular to the substrate is evident from the increased vertical contrast in the AFM image. From 40 wt % SIS to 45 wt % SIS, the morphologies become relatively flat again and curls are seen sporadically in the films. The nano-rose morphology occurs readily at 50 wt % SIS (Figure 3.1) and persists until an SIS fraction of 70 wt %. Beyond 70 wt %, the crystalline structure transitions to a thick branched morphology that incompletely covers the surface. At 100% SIS, the block copolymer is phase separated into a poorly ordered nanostructure. Notably, each of the blend ratio films that exhibits nano-roses does so in the film thickness range between 8 nm and 14 nm. The complete morphology characterization by AFM of representative gradient thickness blend ratio films is provided in the Appendix A, Figures A13-A18. Based on these results, we propose that a critical SIS content of at least 50 wt % and less than 70 wt % is necessary to cause curvature in growing PCL crystals.

The nano-rose blend composition window is centered at a composition slightly greater than 50% SIS, suggesting that an optimal combination of interfacial interactions and spatial confinement is needed to create a barrier to PCL crystal growth parallel to the substrate and cause redirection (curling) and reorientation of growing lamellae. At sufficiently high SIS fraction, the SIS domains will limit the avenues of supply of PCL chains to the growth front. The presence of SIS also affects the space and chemical environment in which the PCL can crystallize. These effects explain why curling occurs and why the roses are relatively monodisperse. At higher SIS fractions (e.g., 75 wt %), we believe that partial vertical phase separation of SIS and PCL allows PCL to grow predominantly outwards and parallel to the substrate without strong enough lateral confinement to cause the spiraling needed to form the nano-rose morphology.

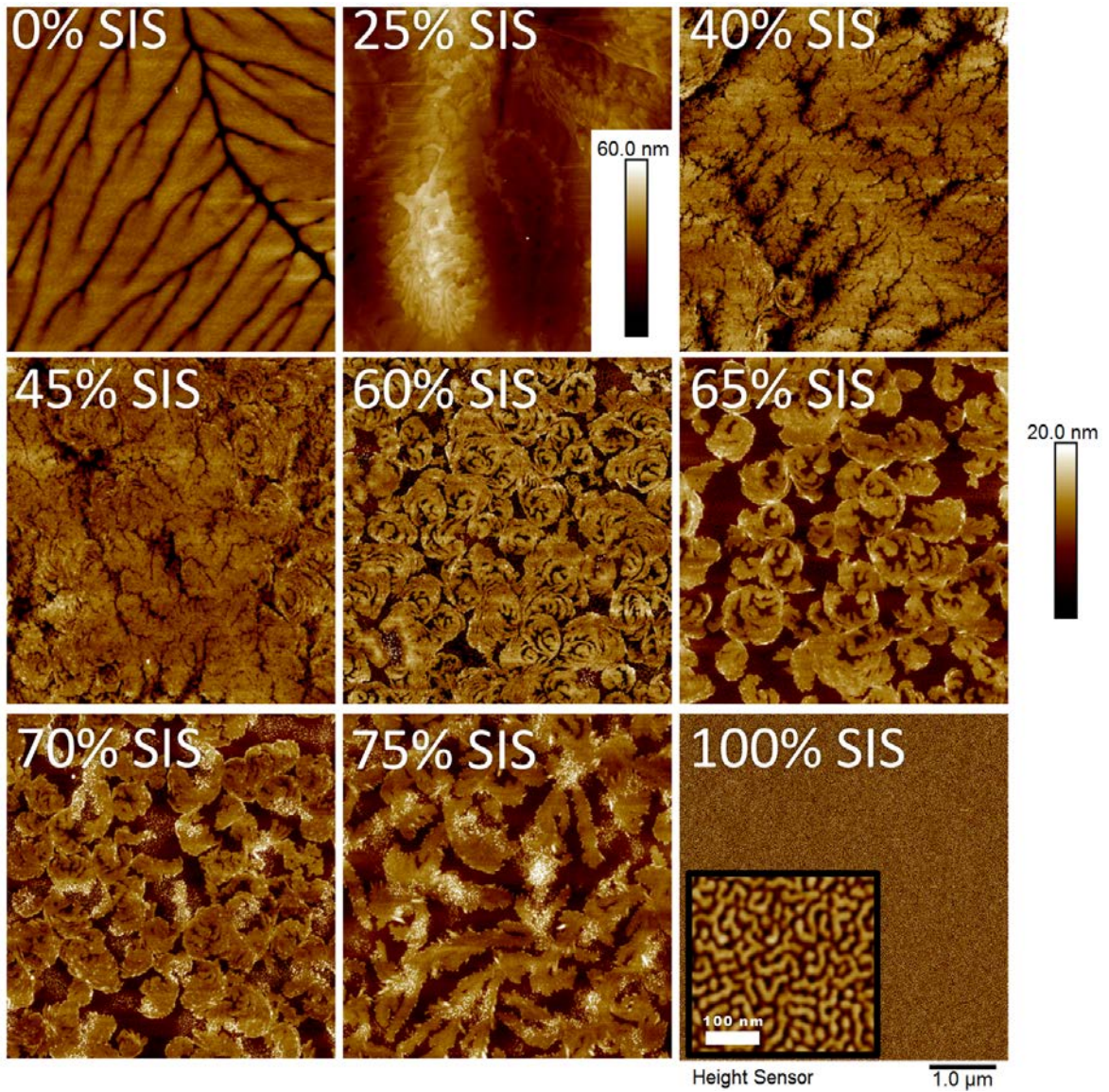


**Figure 3.6.** AFM height images of 45 kDa PCL/SIS vector 4293A blends at 10 - 14 nm thickness. Inset for 100 wt % SIS shows the presence of block copolymer nanostructure.

### Effect of Substrate Modification on Morphology

To further support our hypothesis that differential surface stresses are responsible for the curved nano-rose morphology, we effectively neutralized this imbalance by modifying the silicon substrate with a benzyl silane monolayer to reduce the substrate surface energy. A benzyl silane monolayer has a surface energy of  $41.3 \text{ mJ/m}^2$ <sup>152</sup>, which is much closer in value to the surface energy of SIS ( $33.4 \text{ mJ/m}^2$ )<sup>3, 33</sup> as well as toluene ( $28.4 \text{ mJ/m}^2$ )<sup>153</sup> compared to the unmodified silicon substrate ( $77.4 \text{ mJ/m}^2$ )<sup>152</sup>. As shown in Figure 3.7, films cast on substrates modified with the benzyl silane did not exhibit the nano-rose morphology in the aforementioned film thickness window. We attribute this result to the removal of imbalanced surface stresses during the growth of crystalline lamellae.

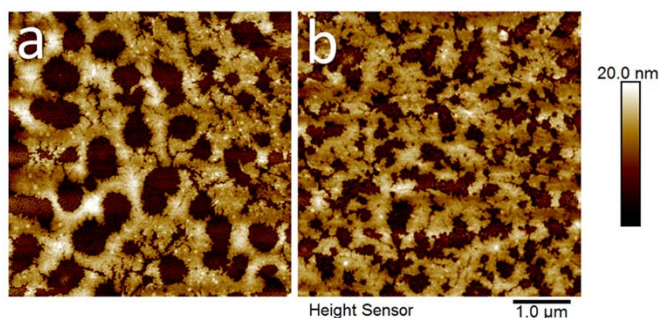


**Figure 3.7.** AFM height images of 45 kDa PCL/SIS vector 4293A blends at thicknesses of (a) 11 nm; and (b) 14 nm cast on substrates modified with benzyl silane.

### **Effect of PCL Molecular Weight on Morphology**

At the nano-rose film thickness of approximately 10 nm, both polymers are subject to molecular scale confinement. Thus, we hypothesized that by changing the PCL chain length, we would alter the extent of confinement and possibly change the film thickness at which the nano-rose morphology occurred, alter the size of the nano-roses, or suppress

their formation altogether. Since our initial system used 45 kDa PCL, we studied two additional PCL species: one lower in molecular weight ( $M_n = 10$  kDa) and one higher in molecular weight ( $M_n = 80$  kDa). As shown in Figure 3.8, both 10 kDa PCL and 80 kDa PCL exhibit the nano-rose morphology.

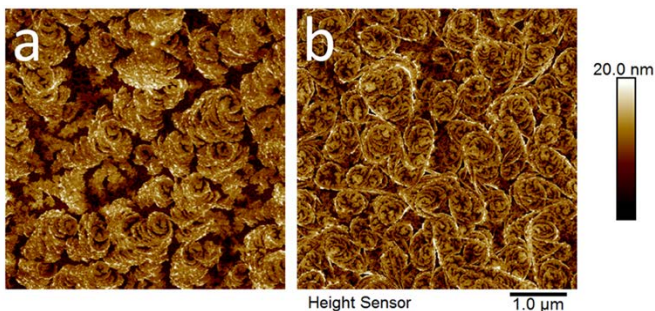


**Figure 3.8.** AFM height images of blends of (a) 10 kDa PCL and SIS vector 4211A containing 50 wt % SIS and (b) 80 kDa PCL and SIS vector 4293A containing 50 wt % SIS.

Surprisingly, the three systems form roses of indistinguishable diameter, approximately 500 nm irrespective of molecular weight (see Appendix A, Figure A19). Accordingly, we conclude that the radius of curvature is independent of the chain length. Likewise, the nano-rose morphology occurs around 10 nm film thickness irrespective of molecular weight. This film thickness is commensurate with the typical lamellar thickness of PCL over a wide range of molecular weights<sup>10, 27</sup>. Therefore, we have evidence that the confinement effects that give rise to lamellar reorientation and curling seen in the nano-rose morphology are more closely related to the length scale associated with the lamellar thickness than macromolecular size. This result is consistent with single-component systems in which the crystalline lamellae dictate morphological transitions in thin and

ultra-thin films dependent on free surface and substrate surface energies, degree of crystallinity, and other factors as a function of film thickness<sup>1, 34, 38</sup>.

### Effect of Casting Solvent on Morphology

Because the nano-roses form upon casting films from solution, casting solvent is critical to the morphological behavior of the film. Solvent choice affects solution characteristics such as viscosity, polymer-solvent interactions, as well as how quickly the film forms (volatility). In thin film work, one of the most widely used casting solvents is toluene due to its well-known polymer-solvent interactions, moderate boiling point, and ability to solubilize many polymers. We chose four additional solvents for comparison: benzene, which is nonpolar like toluene but more volatile, and three polar solvents: 1,4-dioxane, chloroform, and tetrahydrofuran (THF).

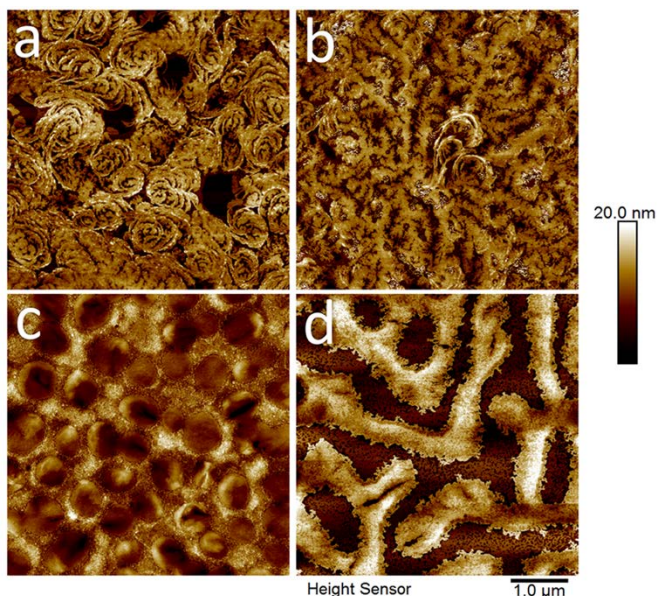


**Figure 3.9.** 45 kDa PCL SIS vector 4293A blend containing 50 wt % SIS cast from (a) benzene at 12 nm; (b) 1,4-dioxane at 12 nm; (c) THF at 14 nm; and (d) chloroform at 14 nm.

We found that the nano-rose morphology appears in films cast from benzene (Figure 3.9a) and 1,4-dioxane (Figure 3.9b). In both cases, the nano-rose morphology occurs in the film thickness window of 12 - 14 nm. Surprisingly, the roses formed are still approximately 500 nm in diameter. Like films cast from toluene, those cast from benzene exhibit nano-roses everywhere; however, the nano-roses appear slightly less organized and there is a higher prevalence of film dewetting. Nano-roses in samples cast from 1,4-dioxane were also approximately 500 nm in diameter but occurred only at the nucleation points of crystallization, similar to the 7 - 8 nm toluene-cast films. Films cast from chloroform do not form the nano-rose morphology, but the PCL phase separates into droplets within an SIS matrix with a diameter  $\approx$  500 nm, similar to that of the well-formed roses (Figure 3.9c). At film thicknesses around the nano-rose morphology film thickness of 9 - 14 nm, casting from THF led to a significantly different morphology that appears to be the result of phase separation by spinodal decomposition with breakthrough crystallization occurring at the fringes of the SIS domains (Figure 3.9d).

We have shown that films cast from toluene, benzene and 1,4-dioxane form nano-roses at film thickness around 12 nm. The comparison between toluene and benzene shows that nano-rose formation is not a strong function of solvent volatility, as the vapor pressures of these solvents differ by a factor of three at 20 °C (toluene: 2.8 kPa, benzene: 10 kPa)<sup>1,3</sup>. In contrast, solvent polarity appears to have a greater influence on nano-rose formation. The polar component of the Hansen solubility parameters for benzene, toluene, 1,4-

dioxane, chloroform, and THF are  $\delta_p = 0, 1.4, 1.8, 3.1,$  and  $5.7 \text{ MPA}^{1/2}$ , respectively<sup>1, 3</sup>. We hypothesize that the polarity of the ester group in PCL paired with the polarity of the solvent causes differences in phase separation for films cast from polar versus non-polar solvents. Toluene and benzene are essentially non-polar (full nano-rose formation), and 1,4-dioxane (partial nano-rose formation) is significantly less polar than chloroform and THF (no nano-rose formation).

### **Proposed Mechanism**

Studied independently, our results highlight the cause and effect of a number of variables on the growth of PCL lamellar crystals in ultrathin films when blended with styrene-isoprene block copolymers. When the results discussed above are considered as an ensemble, they begin to illustrate a preliminary mechanism for nano-rose formation. First, film thickness and blend ratio provide a very specific confinement condition that causes the growing crystalline lamellae to propagate in a non-linear direction, curling and growing vertically instead of parallel to the substrate. Second, this phenomenon occurs at a film thickness commensurate with the thickness of a single lamella and the height of the nano-rose spirals is commensurate with the lamellar thickness of PCL. These findings coupled with evidence from GIWAXS that the molecular-level organization of polymer chains is the same in the nano-rose as in pure PCL films but the crystal orientation distributions are different between pure PCL and the nano-rose morphology films indicate that we are seeing a reorientation of the PCL crystalline lamellae as they grow.

AFM images captured immediately after flow coating (approximately 3 minutes) of blend films containing 45 kDa PCL and SIS vector 4293 with 50 wt % SIS support this

assessment. While we are unable to expand on precise crystallization kinetics due to the relatively slow speed of image capture (approximately 45 seconds), the process of crystallization in this system takes about 30 minutes to reach completion, which allowed us to collect snapshots of the crystal growth directions. As shown in Figure 3.10, we observed evidence of an initial curl upward as the growing lamella starts to deviate in growth direction (Figure 3.10a), formation of the initial nano-rose (Figure 3.10b), and subsequent nano-rose growth and propagation as new lamellar layers form at the edge of the nano-rose (Figure 3.10c) and existing lamellae leave one nano-rose, continue curling, and begin to form new nano-roses (Figure 3.10b-c,d).

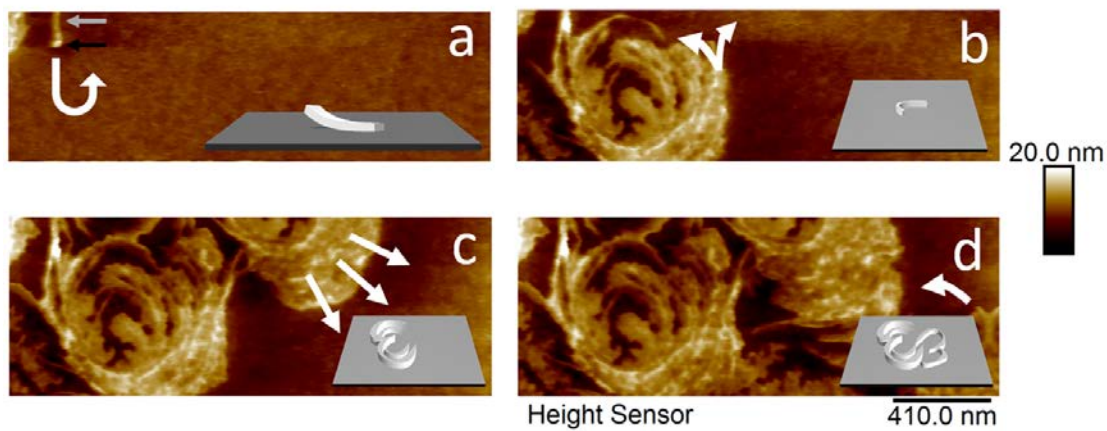


**Figure 3.10.** *In situ* AFM study of nano-roses as they form: (a) initial lamella begins to curve up due to competing surface stresses; (b) the initial curved lamella grows into a full nano-rose; (b)-(c) existing lamellae give birth to subsequent lamellae that either continue curling into the original nano-rose or curve out to spawn new nano-roses; (c) new lamellar layers form at the edges of existing nano-roses; (d) sustained lamellar curvature continues, both filling in edges of nano-roses or continuing to crystallize out from the edges of formed

nano-roses. Arrows show direction of crystal growth. Inset schematics depict dynamics of a single crystalline lamella; amorphous phase of PCL and SIS not shown.

We propose that the cause of lamellar reorientation in our system is a combination of two factors: (1) unbalanced surface stresses acting on growing PCL lamellae, and (2) the SIS component acting as an “impurity” to redirect crystal growth. With respect to unbalanced surface stresses, we postulate that the PCL lamellae will be trapped by three interfaces: a high surface energy substrate below (silicon oxide) and low surface energy amorphous layers above and in plane (SIS and solvent). Surface segregation of SIS is expected due to its lower surface energy compared to PCL, and blend films tens of nanometers thicker provide evidence of SIS segregation to the free surface (see Appendix A, Figure A20); comparison of unwashed and washed nano-rose films (see Appendix A, Figures A2 and A3) provides evidence for lateral segregation of SIS. Similar to the phenomena described by Keith and Padden, this arrangement of components in the film provides a sufficient difference in surface stresses between opposing interfaces of the lamellae that they turn/curve up (Figure 3.10a). Height sectioning analysis of the AFM image in Figure 3.10a shows that the initial lamella (grey arrow) has a height of  $5.69 \pm 0.29$  nm and as the lamella starts to turn/curve, its thickness increases to  $7.77 \pm 0.67$  nm (black arrow), which is commensurate with the literature values for the lamellar thickness of PCL and consistent with the average thickness of the final nano-rose spirals (Figure 3.1). After the initial lamella has reoriented, it grows laterally within the confinement conditions imposed by the film thickness and the styrene-isoprene block copolymer, which leads to lamellar curling (Figure 3.10a-3.10b). These curls continue to propagate with a

characteristic radius of approximately 250 nm (one half the final 500 nm diameter), sometimes creating a single multi-curl nano-rose or continuing on to form new, linked nano-roses (Figure 3.10c-3.10d). Our theory that the nano-rose phenomenon is caused by an imbalance in surface stresses is supported by our finding that we can effectively turn off this imbalance by modifying the substrate surface energy. By modifying the substrate with benzyl silane, we were able to decrease the substrate surface energy from 77.4 mJ/m<sup>2</sup> to 41.3 mJ/m<sup>2</sup>. Approximating the surface energy of SIS as 33.4 mJ/m<sup>2</sup>, this modification translates to a decrease in the surface stress differential from 44.0 mJ/m<sup>2</sup> to 7.9 mJ/m<sup>2</sup>. However, this imbalance in surface stress is not the only factor that dictates nano-rose formation. It is important to consider the styrene-isoprene block copolymer not only as a second component in this system, but also as an impurity to the crystallization of PCL. This “impurity” plays two roles: First, it provides separation and loose packing to the growing lamellae; second, the rejection of impurity provides an additional instability to the growing crystals, as has been shown by Janimak and Bassett in a linear low-density polyethylene system<sup>135</sup>. As crystals propagate, SIS will build at the growth front of the melt and will be rejected laterally in the growth direction as the outwardly growing crystal displaces it. This explanation is consistent with our observation that the amorphous SIS eventually segregates to the edges of the “rose petals” in the dry film (Figure 3.3). In the film thickness range of 5 nm to 8 nm, rejection of the SIS impurity and instability in the growing crystal leads a highly branched dendritic morphology. From 9 nm to 15 nm, the amount of material in the film remains sufficiently small that exclusion of the SIS impurity results in the curved, isolated lamellae of the nano-rose (Figure 3.4a-3.4e). At film thicknesses above this range, there is enough material such that the space between the isolated nano-rose

lamellae begin to fill in, eventually leading to the larger branched structure (Figure 3.4f). Altogether, we theorize that the significant imbalance in surface stresses paired with the rejection of impurity and the instability it provides causes the dramatic curling we see in the nano-rose morphology.

### 3.4 Conclusions

In summary, a new polymer blend morphology was discovered in ultrathin films containing poly( $\epsilon$ -caprolactone) and various styrene-isoprene block copolymers. This “nano-rose” morphology presents itself as a monodisperse collection of spiraling crystals that are remarkably different from previously observed semi-crystalline polymer morphologies in bulk or in thin films. We have shown that the nano-rose morphology is confinement driven (film thickness and blend composition-dependent), is dependent on the presence of a block copolymer sequence in the non-crystalline component, is reliant on having a surface energy difference between the substrate and the other blend components, is independent of the semi-crystalline component molecular weight, and forms only in films cast from non-polar or minimally-polar solvents. Considering the many theories on the origin of lamellar scrolling, twisting, and other non-linear crystal growth phenomena, our results support the ideas that an imbalance in surface stresses causes growing crystalline lamellae to grow in an unconventional manner and that non-crystallizable impurities can lead to non-linear crystal growth. The nano-rose features are exceptionally monodisperse in size and present a large surface area. Thus, the nano-rose morphology may be useful for applications where the importance of contact area is paramount, such as biological studies or surface catalysis.

## Chapter 4

### **THERMAL TRANSITIONS IN SEMI-CRYSTALLINE POLYMER THIN FILMS STUDIED VIA SPECTRAL REFLECTANCE**

Herein we report the finding that spectral reflectance (SR) can be used to identify thermal transitions in semi-crystalline polymer thin films. By studying film thickness as a function of temperature, we found that semi-crystalline polymers exhibit characteristic expansion and contraction profiles during the melting ( $T_m$ ) and crystallization ( $T_c$ ) transitions, respectively. Prior to this discovery, studies on the crystalline  $T_m$  in thin films have involved more expensive and complex techniques such as atomic force microscopy (AFM), ellipsometry, and grazing-incidence wide-angle X-ray scattering (GIWAXS). We correlate  $T_m$  and  $T_c$  as measured by SR with differential scanning calorimetry (DSC) in the bulk and temperature-controlled GIWAXS or AFM in thin films. We show that SR is accurate for measuring changes in films with thicknesses of 500 nm down to 21 nm and for detecting melting point depression due to thin film confinement. Thus, we demonstrate that SR is a powerful tool for measuring thermal transitions in semi-crystalline polymer films with single-degree resolution. Furthermore, many studies on thin film crystallization focus on the kinetics observed during isothermal crystallization as well as measuring the degree of crystallinity. The ability to detect  $T_m$  and  $T_c$  beg the question of whether spectral reflectance can be used to study these additional crystallization characteristics, such as

isothermal crystallization, growth rates, degree of crystallinity, and other factors. Sections 4.4 and 4.5 discuss some of the experiments conducted thus far to address these questions.

Sections 4.1-4.3 are based on the published work: Kelly, Giovanni M., et al. "Thermal transitions in semi-crystalline polymer thin films studied via spectral reflectance." *Polymer* (2018).

## 4.1 Introduction

Characterization of the physical properties and morphologies of polymers confined to thin and ultrathin film geometries is an important area of research in polymer science and engineering<sup>21, 34, 126-127, 145, 154-155</sup> due to the wide applicability of such materials to a variety of technologies, including lithography<sup>122, 127, 139, 141, 156</sup>, water purification<sup>157-158</sup>, fuel cells<sup>159-160</sup>, photovoltaics<sup>30, 79-81</sup>, and biological studies<sup>161-162</sup>. The pace of study and interest in polymer thin films has driven researchers to develop new methods to probe their many defining physical characteristics. For example, in amorphous polymers, the glass transition temperature ( $T_g$ ) dictates the onset of chain mobility, which is an important physical change that can determine annealing kinetics<sup>139-140, 163-164</sup>, affect polymer-drug composite stability<sup>165-167</sup>, and govern the ductility of consumer plastics<sup>168-170</sup>, among other properties. In substrate-supported thin films, many studies have focused on how the glass transition is affected by the substrate chemistry. This body of work has shown that attractive versus repulsive interactions between the substrate and polymer can lead to  $T_g$  elevation or depression, respectively<sup>106, 145, 171-172</sup>. Semi-crystalline polymers, such as poly(caprolactone) (PCL), polyethylene, poly(ethylene glycol) (PEG), and poly(lactic acid) (PLA), have a second characteristic thermal transition, the melting point<sup>27, 41, 146</sup>. Most of these polymers are used at temperatures well above their glass transition where crystallinity rather than glassiness dictates chain mobility; thus, the melting point ( $T_m$ ) rather than  $T_g$  determines material stability and applicability for these polymers. In thin films, much work has been done to understand the effect that blending with both polymeric and non-polymeric additives, as well as the thin film geometry itself, has on crystallization. The groups of T. Ogihara<sup>19</sup>, Q. Fu<sup>11, 20, 33</sup>, T. Nishi<sup>16</sup>, R.E. Prud'homme<sup>10, 71</sup>, and others

have shown that the interaction between miscible and immiscible components can increase or decrease crystallization rates and thermal transition temperatures, and that the substrate and second component have large effects on both overall morphology and substrate wettability<sup>1, 6, 34, 38, 69, 111</sup>.

There are a number of methods for probing the thermal transitions of polymers. Differential scanning calorimetry (DSC) has been used for decades to indirectly quantify thermal transitions in both semi-crystalline and amorphous polymers in the bulk. However, thin films ranging from tens to hundreds of nanometers do not contain sufficient material for this technique to maintain accuracy<sup>12, 22, 43-44, 46, 100-101, 128</sup>. Several companies and research groups have pioneered and utilized advanced calorimetry techniques, including “micro-DSC” and “nano-DSC” as well as differential fast scanning calorimetry (DFSC) units; however, these units come with a significant cost and most prior studies have used orders of magnitude more material than is available in nanometer thin films<sup>173-176</sup>. Even for units that require only nanograms of material, the film must still be removed from the substrate prior to measurement, as detailed in the experimental work by Balko et al. in which they studied the crystallinity of poly(3-hexylthiophene) in films down to 26 nm thickness using DFSC<sup>177</sup>. Unfortunately, removal of the film from the substrate prior to measurement renders studies on the effect of surface interactions on melting and crystallization transitions in thin films impossible by this method. Alternatively, polymer can be deposited and melted directly on the measurement cell, as was done by Tardif et al. in studying the crystallization of polyether ether ketone (PEEK)<sup>178</sup>, but this technique results in micron rather than nanometer thick films. Several groups have utilized fluorescence, Brillouin light scattering (BLS), and ellipsometry to study the glass transition

temperature in substrate-supported and free standing thin films of polystyrene (PS), PS/poly(2-vinyl pyridine), poly(methyl methacrylate) (PMMA), and cyclic polystyrene<sup>103, 105-106, 145, 147, 172, 179-182</sup>. Kim et al. used ellipsometry to study melting point depression in poly[ethylene-co-(vinyl acetate)] thin films<sup>183</sup>. Thermal transitions also can be probed using shear force modulus (SFM) measurements as was done by Wang et al., although this can be a destructive and expensive method<sup>146</sup>.

In this work, we describe our finding that spectral reflectance (SR), a technique for measuring the film thickness of polymeric and non-polymeric materials, can be used to identify the thermal transitions of semi-crystalline PCL and PEG thin films due to the thermal expansion or contraction of these films during melting or crystallization, respectively. PCL serves as a model polymer for crystallization studies due to the similarity of its crystal structure to that of polyethylene, a widely used commodity plastic<sup>29</sup>, its accessible melting temperature (59-64 °C)<sup>184</sup>, and its relatively slow crystal growth rate (e.g., it is orders of magnitude slower than PEG<sup>71</sup>), which facilitates study of morphology development and kinetics. PEG, typically used in biomedical, solution, and drug delivery applications, was chosen for comparison to PCL because it has a similar bulk melting temperature (64-66 °C)<sup>185</sup> but exhibits different thin film properties that highlight the accuracy of this technique. Spectral reflectance has been used previously by Lu et al. to investigate the stress relaxation and glass transition temperature ( $T_g$ ) of polystyrene films on ionic liquids<sup>108</sup>. To the best of the authors' knowledge, this work represents the first time that spectral reflectance has been used to probe the melting and crystallization of semi-crystalline polymers and its first application to identifying thermal transitions in substrate-supported polymer thin films. Spectral reflectance offers a variety of benefits over the

previously discussed techniques. These units are tens of thousands of dollars less expensive than ellipsometers and advanced calorimetry units, making them much more accessible to researchers. Unlike calorimetry experiments, spectral reflectance measurements can be performed *in situ* without removing the film from the surface, which means that these measurements will capture the effect of substrate surface interactions on the melting and crystallization transitions in thin films, if present. Compared to SFM and X-ray studies, spectral reflectance is less destructive to the sample. The small footprint and equipment simplicity make spectral reflectometers mobile and easily-modified for non-ambient experiments such as the ones described in this work. Finally, the resolution afforded by spectral reflectance makes nanometer changes in film thickness readily quantifiable<sup>109</sup>.

## 4.2 Experimental Section

### **Materials**

Hydroxyl-terminated linear poly( $\epsilon$ -caprolactone) (PCL) (Sigma Aldrich,  $M_n = 45$  kDa,  $D = 1.5$ ) as well as poly(ethylene glycol) (PEG) (Sigma Aldrich,  $M_n = 20$  kDa) were used as received.

### **Film Preparation**

PCL and PEG films were cast via spincoating from dilute toluene or chloroform solutions, respectively, onto ultra-violet ozone cleaned silicon wafers. Both solvents were ACS grade and used as received. Solution concentrations ranged from 0.25 wt. % to 7.5 wt. % depending on the final film thickness desired as well as the polymer molecular weight. After casting, all films were heated to 100 °C for 10 minutes to erase thermal

history and subsequently quenched to room temperature (25 °C) where they were allowed to crystallize for several hours prior to performing thermal characterization experiments.

### **Characterization**

Bulk thermal transitions were studied via differential scanning calorimetry (DSC) (TA Instruments Q200) in an inert nitrogen atmosphere with heating and cooling rates of 1 °C/min. This data was analyzed using the TA Instruments Universal Analysis software.

To probe the thin film melting point on a molecular level, PCL thin films were studied via temperature-controlled grazing incidence wide-angle X-ray scattering (GIWAXS). GIWAXS measurements were performed at beamline 8-ID-E of the Advanced Photon Source at Argonne National Laboratory<sup>42</sup> with a heater/cooler stage constructed in-house. An X-ray wavelength of  $\lambda = 1.1417 \text{ \AA}$  (energy 10.86 keV) was used. The sample was measured under vacuum at an incident angle  $\theta = 0.14^\circ$  and exposure time of 1 s. Starting from 25 °C, the temperature was increased at a rate of 1 °C/min up to 85 °C and subsequently cooled at 1 °C/min to 25 °C, with measurements taken every minute. Due to the overall exposure time (120 seconds total) we observed some radiation damage on the exposed sample section. However, it is likely that this damage did not occur until the polymer film reached the melt state (~35 seconds total exposure) based on a systematic study by Stein and coworkers<sup>186</sup>. Additionally, these sections were not used in spectral reflectance measurements. The acquired GIWAXS data (as two-dimensional images) were further treated and analyzed using *GIXSGUI* software package<sup>144</sup>. The degree of crystallinity was determined by integrating the 2D GIWAXS data to generate a 1D Intensity vs.  $q$  curve; fitting this curve with four Gaussian peaks, one representing the

amorphous component and three representing the crystalline peaks ((003), (110), and (200))<sup>76, 187</sup>; and then taking the ratio of the crystalline peak area to the overall area (amorphous plus crystalline peak fits) as the degree of crystallinity (see Appendix B, Figure B1). Although GIWAXS is not the preferred method to calculate true crystallinity, this analysis enabled us to correlate the film thickness trend measured by SR with well-defined characteristics of the melting transition.

Temperature-controlled atomic force microscopy (AFM) experiments were conducted on a Bruker Dimension ICON AFM operating in PeakForce Quantitative Nanomechanical Mapping (PF-QNM) mode and using ScanAsyst-Air tips ( $k = 0.4 \text{ N/m}$ ; resonant frequency = 70 kHz). The temperature was increased manually in 1 °C increments and rapid (~30 sec) scans were taken after each step change to mimic an approximate 1 °C/min heating rate used in the SR experiment.

### **Spectral reflectance**

Spectral reflectance measurements were taken using the Filmetrics F20-UV system. This system is able to resolve polymeric and non-polymeric film thicknesses from 1 nm to 40  $\mu\text{m}$  (with resolution the greater of 1 nm or  $\pm 0.2 \%$ ). The instrument measures the intensity of sample-reflected UV and visible light (200-1100 nm) and the FILMeasure software is used to determine the film thickness by fitting a calculated optical model spectrum to the observed reflectance spectrum. This model is constructed based on the properties of the substrate, the thin film material, and the measurement medium. The thin film material properties used in the model include the wavelength dependence for the refractive index ( $n$ ) and extinction coefficient ( $k$ ), which were calculated by the

FILMeasure software. For both PCL and PEG, the calculated extinction coefficient was negligible ( $k < 0.0001$ ) signifying no absorption of light energy which is typical for non-aromatic, non-conjugated polymers<sup>188-189</sup>. However, because the FILMeasure software can be used to fit  $n$  and  $k$  for materials exhibiting strong absorptions in the visible spectrum,<sup>109</sup> the approach described herein is expected to be readily extendable to light-absorbing polymers. Additionally, the dependence of refractive index on temperature is assumed to be negligible for PCL and PEG under these conditions, as several groups have shown that refractive index decreases by less than 1% over the span of many tens of degrees<sup>190-191</sup>. We also observed no evidence that the degree of crystallinity or increase in amorphous fraction through melting affected the calculated refractive index model. Details on the film thickness models used in this study are provided in the Appendix B, Figure B2. A deeper discussion of the fundamentals of spectral reflectance is beyond the scope of this manuscript, and more exhaustive application notes are available from Filmetrics Inc. Although the full range of UV and visible light wavelengths were used in this study, measurements can be conducted using only visible light wavelengths (i.e., without the UV lamp) for samples that are UV-sensitive. Ambient measurements were conducted on a simple sample stage. Measurements at elevated temperature were conducted with the sample held on a separate Linkam heater/cooler stage (Linkam THMS600E) so that film thickness could be measured accurately as a function of temperature.

In a typical melting point experiment, the initial temperature was 25 °C, the heating rate was 1 °C/min, and film thickness was measured in triplicate every 5 °C from 25 °C to 50 °C, every 1 °C from 50 °C to 65 °C, and every 5 °C from 65 °C to 85 °C. This heating rate was used to correspond to the heating rate capabilities of both *in situ* elevated

temperature GIWAXS as well as DSC. In crystallization experiments, the film was heated to 100 °C, held for 10 minutes, and then the film was cooled at a rate of 1 °C/min down to 25 °C. In these experiments, measurements were taken every 5 °C from 100 °C to 50 °C and every 1 °C from 50 °C to 25 °C.

#### 4.3 Determination of $T_m$ and $T_c$ by SR

##### **$T_m$ of thin film PCL via spectral reflectance (SR)**

The film thickness as measured by SR during melting of a 500 nm thick film of PCL is presented in Figure 4.1a (open diamond symbols). Corresponding to the shading in Figure 1a, the film exhibits three distinct thermal expansion phenomena in different temperature ranges. From 25 °C to approximately 51 °C, the film expands almost-linearly due to the thermal expansion of the amorphous regions of the semi-crystalline PCL. During the melting transition, we observe a large increase in thickness as melting destroys the dense crystalline lamellae, which leads to a sharp rise in material volume. It is well-known that there is a substantial increase in the specific volume upon melting<sup>192</sup>. In the fully melted state, the film again expands linearly, as it is entirely amorphous and of uniform density. The boundary between the melting transition region and the fully melted state is readily identified by the sharp change in the slope of the film thickness versus temperature curve and occurs at  $61\text{ °C} \pm 1\text{ °C}$ , which is in good agreement with the bulk  $T_m$  observed via DSC ( $60\text{ °C} \pm 1\text{ °C}$ ) (see Appendix B, Figure B3). Repeated trials exhibit the same characteristic curve and transition point accurate to within 1 °C regardless of the starting film thickness (see Appendix B, Figure B4). Additional experiments were conducted at heating rates of 5 °C/min and 10 °C/min to illustrate the resolution of SR with faster heating

rates (see Appendix B, Figure B5). With increasing heating rates, the  $T_m$  shifts to slightly lower values (59 °C at 5 °C/min and 57 °C at 10 °C/min). The phenomenon of decreasing  $T_m$  with increasing heating rate has been shown in polyethylene terephthalate (PET) and is caused by polymer crystals reorganizing during heating to form higher melting point crystals with slower heating rates<sup>99</sup>.

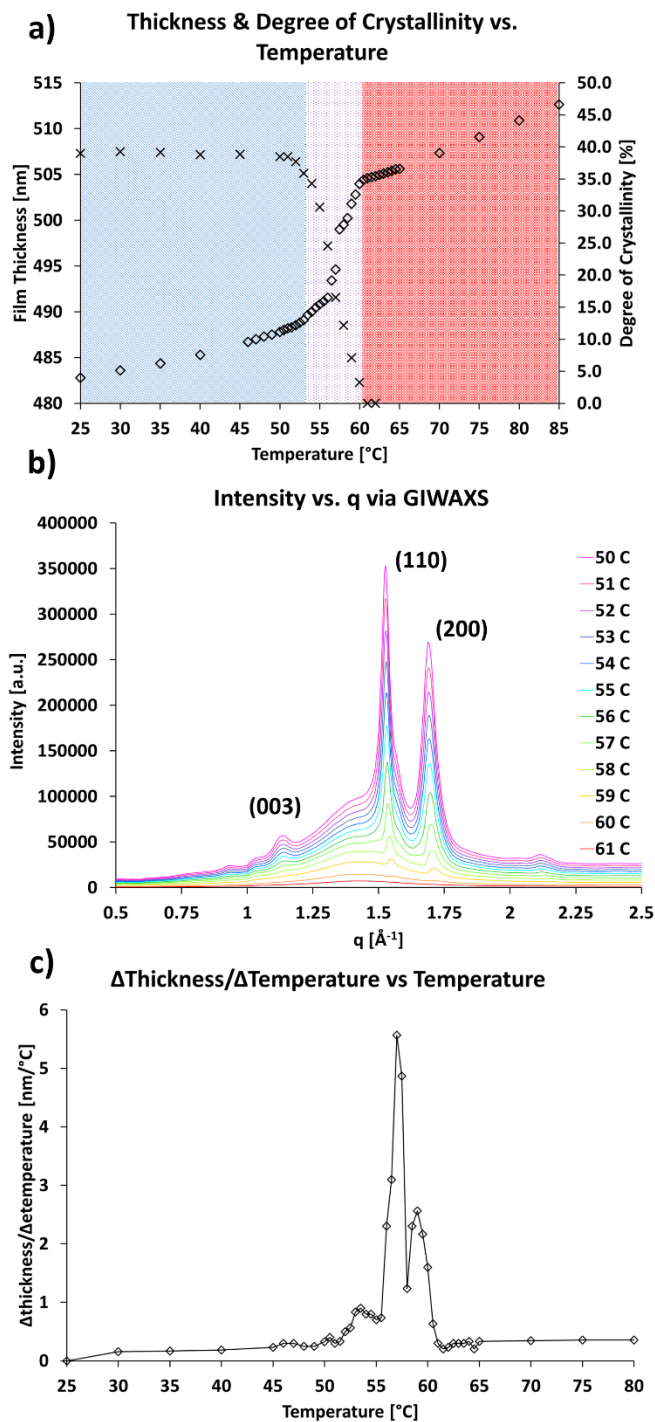


**Figure 4.1.** Melting point determination for a 500 nm 45 kDa PCL thin film: a) Thickness vs. temperature (open diamond symbols) and degree of crystallinity vs. temperature as determined from GIWAXS (black X's). This film exhibits characteristic expansion upon

melting with a transition at approximately 61 °C. Blue, purple, and red shading indicate the semi-crystalline, melting transition, and melt state regions, respectively. b) Melting point studied via elevated temperature GIWAXS showing loss of crystalline order between 60 °C and 61 °C. c) Analysis of slope of the thickness versus temperature curve from (a) showing a primary peak value at 57 °C. This value corresponds to when the degree of crystallinity has decreased by half during melting and can be considered the midpoint of the melting transition region.

We next verified the melting temperature of 500 nm thick PCL films using GIWAXS (see Figure 4.1b). This technique probes the molecular level organization of materials making it a highly sensitive technique for detecting the disappearance of PCL crystals upon melting, and because GIWAXS measurements were taken every minute during the temperature ramp, we obtained excellent resolution of the melting temperature from this study. Figure 4.1b shows the intensity versus  $q$  plots as a function of temperature for the sample depicted in Figure 4.1a. As can be seen in Figure 4.1b, the sharp peaks that are characteristic of the crystalline regions in PCL [72, 73] disappear at approximately 61 °C, which is in good agreement with DSC and our determination of  $T_m$  from SR data.

The above analysis identifies  $T_m$  as the temperature above which crystallinity is no longer detectable in the polymer thin film. However, it is difficult to characterize the onset of melting from visual analysis of the intensity vs.  $q$  curves in Figure 4.1b. Thus, we calculated the degree of crystallinity as a function of temperature from the GIWAXS data for comparison with SR data, as described in the Experimental section. This analysis enabled us to correlate the film thickness trend measured by SR with three additional

characteristics of the melting transition. First, the most dramatic film thickness increase (primary peak in the slope of the film thickness versus temperature curve, see Figure 4.1c) at 57 °C corresponds to where the degree of crystallinity has decreased by half and can be considered the midpoint of the melting transition. Second, we see that the onset of melting is gradual from  $\approx 50$  to 53 °C and then the degree of crystallinity drops off sharply; this sharp decrease is consistent with the beginning of the melting transition region we would calculate from SR data (53 °C) based on identification of the end-point (61 °C) and the midpoint (57 °C). Finally, we observe two distinct peaks in the slope of film thickness vs. temperature curve (Figure. 4.1c), signifying two sharp increases in the film thickness with temperature, and therefore two separate melting events during the overall melting of the PCL crystals. Correspondingly, the melting peak in DSC has a low shoulder (see Appendix B, Figure B3). The phenomenon of multiple melting in PCL has been observed by Cordova et al. <sup>7</sup> and can be attributed to partial reorganization of PCL crystals during the slow heating ramp as described above.

### **Ultrathin PCL films and PEG**

To test the robustness of SR for even thinner films and other polymers, we studied additional PCL thin and ultrathin films ranging from 107 nm down to 21 nm as well as bulk film and thin film PEG samples. While melting point depression has been shown to occur in polyethylene using SFM <sup>146</sup> and poly[ethylene-co-(vinyl acetate)] thin films using ellipsometry <sup>183</sup>, to the best of our knowledge no previous studies have focused on  $T_m$  depression in PCL or PEG thin films. Knowledge of the existence and magnitude of  $T_m$  depression is vital for kinetics studies, as any deviation from the bulk and equilibrium  $T_m$

also shifts the crystallization degree of supercooling, which greatly affects nucleation and growth phenomena<sup>1</sup>. From SR measurements on the PCL films, we found that PCL in this film thickness range did not exhibit appreciable  $T_m$  depression (see Appendix B, Figure B6). However, our data show that SR is sensitive enough to measure the characteristic thermal expansion upon melting despite the very low amount of material in these films.

To validate SR as a valuable technique for measuring the thermal transitions of various polymer systems while retaining the accuracy necessary to examine  $T_m$  depression, we then studied four PEG films. The bulk film (1130 nm thickness) had a melting temperature of 64 °C as determined by SR (see Figure 4.2a), which is in good agreement with the bulk  $T_m$  reported in the literature of 64-66 °C<sup>185</sup>. Films at 659 nm and 316 nm exhibited melting points of 63 °C and 58 °C, respectively (see Appendix B, Figure B7). Finally, the thinnest sample (147 nm) was an order of magnitude lower in film thickness as compared to the bulk sample (1130 nm) and exhibited a melting temperature of 53 °C (see Figure 4.2b). To verify the accuracy of the melting point determined by SR for the 147 nm PEG film, we additionally studied this film using elevated-temperature atomic force microscopy (AFM) (see Appendix B, Figure B8). By capturing images of the PEG film morphology as a function of temperature, we identified the melting temperature as 53 °C, the same as determined by SR.

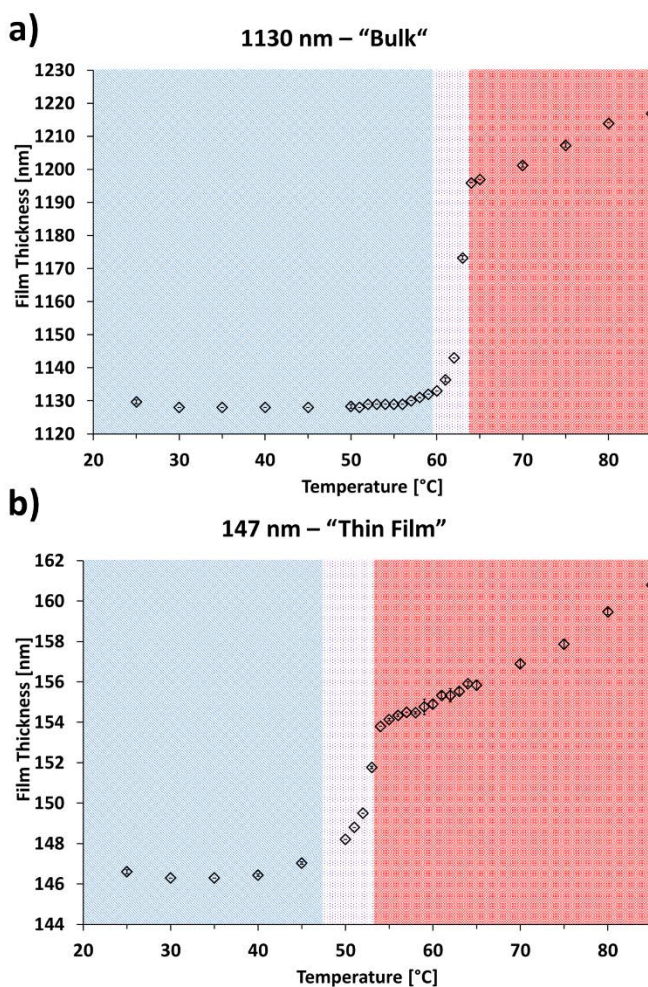


**Figure 4.2.** Film thickness vs. temperature for: a) “bulk” 1130 nm 20 kDa PEG film; and b) 147 nm 20 kDa PEG thin film. This comparison shows that SR can be used to detect  $T_m$  depression in PEG due to thin film confinement. Blue, purple, and red shading indicate the semi-crystalline, melting transition, and melt state regions, respectively.

As shown in Figure 4.3, by comparing the melting points of PCL (open squares) and PEG (open diamonds) as a function of film thickness, it is apparent that these two materials experience different confinement-driven melting point depression. Even in ultrathin films at thicknesses as low as 21 nm, the observed  $T_m$  for PCL remains within the

temperature range measured via DSC in the bulk ( $60\text{ }^{\circ}\text{C} \pm 1\text{ }^{\circ}\text{C}$ ), whereas the  $T_m$  of PEG begins to decrease at film thicknesses in the hundreds of nanometers. A deeper analysis and discussion of the possible chemical and physical origins of this difference is beyond the scope of this manuscript. However, these results verify that the SR technique is sensitive to quantifying  $T_m$  depression (if present) for changes that are greater than  $1\text{ }^{\circ}\text{C}$  and illustrate its extension to another polymer system.

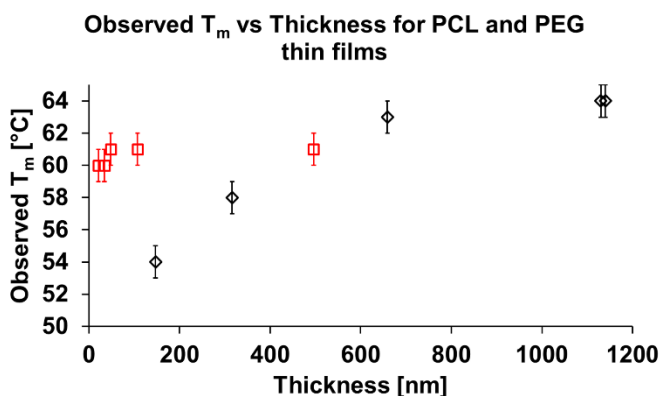


**Figure 4.3.** Observed  $T_m$  vs film thickness for 45 kDa PCL (red open squares) and 20 kDa PEG (black open diamonds). This comparison illustrates the confinement driven melting point depression in these two materials. No appreciable  $T_m$  depression is observed in 45 kDa PCL, even in films as thin as 21 nm. In 20 kDa PEG films, the onset of  $T_m$  depression can be seen in the 659 nm film ( $T_m = 63\text{ }^{\circ}\text{C}$ ) and becomes more dramatic as the film thickness decreases. Error bars represent the  $\pm 1\text{ }^{\circ}\text{C}$  window we report as the uncertainty associated with determining  $T_m$  from SR data.

## Crystallization temperature via SR

Finally, we aimed to correlate the film thickness vs. temperature data measured by SR with the crystallization of PCL from the melt. We hypothesized that since there is a characteristic expansion upon melting, there will be corresponding contraction when crystallization occurs and more densely packed chains order from the amorphous melt. Using a cooling rate of 1 °C/min, we again observed three regions in the film thickness versus temperature plots: first, a linear trend as the amorphous melt contracts; second, a sharp drop in film thickness through the crystallization transition; and third, a nearly-linear trend below the crystallization temperature as the amorphous regions of the semi-crystalline film continue to contract (see Figure 4.4). However, the crystallization transition does not occur at the observed melting point. Instead, the onset of crystallization as determined from SR occurs at approximately 47 °C, where the linear decrease in film thickness through the melt state turns into a sharp drop in film thickness through the crystallization transition. This temperature value is within a few degrees of the onset of the exothermic trace observed in DSC (45 °C) (see Appendix B, Figure B3).

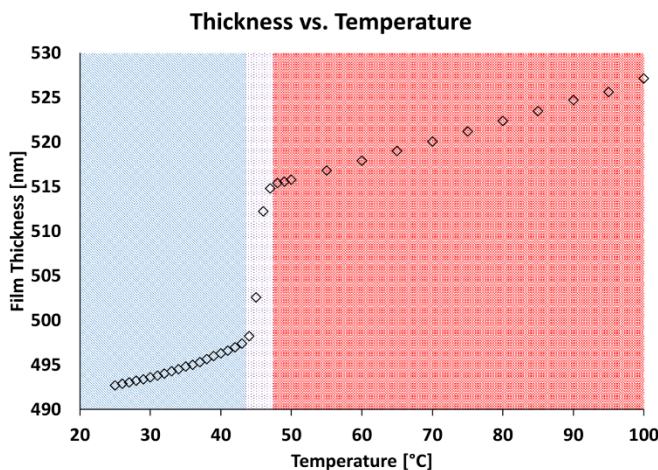


**Figure 4.4.** Thickness vs. temperature of 500 nm 45 kDa PCL for a 1 °C/min recrystallization from 100 °C. This film exhibits a sharp decrease in film thickness starting at 47 °C, which is within a few degrees of the onset of crystallization in the DSC endotherm. Red, purple, and blue shading indicate the melt state, crystallization transition, and semi-crystalline regions, respectively.

#### 4.4 Tracking Isothermal Recrystallization by SR

As discussed in Chapter 1, crystallization is a nucleation and growth process. When the thermodynamic conditions are right, i.e. the system is below its melting temperature, crystals are energetically favorable and will grow given sufficient time. The kinetics of crystal growth are dependent on the temperature at which this crystallization occurs. Crystal growth is based on the degree of supercooling ( $\Delta T$ ), or how far below the equilibrium melting temperature ( $T_{m,0}$ ) the system exists. Of course, we can control the crystallization process by choosing the crystallization temperature. By doing so, we can affect the crystal growth rate, nucleation density, crystal size, and morphology. This is because crystal growth rate increases as degree of supercooling increases, although groups have shown that there is a maximum growth rate that is approximately halfway between the melting and glass transition temperatures<sup>1, 193</sup>. Between the melting point and glass transition temperature, crystallization is a delicate interplay of nucleation and growth. At high crystallization temperatures, the system is nucleation limited with very slow growth, leading to large crystals. This is due to the low thermodynamic driving force of crystallizing versus remaining in the melt state. At low crystallization temperatures, the system is instead growth-limited due in part to the higher viscosity of the melt which slows

polymer chains moving towards and attaching to the growth front. Thus, studies on crystallization using isothermal conditions are insightful in terms of growth rate as a function of temperature, polymer chemistry, architecture, etc.

Typically, isothermal crystallization in polymer thin films has been studied via microscopy techniques; most often optical or polarized light optical microscopy. These techniques allow researchers to watch the formation of spherulites in real time, track the nucleation density, and quantify the velocity of the growth front, which is one of the most commonly reported kinetics values. However, this method is subjective, and due to the small viewing area, is more of a locally as opposed to globally precise technique. Furthermore, because this method relies on optical techniques, the researcher can only observe the surface of the film, with less of an idea on what is occurring in the bulk of the film

Thus, and similar to how spectral reflectance was used to quantify film thickness as a function of temperature, we have attempted to study the isothermal recrystallization of PCL via the film thickness as a function of time. Since the film thickness showed a characteristic expansion and contraction through the melting transition, it seemed as though it would very likely show a characteristic contraction during isothermal recrystallization.

To conduct these experiments, the spectral reflectance setup was combined with a well-controlled Linkam hot stage as done previously. All materials and methods used previously were similarly utilized in these experiments (see Section 4.2). In these experiments, the films were melted at 100 °C for 10 minutes to ensure that thermal history was erased. Then, using the liquid nitrogen cooling capability of the Linkam hot stage, the film was quenched at 50 °C/min to the pre-determined isothermal recrystallization

temperature, and film thickness was measured at pre-determined intervals (every 10 seconds for 30 °C recrystallization and 20 seconds for 40 °C recrystallization). In our initial experiments, we studied isothermal recrystallizations at 30 °C and 40 °C. The 10 °C spread between crystallization temperatures would lead to a very obvious difference in the crystallization rates. This can be clearly observed in Figure 4.5:

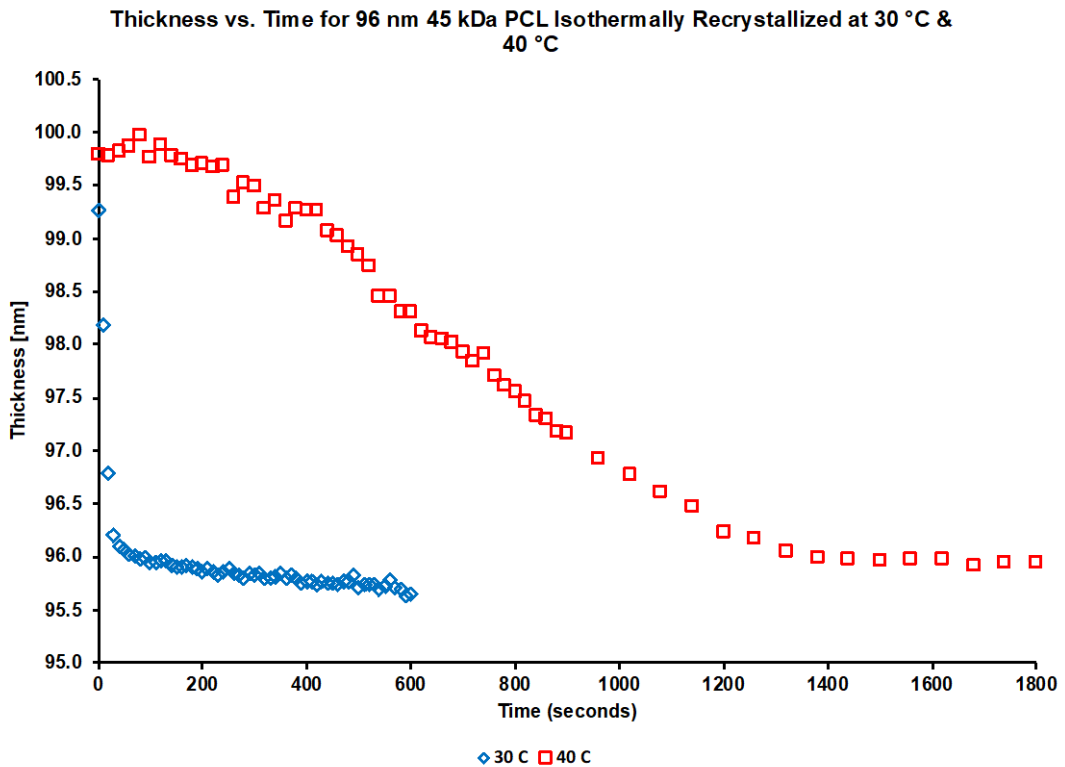


**Figure 4.5.** Thickness vs. time of 96 nm 45 kDa PCL films measured during isothermal recrystallization at 30 °C (blue diamonds) and 40 °C (red squares).

The first significant observation from this experiment is, as expected, the film crystallized at 30 °C does so significantly more quickly than the one crystallized at 40 °C. This further confirmed our results from the initial spectral reflectance work that the film thickness is

very closely related with the crystallization process in the film. If the contraction was independent of crystallization and was due to normal thermal expansion and contraction, there would not be this drastic of a difference. As expected, in both cases, the film contraction eventually leads back to approximately the same thickness regardless of crystallization temperature.

In the interest of comparing this to tangible crystallization values, temperature controlled GIWAXS experiments were conducted in parallel to study the degree of crystallinity as a function of time (see Section 4.2 for discussion on calculation methods). While GIWAXS is unable to determine exact degree of crystallinity values, we can observe the trend as a function of time. Importantly, these GIWAXS experiments were conducted on the same films as the spectral reflectance experiments, and therefore we have sufficient comparability between the two sets of data. As can be seen in Figures 4.6 and 4.7, the film thickness trend from spectral reflectance shows exceptional correlation with the degree of crystallinity from GIWAXS when isothermally recrystallized at 30 °C and 40 °C:

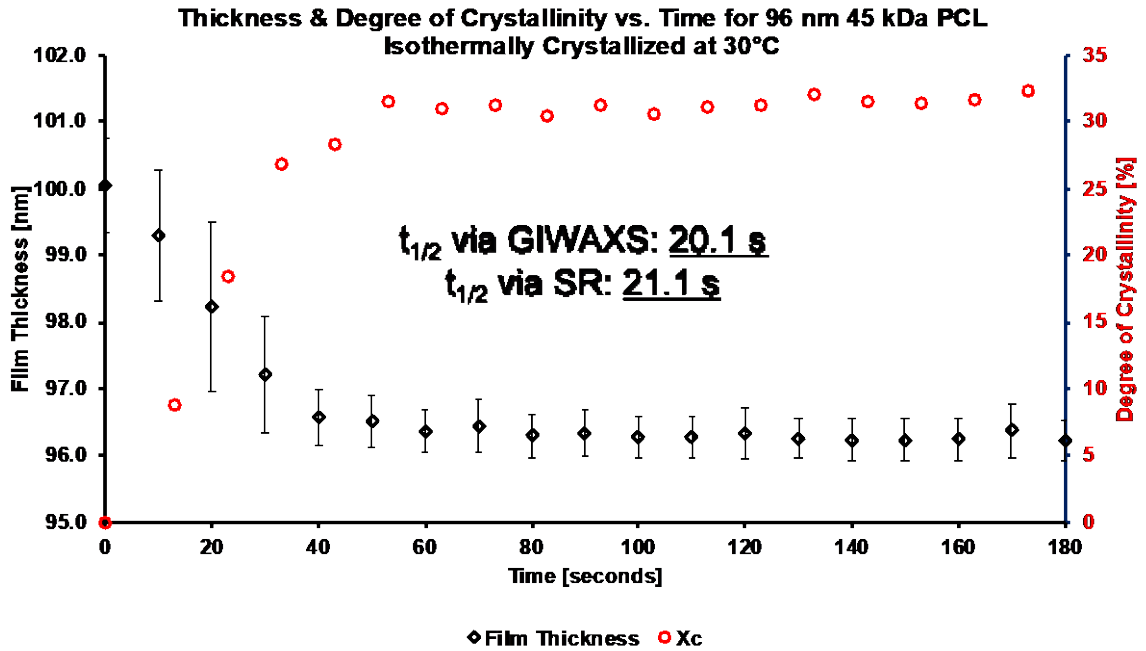


**Figure 4.6.** Thickness (measured via spectral reflectance) & degree of crystallinity (measured via GIWAXS) vs. time for 96 nm 45 kDa PCL isothermally crystallized at 30 °C.  $t_{1/2}$  for GIWAXS refers to the crystallization half time, or the time it takes the system to reach 50 % relative crystallinity.  $t_{1/2}$  for SR refers to the crystallization half time measured as the time it takes to reach the midpoint in the thickness decrease. Error bars illustrate the standard deviation of the SR prediction from three separate isothermal crystallization trials.

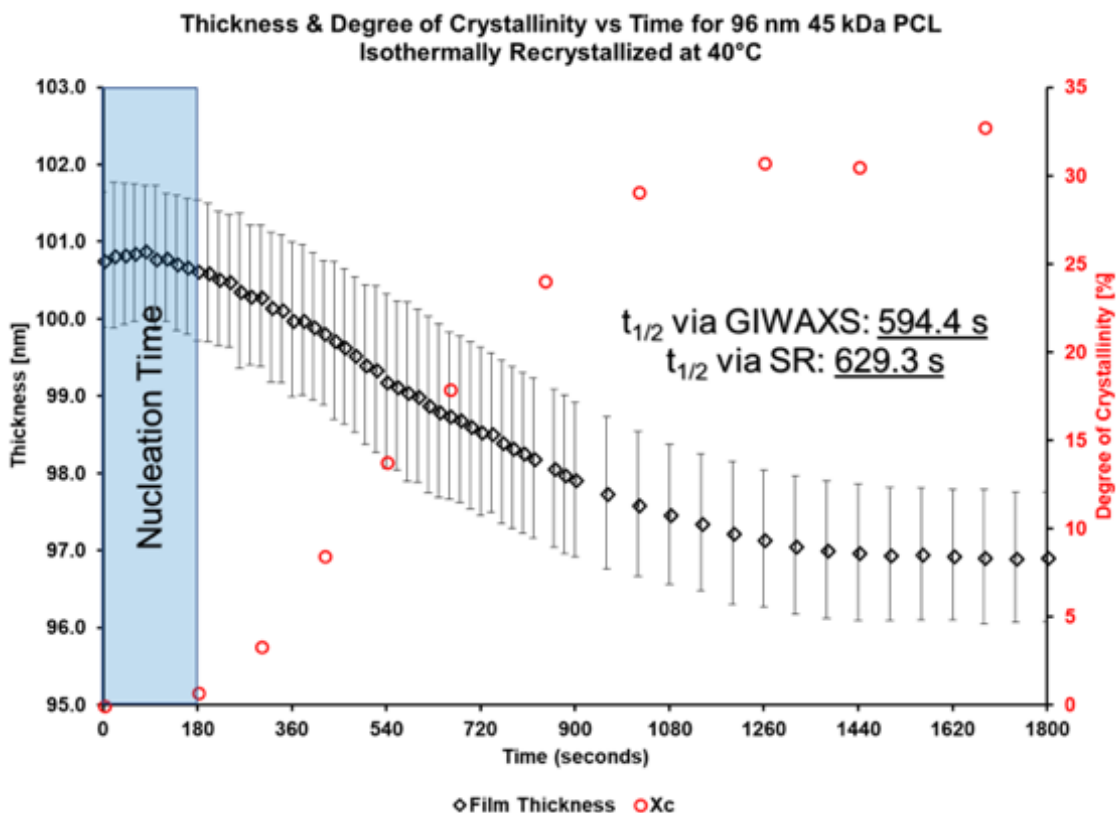


**Figure 4.7.** Thickness (measured via spectral reflectance) & degree of crystallinity (measured via GIWAXS) vs. time for 96 nm 45 kDa PCL isothermally crystallized at 40 °C. Blue box illustrates the nucleation or induction time prior to crystal nucleation and growth.  $t_{1/2}$  for GIWAXS refers to the crystallization half time, or the time it takes the system to reach 50 % relative crystallinity.  $t_{1/2}$  for SR refers to the crystallization half time measured as the time it takes to reach the midpoint in the thickness decrease.

To try and quantify the correlation between these two methods, we have opted to use the crystallization half time ( $t_{1/2}$ ) which is defined as the time it takes for the system to reach half relative crystallinity in the case of the GIWAXS data. Because film thickness shows an obvious correlation with degree of crystallinity, here we have defined  $t_{1/2}$  as the time it takes to reach the mid-point in the film thickness decrease. In the 30 °C isothermal

recrystallization, we calculated half times for GIWAXS and SR of 20.1 seconds and 21.3 seconds, respectively. For the 40 °C isothermal recrystallization, we calculated half times for GIWAXS and SR of 594.4 seconds and 712.2 seconds, respectively. While it is true that the GIWAXS results do not match up perfectly with the spectral reflectance results, especially in the case of the 40 °C isothermal recrystallization. the fact that they correlate so well is remarkable, considering thin film crystallization studies required long experiments using optical microscopy techniques or some form of X-ray scattering up until this point. Furthermore, due of the time it takes to run one experiment on the beamline, we are unable to quantify the error in the GIWAXS measurements, and therefore our results very well could be within the standard deviation as measured via GIWAXS. These results show that spectral reflectance is not only able to map the beginning and end of crystallization, but it also sensitive enough to track the nucleation time. (see Figure 4.7).

#### 4.5 Determining Degree of Crystallinity from Spectral Reflectance Data

Following from the above, the next logical step in this work is studying whether spectral reflectance can be used to calculate the degree of crystallinity in semi-crystalline polymer thin films. As described in Chapter 1, the degree of crystallinity ( $X_c$ ) is the ratio of crystalline material to the sum of crystalline and amorphous material in the polymer. Because most of the important characteristics of semi-crystalline polymers, such as mechanical and optical properties are dependent on the degree of crystallinity, it is a vital quantity to be able to quantify. In the bulk, the degree of crystallinity is typically measured via differential scanning calorimetry (DSC) or wide-angle X-ray scattering (WAXS/WAXD). There are fewer methods for thin films. Nano-DSC and other methods

can be used to determine degrees of crystallinity when a small amount of material is present, but the film typically needs to be removed to utilize this method. In the preceding sections, we used GIWAXS and the ratio of crystalline peaks to the sum of crystalline and amorphous peak areas to calculate a qualitative degree of crystallinity with time. However, because GIWAXS is a grazing incidence method, there is a small amount of scattering data missing from the full integration of the data, which causes GIWAXS to systematically underestimate the degree of crystallinity. Thus, GIWAXS is a good qualitative method for measuring degree of crystallinity, but a poor quantitative one.

Since we found that spectral reflectance is able to track crystallization with time, we then studied whether or not this method is able to measure and track the degree of crystallinity. The method is relatively simple. Spectral reflectance allowed us to measure the film thickness with temperature or time. The film thickness is obviously correlated with the film volume. As shown in Figure 4.1, the film thickness (and therefore volume) changes characteristically through the melting transition. After the film melts, the expansion with time is linear. Thus, by taking the film thickness as a function of temperature, we can determine the expansion of amorphous PCL with time. We then use this linear trend and extrapolate to the theoretical thickness and mass per unit area at 25 °C. By using this known trend of amorphous density with temperature paired with the literature value of the crystalline density of PCL, we can then calculate a degree of crystallinity based on the instantaneous film thickness.

We used this analysis method and compared it to the degree of crystallinity calculated using the GIWAXS method from one additional study mimicking the expansion experiments shown in Figure 4.1 and the two-mentioned isothermal crystallization

experiments and 30 °C and 40 °C. As shown in Figures 4.8 & 4.9, the two methods of  $X_c$  calculation correlate remarkably well for the expansion experiment:

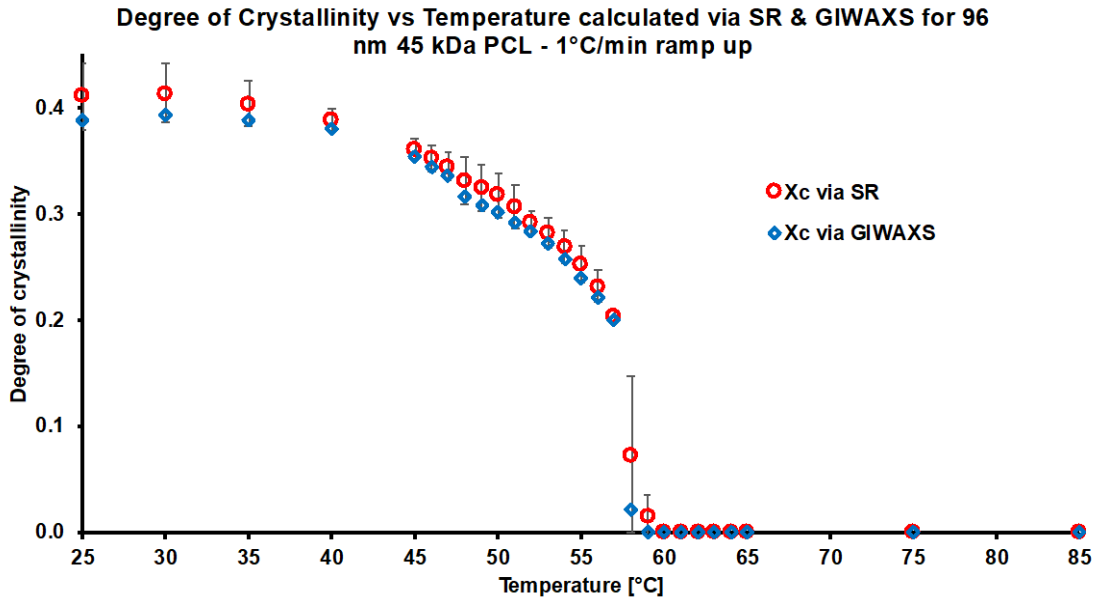


**Figure 4.8.** Degree of crystallinity vs. temperature calculated using both GIWAXS and the spectral reflectance method for 96 nm 45 kDa PCL.

Xc via Spectral Reflectance vs. Xc via GIWAXS for 96 nm 45 kDa PCL -  
1°C/min ramp up

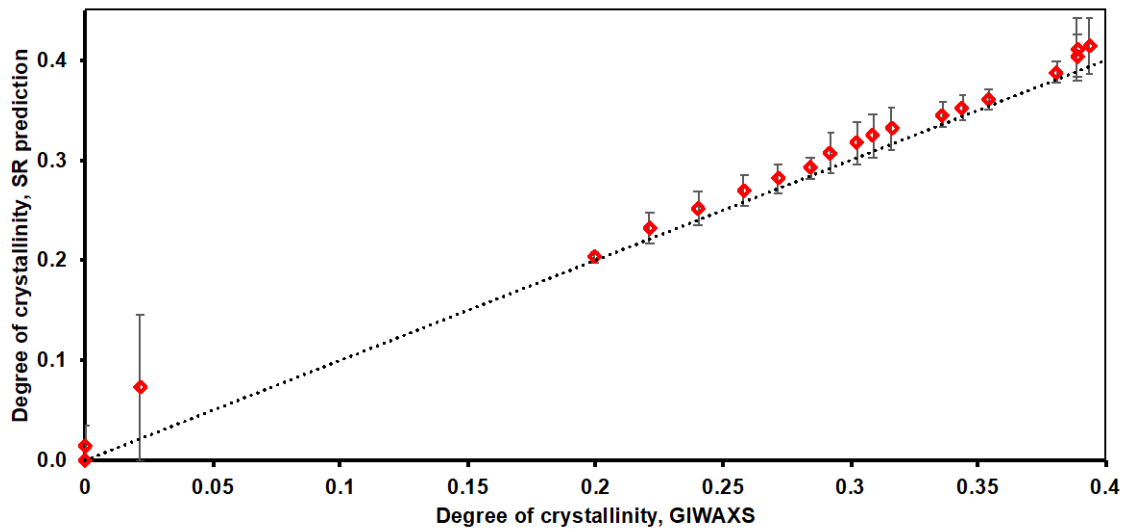


**Figure 4.9.** Degree of crystallinity via spectral reflectance vs. degree of crystallinity via GIWAXS for 96 nm 45 kDa PCL. Dotted line represents  $y = x$ .

However, the degree of crystallinity measured via spectral reflectance and GIWAXS do not show as close a correlation in the isothermal crystallization experiments (see Figures 4.10-4.13).

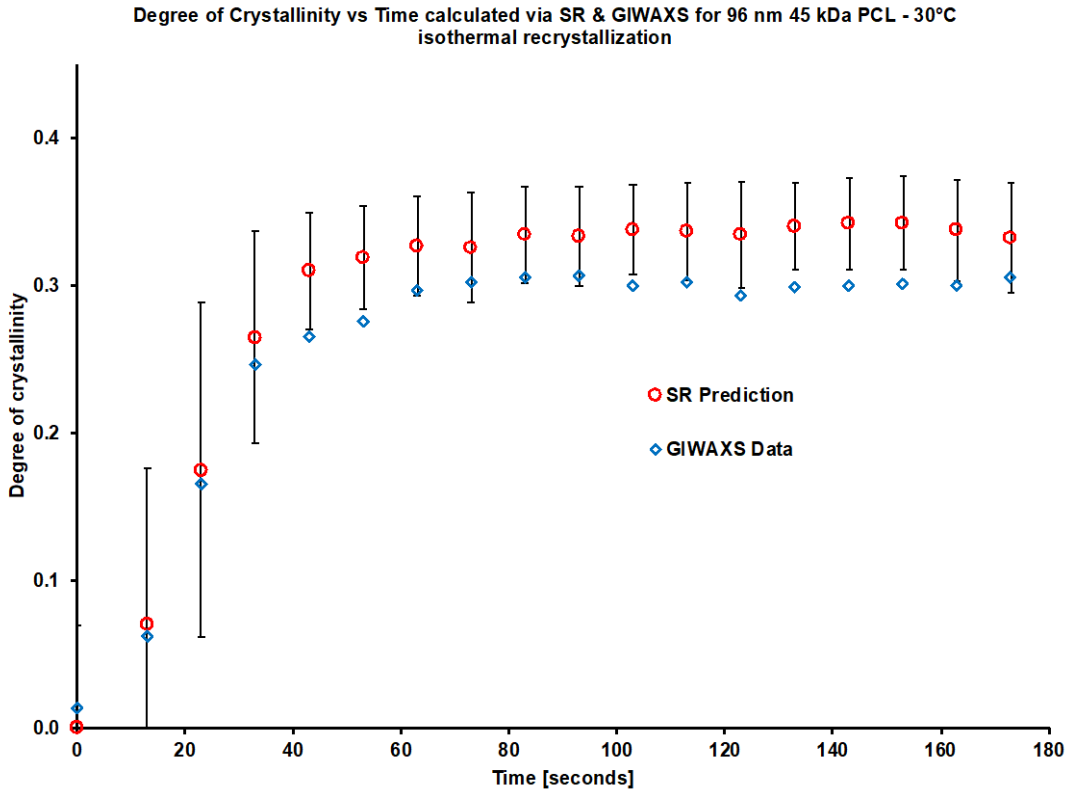


**Figure 4.10.** Degree of crystallinity vs. time calculated using both spectral reflectance and GIWAXS for 96 nm 45 kDa PCL isothermally crystallized at 30 °C. Error bars illustrate the standard deviation of the SR prediction from three separate isothermal crystallization trials.

**Xc via Spectral Reflectance vs. Xc via GIWAXS for 96 nm 45 kDa PCL - 30°C isothermal recrystallization**

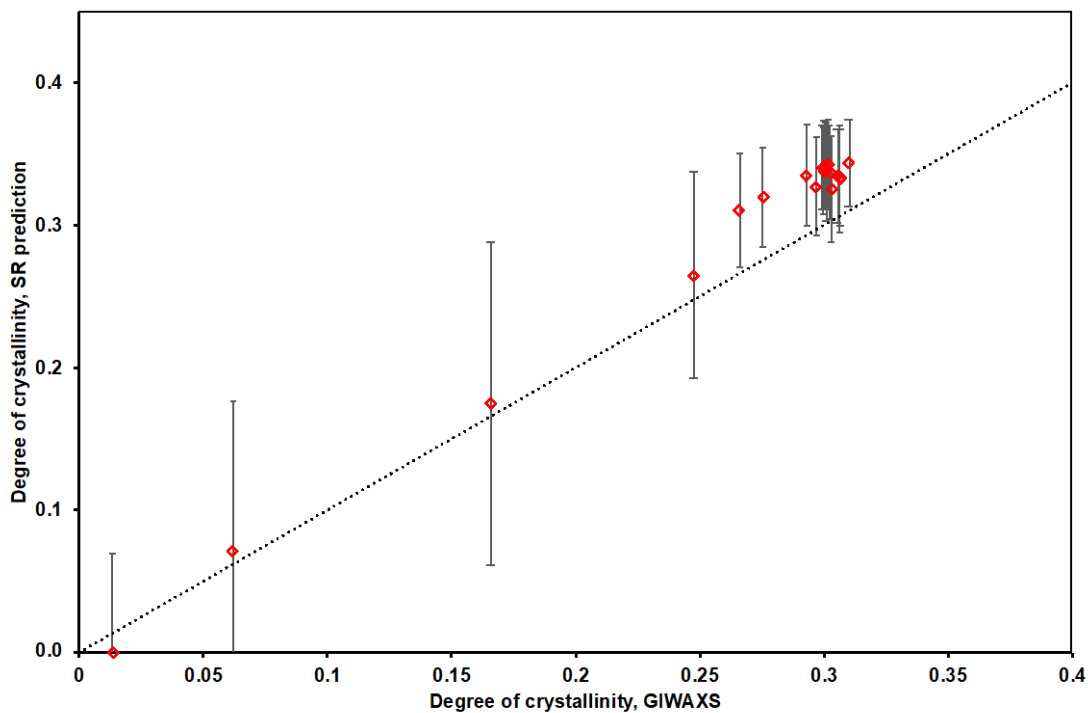


**Figure 4.11.** Degree of crystallinity via spectral reflectance vs. degree of crystallinity via GIWAXS for 96 nm 45 kDa PCL isothermally recrystallized at 30 °C. Dotted line represents  $y = x$ .

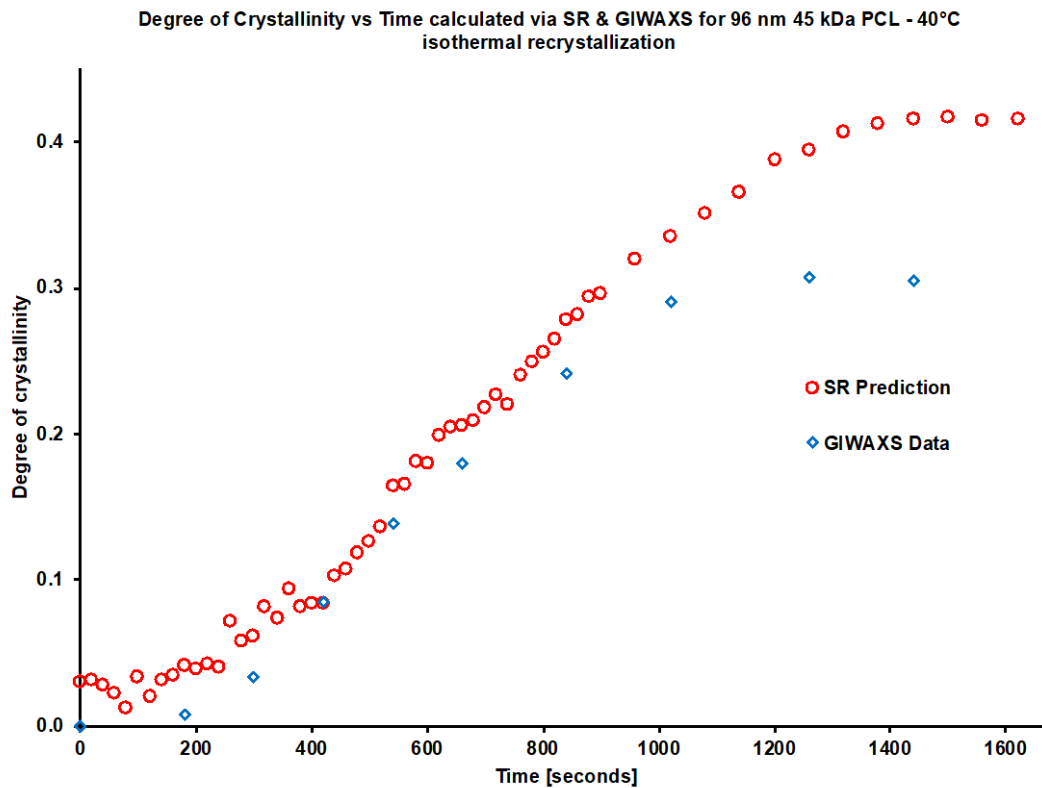


**Figure 4.12.** Degree of crystallinity vs. time calculated using both spectral reflectance and GIWAXS for 96 nm 45 kDa PCL isothermally crystallized at 40 °C.

Xc via Spectral Reflectance vs. Xc via GIWAXS for 96 nm 45 kDa PCL - 40°C isothermal recrystallization

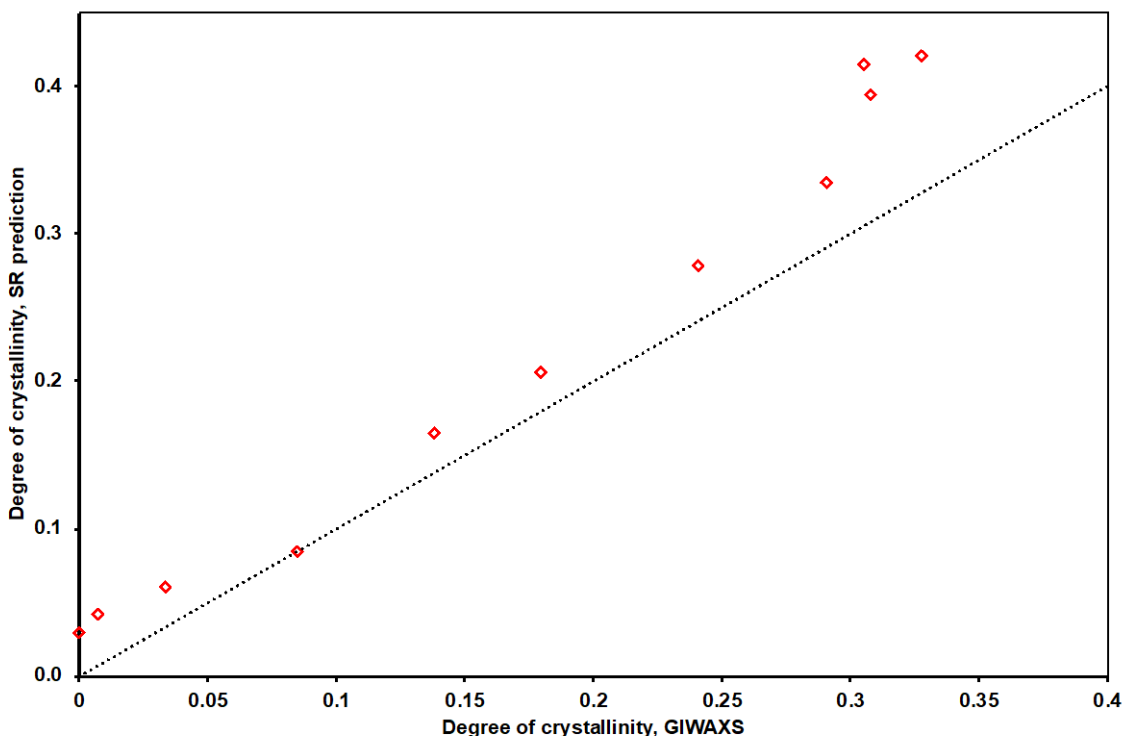


**Figure 4.13.** Degree of crystallinity via spectral reflectance vs. degree of crystallinity via GIWAXS for 96 nm 45 kDa PCL isothermally recrystallized at 40 °C. Dotted line represents  $y = x$ .

In the isothermal recrystallization experiments, the degree of crystallinity measured via spectral reflectance always overestimates the degree of crystallinity determined via GIWAXS. It is possible that GIWAXS is underestimating the degree of crystallinity as described previously, however it is bizarre that the melting experiment correlates rather well. The disagreement between these three experiments could be caused by a number of factors. It is possible that there are slight errors in the film thickness measurements that skew the extrapolation of the amorphous density with temperature, either positively or negatively. Since this is the basis for the Xc calculation, it has significant effects on the

accuracy of the measurement. In that sense, we very well might be reaching a measurement precision limitation of the F20 system. Additionally, the material should show a constant expansion with temperature. However, due to macromolecular effects, there might be some slight hysteresis between the expansion and contraction of the film. This could explain why our expansion calculation correlates so well while our crystallization (contraction) calculations differ from the measured GIWAXS value.

#### 4.6 Conclusions

In this work, we showed that spectral reflectance, a method of determining the film thickness of polymeric and non-polymeric materials, can be used to detect thermal transitions and isothermal crystallization processes in semi-crystalline polymer thin films based on the thermal expansion of the films during melting and contraction of the films during crystallization from the melt. One of the novelties of spectral reflectance is its experimental simplicity. With knowledge of the substrate, film material, and measurement medium (usually air), the user can easily measure film thicknesses ranging from single nanometers to many microns. Through careful temperature studies using SR measurements, we showed that semi-crystalline polymer thin films exhibit characteristic expansion and contraction profiles around the melting and crystallization transitions, respectively, and we correlated these profiles with DSC, temperature-controlled GIWAXS, and temperature-controlled AFM data. Specifically, we showed that from film thickness versus temperature curves constructed from SR data, the melting temperature corresponds to the point at which the thermal expansion becomes linear following the melting transition, and the midpoint of the melting transition corresponds to a maximum in the slope the curve.

Similarly, the onset of crystallization as determined by the point at which the thermal contraction occurs correlates well with DSC measurement. Additionally, we showed that this method is capable of quantifying the significant melting point depression of semi-crystalline PEG films due to thin film geometry. Furthermore, we studied how the spectral reflectance technique can be used to analyze isothermal crystallization processes by studying the contraction of the film with time and comparing it to similar isothermal crystallization experiments done via GIWAXS. In doing these experiments, we found the crystallization half time calculate via GIWAXS correlates remarkably well with the “film thickness half-time” calculated via spectral reflectance. We have also begun to study how this method can be used to measure degree of crystallinity in thin films, however more work needs to be done in this area. Overall, we find that spectral reflectance is a simple, low-cost, and easily accessible technique that can be used to determine the melting and crystallization temperatures of ultrathin films *in situ*, without removal from the substrate, and for which the small amount of material renders other laboratory techniques infeasible.

## Chapter 5

# SUPPRESSION OF MELT-INDUCED DEWETTING IN CYCLIC POLY( $\epsilon$ -CAPROLACTONE) THIN FILMS

This work describes the discovery that cyclic poly( $\epsilon$ -caprolactone) (*c*-PCL<sub>6k</sub>) exhibits enhanced film stability and resistance to dewetting compared to linear poly( $\epsilon$ -caprolactone) (*l*-PCL<sub>6k</sub>). For comparison, a comprehensive study was conducted to examine how topology affects film stability. Linear PCLs containing triazole groups and terminated with hydroxy, propargyl, azide, and acetyl groups all exhibit varying amounts of dewetting despite significantly different end groups and substrate interactions. In contrast, *c*-PCL<sub>6k</sub> retains thin film stability and does not dewet under the same conditions. The reason for enhanced stability of *c*-PCL<sub>6k</sub> films remains unclear based on previous work exploring the physical properties of cyclic PCLs and the numerous efforts to understand dewetting phenomena in thin films. For example, because *c*-PCL<sub>6k</sub> has a lower viscosity than *l*-PCL<sub>6k</sub>, one would expect *c*-PCL<sub>6k</sub> films to dewet more readily than *l*-PCL<sub>6k</sub> films. Herein the opposite behavior is reported. Furthermore, the ability to enhance film stability via the cyclic topology has powerful ramifications in the context of applications that require film stability in thin and ultrathin film geometries.

This chapter is based on published work: Kelly, Giovanni M., et al. "Suppression of Melt-Induced Dewetting in Cyclic Poly ( $\epsilon$ -caprolactone) Thin Films." *Macromolecules* (2017).

## 5.1 Introduction

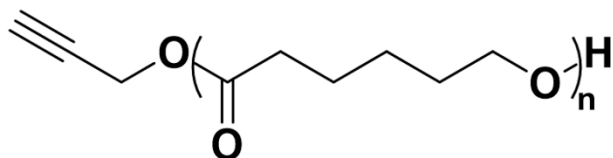
In the last decade, the pace of research studying cyclic and other non-linear polymer architectures has increased dramatically due to the development of novel synthetic routes to control polymer architecture, size, dispersity, and composition while also maintaining the high purity necessary for phenomenological study. Specifically, advances in conjugation reactions have led to the use of the copper(I)-catalyzed azide-alkyne cycloaddition (CuAAC) "click" reactions to efficiently synthesize cyclic homopolymers,<sup>194</sup> cyclic block copolymers,<sup>195</sup> star polymers,<sup>196</sup> and multi-cyclic topologies.<sup>197</sup> It has been known for some time that very small amounts of linear impurities (0.1%) can significantly alter some cyclic polymer properties,<sup>198</sup> making their study challenging and some previously reported results difficult to reproduce. Due to the quantitative and highly efficient nature of the CuAAC coupling chemistry, the presence of linear impurities can be nearly eliminated.<sup>199</sup> These advances have allowed researchers to begin to better understand the fundamental differences between the linear and cyclic topology.

Progress in the synthesis of cyclic polymers has taken place alongside significantly increased interest in studying polymers confined to thin and ultrathin films, which are relevant to applications in photolithography<sup>156, 200</sup> and nanoscale membranes.<sup>157-158, 160, 201-202</sup> However, thin film confinement often produces dramatic and sometimes deleterious effects on physical properties, such as the depression or elevation of thermal transitions.<sup>105-</sup>

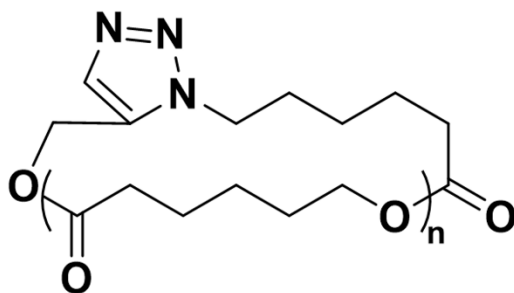
106, 145, 147, 171-172, 179 Additionally, poor substrate adhesion can lead to film dewetting.<sup>11, 20, 33, 35, 155, 203-212</sup> By contrast, several groups have shown that the cyclic architecture exhibits unique and useful phenomena, such as a decrease in domain size in cyclic block copolymer thin films,<sup>200, 213</sup> and a lack of  $T_g$  depression in cyclic polystyrene thin films.<sup>214</sup> In this note, we describe our observation that low molecular weight cyclic poly( $\epsilon$ -caprolactone) (PCL) resists thin film dewetting in the melt state better than its linear analog, regardless of linear PCL end-group chemistry. As research focuses more closely on polymers confined to thin and ultrathin films, the suppression of dewetting will become necessary as an unstable, discontinuous layer is impractical for most applications. Our results show that the cyclic topology may offer a practical solution to the problem of film dewetting.

## 5.2 Experimental Section

**Nomenclature.** The following nomenclature will be used throughout: *l*-PCL<sub>6k</sub> and *c*-PCL<sub>6k</sub> designate the linear and cyclic poly( $\epsilon$ -caprolactone), respectively (see Figure 5.1). Unless otherwise noted, *l*-PCL<sub>6k</sub> refers to  $\alpha$ -propagyl- $\omega$ -hydroxy-poly( $\epsilon$ -caprolactone). The subscript “6k” indicates the molecular weight ( $M_n = 6$  kDa).



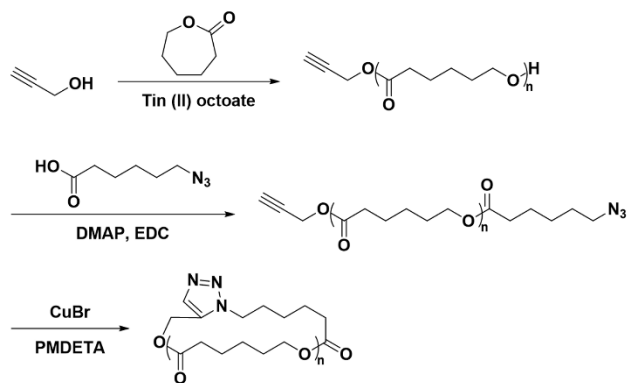
**Linear PCL (*l*-PCL<sub>6k</sub>) (1)**



**Cyclic PCL (*c*-PCL<sub>6k</sub>) (3)**

**Figure 5.1.** Structures of *l*-PCL<sub>6k</sub> and *c*-PCL<sub>6k</sub>. The numbers (1) and (3) correspond to the synthetic identification of these polymers in the “Synthetic Protocols” section of the Appendix C.

**Synthetic and Analytical Methods.** In order to synthesize *l*-PCL<sub>6k</sub>, distilled ε-caprolactone (CL) was polymerized in the presence of propargyl alcohol to install the necessary alkyne moiety. The terminating hydroxy-group allowed for end group functionalization with an azide-containing carboxylic acid using ethyl(dimethylaminopropyl) carbodiimide (EDC) based ester coupling chemistry. With the synthesized α-propargyl-ω-azide-polymer, the final CuAAC “click” cyclization coupling was performed to generate the desired *c*-PCL<sub>6k</sub> (see Scheme 5.1).



**Scheme 5.1:** Synthesis of cyclic PCL.

Gel permeation chromatography (GPC) was used to quantify relative molecular weights ( $M_n$  and  $M_w$ ) and dispersity ( $\mathcal{D}$ ). GPC also was used to confirm cyclization based on the increased retention time of the cyclic due to the decreased hydrodynamic volume.<sup>215-216</sup> Matrix-assisted laser desorption/ionization time of flight (MALDI-TOF) mass spectrometry (MS) offered complementary results, providing precise molecular weight information, while simultaneously detailing exact molecular weight values of specific  $n$ -mers to confirm end group modification.<sup>94</sup> A more extensive discussion of the analytical and synthetic methods can be found in Appendix C.

**Film Casting and Characterization.** Thin films were cast via spincoating from dilute solutions in toluene onto UV-ozone treated silicon wafers. Films were melted for 10 minutes at 100 °C and quenched to 25 °C, where they were left to crystallize for at least 24 hours. Although the melting temperature of cyclic PCL has been reported to be slightly higher than linear PCL ( $T_m \approx 55$  °C and 59 °C, respectively, for 7.5 kDa PCL)<sup>7</sup>, the films were melted at 100 °C, which is significantly above both melting temperatures such that any differences in dynamics due to the slightly higher  $T_m$  of cyclic PCL are negligible. Films were subsequently studied via optical microscopy (Olympus BX53) to examine the

global morphology as well as via atomic force microscopy (Bruker Dimension ICON) to examine local morphology and monitor dewetting. Film thicknesses ranged from 106 nm to 116 nm and were quantified using spectral reflectance (Filmetrics F20-UV). Static water contact angles (three drops per film) were quantified using a Ramé-Hart goniometer to study surface energy differences between linear PCL and cyclic PCL.

### 5.3 Results

Initial characterization by GPC revealed that the PCLs synthesized via the methods outlined above have low dispersity (see Figure 5.2a, Table 5.1). Successful cyclization was confirmed by the slightly longer elution time due to decreased hydrodynamic volume of the cyclic architecture while exhibiting unchanged mass by MALDI-TOF MS. MALDI-TOF MS analysis also verified low dispersity and provided accurate molecular weights for all species (see Figure 5.2b-5.2c). Finally, end-group transformations performed to provide a series of linear controls (see Appendix C, Figure C1) were confirmed by MALDI-TOF MS.

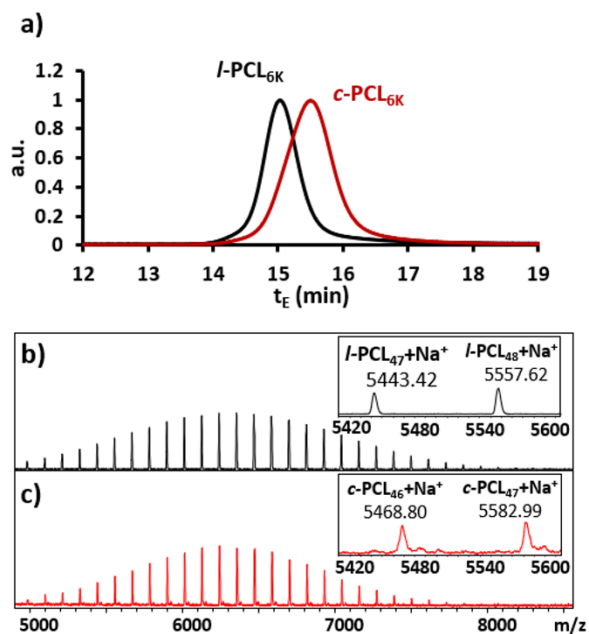


**Figure 5.2.** Molecular weight characterization data for *l*-PCL<sub>6k</sub> and *c*-PCL<sub>6k</sub>. a) GPC chromatograms illustrate the longer elution time for the *c*-PCL<sub>6k</sub> due to its decreased hydrodynamic radius. b-c) MALDI-TOF MS spectra of *l*-PCL<sub>6k</sub> and *c*-PCL<sub>6k</sub> indicate exceptional uniformity in both species with respect to end group functionalities and architectural transformations.

**Table 5.1:** Mass determination of *l*-PCL<sub>6k</sub> and *c*-PCL<sub>6k</sub> by GPC and MALDI-TOF MS.

	M <sub>n</sub>			Đ	
	GPC <sup>a</sup>	GPC <sup>b</sup>	MALDI	GPC	MALDI
<i>l</i> -PCL <sub>6k</sub>	12400	6390	6360	1.08	1.01
<i>c</i> -PCL <sub>6k</sub>	12200*	6270*	6420	1.12	1.01

<sup>a</sup>Calibrated based upon linear polystyrene standards

<sup>b</sup>Corrected value for PCL,<sup>217</sup> using  $M_n(\text{PCL}) = 0.259M_n(\text{PS})^{1.073}$

\*Corrected cyclic M<sub>n</sub> values based on retention time and ratios of M<sub>n c-PS</sub>/M<sub>n l-PS</sub> reported by Alberty et al<sup>216</sup> as 0.70 for PS<sub>22000</sub>

In order to explore the effect of chain topology on dewetting behavior, thin films ( $\approx 110$  nm thickness) of 6 kDa PCLs were spincoated and subsequently melted and recrystallized to study their thermal stability in the melt state. A molecular weight of 6 kDa was chosen because polymers of this molecular weight can be readily cyclized and because 6 kDa is sufficiently above the entanglement molecular weight of linear PCL (2-3 kDa) such that dewetting of *l*-PCL<sub>6k</sub> cannot be attributed to lack of entanglements.<sup>7</sup> Furthermore, several groups have shown that the number of entanglements in cyclic polystyrene and polybutadiene is two to five times lower than their linear analogues.<sup>218-219</sup> Thus, one would expect the *l*-PCL<sub>6k</sub> film to be more resistant to dewetting than the *c*-PCL<sub>6k</sub> film due to the greater presence of entanglements in *l*-PCL<sub>6k</sub> and fewer entanglements in *c*-PCL<sub>6k</sub>; however, we observe the opposite result. As seen by comparing Figures 5.3a and 5.3d, *l*-PCL<sub>6k</sub> has an as-cast morphology similar to that of the cyclic analog. After melting and recrystallization, dewetting of the *l*-PCL<sub>6k</sub> film can be observed optically by substrate

exposure (tan colored regions) and the raised edges of the dewet film (light blue) (Figure 5.3b). In contrast, the melted and recrystallized *c*-PCL<sub>6k</sub> film (Figure 5.3e) showed no evidence of dewetting by optical microscopy. To verify the dewetting of the *l*-PCL<sub>6k</sub> film, AFM height images were collected of both linear and cyclic species after melting and recrystallization, and height sections were taken across the regions of interest (Figure 5.3c, 3f). The depression imaged in the *l*-PCL<sub>6k</sub> film is broad in width (~10 μm), and its depth ( $104.6 \pm 7.58$  nm) is approximately equal to the film thickness, which is indicative of dewetting. In comparison, the width of the depression imaged in the *c*-PCL<sub>6k</sub> film is narrow (~1 μm) and its depth ( $64.7 \pm 6.46$  nm) is much less than the film thickness, consistent with a crystal grain boundary.

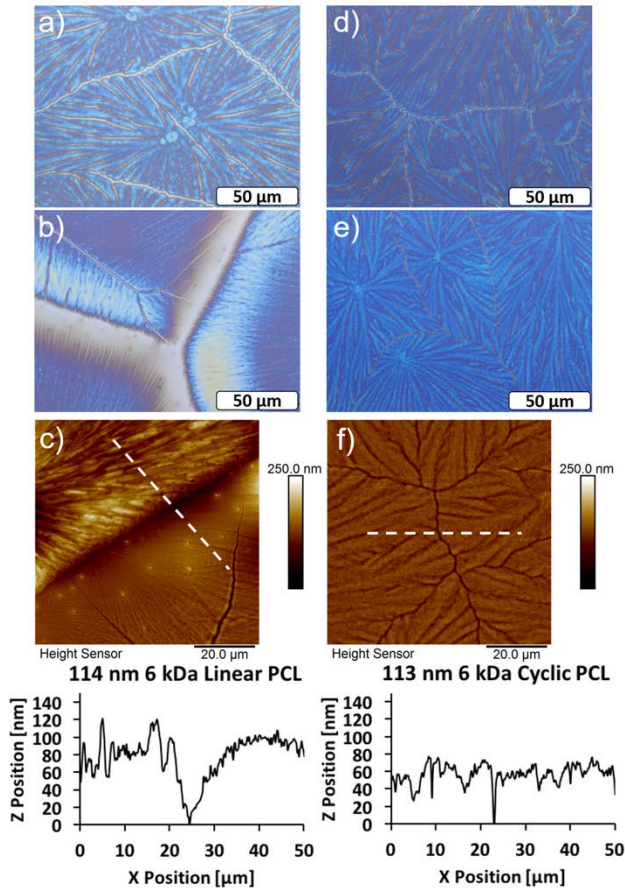
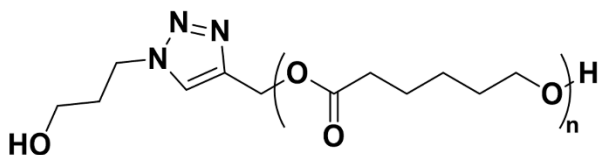


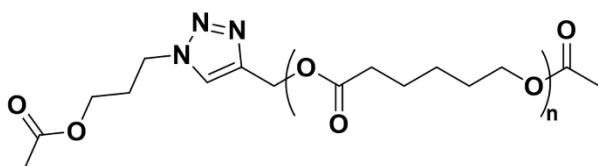
**Figure 5.3.** Comparison of *l*-PCL<sub>6k</sub> and *c*-PCL<sub>6k</sub> before and after melting and recrystallization: a) optical image of *l*-PCL<sub>6k</sub> as cast; b) optical image of *l*-PCL<sub>6k</sub> melted and recrystallized; c) AFM height image of *l*-PCL<sub>6k</sub> melted and recrystallized showing a section taken across the dewet area (average depth:  $104.6 \pm 7.58$  nm); d) optical image of *c*-PCL<sub>6k</sub> as cast; e) optical image of *c*-PCL<sub>6k</sub> melted and recrystallized; f) AFM height image of *c*-PCL<sub>6k</sub> melted and recrystallized showing a section across a grain boundary (average depth:  $64.7 \pm 6.46$  nm).

Static water contact angle measurements on as-cast films of *l*-PCL<sub>6k</sub> and *c*-PCL<sub>6k</sub> revealed water contact angles of  $73.7^\circ \pm 0.2^\circ$  and  $79.1^\circ \pm 0.7^\circ$ , respectively. These values are commensurate with advancing and receding contact angles reported previously for linear PCL ( $\theta_A = 78.5^\circ$  and  $\theta_R = 71.6^\circ$ , corresponding surface tension  $\gamma = 37.9$  mN/m)<sup>220</sup> and show that the enhanced film stability of cyclic PCL is not due to a difference in surface tension. These data suggest that the cyclic topology of *c*-PCL<sub>6k</sub> may inhibit thin film dewetting. To support this assertion and eliminate the competing hypothesis that chemical differences between *l*-PCL<sub>6k</sub> and *c*-PCL<sub>6k</sub> (*i.e.*, identity of the *l*-PCL<sub>6k</sub> end-groups, or the presence of the triazole in *c*-PCL<sub>6k</sub>) could account for the differences in film stability, several additional control *l*-PCLs were synthesized with varying end groups (see Figure 5.4; Appendix C, Figure C1), and the same film stability experiments were performed (see Appendix C, Figure C2). End groups were chosen to address the possible roles of end-group polarity and presence of the triazole group on film stability. The triazole-containing- $\alpha,\omega$ -dihydroxy-PCL<sub>6k</sub> film exhibited partial dewetting during melting and recrystallization, much like the *l*-PCL<sub>6k</sub> in Figure 5.3b, albeit with significantly wider dewet regions. Films

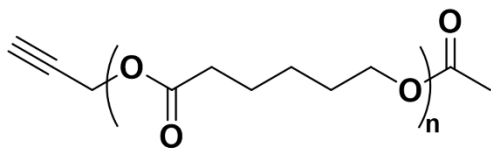
of the triazole-containing- $\alpha,\omega$ -diacetyl-PCL<sub>6k</sub> and  $\alpha$ -propargyl- $\omega$ -acetyl-PCL<sub>6k</sub> dewet completely upon melting. Finally, the  $\alpha$ -propargyl- $\omega$ -azide-PCL<sub>6k</sub> film dewet upon casting.



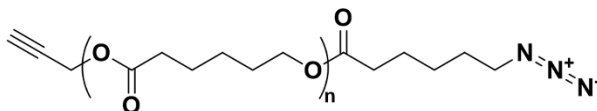
**Triazole-containing  $\alpha,\omega$ -dihydroxy-PCL (4)**



**Triazole-containing  $\alpha,\omega$ -diacetyl-PCL (5)**



**$\alpha$ -propargyl- $\omega$ -acetyl-PCL (6)**



**$\alpha$ -propargyl- $\omega$ -azide-PCL (2)**

**Figure 5.4.** Chemical structures of the additional linear PCL controls. The numbers (2), (4), (5), and (6) correspond to the synthetic identification of these polymers in the “Synthetic Protocols” section of the Appendix C.

#### 5.4 Discussion

Dewetting is a complex and important phenomenon that can largely be attributed to a few important factors, namely, film thickness, polymer-substrate/polymer-polymer

interactions, temperature, and molecular weight.<sup>11, 20, 33, 35, 155, 203-206, 209, 212, 221</sup> In sufficiently thick films (microns and above), molecular forces that drive film instability are overcome by gravity, which allows the polymer film to resist dewetting.<sup>203, 221</sup> Below a critical thickness, molecular forces become dominant, and the film may break up into droplets on the substrate through homogeneous or heterogeneous nucleation and propagation of dewetting holes.<sup>155, 203, 205</sup> A polymer also may be forced into an unstable or metastable state by casting onto a highly non-wettable substrate.<sup>155, 222</sup> Because of unfavorable polymer-substrate interactions, the film will spontaneously dewet upon casting, or if metastable, any perturbation, such as an increase in temperature above the thermal transition, will cause rupture of the film and dewetting from the substrate. Finally, the polymer molecular weight also plays a role in the dewetting rate due to the relationship between molecular weight and fluid viscosity; thus, a more highly-entangled polymer has significantly lower mobility and will resist dewetting.<sup>203, 205, 223</sup>

In our study, film thickness and molecular weight were held constant and the melting procedure was standardized so that topology (*l*-PCL<sub>6k</sub> versus *c*-PCL<sub>6k</sub>) and end-group chemistry (of the control *l*-PCLs) were the only variables that could account for differences in film dewetting. The end group chemistries ranged from polar hydrophilic groups to non-polar hydrophobic groups. Although end groups can affect intermolecular interactions, all of the linear PCLs and *c*-PCL<sub>6k</sub> exhibit crystallization upon film casting (see Figure 5.3a, Appendix C, Figure C2) suggesting that the end groups minimally impact intermolecular interactions. However, the differences in dewetting behavior show that the end groups have a substantial impact on the interaction of the polymer chains with the substrate. For example, hydrophilic polymers and end groups can more easily interact with

and wet polar substrates than hydrophobic polymers, potentially improving film stability. This observation may explain the lesser extent of dewetting exhibited by *l*-PCLs containing polar hydroxy end-groups compared to *l*-PCLs containing only hydrophobic end-groups (see Figure 5.3, Appendix C, Figure C2). However, dewetting arises even in the presence of favorable end-group interactions with the substrate. Reiter and others have described the phenomenon of “autophobic dewetting” which can occur when the confined polymer has “sticky ends” or end-groups that are more inclined to complex with the substrate than the rest of the polymer chain.<sup>204, 207-208, 210-211, 224</sup> Repulsive interactions between the adsorbed polymer layer and the bulk polymer layer increase the likelihood of dewetting. Thus, films of *l*-PCLs containing polar hydroxy groups to facilitate favorable substrate interactions may still dewet by autophobic dewetting.

Although the dewetting behavior of the *l*-PCL<sub>6k</sub> films can be explained based on analysis of interactions between the end-groups and the substrate, this assessment provides an insufficient explanation for the dramatic increase in stability afforded by the cyclic topology. Furthermore, several groups have shown that analogous cyclic polymers have significantly lower viscosities than their linear counterparts which should enhance their mobility in thin films.<sup>17, 26-27, 215-216</sup> Based on these facts, the cyclic polymer film would be expected to dewet more readily than films of exact linear analogues due to lack of end-group stabilization and greater polymer mobility. Additionally, the presence of a triazole group, which has been suggested may affect PCL crystallization kinetics,<sup>25</sup> does not explain the stability of *c*-PCL<sub>6k</sub> films, as triazole-containing linear controls readily dewet. Although there are many factors that dictate film stability, this initial investigation points

to the cyclic topology as the strongest contributing factor to the greatly enhanced thin film stability of *c*-PCL.

## 5.5 Conclusions

In this work, we described the discovery that low molecular weight cyclic poly( $\epsilon$ -caprolactone) exhibits enhanced thin film melt stability when compared to exact linear analogs. Although multiple end group chemistries were studied, a stable *l*-PCL<sub>6k</sub> was not observed. This finding is intriguing given that the physical characteristics of cyclic polymers compared to linear analogues (greater chain mobility, lower viscosity, and lower density of molecular entanglements) are all properties that are known to facilitate rather than inhibit film dewetting processes. Although the underlying mechanism responsible for the enhanced stability of *c*-PCL<sub>6k</sub> films over *l*-PCL<sub>6k</sub> analogues has yet to be elucidated, this initial investigation provides compelling evidence that the cyclic topology is the strongest contributing factor. Finally, the ability to enhance film stability via the cyclic topology has the potential for far-reaching impacts on applications that require film stability in thin and ultrathin film geometries.

## **Chapter 6**

### **MORPHOLOGY AND KINETICS OF CRYSTAL GROWTH IN LINEAR AND CYCLIC PCL**

As discussed in Chapter 5, a great deal of work has been done to better understand the phenomena exhibited by cyclic polymers. This has mainly focused on the bulk, and characteristics such as degradation<sup>225</sup>, mechanical properties<sup>226</sup>, rheological characteristics<sup>227</sup>, and thermal properties<sup>7, 9, 17, 27, 215</sup>. In the case of semi-crystalline polymers, work has focused on studying the kinetics of crystal growth in linear and cyclic polymers such as PCL and PLA<sup>7, 17, 27, 225, 228-229</sup>. Because of the significant amount of time it took to develop adequate synthetic methods leading to pure cyclic materials, the pace of study into cyclic polymers confined in thin and ultrathin film geometries has lagged behind that of the bulk materials. However, many high impact studies have been done recently, including our own described in Chapter 5. The overarching goal of these studies, as in this thesis as a whole, is to understand how the confinement geometry affects the major characteristics of semi-crystalline polymers. This chapter outlines the initial work into the morphology and kinetics of crystal growth in linear and cyclic PCL in thin and ultrathin films.

## 6.1 Thin Film Morphology

The differences between linear and cyclic PCL in terms of molecular-level crystal structure have largely already been established. For example, Su et al. have shown that cyclic PCL exhibits a slightly larger lamellar thickness as compared to its exact linear analog<sup>27</sup>. Unsurprisingly, this leads to significant differences in the morphology in thin films, even when the films are cast using the same conditions. We have studied pairs of linear and cyclic PCL ranging from 1.2 kDa up to 6 kDa (the system studied in the preceding chapter) and at a range of film thicknesses. As can be seen in Figures 6.1-6.4, at multiple film thickness and at multiple molecular weights, the as-cast morphology is remarkably different between the linear and cyclic species, despite being at the same confinement and exact same molecular weight:

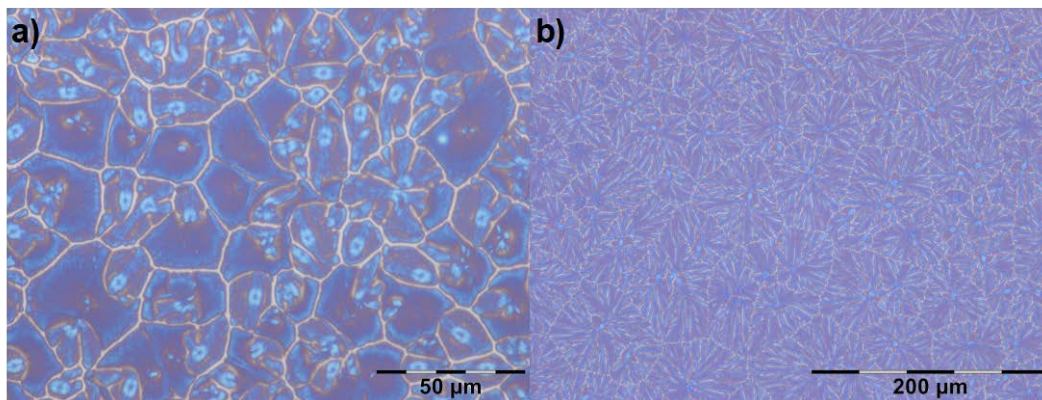


**Figure 6.1.** Bright field optical microscopy images of: a) 90 nm 1.2 kDa linear PCL as cast from toluene and b) 85 nm 1.2 kDa cyclic PCL as cast from toluene.

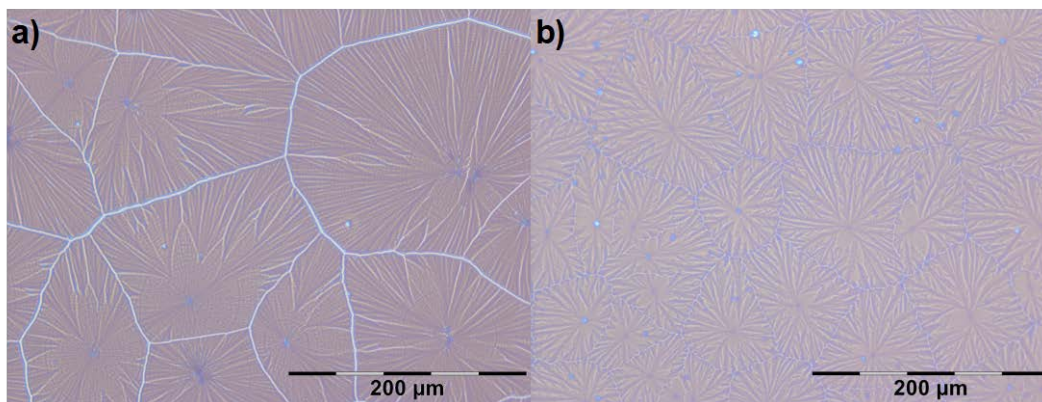


**Figure 6.2.** Bright field optical microscopy images of: a) 79 nm 4 kDa linear PCL as cast from toluene and b) 80 nm 4 kDa cyclic PCL as cast from toluene.

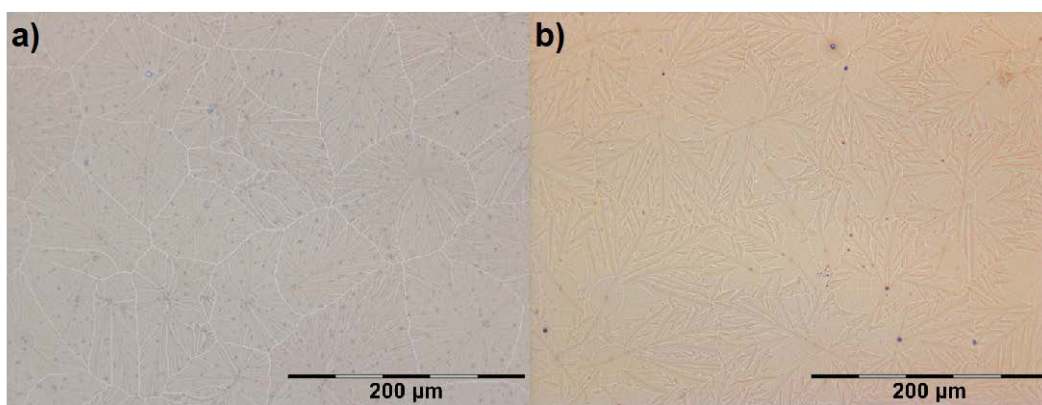


**Figure 6.3.** Bright field optical microscopy images of: a) 58 nm 6 kDa linear PCL as cast from toluene and b) 56 nm 6 kDa cyclic PCL as cast from toluene. Note: Contrast in images enhanced to better illustrate the morphology.

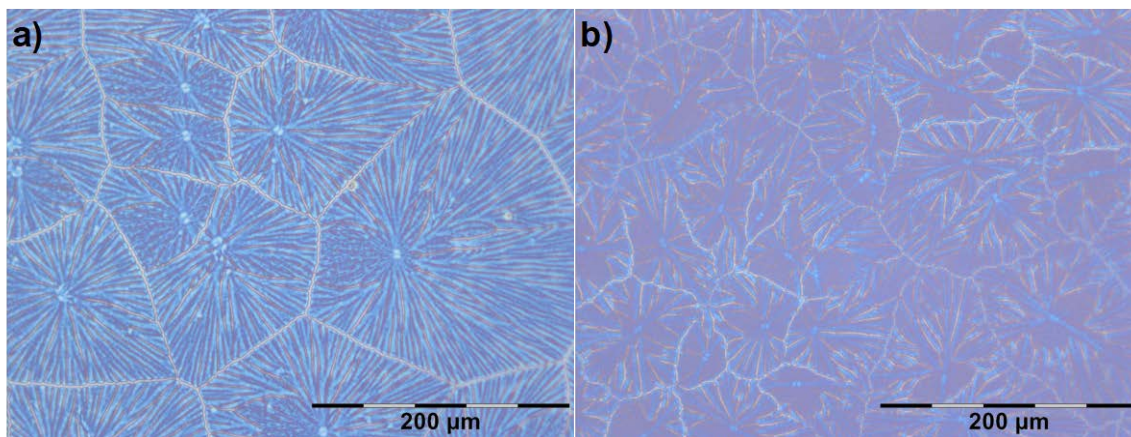


**Figure 6.4.** Bright field optical microscopy images of: a) 117 nm 6 kDa linear PCL as cast from toluene and b) 106 nm 6 kDa cyclic PCL as cast from toluene.

As cast images were used because melted and recrystallized linear samples at these molecular weights dewet from the substrate upon melting to erase the thermal history (see Chapter 5). However, several observations can be made from these as cast samples.

First, in each of the four examples, the cyclic generally exhibits crystals with smaller radii as compared to its linear analog. Because crystal size is directly related to the nucleation density, this is indicative that cyclic PCL tends to show an inherently higher nucleation density. For example, in Figure 6.2, the linear PCL shows 7 crystal nucleation sites, while the linear exhibits 28 nucleation sites. In some cases, such as Figure 6.1, they are roughly equivalent (79 linear vs. 73 cyclic). There is obviously a dependence on both the molecular weight and the film thickness. That the nucleation density tends to be higher in the cyclic molecules is not surprising considering that the ring structure will lead to a more compact amorphous structure which will force chains to be in closer contact and thus generate nuclei more freely.

Another major observation from this data set is that the morphology of the grain boundaries is different. As in typical polymer spherulites, the grain boundaries in the linear samples shows the typical smooth interface. In the case of the cyclic however, the grain boundaries are jagged, rough interfaces between the impinging crystals. This may also be due to the more compact nature of the cyclic molecule. Since it can form more compact crystals as it attaches to the growth face, it creates a more uneven surface.

Finally, the morphology inside the crystals themselves is quite different between the two. Linear PCL at this range of molecular weights shows a flattened spherulitic morphology, as expected. In the case of the cyclic, the morphology appears spherulitic, but with a much rougher spherulite surface.

## 6.2 Crystal Orientations via GIWAXS

As discussed by Zhang et al.<sup>214</sup>, much of the dynamics and phenomena exhibited by cyclic polymers in thin films has been hypothesized to be due, at least in part, to the orientation these molecules assume in thin films. It is well known that the substrate can have an enormous impact on the orientation that polymer chains can assume<sup>32, 34, 146, 152, 204, 230</sup>. Thus, we have studied several examples of linear and cyclic PCL thin films via GIWAXS. By studying the two-dimensional scattered intensity in  $q$ , it is obvious that the architecture of the polymer has a significant effect on the orientation of the crystalline lamellae:

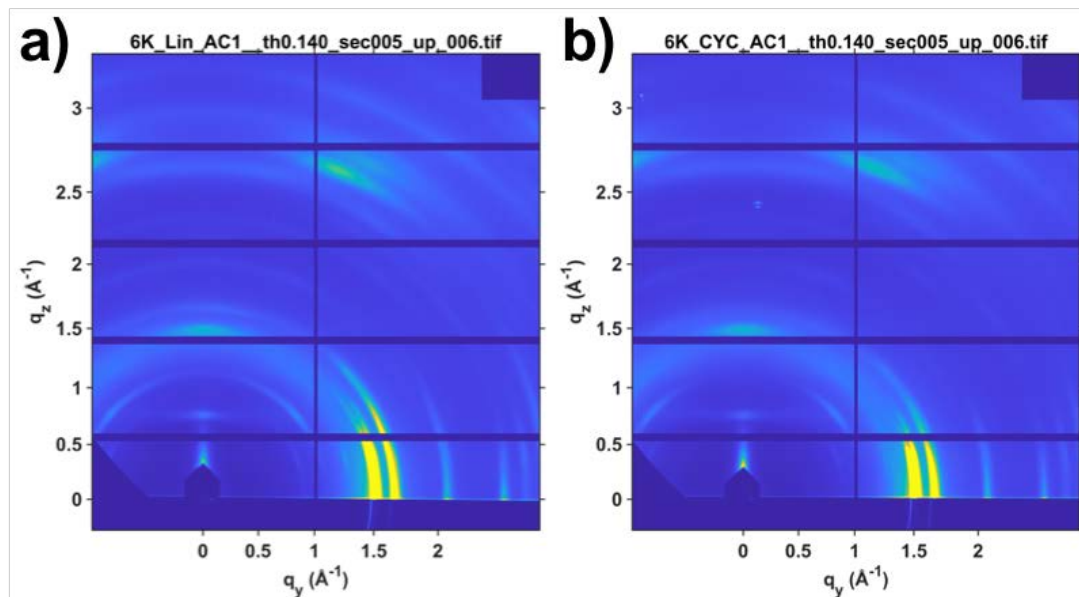


**Figure 6.5.** Two-dimensional scattering intensity measured via GIWAXS for a) 117 nm 6 kDa linear PCL as cast from toluene; and b) 106 nm 6 kDa cyclic PCL as cast from toluene.

As shown in Figure 6.5, the as cast orientations of both linear and cyclic PCL are similar, however examined more closely it becomes obvious that there is less of an orientation distribution in the case of the cyclic. The difference becomes more dramatic once the films are melted and recrystallized to erase film casting history:

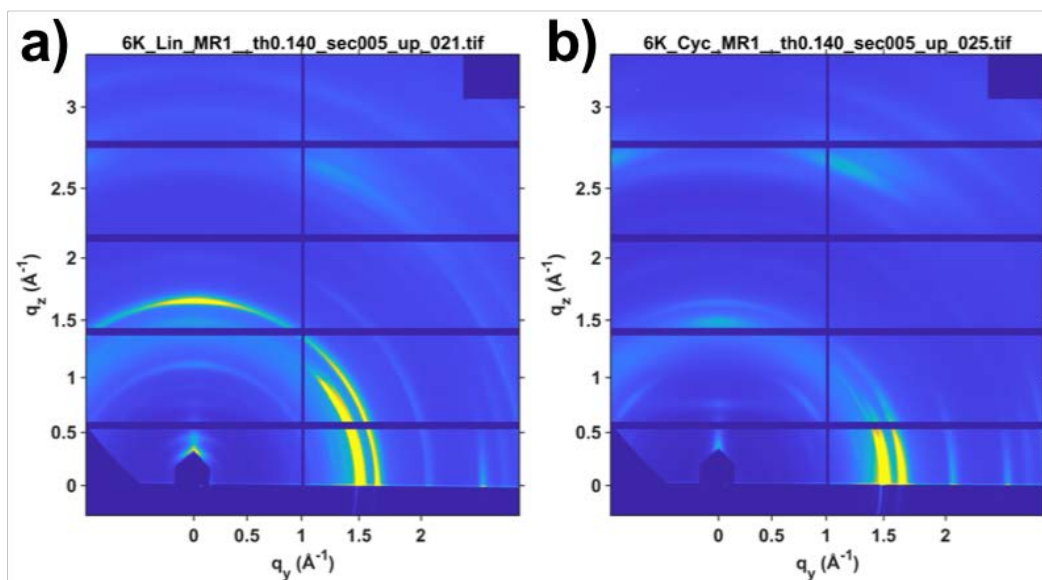


**Figure 6.6.** Two-dimensional scattering intensity measured via GIWAXS for a) 114 nm 6 kDa linear PCL melted and recrystallized at 25 °C; and b) 113 nm 6 kDa cyclic PCL melted and recrystallized at 25 °C. Note: as discussed in Chapter 4, the linear sample suffers slight dewetting, which contributes to the halos directly above the beam stop.

Figure 6.6 offers an interesting insight, however more work needs to be done to study it further. By comparing the crystal orientation between the as cast (Figure 6.5b) and melted and recrystallized (Figure 6.6b), it appears the cyclic film does not undergo a significant change in crystal orientation. This could be due to the compact nature of the cyclic molecule allowing it to find its preferred orientation more readily than the linear. Alternatively, it could be due to the lack of chain ends, which restricts any large orientation shifts even in the melt state. It is important to note that the linear film suffers slight dewetting upon melting, however this effect is largely observed in the periodic banding directly above the beamstop due to the silicon substrate. This is contrasted with the linear which has more segmental mobility due to the linear architecture. We found this same

result in comparing even thinner films of linear and cyclic PCL (see Figure 6.7), however the large extent of dewetting in the linear creates a significant noise in the GIWAXS data:

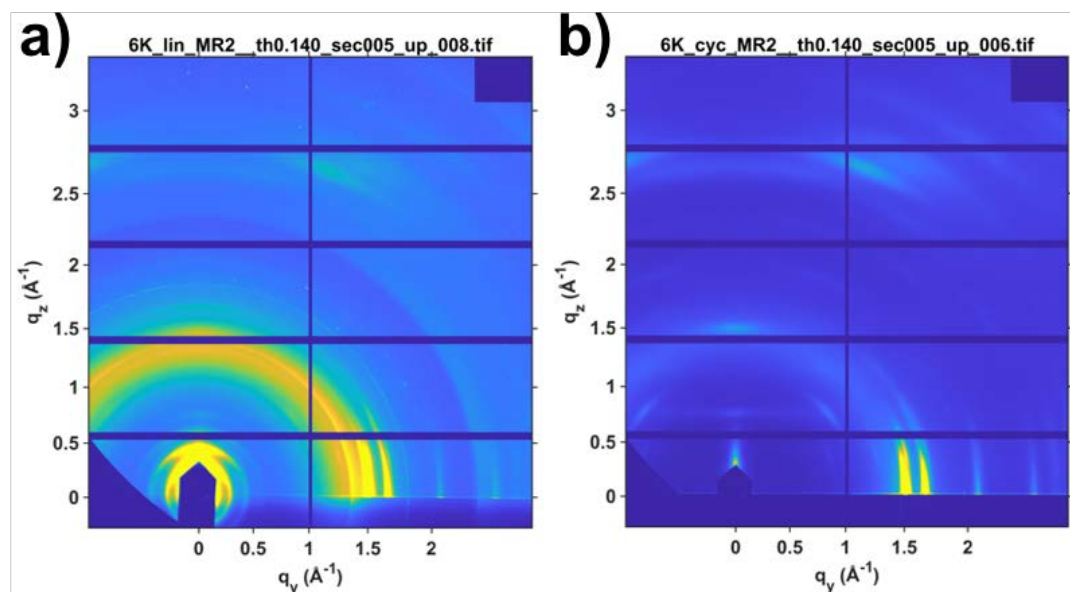


**Figure 6.7.** Two-dimensional scattering intensity measured via GIWAXS for a) 58 nm 6 kDa linear PCL melted and recrystallized at 25 °C; and b) 57 nm 6 kDa cyclic PCL melted and recrystallized at 25 °C. Note: as discussed in Chapter 4, the linear sample suffers slight dewetting, which contributes to the halos directly above the beam stop.

To study whether this difference in orientations between linear and cyclic PCL was due to the ultrathin film confinement in films at approximately 100 nm and below (as the preceding films were), we also studied thicker films of the 6 kDa linear and cyclic PCL:

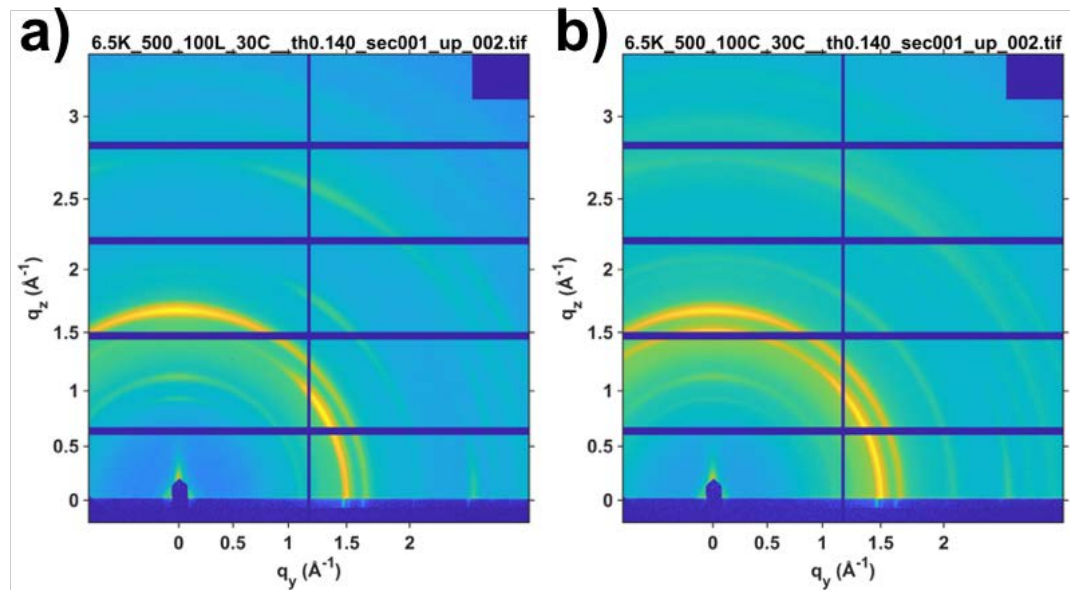


**Figure 6.8.** Two-dimensional scattering intensity measured via GIWAXS for a) 474 nm 6 kDa linear PCL melted and recrystallized at 25 °C; and b) 502 nm 6 kDa cyclic PCL melted and recrystallized at 25 °C.

The preceding results lead to two preliminary conclusions. First, in thinner films, it appears cyclic PCL assumes a preferred orientation when cast from organic solution, and that this orientation is favored even after the film is melted and recrystallized to erase the thermal history. This is contrasted by the linear results, which shows an appreciable shift in crystal orientation once the film is melted and recrystallized. Second, whether studying the film before or after melting and recrystallizing, it is obvious that the cyclic PCL shows a different orientation as compared to its exact linear analog. While it is unclear if this orientation difference contributes to the differences in morphology and film stability discussed thus far in this thesis, it does show that the cyclic architecture affects the crystal structure on a molecular and lamellar level.

### 6.3 Crystal Growth Kinetics

One of the main areas of study in semi-crystalline polymers, regardless of bulk or thin film geometry, is the crystallization kinetics. As discussed in Chapter 1, crystallization is a growth process that is affected by several factors, especially the temperature at which the crystals grow. We would also like to better understand what effect the substrate has on crystal growth. To this end, we have begun to study the crystal growth kinetics and the differences exhibited by linear and cyclic PCL when isothermally recrystallized at different temperatures. This study lagged the other preliminary studies due to the dewetting of low molecular weight linear PCL. This dewetting renders the film useless for kinetics studies. As such, we studied films approximately 500 nm films of pure linear and pure cyclic 6.5 kDa PCL. Additionally, since an eventual goal of this project is to study how blending the two architectures affects morphology, crystallization kinetics, and stability, we also studied a 50/50 linear-cyclic blend film. These films were isothermally crystallized at temperatures ranging from 25 °C to 40 °C after being thermally treated to erase film casting history. As shown in Figure 6.9, different isothermal crystallization temperatures lead to a significant difference in crystal growth rates:

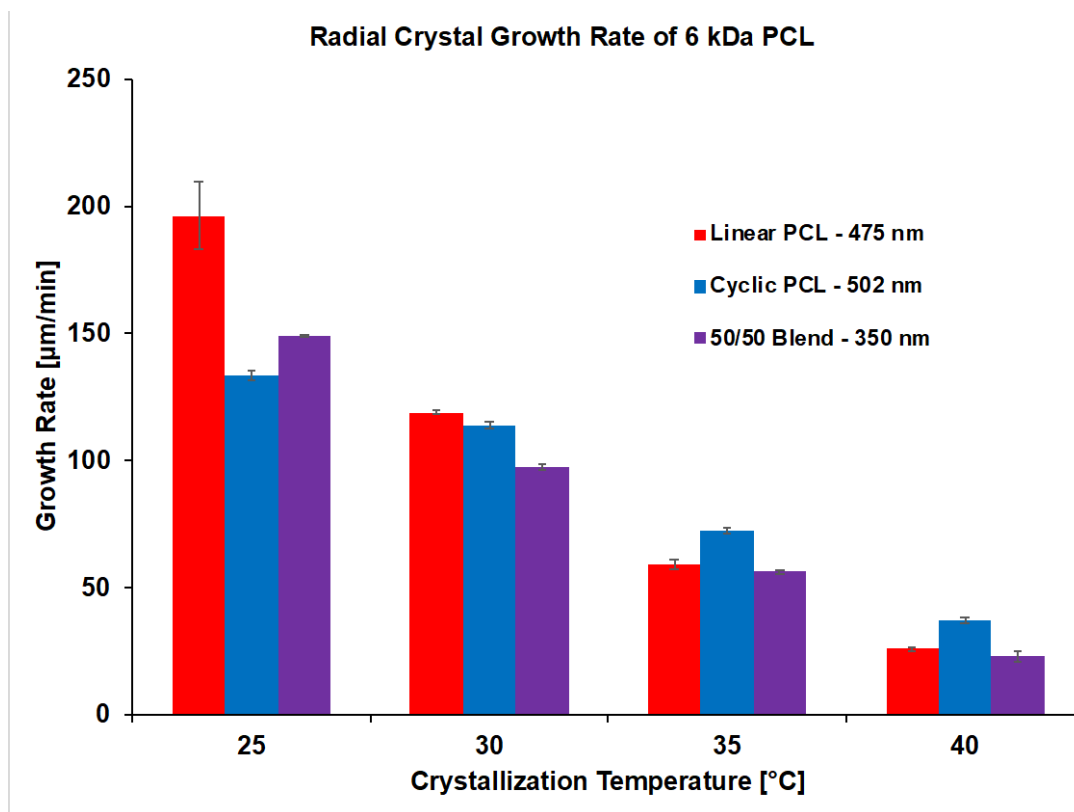


**Figure 6.9.** Radial growth rate at multiple isothermal recrystallization temperatures for 475 nm linear PCL; 502 nm cyclic PCL; and 350 nm 50-50 blend of linear and cyclic PCL.

As reported previously in the bulk, cyclic PCL shows a higher radial growth rate than its exact linear analogues at temperatures of approximately 35  $^{\circ}\text{C}$  and higher<sup>7</sup>. This has been explained by the lower viscosities exhibited by cyclic polymers, as well as the hypothesis that cyclic PCL has a higher equilibrium melting temperature, and therefore at equivalent temperatures the cyclic is at a higher degree of supercooling.

Interestingly, at lower temperatures, (25 $^{\circ}\text{C}$  to 30 $^{\circ}\text{C}$ ), we observe a reversal of the crystallization speeds. At these temperatures, the linear PCL grows more rapidly than the cyclic. Considering the aforementioned studies, this is an intriguing result. To study this

further, we conducted temperature controlled GIWAXS studies at Argonne National Laboratory to study the change in the degree of crystallinity as a function of time. Because this method probes the molecular-level structure of the film, it is a different measure of the crystallization kinetics as compared to studying growth rates optically, as GIWAXS combines nucleation and growth into a single degree of crystallinity value. As shown in Figure 6.10, the growth rate of cyclic PCL when studied via GIWAXS is faster than the linear:

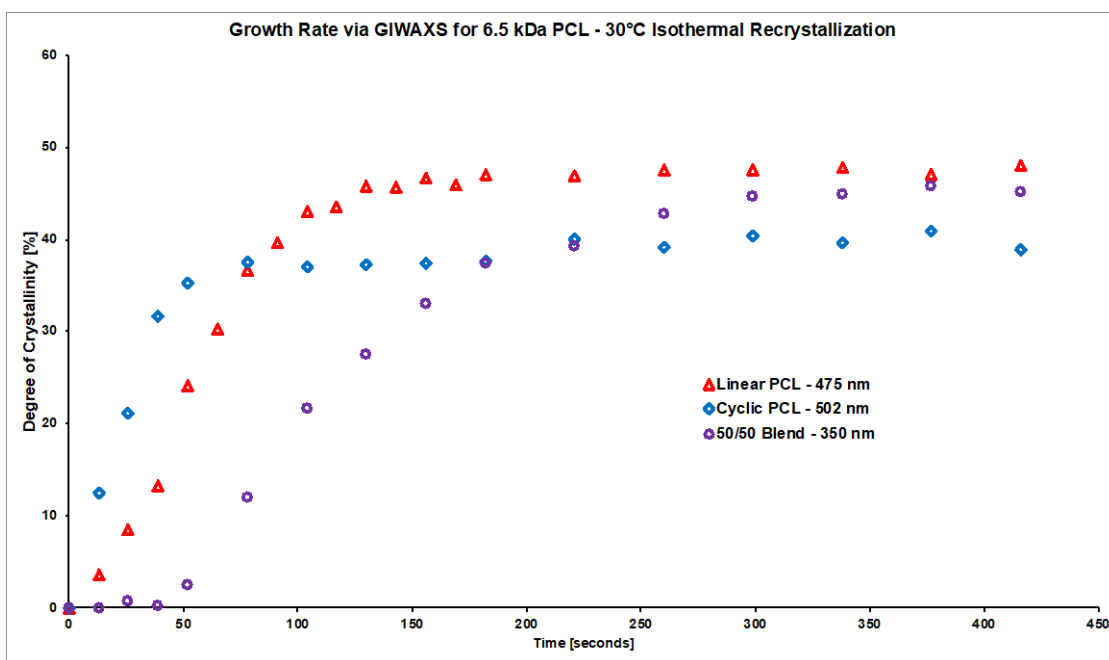


**Figure 6.10.** Increase in degree of crystallinity as a function of time during isothermal recrystallization as studied via GIWAXS for 475 nm linear PCL (red open triangles), 502 nm cyclic PCL (blue open diamonds), and a 350 nm 50-50 linear-cyclic PCL blend film (purple open circles). Degree of crystallinity calculations are discussed more thoroughly in Chapter 4 and Appendix D.

These results show that cyclic PCL does in fact crystallize quicker at 30°C than the linear PCL, reaching nearly constant final crystallinity after approximately 60 seconds, while the linear takes 140 seconds. The blend takes the longest to reach final crystallinity, at approximately 300 seconds. It also takes longer for the blend film to show any signs of nucleation/crystallization (approximately 40 seconds). The blend result is in line with our initial growth rate result (see Figure 6.9) and this effect, where blends of linear cyclic lead to slower overall crystallization than the two individual parts has been seen by Lopez et al. and is explained as being due to the linear “threading” the cyclic chains and slowing the entire system down<sup>229</sup>. Interestingly, we found that the final crystallinity in the cyclic sample is lower than that of the pure linear and blend sample, corresponding to other studies finding that cyclic PCL exhibits higher crystallinity<sup>17</sup>. However, as discussed in Chapter 2, it is important to note that GIWAXS is unable to quantitatively describe crystallinity, and because orientation differences can affect the crystallinity measurement, we cannot say for sure whether the significantly lower crystallinity in the cyclic thin films is a true result.

Since GIWAXS experiments combine nucleation and growth into a single quantity (the degree of crystallinity) whereas nucleation and growth are independent in crystal growth rate studies, it is obvious that the crystal nucleation is behind the disconnect between these two studies. This can be better understood by looking at the crystal morphology of the films crystallized at 30 °C via optical microscopy as shown in figure 6.11:

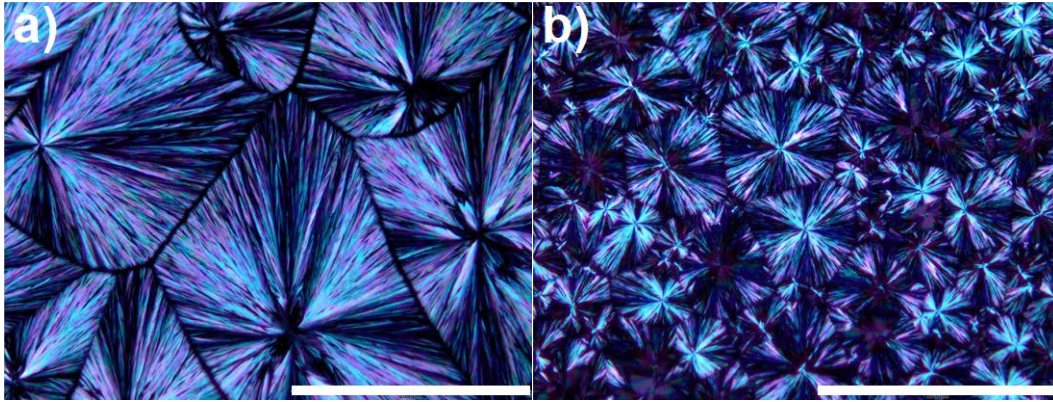


**Figure 6.11.** Polarized optical microscopy images of a) 475 nm 6 kDa linear PCL isothermally crystallized at 30°C; and b) 502 nm 6 kDa cyclic PCL isothermally crystallized at 30 °C. Scale bar corresponds to 200  $\mu\text{m}$ .

Clearly shown by these results is the significant difference in crystal size between linear and cyclic PCL, even when isothermally crystallized at the same temperature and within the same film thickness regime. This, in turn, is related to the nucleation density. As can be seen in these two images, the nucleation density in cyclic PCL is many times higher than that of linear. Thus, the linear PCL having a faster radial growth rate still causes it to crystallize more slowly, since it will take longer for all of the crystals to impinge upon each other as compared to the cyclic film.

Still, the fact that the cyclic crystals grow significantly more slowly at these temperatures is a conflicting result in the grand scheme of linear and cyclic crystallization kinetics data that have been reported in the literature. Why is it that the cyclic growth rate is faster at higher temperatures but significantly slower at lower temperatures? Unfortunately, all of the studies done so far on linear versus cyclic crystal growth rate have studied temperatures at approximately 35°C and above<sup>7,29</sup>. At this range, it is obvious that

the cyclic grows more quickly than the linear, and our results verify the results observed previously. However, to the best of our knowledge, we are the first group to study growth rates at these lower temperatures. The only work done previously in this area was by Wang et al<sup>231</sup>. who studied bulk crystallization kinetics using fast-scan chip calorimetry in 2 kDa linear and cyclic PCL. While they were able to verify previous results showing faster cyclic crystallization rates at low degrees of supercooling, they found that below 20 °C, the difference in growth rate between the linear and the cyclic is “insignificant”. We would not classify the difference we observe as insignificant. Furthermore, since their 2 kDa system is below the reported entanglement molecular weight, it very well might be a more pronounced effect in an entangled PCL (as it would be in the case of our 6 kDa system). While we are fairly certain that the results at higher temperatures are valid, the major unknown is the trend of growth rate with temperature at lower temperatures. Based on the theory of spherulitic growth, there is a maximum growth rate at approximately halfway between the melting temperature ( $T_m$ ) and the glass transition temperature ( $T_g$ ), usually termed “ $G_{max}$ ”<sup>193</sup>. This point is the crossover between the nucleation-limited growth and diffusion-limited growth regimes. Below this point, crystal growth slows down due to an increase in the melt viscosity limiting diffusion of amorphous polymer chains to the growth surface. This has been studied and reported in a variety of semi-crystalline polymer systems<sup>193</sup>. An example of this phenomena reported previously can be seen in Figure 6.12:

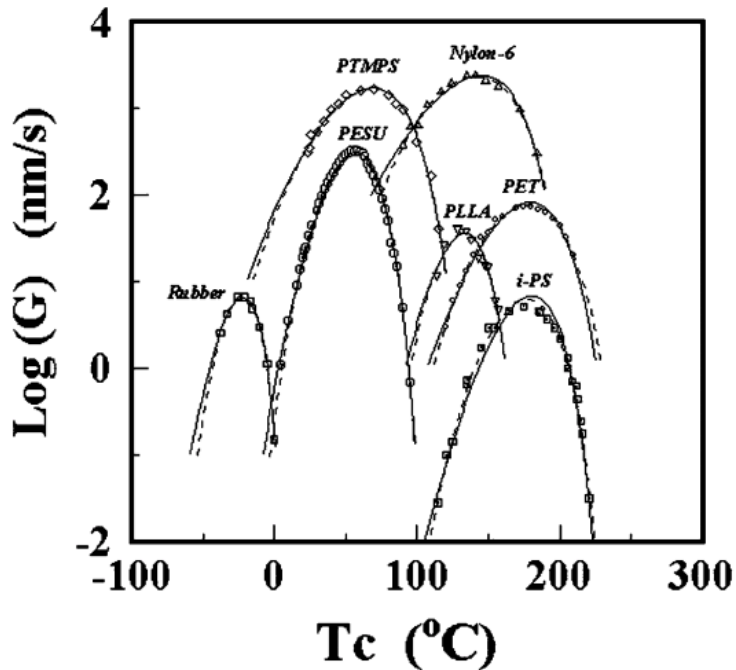


**Figure 6.12.** Temperature dependence of crystal growth rate from the melt for a variety of polymers; rubber, Nylon6, PTMPS, PET, i-PS, PLLA, PESU. Solid and broken lines are best fitting by Arrhenius and WLF expressions, respectively. Reproduced with permission from Umemoto, Susumu, and Norimasa Okui. "Master curve of crystal growth rate and its corresponding state in polymeric materials." *Polymer* 43.4 (2002): 1423-1427<sup>193</sup>.

Because we are at the forefront of studying crystallization in cyclic semi-crystalline polymer thin films, many questions pertaining to the kinetics remain unanswered. In the case of this bizarre crossover in growth rates, a great deal of work needs to be done to better understand  $G_{\max}$ , especially the differences in  $G_{\max}$  exhibited by different architectures. The biggest contribution to this  $G_{\max}$  might be the difference in viscosity between linear

and cyclic polymers, and very well might lead to a flatter growth curve and lower  $G_{\max}$  for the cyclic species.

#### 6.4 Conclusions

The most common goals in the study of semi-crystalline polymers, especially when confined in thin films, is to better understand the thin film morphology, crystal orientations, and crystallization kinetics, especially in terms of how they are affected by the substrate. In this Chapter, we have described some of the work that has been done to study these factors in linear and cyclic poly(caprolactone). They are especially important given our initial finding, described in Chapter 5, of the enhanced stability exhibited by the cyclic species. We have found that beyond having a unique thin film morphology as evidenced by microscopy techniques, cyclic PCL also exhibits unique and different orientations when studied via GIWAXS, both as cast from solution and once the thermal history has been erased by melting and recrystallizing. More work needs to be done on the topic of crystal morphology, especially in thin and ultrathin films. This will allow us to better understand crystal growth at a molecular level. However, this study has as yet been delayed due to the instability of low molecular weight linear PCL. As synthetic methods improve, and higher molecular weights are more easily synthesized, we will be able to understand better the equilibrium morphologies of semi-crystalline linear and cyclic polymers in thin and ultrathin films.

Furthermore, while much work has been done to try and better understand the crystallization kinetics of linear and cyclic polymers in the bulk, to the best of our knowledge, we are the first group to begin to study these kinetics in thin films. While we

have observed that the crystallization kinetics match that of the previously reported bulk phenomena, we find that the cyclic species grows more slowly at higher degrees of supercooling, which is a conflicting, albeit very intriguing result.

To better study these observations, the main next steps in this project are twofold: First, multiple molecular weights should be studied to better understand whether this effect is isolated to a certain molecular weight. Assuming this crossover is seen in multiple systems, the next step is to extend the isothermal recrystallization studies in the low temperature regimes below 25 °C. This is a non-trivial endeavor, however, as crystallization at even 30 °C occurs very rapidly. Moving to lower and lower isothermal recrystallization temperatures very well might require higher magnifications, or fast-scanning capabilities in AFM study.

## Chapter 7

### CONCLUSIONS AND FUTURE WORK

The previous four chapters have described several endeavors to better understand polymer crystallization in thin films. Specifically, we have used polycaprolactone, a biocompatible and biodegradable polyester as the model polymer system. This is because of the various advantageous characteristics of PCL that make studying polymer crystallization simpler, such as low melting and crystallization temperatures and slower crystal growth. These studies have primarily focused on some of the unique characteristic that PCL exhibits. They have included the ways that blending with a second, non-crystalline component can affect the direction of crystallization and morphology, new ways to detect and quantify thermal transitions due to thin film confinement, and the unique characteristics exhibited by cyclic PCL. While the data and interpretation of the data generated by these studies is insightful in and of itself, it is vital to consider both the short and long-term outlook in the study of polymer crystallization in thin films, and how our findings can be used in various applications using PCL as well as other semi-crystalline and non-crystalline polymers. To keep a level of continuity, the conclusions and next steps have been broken up into four sections, mirroring the four individual studies contained herein.

## 7.1 Polymer Crystallization in Thin and Ultrathin Film Blends

The nano-rose work, above all else, showed that the direction of crystal growth at the nanoscale can be affected by blending with the “right” component. Previously, non-linear crystal growth that led to lamellar twisting and banded spherulites was believed to be due to the characteristics of the pure polymer component, or in some cases, the crystallization conditions<sup>52-53, 130-132</sup>. Here, we found that the right characteristics in the non-crystalline component, such as a difference in surface energy and mechanical properties, can cause bizarre, non-conventional crystal growth. At a high level, this signifies that we have some level of control on the direction and overall morphology of crystal growth. This is powerful, because crystal morphology had typically been based on either the kinetics of crystal growth (temperature, degrees of supercooling, etc.), outside mechanical treatment (such as drawing or shear), or, in two-component systems, Flory-Huggins dependent phase separation. There are a few next steps that would further elucidate our understanding of the phenomena that lead to the nano-rose and other non-linear crystal growth morphologies, as well as our ability to control it.

There was something obviously advantageous about the styrene-isoprene block copolymer that was characteristic to the block copolymer architecture itself, since the nano-rose morphology was not observed with PCL blended with styrene or isoprene homopolymers. Was it the mechanical properties of styrene-isoprene-styrene, a glassy-rubbery-glassy block copolymer? Could it be a function of the volume fraction of the components? This factor would affect the nano-structured phase separated block copolymer morphology itself, however we did not find evidence of phase separation via

GISAXS. Is it the chemistry of the styrene-isoprene block copolymer? These are all important follow-up questions worth asking and attempting to answer.

The easiest way to approach this problem is to use synthetic techniques already in progress in our lab to synthesize a new, modular block copolymer system that can test some of these questions. Based on previous work done in our lab, the ideal candidates for these studies are styrene-vinylmethylsiloxane and methyl methacrylate-vinylmethylsiloxane block copolymers. These two block copolymer systems will shed light on the above-mentioned questions. First, thin film studies of PCL with PS-PVMS block copolymers can show whether the styrene-isoprene chemistry leads to the nano-rose morphology. Furthermore, the ability to synthesize PS-PVMS-PS vs PVMS-PS-PVMS block copolymers and study their blend morphology in thin films with PCL can show whether it is the mechanical properties of the block copolymer that leads to the nano-rose morphology. Obviously, a logical step would also be to study how altering volume fractions of the individual blocks affects blend morphology.

Of course, there are also questions regarding the semi-crystalline component in the nano-rose blends. Our initial study focused solely on blends using PCL. We did, however, study the molecular weight dependence of nano-rose formation and observed the nano-rose morphology using a wide range of PCL molecular weights (10 kDa to 80 kDa). A more important factor might be the chemistry of the semi-crystalline component. To this end, it would be worth studying similar blends containing styrene-isoprene block copolymers and other semi-crystalline polymers such as poly(lactide) or poly(ethylene). The challenge in conducting studies with the latter component is the low solubility in common casting solvents such as toluene at ambient conditions.

## 7.2 Spectral Reflectance to Examine Thermal Behavior of Semi-Crystalline Polymers

In our initial study on the use of spectral reflectance to detect the thermal transitions of semi-crystalline PCL, we found that by studying the expansion phenomena of these films as a function of temperature, we were able to easily pinpoint the melting and crystallization temperatures that we could then correlate via methods such as DSC, AFM, and GIWAXS. We then carried this one step further and did various isothermal crystallization studies where we correlated the film thickness observed via spectral reflectance with the degree of crystallinity measured via GIWAXS. Of course, this means that spectral reflectance is one of a few methods that can detect thermal behavior in semi-crystalline thin films when still confined on solid substrates. Additionally, it is a more accessible method than AFM, X-ray scattering, and calorimetry. There is, however, a trade off when it comes to the information that is possible to gain with calorimetry methods, such as the heats of crystallization, degree of crystallinity, etc. The question then becomes: can we fine-tune the thermal transitions and kinetics studies, including degree of crystallinity over time, to justify spectral reflectance as one of the first choices for thin film crystallization studies?

As discussed in chapter 1, the degree of crystallinity dictates many of the favorable characteristics of semi-crystalline polymers as well as how and why they are used in a variety of applications. Therefore, it would be advantageous to be able to detect and describe the degree of crystallinity as a function of crystallization conditions, polymer, etc. Unfortunately, the typical methods for measuring the degree of crystallinity, such as DSC and WAXS, are only applicable to thick, bulk materials. Nano DSC and other methods where calorimetry is done on small amounts of polymer always require removal of the

polymer from any substrate it started on. Thus, the situation is more complicated for thin films confined to solid substrates. Since one of the goals is to comment specifically on the effect of the substrate, the ability to measure the film on the substrate is vital.

As discussed in Chapter 4, despite the conflicting results when trying to calculate the degree of crystallinity using spectral reflectance, it is remarkable that we can use a relatively simple and accessible method that provides us so much insight into the crystallization in these thin and ultrathin films. Through our comparisons so far between spectral reflectance and either DSC or GIWAXS, we feel as though we have validated the technique in the general sense of being able to qualitatively observe the crystallization process. The ultimate goal, and one which would be hugely impactful, is being able to more precisely measure crystallization and the degree of crystallinity using the spectral reflectance technique. Doing so will allow researchers to definitively correlate degree of crystallinity values with various characteristics exhibited by semi-crystalline polymers in thin films and due to the thin film confinement geometry. Planned additional experiments using nano-DSC techniques and further beamline study will provide further clues into the strengths and weaknesses of our model. Specifically, it would be useful to be able to more accurately measure the crystalline and amorphous densities of PCL.

Put together, fine tuning the physical characteristics that go into our mathematical model while also having more precise techniques to compare our results to will allow us to improve the use of spectral reflectance for both thermal behavior and degree of crystallinity. Because the pace of study into semi-crystalline polymers in thin films is increasing, a new technique for monitoring crystallization and crystallinity will have significant impact.

### 7.3 Thin Film Stability of Cyclic Polycaprolactone

Our finding that low molecular weight cyclic polycaprolactone resists dewetting in thin films as compared to exact linear analogs was some of the first commentary on the phenomena exhibited by cyclic polymers in thin films, and certainly one of, if not the first study on thin film cyclic crystallization. Since it was a very preliminary study where we aimed only to study one factor, in our case the chemistry of the end groups, we did find a very unexpected albeit very powerful result in the stability of cyclic PCL. It was especially interesting how drastic the differences were by simple chemical changes to the end group of the linear PCL. More work remains to be done, because although the cyclic architecture was the only common denominator in that study, we still have not answered all the questions regarding why cyclic PCL remains stable.

Most of the prior studies on the dewetting and film stability used amorphous polymers such as polystyrene. When these materials are heated above their glass transition temperature, it was found that systems at low molecular weights, on non-wetting substrates, or at low film thicknesses readily dewet either via the opening of dewetting holes or by complete spinodal dewetting. This was found to be due to the film undergoing a phase transition from glassy to rubbery, and the enhanced motion caused the film to become unstable and rupture. Given the combination of these findings and our findings, it would be worth studying if the stability exhibited by cyclic PCL is inherent to a) PCL itself, or b) semi-crystallinity. There are two worthwhile follow-ups that may shed light on these considerations.

First, a similar study on the stability exhibited by linear and cyclic polystyrene can be conducted. Given the synthetic expertise of our laboratory and our collaborators, the

synthesis should pose little issue. In this study, a comparison between exact linear analogues of linear and cyclic polystyrene will be insightful, because if it similarly shows that the cyclic architecture lends stability to the mobile rubbery state of polystyrene, it will support the idea that the cyclic architecture itself is causing the stability. Furthermore, it will answer the questions of whether the stability is inherent to PCL or semi-crystallinity.

If it is instead found that the cyclic architecture does not offer stability to cyclic polystyrene over the exact linear analog, the situation becomes somewhat more complicated. The question then returns to whether the stability of cyclic PCL is inherent to the semi-crystalline state or the chemistry of PCL. To study these factors, we would instead opt to synthesize and study a different linear and cyclic semi-crystalline polymer. Mueller et al. recently discussed their findings on the kinetics of linear and cyclic poly(lactide)<sup>228</sup>. Therefore, the synthetic methods are established, and poly(lactide) is an excellent semi-crystalline candidate for this purpose.

In the end, we would like to better understand the factors that lead to film stability in cyclic PCL, cyclic semi-crystalline polymers, and cyclic polymers in general. As we gain a better understanding of the factors that lead to film stability in each of these examples, we can then focus our efforts on where this characteristic can be used from an applications standpoint. This is especially important in more hydrophobic or unstable polymer films where film dewetting and other instabilities have become a dead end or road block when it comes to using these materials in applications where they are otherwise significantly advantageous.

#### 7.4 Thin Film Morphology and Kinetics of Cyclic Polycaprolactone

As described in Chapters 5 and 6, we have positioned ourselves on the forefront of studying cyclic polymer crystallization in thin films. Besides the bizarre and intriguing film stability results outlined in Chapter 5, we have taken a deeper look into the morphology and crystal growth of cyclic PCL and how it compares to its exact linear analogue. Primarily, we have concluded that not only is the morphology of cyclic PCL different on a global level, such as its higher nucleation density, significantly smaller crystal size, and rough grain boundaries, but through GIWAXS studies we can confidently state that the cyclic PCL assumes a preferred orientation upon casting that is not appreciably changed when melted and recrystallized. Furthermore, this orientation is unique to cyclic PCL when compared to its exact linear analog. Thus, the crystallization of cyclic PCL in thin films is unique on a molecular, lamellar, and spherulitic scale.

Additionally, through detailed experiments into the crystal growth rate via optical microscopy, we have shown that as reported previously, the crystallization rate of cyclic PCL is faster than that of its linear analog when studied via GIWAXS. However, cyclic PCL shows a crossover in growth rate with linear PCL and is slower than linear PCL when studied via optical microscopy at temperatures of 30 °C and below. Mueller et al. saw a similar effect when studying linear and cyclic PCL crystallization via fast scan chip calorimetry, albeit they commented that the difference between the two was negligible<sup>231</sup>.

Further work must be done in this specific area, looking into the crystallization differences at the entire temperature range. This includes the differences in kinetics at different temperatures, film thicknesses, and in multiple molecular weights. The reason for this is simple: from an applications standpoint, our goal is to show that linear and cyclic

PCL have unique crystallization characteristics, and therefore we can control them by blending them together. By gaining a better understanding of how each of these variables affects the final state of the crystallized system, we can see the true level of control we have over the final “product” so to speak.

From a thin films standpoint, this is important because we would like to have a better understanding about how the substrate affects different architectures. We have already shown the way that the architecture affects film stability, but subtle changes in orientations in thin films very likely lead to significant differences in kinetics, morphology, etc. that will affect if and how these polymers are used for the various applications that utilize thin film semi-crystalline polymers.

All in all, this work is significantly non-trivial, and will take many years. This is because a proper commentary on the differences between linear and cyclic PCL as well as their blend behavior will require experiments that span multiple molecular weights. This means that the project will require significant synthetic optimization, as well as physical characterization into growth rate, orientation via X-ray scattering, thermal behavior via spectral reflectance and calorimetry techniques, and likely some form of neutron scattering to more closely monitor the effects of the linear end groups. However, filling in this gap in knowledge of how linear behaves differently from cyclic is undoubtedly necessary. As stated multiple times, applications using these materials do and will continue to rely on precise control over the many characteristics of semi-crystallinity, which will require precise knowledge on the factors that affect those characteristics.

## **Appendix A**

# **SUPPORTING INFORMATION FOR ULTRATHIN FILM CRYSTALLIZATION OF POLY( $\epsilon$ -CAPROLACTONE) IN BLENDS CONTAINING STYRENE-ISOPRENE BLOCK COPOLYMERS: THE NANO-ROSE MORPHOLOGY**

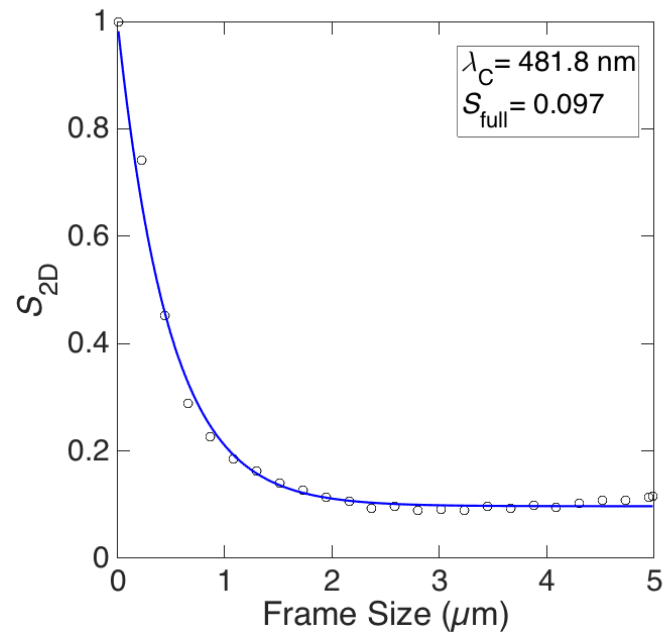
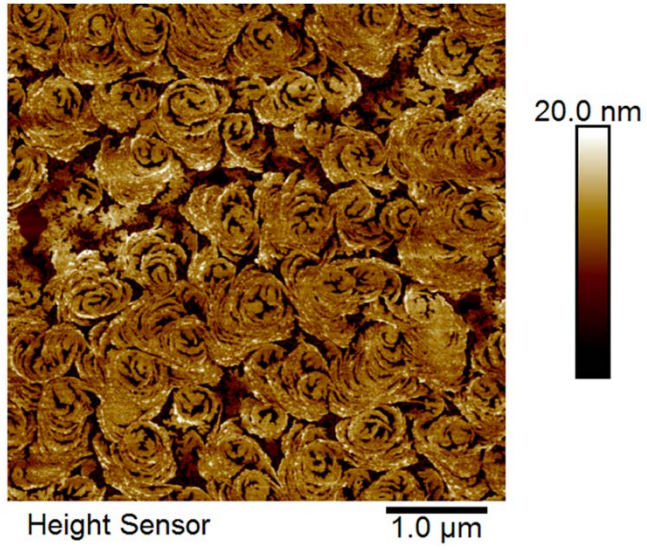


**Figure A1.** Nano-rose size distributions as quantified using the GT Fiber program (N. Perrson et al. Chem. Mater. 2017, 29, 3–14) for 45 kDa PCL/SIS Vector 4293A blend containing 50 wt. % SIS. The following parameters were used in the GT Fiber processing: Gaussian Smoothing 10; Orientation Smoothing 30; Diffusion time 5 s; Top Hat Size 30 nm; Adaptive Threshold Surface; Global Threshold 0.3; Noise Max Area 2500 sq.; Skeletonization Fringe Removal 40 nm; Grid Step 400 nm; Frame Step 200 nm.

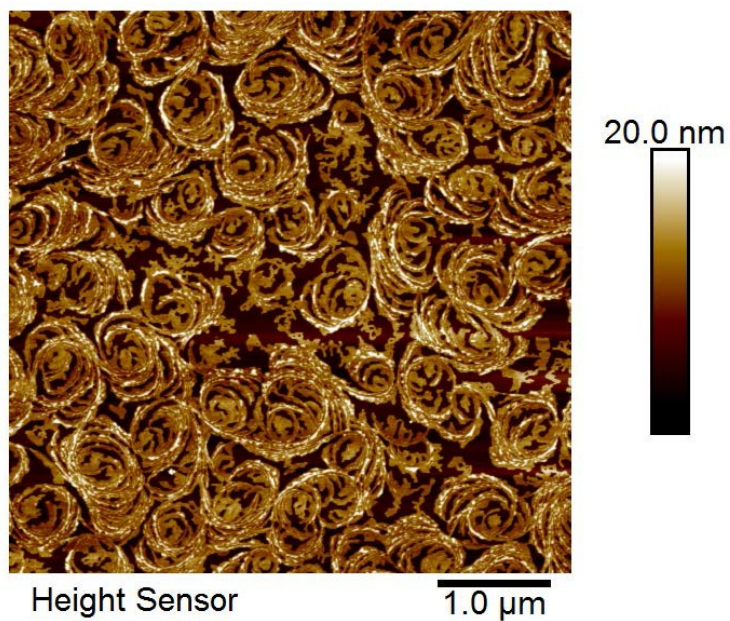
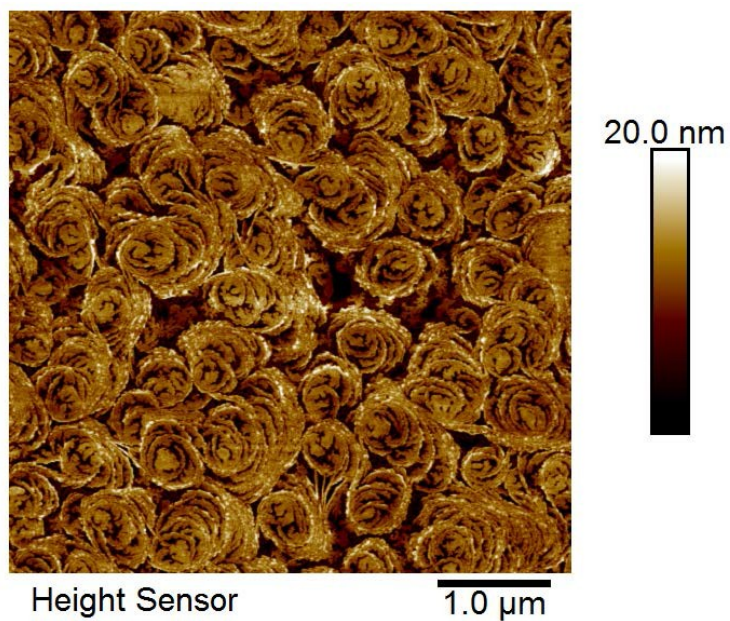


**Figure A2.** AFM height images of 45 KDa PCL/SIS vector 4211A blend containing 50 wt % SIS. This film exhibits the nano-rose morphology: as cast (top) and washed with cyclohexane to remove SIS component (bottom).

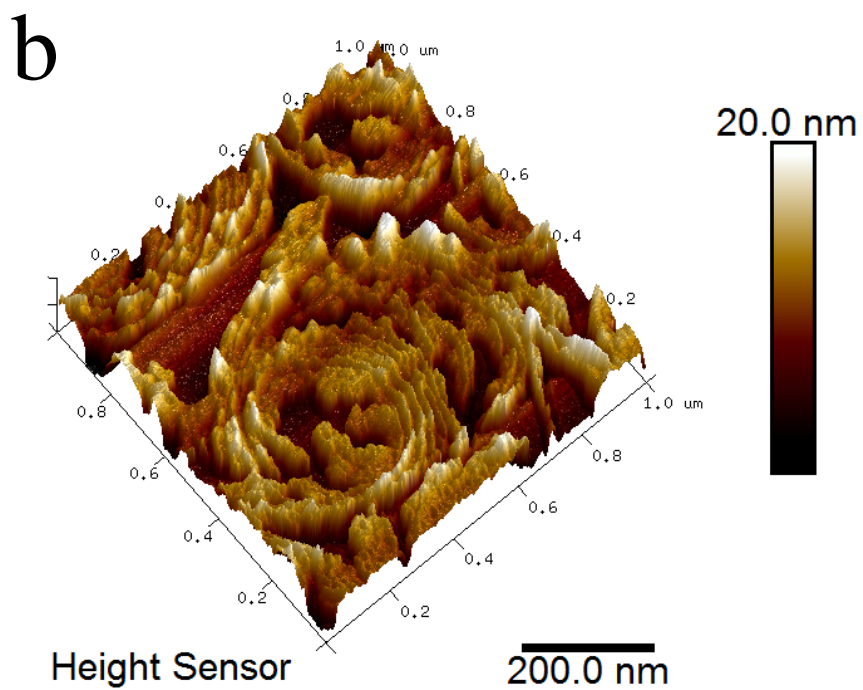
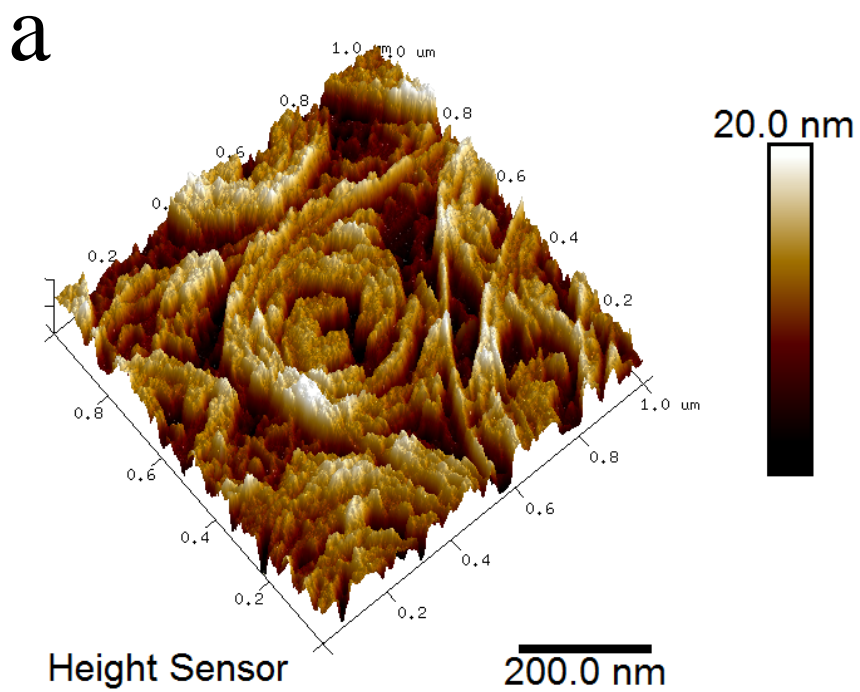


**Figure A3:** 3-dimensional AFM height images of: (a) 45 kDa PCL/SIS Vector 4293A SIS containing 50 wt. % SIS; and (b) 45 kDa PCL/SIS Vector 4293A containing 50 wt. % SIS

washed with cyclohexane to remove SIS. Both films exhibit the nano-rose morphology. These images correspond to the AFM data in Figure A2.

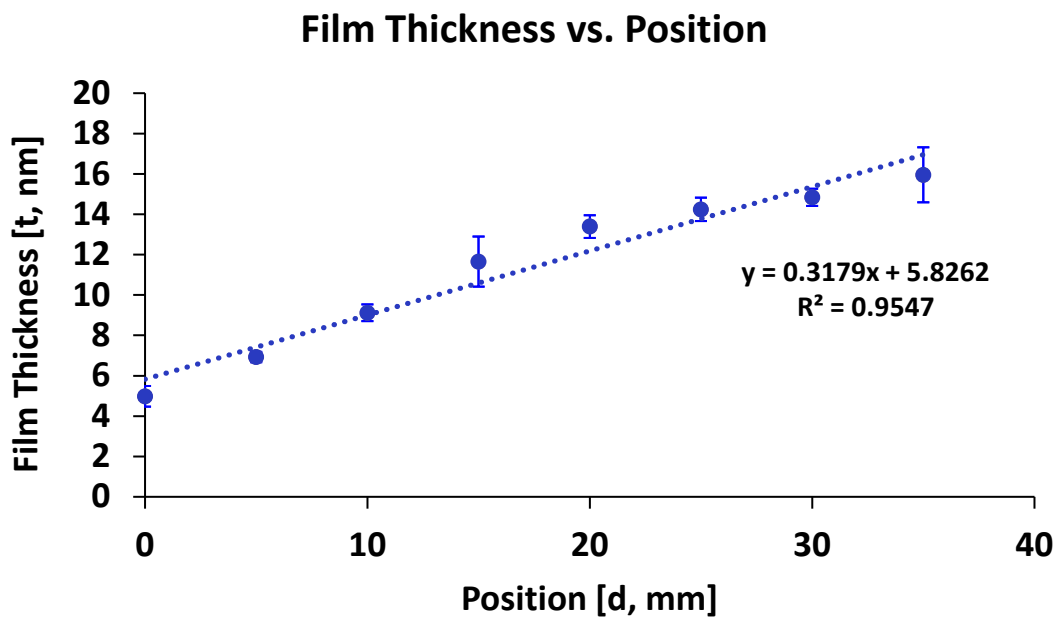


**Figure A4:** Calibration curve for film thickness as a function of position for a representative gradient blend film of 45 kDa PCL/SIS vector 4293A containing 50 wt % SIS. The zero position was defined 1-2 mm from the start of the film so that it was beyond the startup region of flow coated film. From the zero position, 5 mm increments were marked on the film using a scribe. These markings were used to identify position during spectral reflectance measurements to generate the calibration curve. The markings were used again to identify position during AFM measurements so that morphology could be accurately correlated with film thickness through use of the calibration curve.

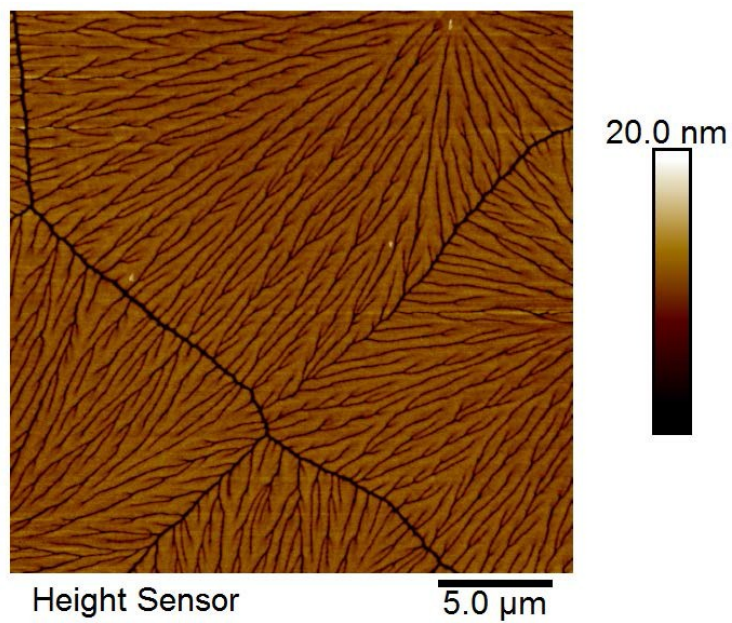


**Figure A5.** AFM height image of 12 nm thick 45 kDa PCL film exhibiting the dense branching morphology.

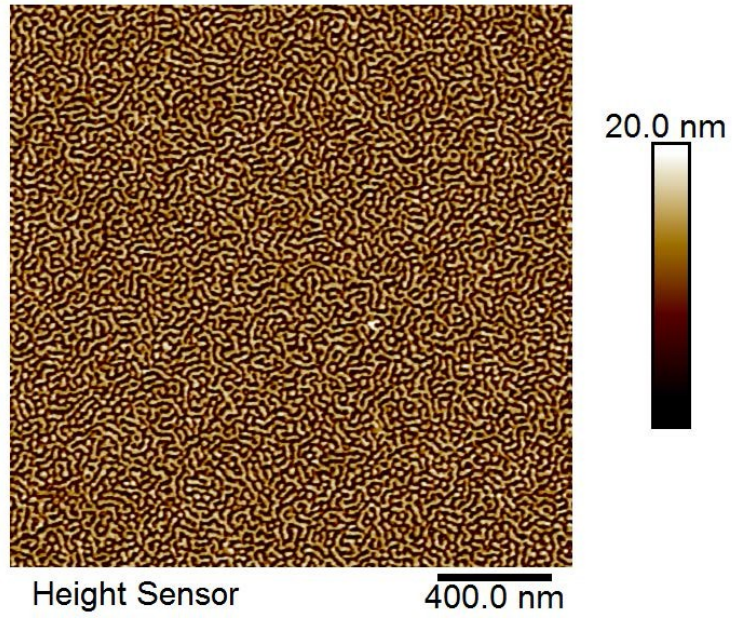


**Figure A6.** AFM height image of 14 nm thick SIS vector 4293A film exhibiting a disordered cylindrical block copolymer nanostructure.

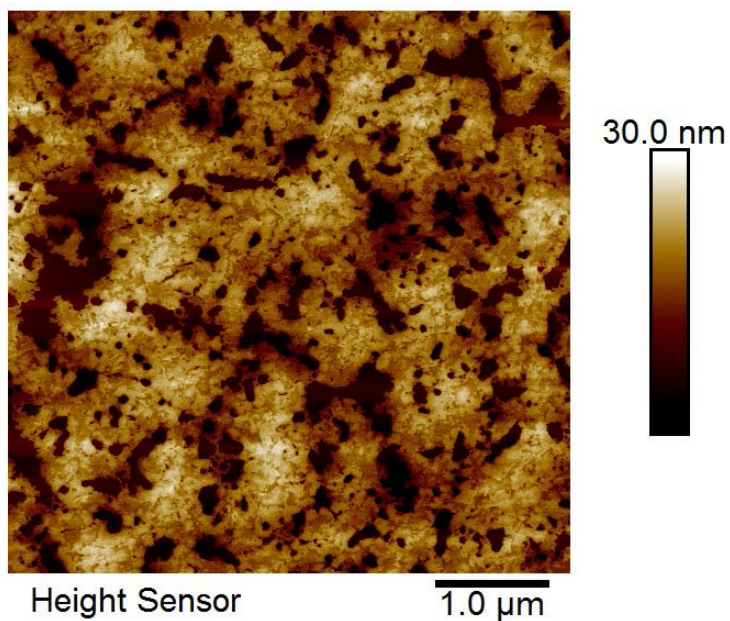


**Figure A7.** AFM height image of 45 kDa PCL/SIS vector 4293A blend containing 50 wt % SIS after melting at 75 °C for 5 minutes and recrystallizing at 25 °C. This film exhibited the nano-rose morphology prior to melting and recrystallization.

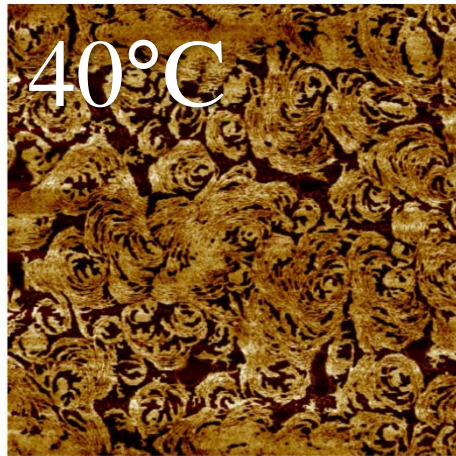


**Figure A8.** Morphology evolution as a function of temperature showing the melting transition starting at 45°C in 45 kDa PCL/SIS vector 4293A blend film exhibiting the nano-rose morphology.

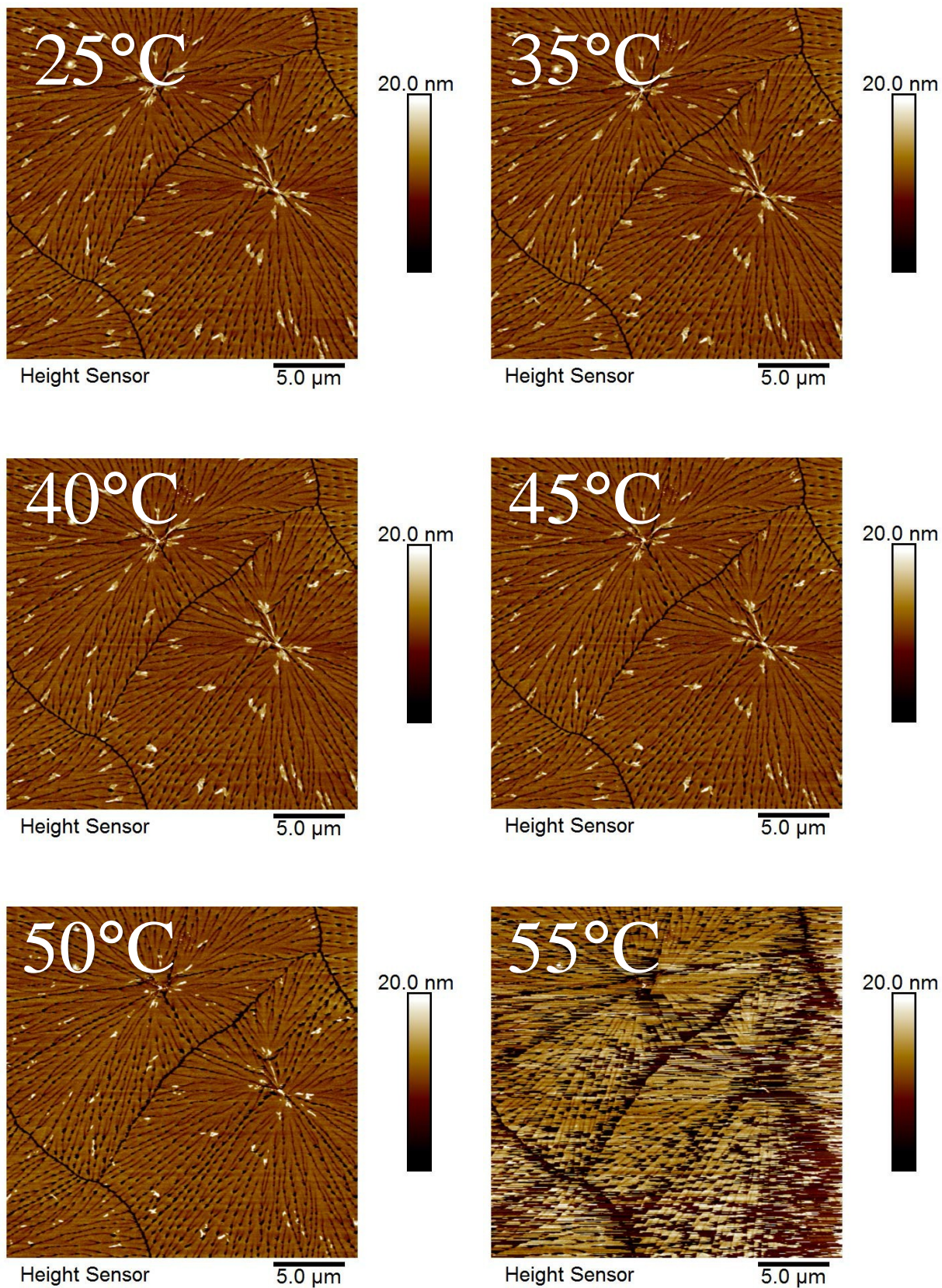


**Figure A9.** Morphology evolution as a function of temperature showing melting transition starting around

55°C in a 13 nm thick film of 45 kDa PCL.

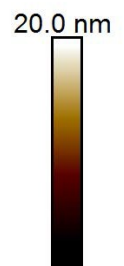
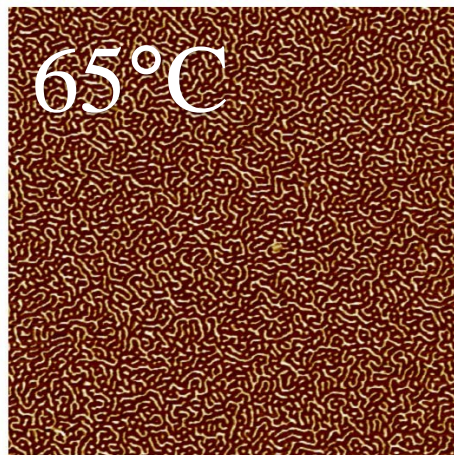
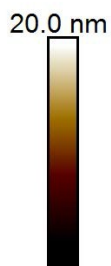
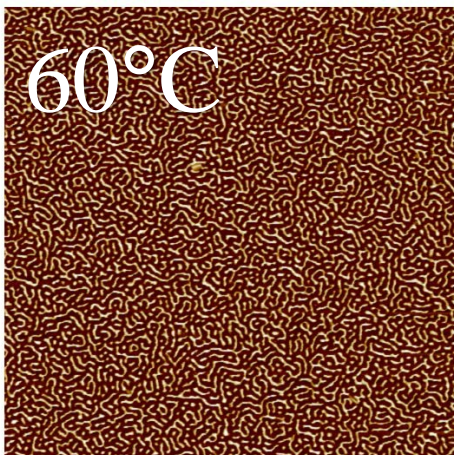
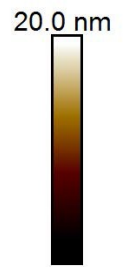
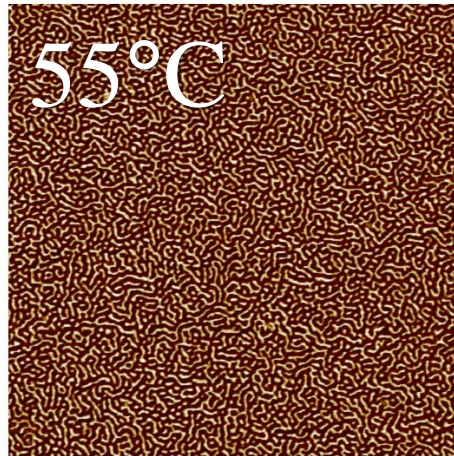
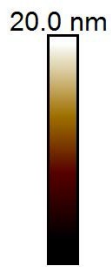
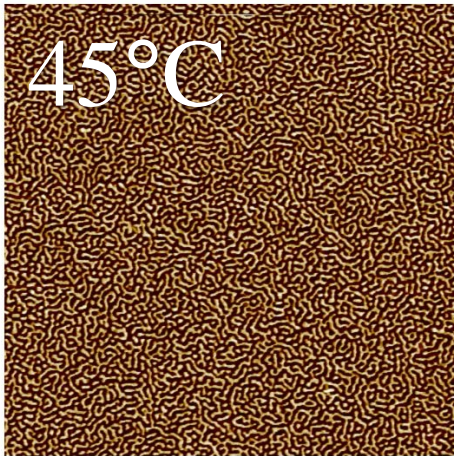
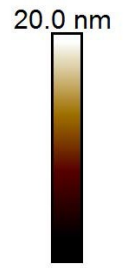
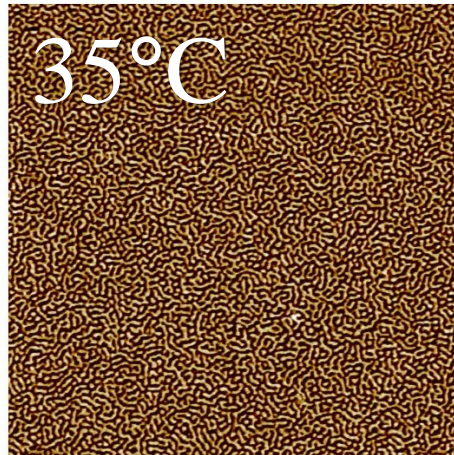
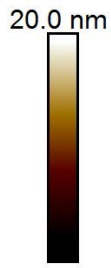
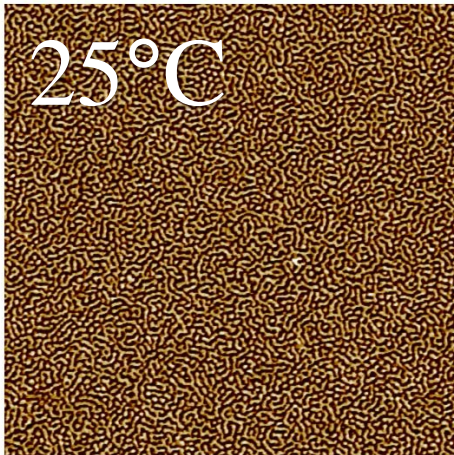


**Figure A10.** Morphology evolution as a function of temperature showing enhanced mobility starting around 55°C in a 14 nm thick film of SIS vector 4293A. Bulk films of SIS have expected mobility around 100°C, close to the glass transition temperature of polystyrene.

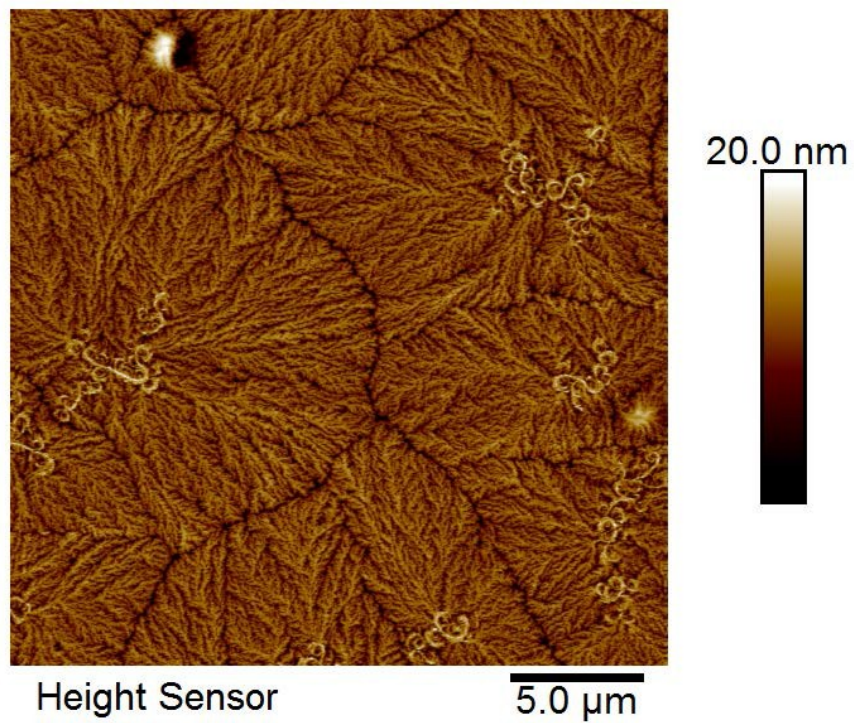


**Figure A11.** AFM height image of 45 KDa PCL/SIS vector 4293A blend containing 50 wt % SIS exhibiting a partial nano-rose morphology at ~7 nm shown here to illustrate nano-roses forming at the nucleation points of crystallization.

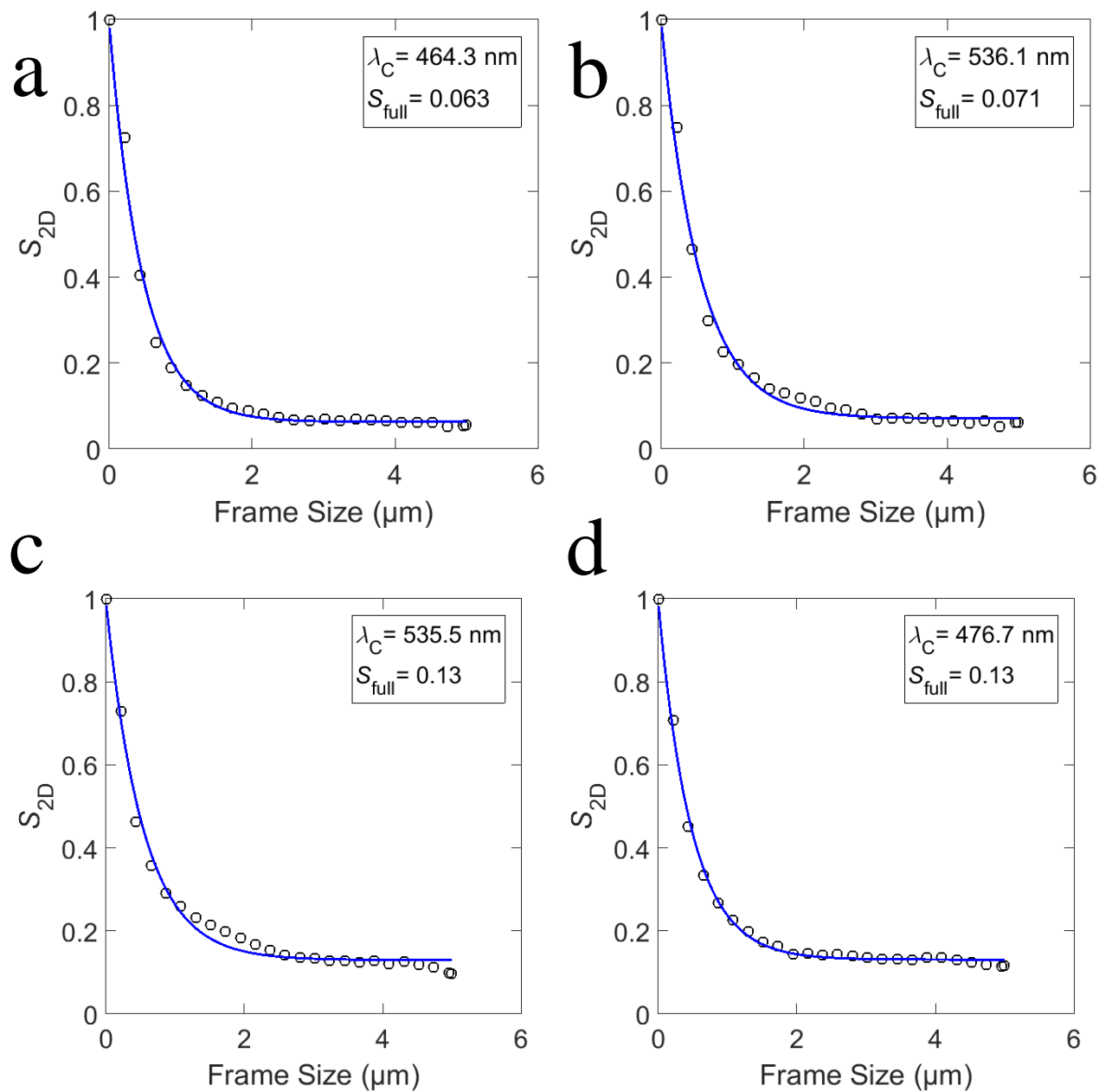


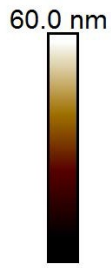
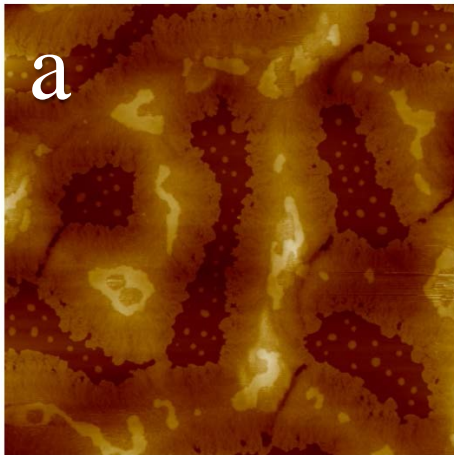
**Figure A12.** Nano-rose size distributions as quantified using the GT Fiber program (N. Perrson et al. Chem. Mater. 2017, 29, 3–14) for: (a) 45 kDa PCL/SIS Vector 4211A blend containing 50 wt. % SIS; (b) 45 kDa PCL/SIS Vector 4215A SIS blend containing 50 wt. % SIS; (c) 45 kDa PCL/P2208 SI blend containing 50 wt. % SI diblock; (d) 45 kDa PCL/P3868 SI diblock blend

containing 50 wt. % SI diblock. The following parameters were used in the GT Fiber processing:

Gaussian Smoothing 10; Orientation Smoothing 30; Diffusion time 5 s; Top Hat Size 30 nm;

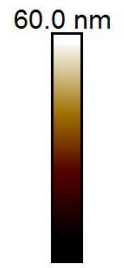
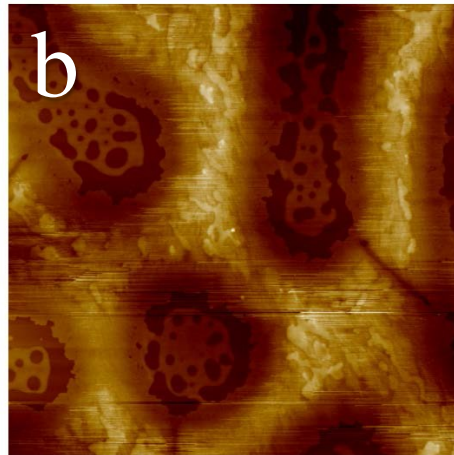
Adaptive Threshold Surface; Global Threshold 0.3; Noise Max Area 2500 sq.; Skeletonization

Fringe Removal 40 nm; Grid Step 400 nm; Frame Step 200 nm.



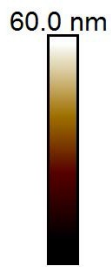
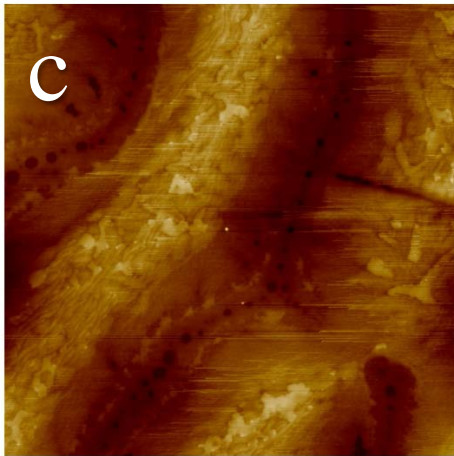
Height Sensor

1.0  $\mu\text{m}$



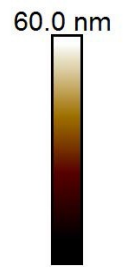
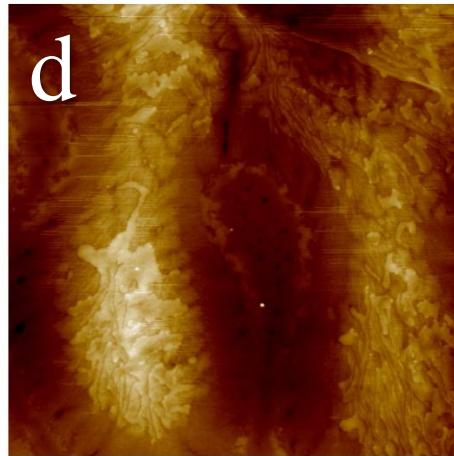
Height Sensor

1.0  $\mu\text{m}$



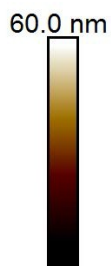
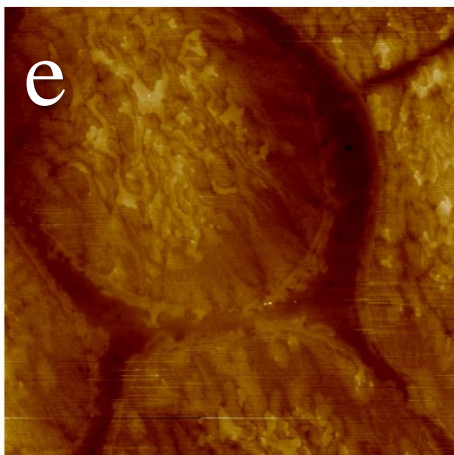
Height Sensor

1.0  $\mu\text{m}$



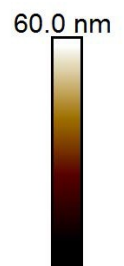
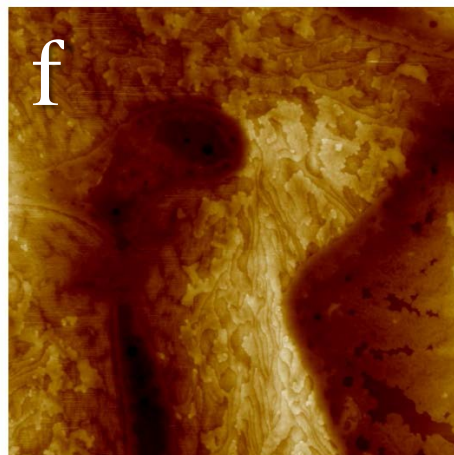
Height Sensor

1.0  $\mu\text{m}$



Height Sensor

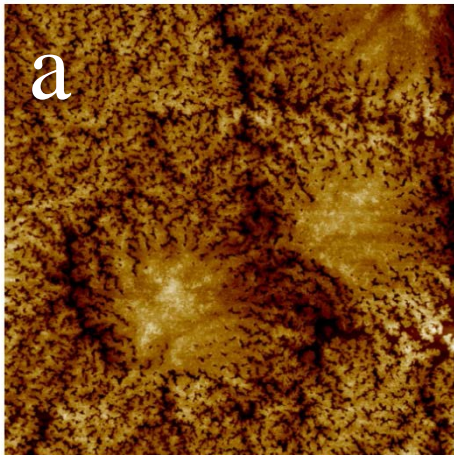
1.0  $\mu\text{m}$



Height Sensor

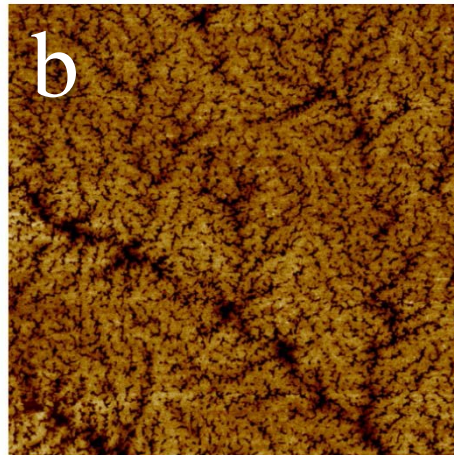
1.0  $\mu\text{m}$

**Figure A13.** Morphology evolution as a function of film thickness for 45 KDa PCL/SIS vector 4293A blend containing 25 wt % SIS at film thicknesses (a) 6 nm, (b) 9 nm, (c) 10 nm, (d) 15 nm, (e) 16 nm, and (f) 17 nm.



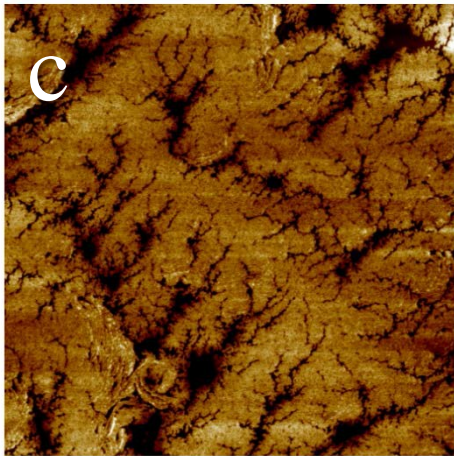
Height Sensor

1.0 μm



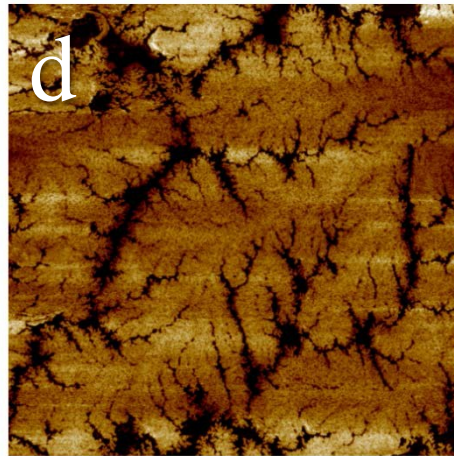
Height Sensor

1.0 μm



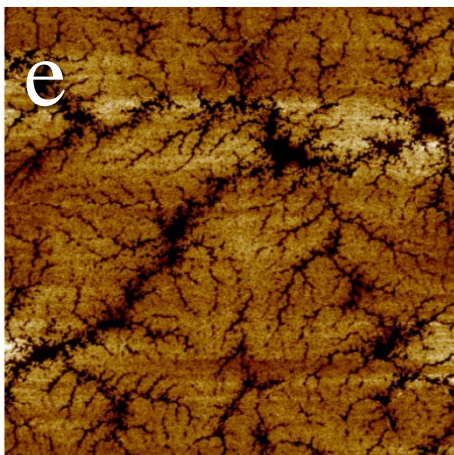
Height Sensor

1.0 μm



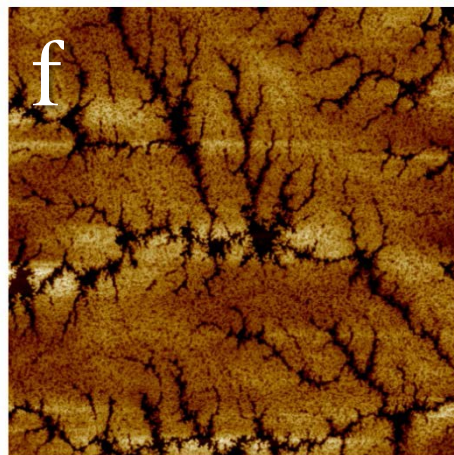
Height Sensor

1.0 μm



Height Sensor

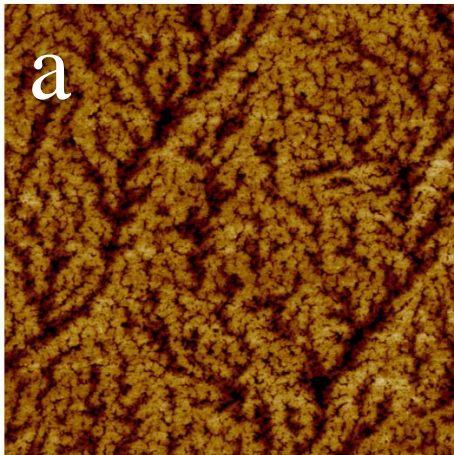
1.0 μm



Height Sensor

1.0 μm

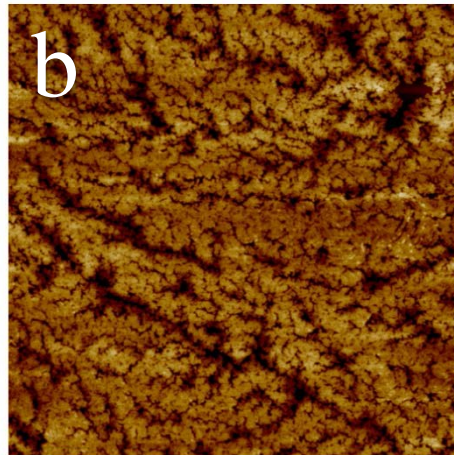
**Figure A14.** Morphology evolution as a function of film thickness for 45 KDa PCL/SIS vector 4293A blend containing 40 wt % SIS at film thicknesses (a) 11 nm, (b) 12 nm, (c) 13 nm, (d) 14 nm, (e) 15 nm, and (f) 16 nm.



Height Sensor

1.0  $\mu\text{m}$

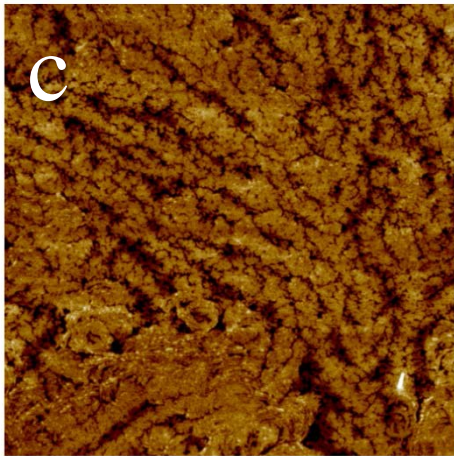
20.0 nm



Height Sensor

1.0  $\mu\text{m}$

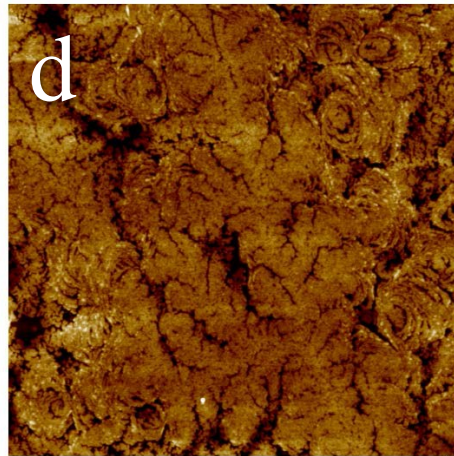
20.0 nm



Height Sensor

1.0  $\mu\text{m}$

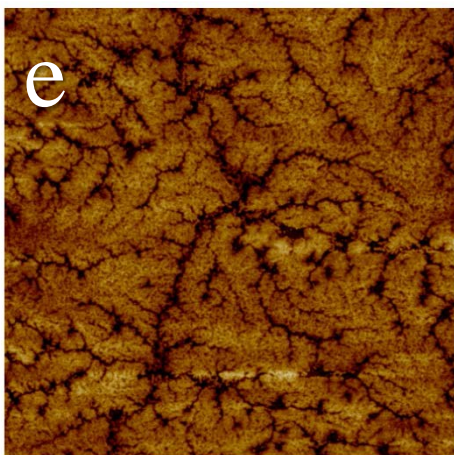
20.0 nm



Height Sensor

1.0  $\mu\text{m}$

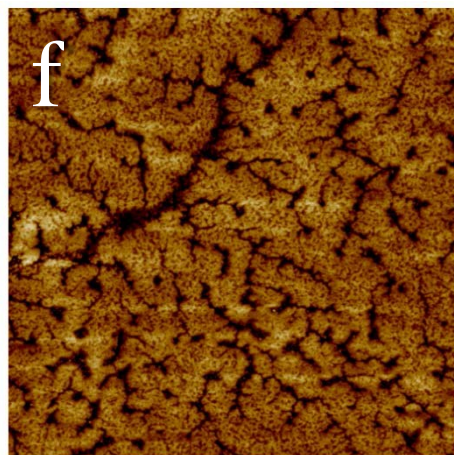
20.0 nm



Height Sensor

1.0  $\mu\text{m}$

20.0 nm



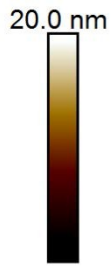
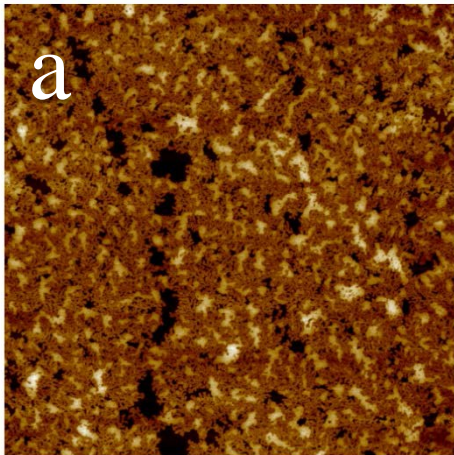
Height Sensor

1.0  $\mu\text{m}$

20.0 nm

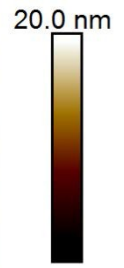
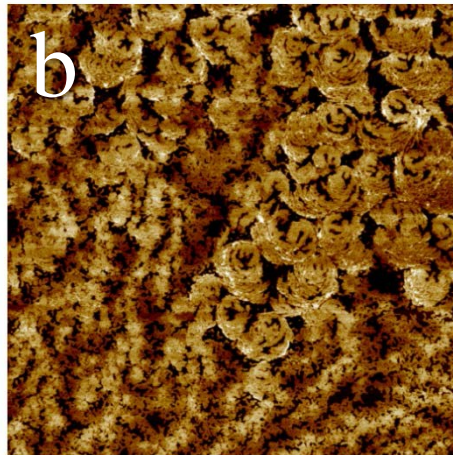


**Figure A15.** Morphology evolution as a function of film thickness for 45 KDa PCL/SIS vector 4293A blend containing 45 wt % SIS at film thicknesses (a) 8 nm, (b) 9 nm, (c) 9 nm, (d) 10 nm, (e) 13 nm, and (f) 15 nm.



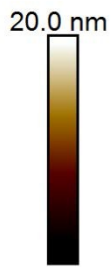
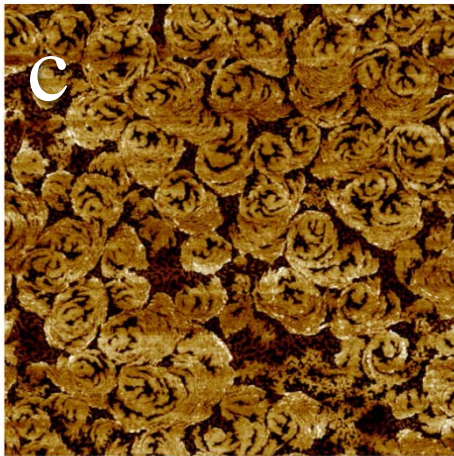
Height Sensor

1.0  $\mu\text{m}$



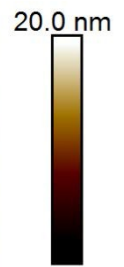
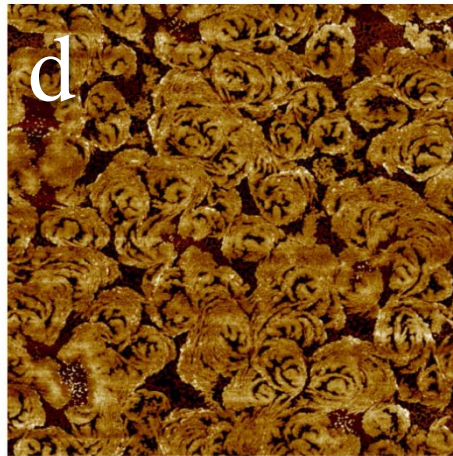
Height Sensor

1.0  $\mu\text{m}$



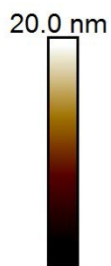
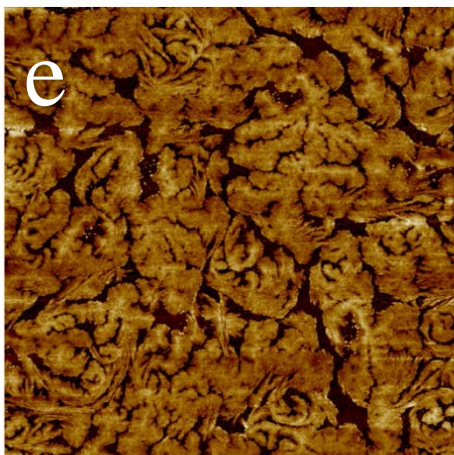
Height Sensor

1.0  $\mu\text{m}$



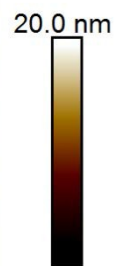
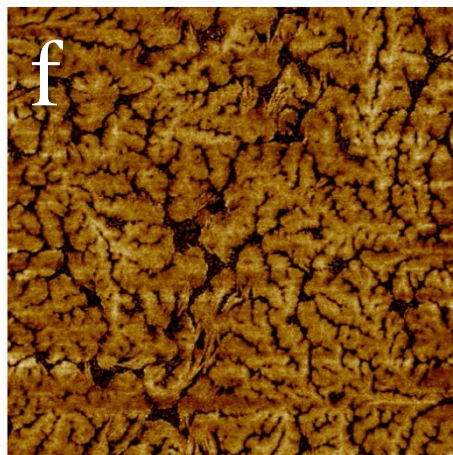
Height Sensor

1.0  $\mu\text{m}$



Height Sensor

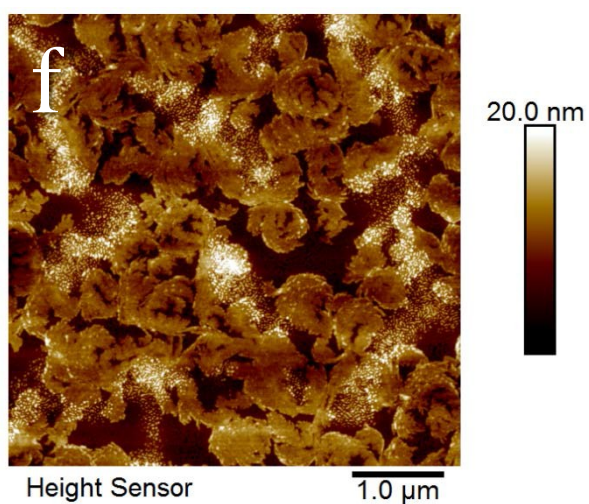
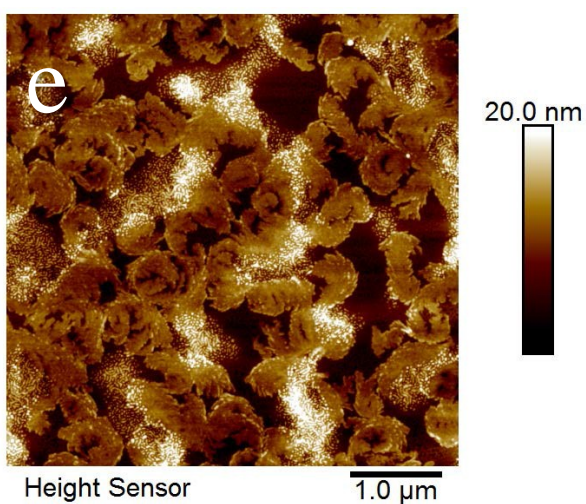
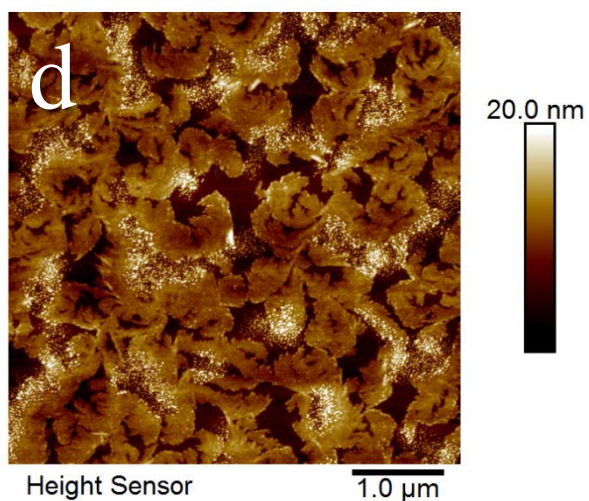
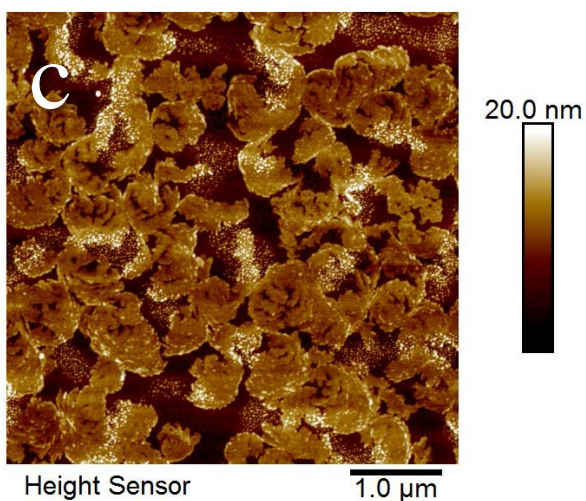
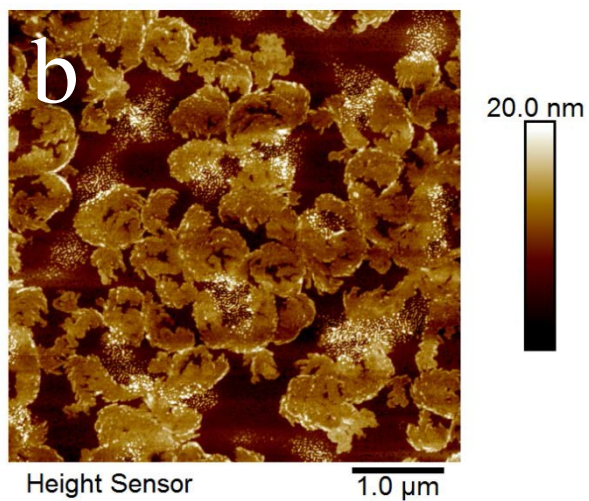
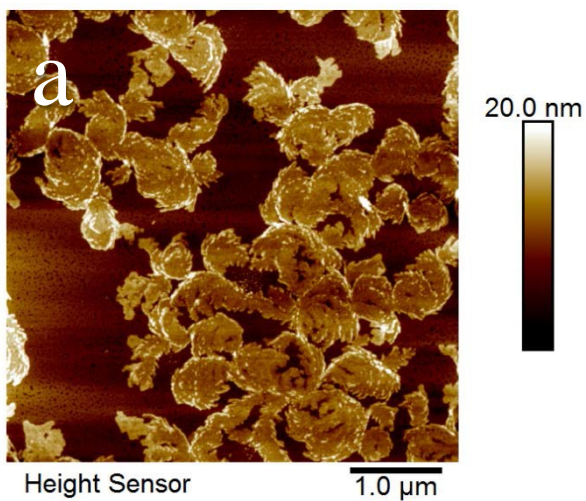
1.0  $\mu\text{m}$



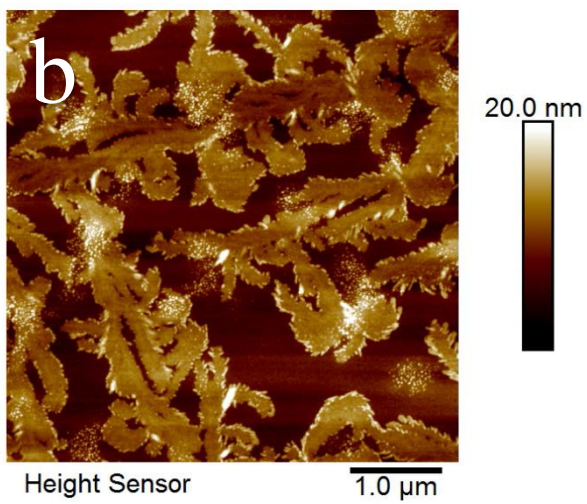
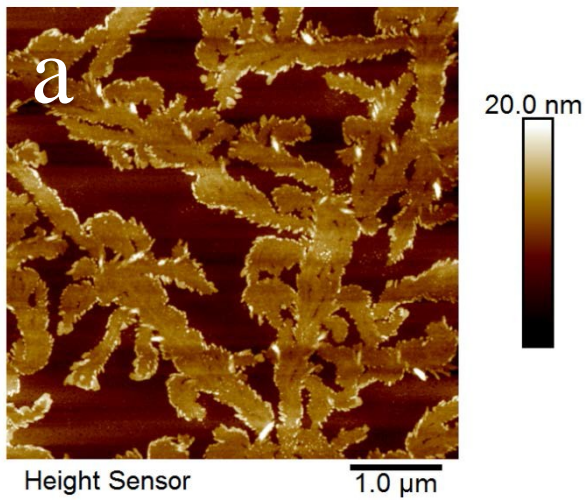
Height Sensor

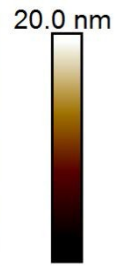
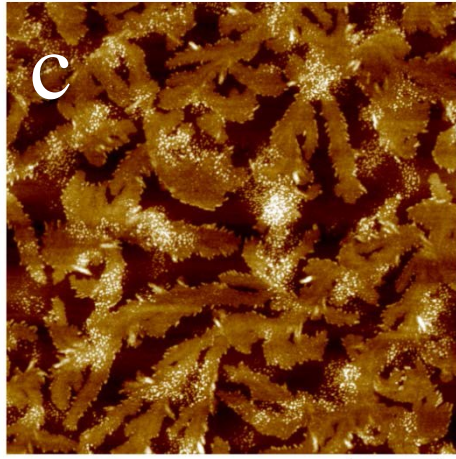
1.0  $\mu\text{m}$

**Figure A16.** Morphology evolution as a function of film thickness for 45 KDa PCL/SIS vector 4293A blend containing 60 wt % SIS at film thicknesses (a) 8 nm, (b) 10 nm, (c) 11 nm, (d) 12 nm, (e) 13 nm, and (f) 15 nm.



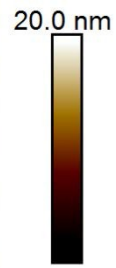
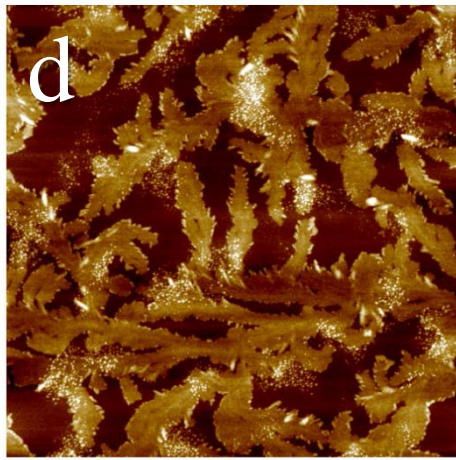
**Figure A17.** Morphology evolution as a function of film thickness for 45 KDa PCL/SIS vector 4293A blend containing 70 wt % SIS at film thicknesses (a) 8 nm, (b) 11 nm, (c) 12 nm, (d) 15 nm, (e) 15 nm, and (f) 14 nm.





Height Sensor

1.0  $\mu\text{m}$



Height Sensor

1.0  $\mu\text{m}$

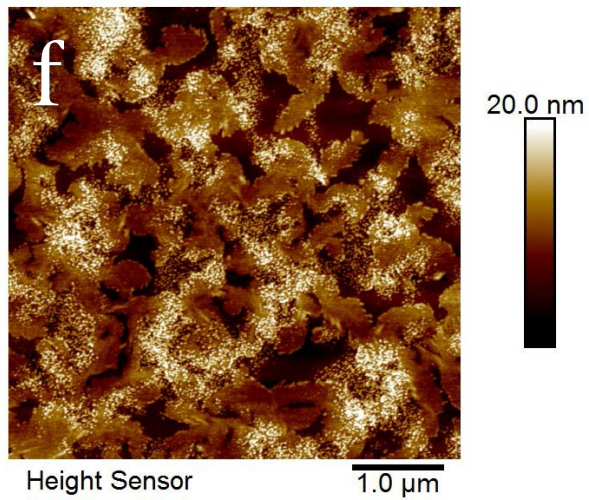
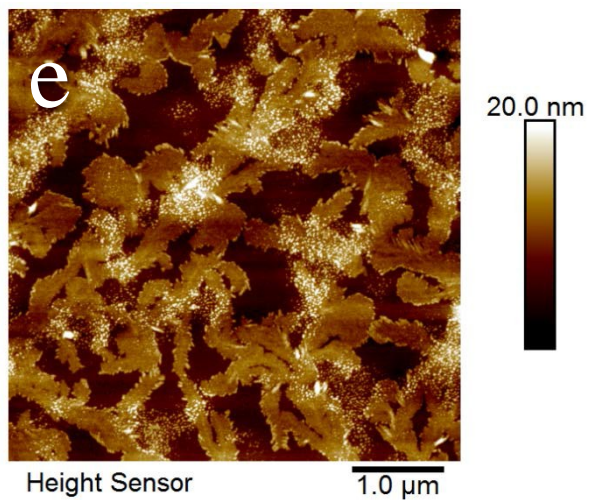


**Figure A18.** Morphology evolution as a function of film thickness for 45 KDa PCL/SIS vector 4293A blend containing 75 wt % at film thicknesses (a) 9 nm, (b) 11 nm, (c) 12 nm, (d) 13 nm, (e) 14 nm, and (f) 15 nm.

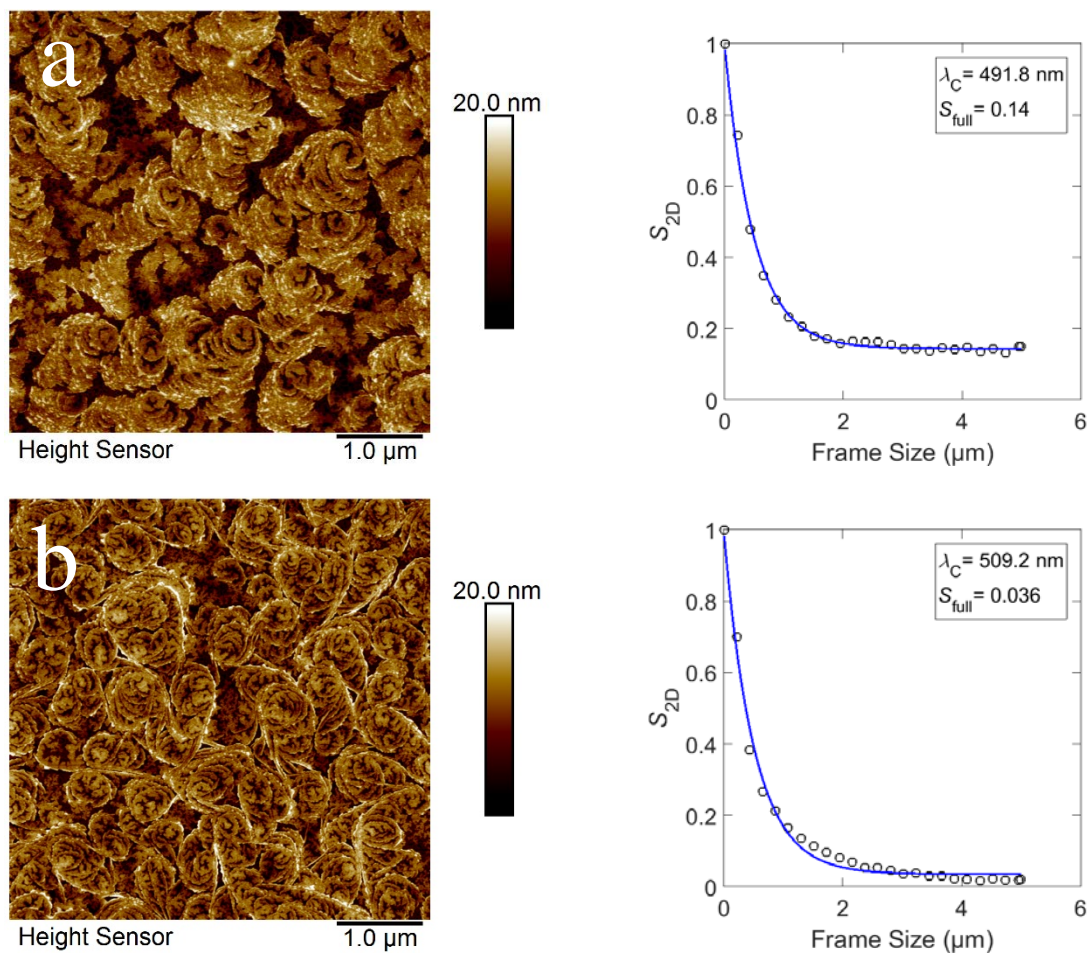
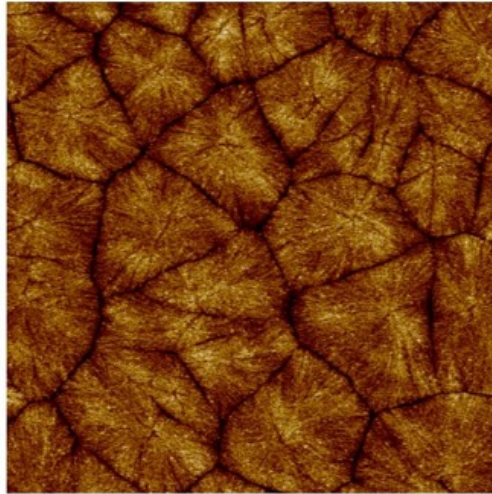


**Figure A19.** Nano-rose size distributions as quantified using the GT Fiber program (N. Perrson et al. Chem. Mater. 2017, 29, 3–14) for: (a) 10 kDa PCL/SIS Vector 4211A blend containing 50 wt. % SIS; (b) 80 kDa PCL/SIS Vector 4293A SIS blend containing 50 wt. % SIS. The following parameters were used in the GT Fiber processing: Gaussian Smoothing 10; Orientation Smoothing 30; Diffusion time 5 s; Top Hat Size 30 nm; Adaptive Threshold Surface; Global Threshold 0.3; Noise Max Area 2500 sq.; Skeletonization Fringe Removal 40 nm; Grid Step 400 nm; Frame Step 200 nm.

a



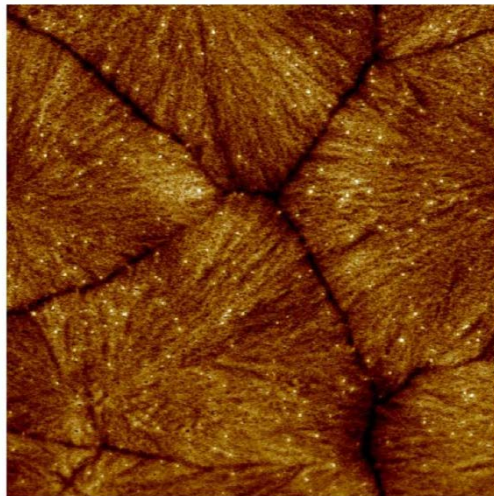
40.0 nm



Height Sensor

20.0  $\mu\text{m}$

b



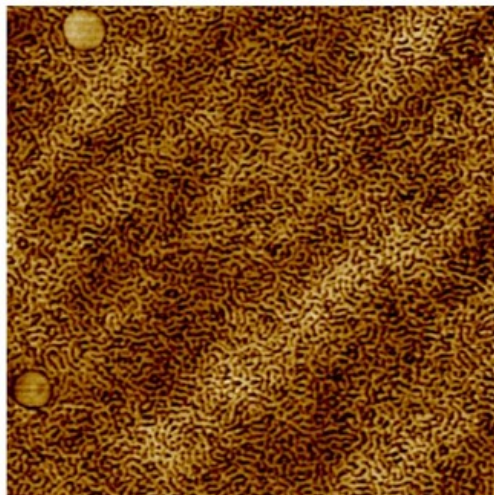
40.0 nm



Height Sensor

5.0  $\mu\text{m}$

c



40.0 nm



Height Sensor

400.0 nm

**Figure A20.** AFM height images of a 75 nm thickness blend of 45 kDa PCL/SIS vector 4211A SIS containing 50 wt % SIS as cast from toluene at scan sizes of (a) 75  $\mu\text{m}$  (b) 25  $\mu\text{m}$  and (c) 2  $\mu\text{m}$ . The morphology is a phase separated combination of spherulitic PCL at the substrate surface with a poorly ordered SIS layer at the free surface.

## **Appendix B**

# **SUPPORTING INFORMATION FOR “THERMAL TRANSITIONS IN SEMI-CRYSTALLINE POLYMER THIN FILMS STUDIED VIA SPECTRAL REFLECTANCE”**

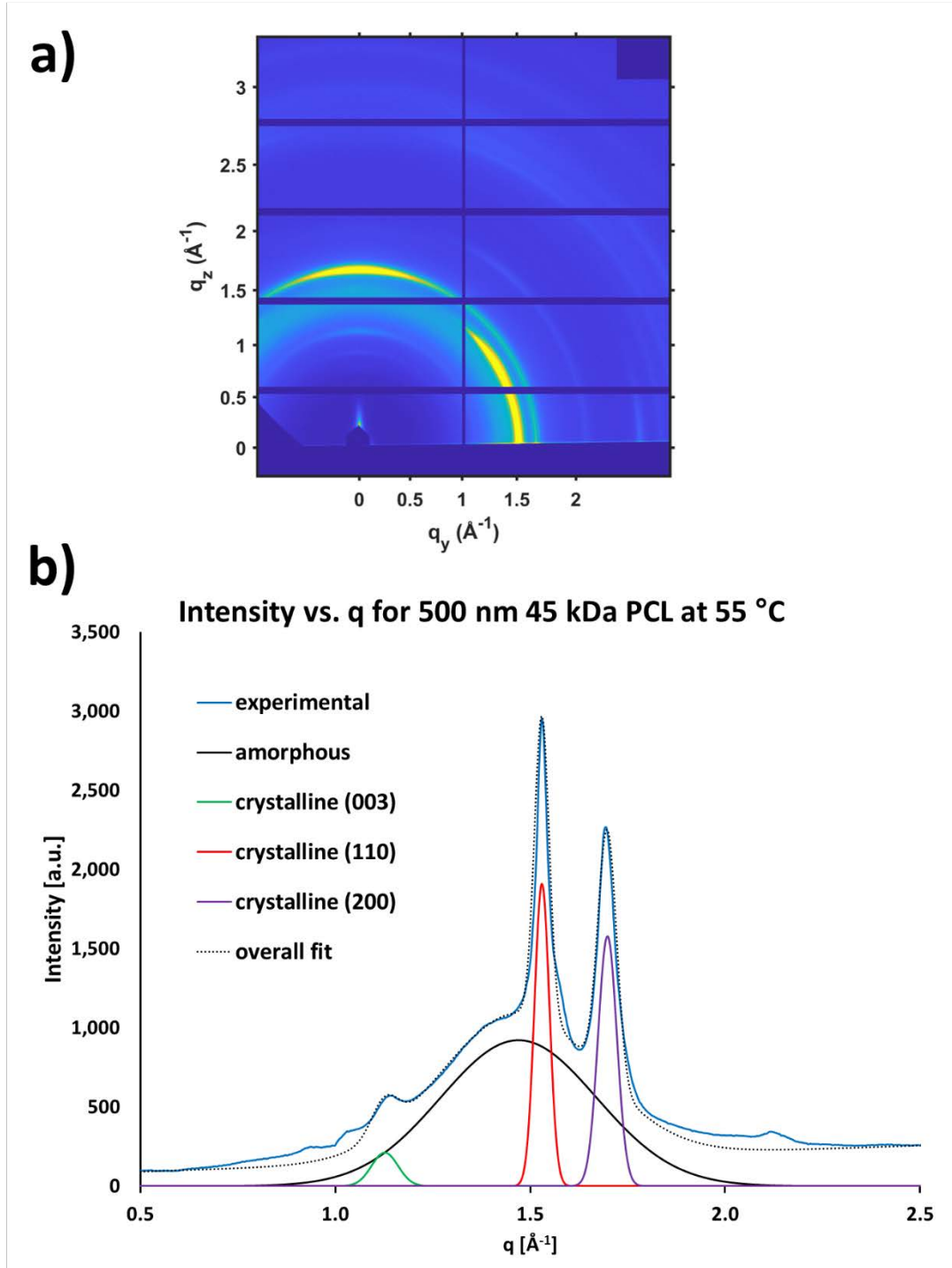


**Figure B1.** Grazing incidence wide-angle X-ray scattering data for a 500 nm film of 45 kDa PCL: a) 2D GIWAXS spectrum at 55 °C during the 1 °C/min heating ramp; b)

Corresponding intensity vs.  $q$  generated from (a). Degree of crystallinity is calculated by fitting this curve with four Gaussian peaks: one representing the amorphous component and three representing the crystalline peaks ((003), (110), and (200))<sup>76, 187</sup>, and then taking the ratio of the crystalline peak area to the overall area (amorphous plus crystalline peak fits).

## Spectral Reflectance Measurement and Model Settings

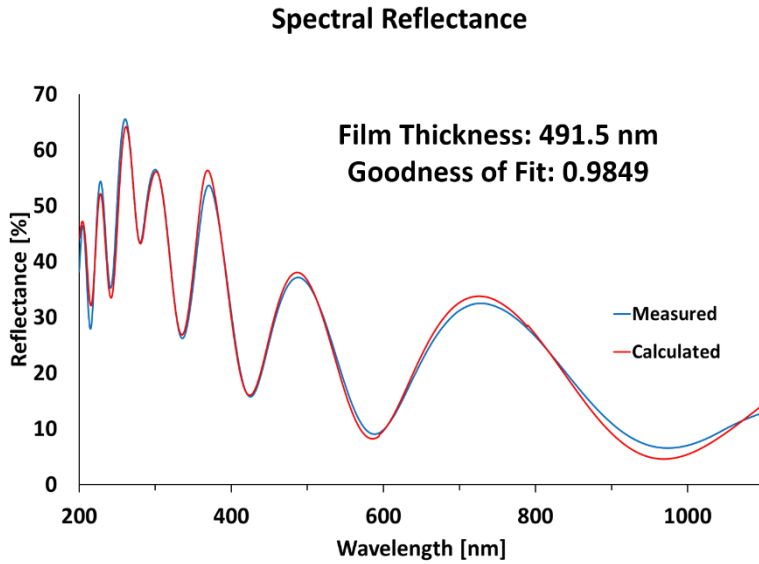


**Figure B2.** Spectral reflectance data and model fit generated for a 500 nm PCL thin film. The Filmetrics F20-UV instrument measures the intensity of sample-reflected UV and visible light (200-1000 nm) and the FILMeasure software is used to fit a calculated optical model spectrum to the data based on the properties of the substrate, thin film material, and measurement medium. The specific FILMeasure Model Settings for PCL are provided below, including the Film Stack, Analysis Options, and Material File. The Film Thickness, Roughness, and Non-uniformity are treated as fitting parameters in this model.

## FILMeasure Model Settings

### PCL Film Stack:

Recipe Name: PCL start

Author: SB  
Last Modified: 8/17/2017 12:37:27 PM

Units: Nanometers (nm)

Layer	Composition	Thickness	Nonuniformity
	±n ±k Meas.	Nominal (nm) Range (%)	(nm) Meas.
Medium	Air		
1	<Roughness>	100	
2	PCL - Tulane	500 ± 100	2
3	SiO2	2 ± 0	0
Substrate	Si		

OK Cancel Apply

### PCL Analysis Options:

Recipe Name: PCL start

Author: SB  
Last Modified: 8/17/2017 12:37:27 PM

Data Selection

Wavelength Range

Displayed data

Fixed range

From: 200 nm

To: 1100 nm

Smoothing

Optical thickness: 5 μm

Source Data

Analyze using (if present):

All

Reflectance 0°

Transmittance 0°

Reflectance 70°

Analysis Method

FFT (thickness only)

Spectrum matching

Robust (adaptive; thickness only)

Exact

Compensate for:

Unmodeled backside reflections

Tilted sample/Lost light

Lock together layers with identical:

Thickness

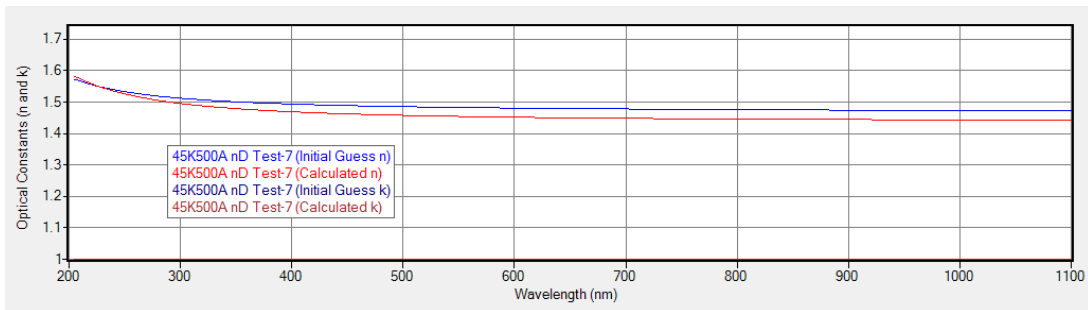
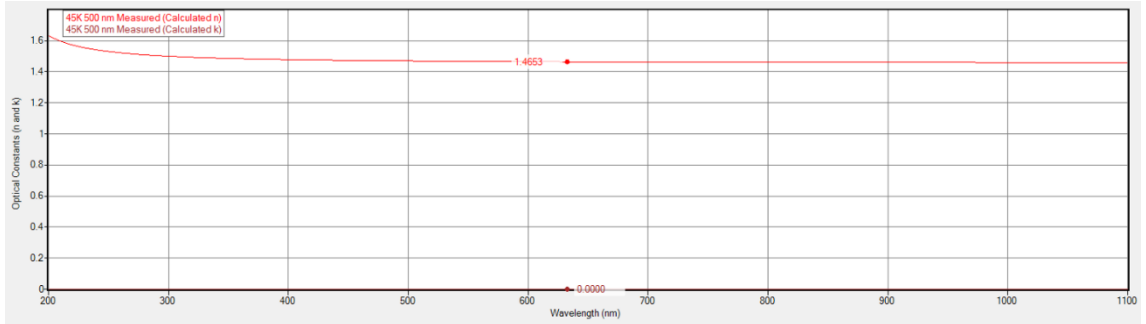
Composition

Advanced...

OK Cancel Apply

PCL Material File:

The “PCL – Tulane” material file contains a measured wavelength-dependent refractive index profile and the extinction coefficient, k, equal to zero for all wavelengths. This data was fit to a PCL film exhibiting semi-crystallinity at room temperature, and was used for all data presented in the manuscript.



We additionally fit the refractive index profile for a fully amorphous PCL film at 85 °C: Comparison shows that the refractive index profile is negligibly affected by temperature and crystallinity over the range of conditions studied ( $n_{632.8 \text{ nm}} = 1.4653$  at 25 °C and 1.4505 at 85 °C; 1% difference)

For PEG, the following Film Stack was used with the same Analysis Options as PCL:

Medium	Air
Roughness [nm]	5% of estimated film thickness
PEG	Generic, $n = 1.460$ ; $k = 0$
SiO <sub>2</sub>	2 nm
Substrate: Silicon	N/A

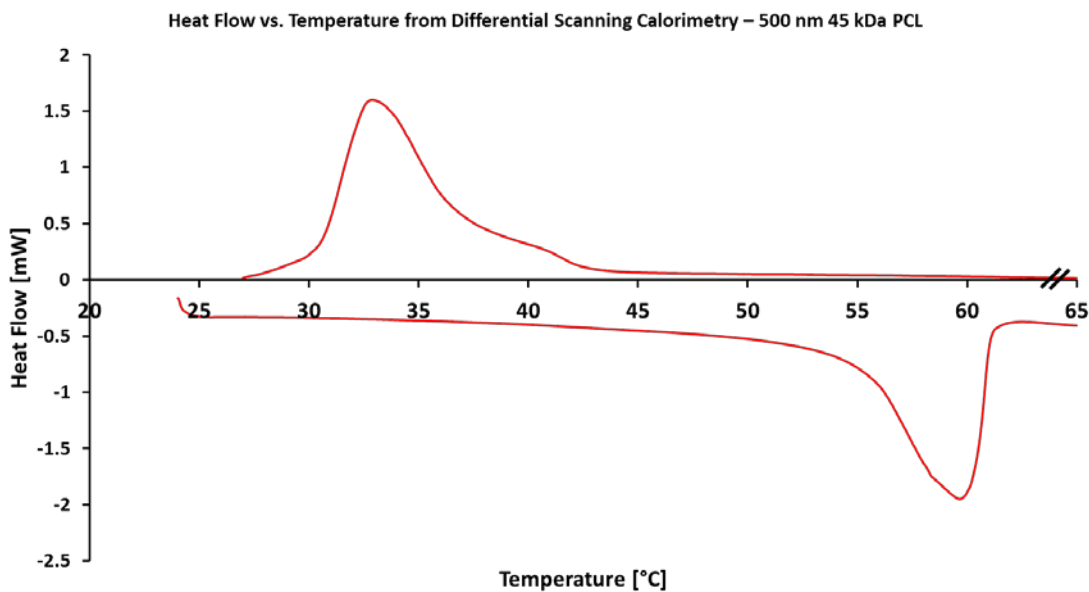


**Figure B3.** Differential scanning calorimetry (DSC) endotherm for bulk 45 kDa PCL, measured in inert atmosphere with a heating rate of 1 °C/min. A melting peak can be observed at  $60 \pm 1$  °C, which is in good agreement with previously measured melting points of PCL [3]. The onset of crystallization occurs at 43 °C, with a  $T_c$  of  $34$  °C  $\pm$  1 °C

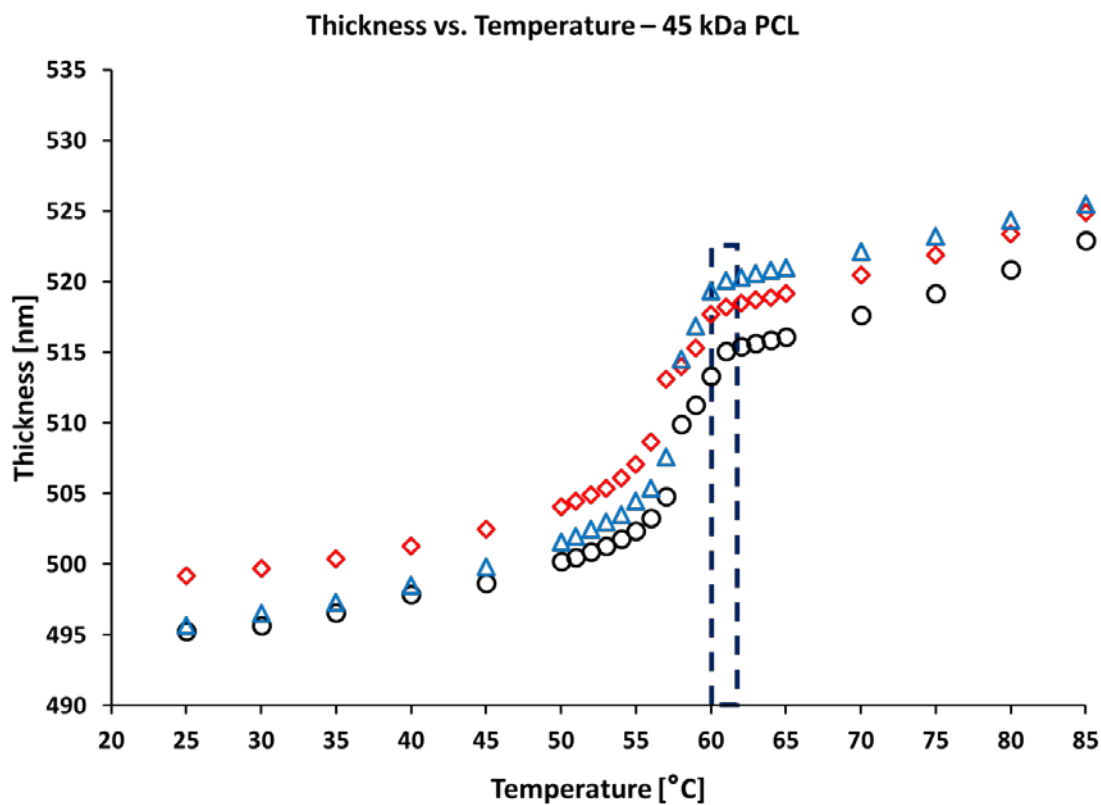


**Figure B4.** Film thickness vs. temperature plot for 500 nm 45 kDa PCL measured in three distinct trials. The dotted bar represents an approximately 1 °C window between the lowest and highest observed transition points. This highlights the accuracy as well as reproducibility of this method of determining  $T_m$ .

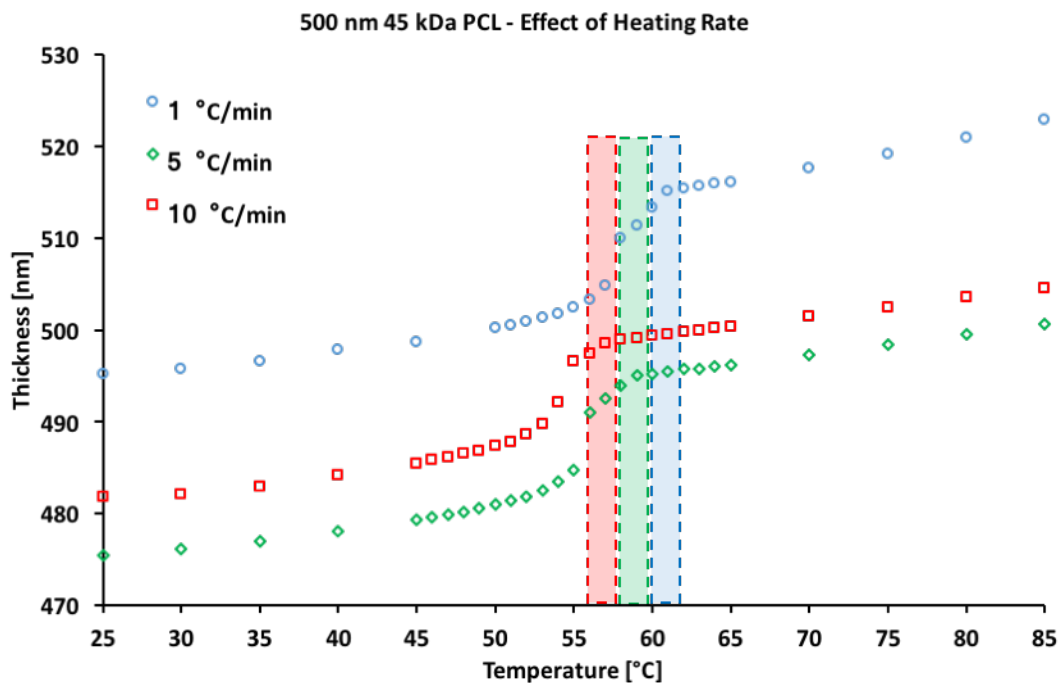


**Figure B5.** Film thickness vs. temperature plots for 500 nm 45 kDa samples measured using three different heating rates. The blue, green, and red dotted bars represent the melting temperature detected at 1 °C/min (61 °C), 5 °C/min (59 °C), and 10 °C/min (57 °C), respectively. The decrease in  $T_m$  with increasing heating rate can be attributed to polymer crystals reorganizing prior to melting during slower heating ramps.

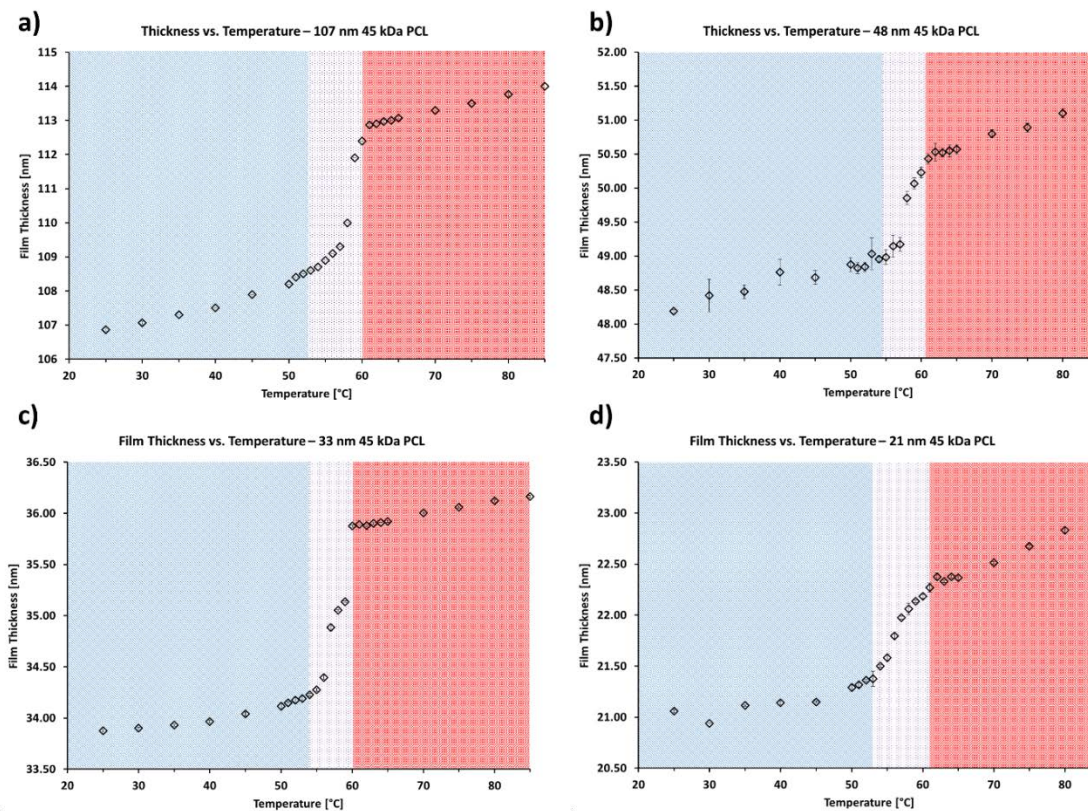


**Figure B6.** Film thickness vs. temperature plot for: a) 107 nm PCL film showing a melting transition at approximately 60 °C; b) 48 nm PCL film showing a melting transition at approximately 61 °C; c) 33 nm PCL film showing a melting transition at approximately 60 °C; and d) 21 nm PCL film showing a melting transition at approximately 61 °C. Regions shaded in blue, purple, and red shading indicate the semi-crystalline, melting transition, and melt state regions, respectively.

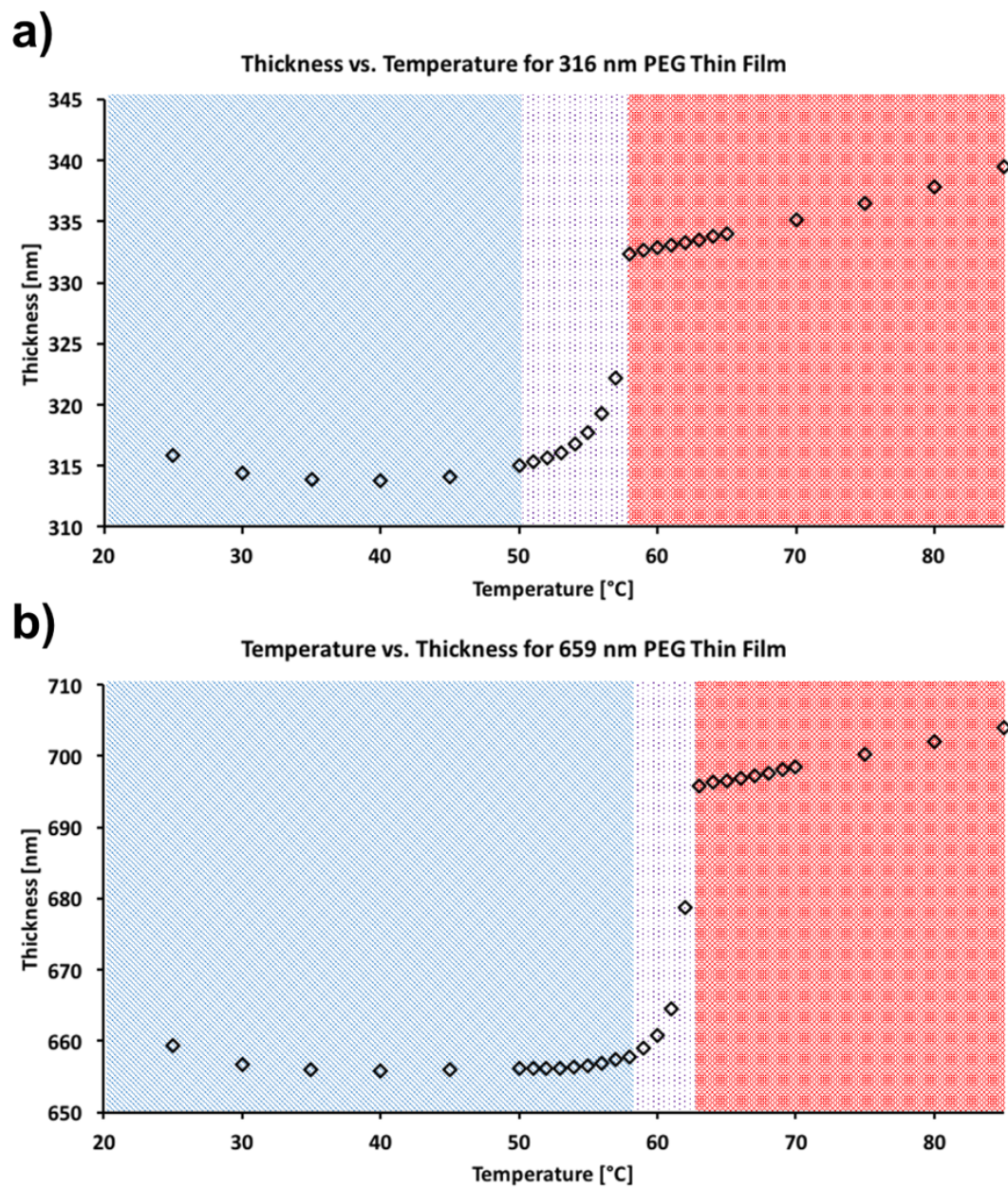


**Figure B7.** Film thickness vs. temperature plot for: a) 316 nm PEG film showing a melting transition at approximately 58 °C; and b) 659 nm PEG film showing a melting transition at approximately 63 °C. Regions shaded in blue, purple, and red shading indicate the semi-crystalline, melting transition, and melt state regions, respectively.

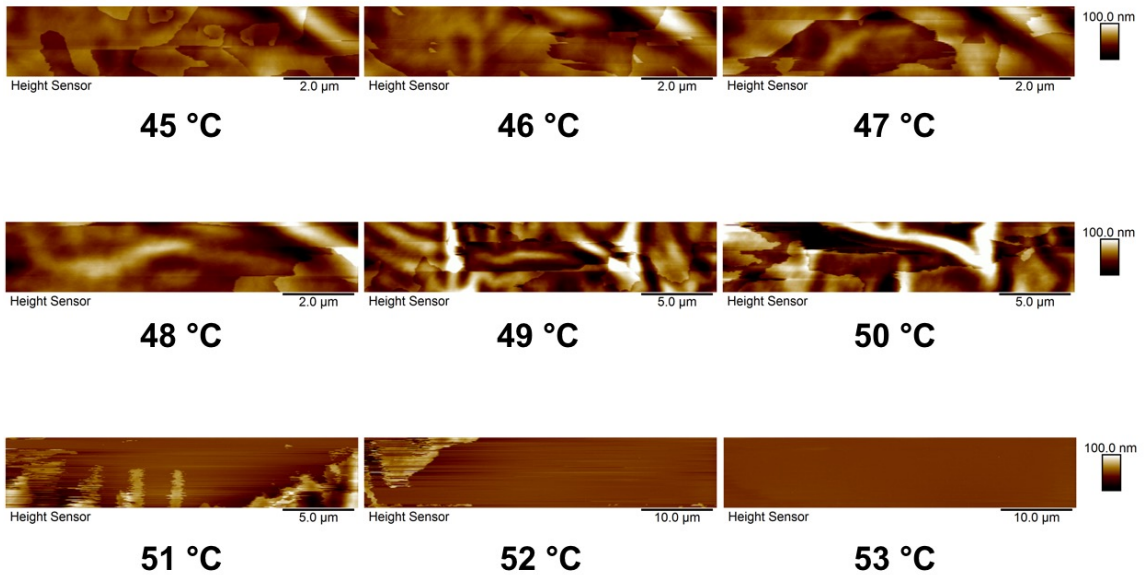


**Figure B8.** AFM height images showing the melting of a PEG film when heated at approximately 1 °C/min. The film completely melts between 52 °C and 53 °C, in good agreement with our SR study (see Figure 4.2). Scan size was increased between 48 °C and 49 °C and between 51 °C and 52 °C to ensure scans did not miss remaining isolated crystalline material.

## **Appendix C**

# **SUPPORTING INFORMATION FOR “SUPPRESSION OF MELT- INDUCED DEWETTING IN CYCLIC POLY(E-CAPROLACTONE) THIN FILMS”**

**Analytical Protocols:**

Gel permeation chromatography (GPC) data were acquired from a Waters model 1515 isocratic pump (Milford, MA) with THF as the mobile phase, a 1 mL/min flow rate, and columns heated at a constant 30 °C by a column oven. This system was operated with a set of two columns in series from Polymer Laboratories Inc. consisting of PSS SDV analytical linear M (8 × 300 mm) and PSS SDV analytical 100Å (8 x 300 mm) columns. A Model 2487 differential refractometer detector was used as a refractive index detector. The instrument was calibrated with Polystyrene ReadyCal Standards from Waters.

Mass spectral data were collected using a Bruker-Daltonics Matrix Assisted Laser Desorption Ionization Time-of-Flight (MALDI-TOF) Autoflex III mass spectrometer in reflector mode with positive ion detection. Typical sample preparation for MALDI-TOF MS data was performed by making stock solutions in THF of matrix (20 mg/ml), polymer analyte (2 mg/ml), and an appropriate cation source (2 mg/ml). The stock solutions were mixed in a 10/2/1 ratio (matrix/analyte/cation), deposited onto the MALDI target plate and allowed to evaporate via the dried droplet method. *trans*-2-[3-(4-*tert*-Butylphenyl)-2-methyl-2-propenylidene]malononitrile (DCTB) and sodium trifluoroacetate were used as matrix and cation, respectively. MALDI-TOF MS data were calibrated against SpheriCal dendritic calibrants from Polymer Factory (Stockholm, Sweden).  $M_n$  and  $\bar{D}$  of the resultant spectra were calculated using Polytools software.

Optical microscopy images were taken using an Olympus BX53 optical microscope operating in bright field mode. Atomic force microscopy images were taken using a Bruker

Dimension ICON AFM operating in Peak Force Quantitative Nanomechanical Mapping (PFQNM) mode and using ScanAsyst-Air tips ( $k = 0.4 \text{ N/m}$ ; resonant frequency = 70 kHz).

### **Synthetic Protocols:**

#### **Synthesis of $\alpha$ -propargyl- $\omega$ -hydroxy-PCL<sub>6k</sub> (*l*-PCL<sub>6k</sub>) (1):**

Tin(II) ethylhexanoate (Sn(Oct)<sub>2</sub>) was dried under vacuum overnight. The  $\epsilon$ -caprolactone ( $\epsilon$ CL) was stirred overnight with calcium hydride, and freshly distilled prior to polymerization into a flask containing activated molecular sieves. Note that all flasks used in this synthesis of polymer (1) were flame dried and placed under inert atmosphere to reduce water and air content. The propargyl alcohol was dried over MgSO<sub>4</sub> and activated molecular sieves directly prior to polymerization. In a representative polymerization, all reagents were dried as mentioned, followed by the syringe-addition of propargyl alcohol (12 mg, 0.21 mmol, 1.1 eq) and  $\epsilon$ CL (4.4 g, 38 mmol, 200 eq) to a flame dried 2-neck round bottom flask. The reaction mixture was inserted into an oil bath at 130 °C, followed by the immediate addition of tin(II) ethylhexanoate (Sn(Oct)<sub>2</sub>) (8 mg, 0.020 mmol, 0.1 eq). Depending on the desired molecular weight, the polymerization could be stopped by exposure to air and dilution with dichloromethane. Alternatively, aliquots could be taken at various time points to have a series of different molecular weights. However, if at any point the stir bar slowed, due to increased solution viscosity, the polymerization would be stopped immediately in order to ensure control over dispersity. The crude solution of polymer in DCM was precipitated into diethyl ether, filtered, and dried *in vacuo* prior to characterization.

**Synthesis of  $\alpha$ -propargyl- $\omega$ -azide-PCL<sub>6k</sub> (2):**

Polymer **1** (100 mg, 16 mmol, 1 eq) was dissolved in 10 mL of dichloromethane. 6-azidohexanoic acid (5.1 mg, 32 mmol, 2 eq), *N*-(3-(dimethylamino)propyl)-*N'*-ethylcarbodiimide hydrochloride (EDC) (5.0 mg, 32 mmol, 2.0 eq), and 4-(dimethylamino)pyridine (DMAP) (0.10 g, 0.81 mmol, 0.05 eq) were added to the reaction flask. The reaction was stirred until MALDI-TOF monitoring indicated the reaction was complete (typically within 24 hours). The crude reaction mixture was washed with saturated aqueous NaHSO<sub>4</sub> (3 x 5 mL), saturated aqueous NaHCO<sub>3</sub> (3 x 5 mL), and brine (5 mL). The organic layer was dried over anhydrous MgSO<sub>4</sub>, filtered, and dried *in vacuo*. The product was isolated in a 90% yield.

### **Synthesis of cyclic-PCL<sub>6k</sub> (c-PCL<sub>6k</sub>) (3):**

A 0.22 mM solution of the hetero-bisfunctional polymer **2** was prepared in 50 mL of DCM and placed under N<sub>2</sub>, and underwent two freeze-pump-thaw cycles. In a separate flask, *N,N,N',N'',N'''*-pentamethyldiethylenetriamine (PMDETA) (100 mg, 16 mmol, 1 eq) was dissolved in dichloromethane (100 mL) and degassed with two freeze-pump-thaw cycles. The PMDETA solution was refrozen, followed by the addition of CuBr (0.159 g, 1.1 mmol) and the final pump-thaw cycle. Upon thawing, a syringe and syringe pump were used to transfer the polymer (**2**) solution to the stirring CuBr/PMDETA solution at a rate of 2 mL/hour. After the complete addition of the polymer **2** solution to the reaction mixture, reaction continued to stir for an additional 2 h. The crude reaction mixture was then washed with saturated ammonium chloride several times, until the blue color was gone. The organic layer was then washed with saturated aqueous NaHSO<sub>4</sub> (3 x 10 mL). The organic layer was dried over anhydrous MgSO<sub>4</sub>, filtered, and dried *in vacuo*. The product was isolated (80% yield) via filtration and dried *in vacuo*.

### **Additional linear controls:**

#### **Synthesis of triazole-containing- $\alpha,\omega$ -dihydroxy-PCL<sub>6k</sub> (4):**

Polymer **1** (100 mg, 16 mmol, 1 eq) was dissolved in DCM (5 mL). 3-Azidopropanol (3.3 mg, 32 mmol, 2 eq) and PMDETA (70 mg, 403 mmol, 25 eq) were added to the reaction mixture. The reaction mixture underwent two freeze-pump-thaw cycles, followed by an additional freeze. CuBr (57 mg, 403 mmol, 25 eq) was added followed by an additional pump-thaw cycle. The reaction was then stirred for 24 hours was then washed with saturated ammonium chloride several times, until the blue color was gone. The organic

layer was then washed with saturated aqueous NaHSO<sub>4</sub> (3 x 10 mL). The organic layer was dried over anhydrous MgSO<sub>4</sub>, filtered, and dried *in vacuo*. The product was isolated via filtration and dried *in vacuo*.

**Synthesis of triazole-containing- $\alpha,\omega$ -diacetyl-PCL<sub>6k</sub> (5):**

Polymer **4** (100 mg, 16 mmol, 1 eq) was dissolved in DCM (5 mL). Acetic anhydride (7.1 mg, 0.070 mmol, 4.1 eq) and 4-(dimethylamino)pyridine DMAP (0.10 mg, 0.81 mmol, 0.05 eq) were added to the reaction mixture, which was then stirred overnight. The crude reaction mixture was concentrated *in vacuo* and then redissolved in dichloromethane. The solution was washed with saturated sodium bicarbonate (1 x 5 mL), water (2 x 5 mL), and 1 M HCl (1 x 5 mL). The organic layer was collected and dried with sodium sulfate. Finally, the organic solvent was removed *in vacuo* yielding the acetylated product for MALDI-TOF MS analysis.

**Synthesis of  $\alpha$ -propargyl- $\omega$ -acetyl-PCL<sub>6k</sub> (6):**

Polymer **1** (100 mg, 16 mmol, 1 eq) was dissolved in DCM (5 mL). Acetic anhydride (3.3 mg, 32 mmol, 2 eq) and 4-(dimethylamino)pyridine (DMAP) (0.10 mg, .81 mmol, 0.05 eq) were added to the reaction mixture, which was then stirred overnight. The crude reaction mixture was concentrated *in vacuo* and then redissolved in dichloromethane. The solution was washed with saturated sodium bicarbonate (1 x 5 mL), water (2 x 5 mL), and 1 M HCl (1 x 5 mL). The organic layer was collected and dried with sodium sulfate. Finally, the organic solvent was removed *in vacuo* yielding the acetylated product for MALDI-TOF MS analysis.

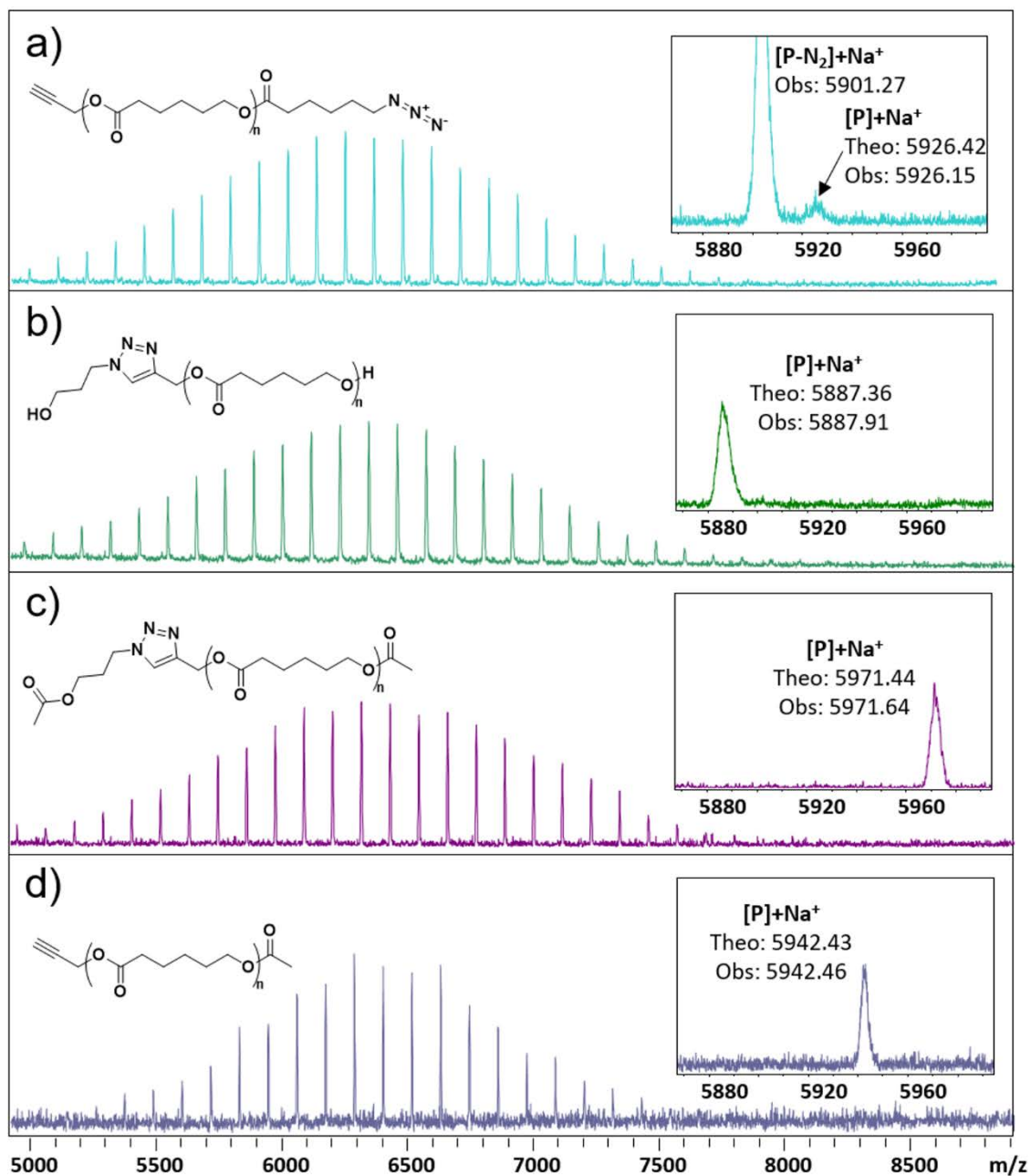


**Figure C1.** MALDI-TOF MS data illustrating the molecular weight distribution and purity of the four additional linear PCL controls: a)  $\alpha$ -propargyl- $\omega$ -azide-PCL<sub>6k</sub>, 5901 Da; b) triazole-containing- $\alpha,\omega$ -dihydroxy-PCL<sub>6k</sub>, 5887 Da; c) triazole-containing- $\alpha,\omega$ -diacetyl-PCL<sub>6k</sub>, 5971 Da; d)  $\alpha$ -propargyl- $\omega$ -acetyl-PCL<sub>6k</sub>, 5942 Da.

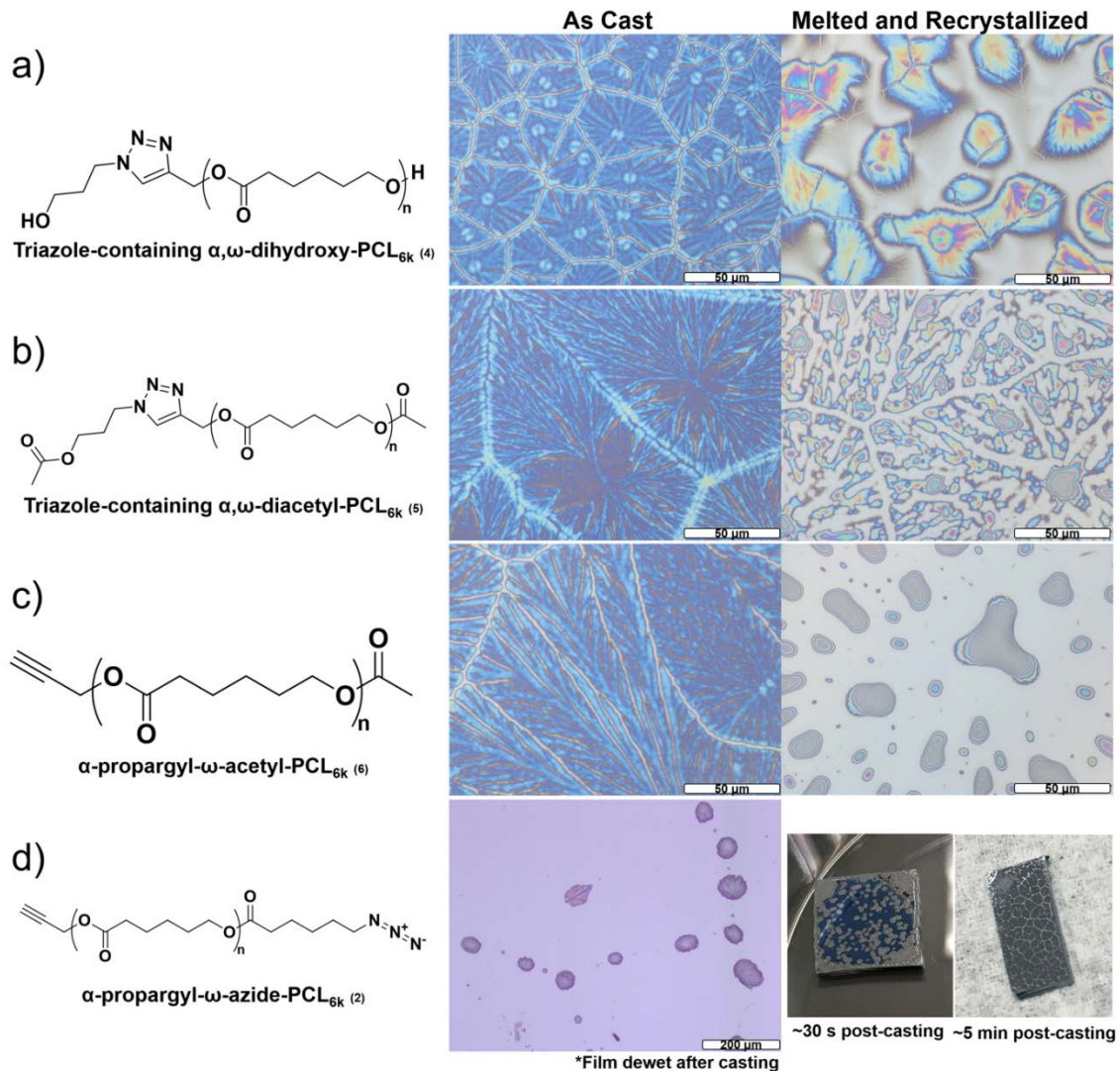


**Figure C2.** Optical microscopy of linear PCL control films before and after melting and recrystallization: a) triazole-containing- $\alpha,\omega$ -dihydroxy-PCL<sub>6k</sub> exhibited a crystalline morphology as-cast but partially dewet during melting; b) triazole-containing- $\alpha,\omega$ -diacetyl-PCL<sub>6k</sub> exhibited a crystalline morphology as cast but dewet completely upon melting; c)  $\alpha$ -propargyl- $\omega$ -acetyl-PCL<sub>6k</sub> exhibited a crystalline morphology as cast but dewet completely upon melting; d)  $\alpha$ -propargyl- $\omega$ -azide-PCL<sub>6k</sub> exhibited dewetting immediately after spin coating.

## Appendix D

# ACQUIRING CRYSTAL ORIENTATION AND DEGREE OF CRYSTALLINITY FROM GIWAXS AND GIXSGUI

### Introduction

As discussed in Chapter 2, grazing incidence wide-angle X-ray scattering (GIWAXS) is a technique that is used to probe the crystal structure and orientation in thin films on a molecular level. This technique excels at determining the range of crystal orientations and extent of order but can also be used to qualitatively study the degree of crystallinity in semi-crystalline thin films. This section will describe the methods by which this data can be extracted and interpreted using the GIXSGUI software created by Zhang Jiang at beamline 8-ID-E at the Advanced Photon Source (APS) at Argonne National Laboratory (ANL)<sup>42, 144</sup>. Note: The GIXSGUI software package and supplementary information can be found on the Advanced Photon Source website: <https://www.aps.anl.gov/Sector-8/8-ID/Operations-and-Schedules/Useful-Links/Sector-8-GIXSGUI>. These resources also include methods for adding the software package to MATLAB.

## Raw Data

GIWAXS (and GISAXS) studies done on a synchrotron X-ray source such as the one at APS involve measuring the scattering of coherent X-rays off a sample and into a two-dimensional detector in the beamline. This two-dimensional data is a representation of the three-dimensional Ewald sphere, which is a geometric construct that relates X-ray reflections to the crystal structure of the material. Therefore, the flattened three-dimensional signal is indicative of the crystal unit cell and orientation of crystals in the polymer. Therefore, the unique placement of discrete high intensity spots or bands at various  $q_y$  and  $q_z$  values are unique to the polymer. Furthermore, the existence of discrete spots vs gradual bands is indicative of discrete orientations or a mix of orientations, respectively. Thus, the first insightful piece of information can be gleaned from this data, i.e. whether there is a preferred or mixed orientation of crystalline features and lamellae. This can be done qualitatively by studying the two-dimensional images.

Developing the two-dimensional image from the data acquired on the beamline requires a couple of simple steps using the GIXSGUI interface (Figure D1):

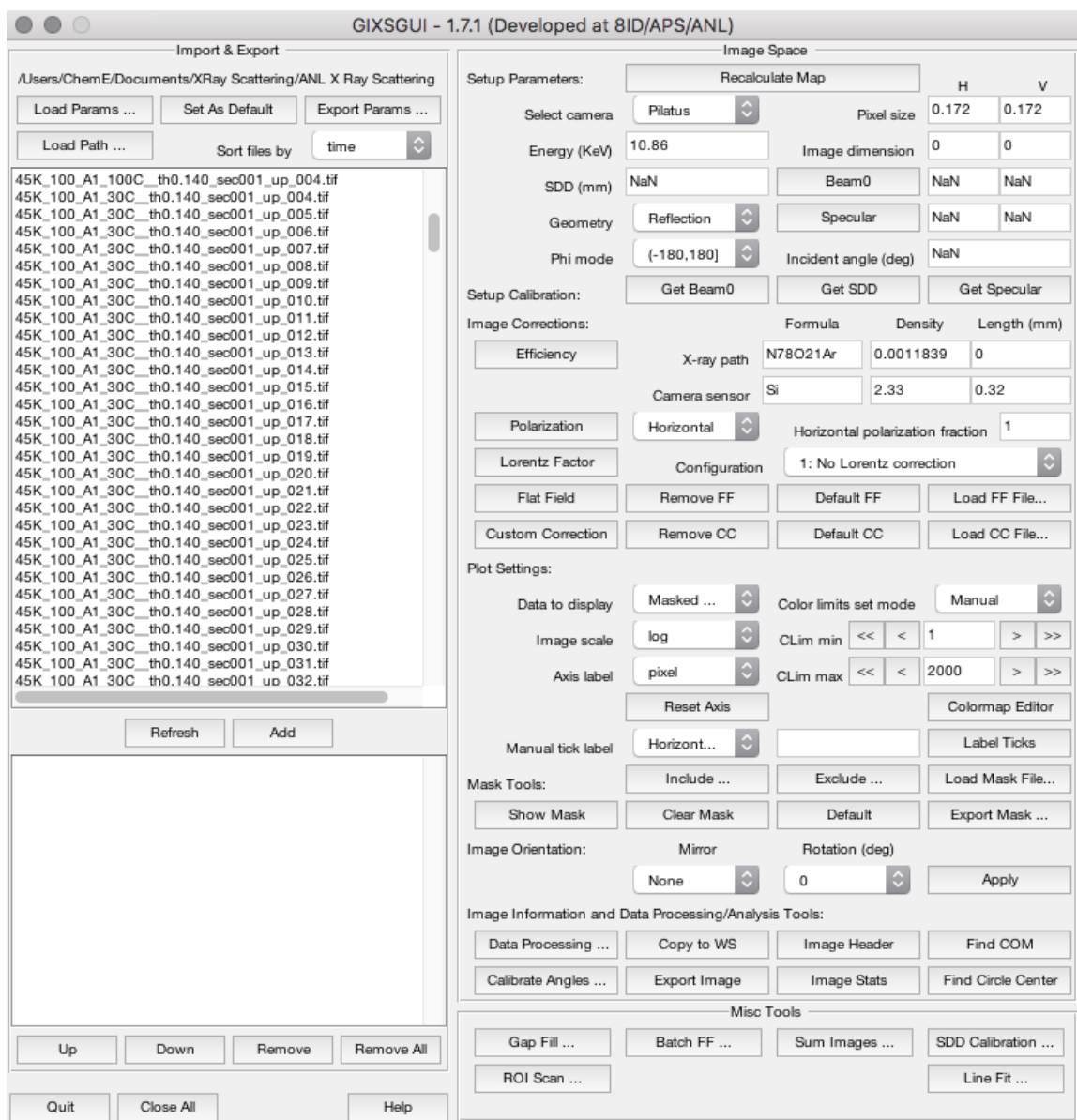


**Figure D1.** GIXSGUI User Interface

Generating a 2D Image:

1. Click “Load Params ...” and select the parameters file created on the beamline during the experiments at APS
2. Click “Load Path ...” to select the folder containing your data. The data will populate in the white box below as shown

3. Select the file of interest from that selection. The two-dimensional image should now appear on the screen: (Figure D2)

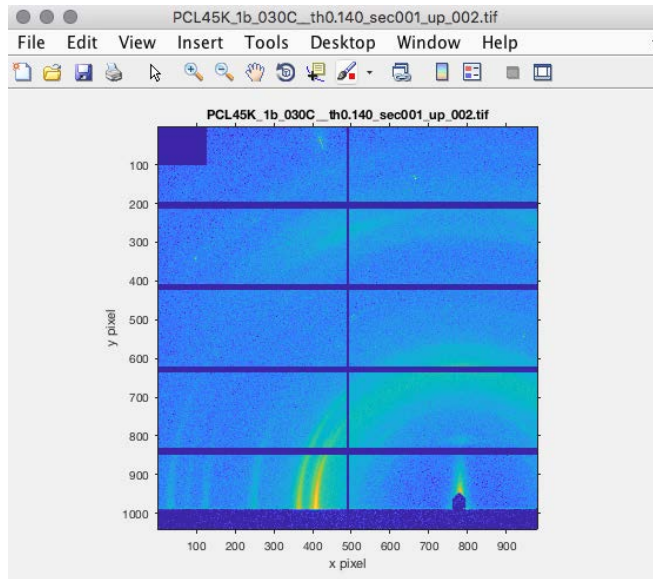


**Figure D2.** 2D scattering map (raw data)

4. In the GIXSGUI UI, under “Plot Settings” change the Axis label to “q”
5. In the GIXSGUI UI, under “Image Orientation” change the mirror to “Left-right”
6. Use MATLAB figure properties editor to change the visual properties of the image as desired. You can also export your figure to various image types using the figure properties editor

\*\*\*For images where the “up” and “down” images were acquired and the gap-filled image is desired

7. In the GIXSGUI UI, under “Misc Tools” press “Gap Fill ...” This menu will appear (Figure D3)



**Figure D3.** Gap Fill User Interface

8. Under “Base Image” click “Load ...” and select the GIWAXS exposure file labeled “up”
9. Under “Vertical Offset Image” click “Load ...” and select the GIWAXS exposure file labeled “down”
10. Under “Gap Fill” click “Fill”
11. Under “Export”, click “To File” and save the combined and gap filled image. If saved in the same path as the raw GIWAXS data, this file should appear in the file list in the GIXSGUI UI

12. Click the gap filled image to load it in the GIXSUI UI
13. In the GIXSGUI UI, under “Mask Tools” click “Load Mask file” and select gapfilled mask file
  - a. Note: Using the raw data causes an area to be displayed with full intensity, causing the curves to be misrepresented. So, uploading the new mask will be needed instead of displaying the raw data. (gap filled mask will be added to the Shared Dropbox folder.) Further, if so desired, one can save a new parameters file with this gap filled mask and flat field correction removed, in order to speed up the process and not have to perform these steps for each and every image to be processed.
14. In the GIXSGUI UI, under “Image Corrections” click “Remove FF”
15. In the GIXSGUI UI, click “Load FF File ...” to load any desired correction of flat field files.
16. As previously, the MATLAB figure properties editor can be used to change the properties of the figure and export it to various file types.

While the two-dimensional image is useful, quantitative information is often needed, such as more precise high intensity positions as a function of  $q$ , or the degree of crystallinity. For these treatments, the user must use more complicated features of the GIXSGUI software.

As described in the Introduction, the degree of crystallinity ( $X_c$ ) is defined as the mass or volume percentage of crystalline domains divided by the entire mass or volume of the system. Since the degree of crystallinity has drastic effects on mechanical properties

such as degradation and solvent permeability and optical qualities such as clarity, the ability to quantify the degree of crystallinity is indispensable. Unfortunately, techniques such as DSC and WAXS that are typically used for determining the degree of crystallinity in bulk materials are not applicable to thin and ultrathin films. Furthermore, because of the incomplete scattering pattern of GIWAXS that does not capture the full 360 degrees of scattering, GIWAXS is unable to quantify the exact degree of crystallinity. However, we can qualitatively study degree of crystallinity by quantifying the ratio of the crystalline peaks to the entire peak area. While this method isn't exact, it does allow us to monitor the trends of crystallization, especially upon heating crystalline material and cooling from the melt.

To quantitatively determine peak positions, orientation distributions, and a qualitative degree of crystallinity, the follow steps are followed:

1. In the GIXSGUI UI, under “Image Information and Data Processing/Analysis Tools” click “Data Processing ...” The following menu will appear (Figure D4):

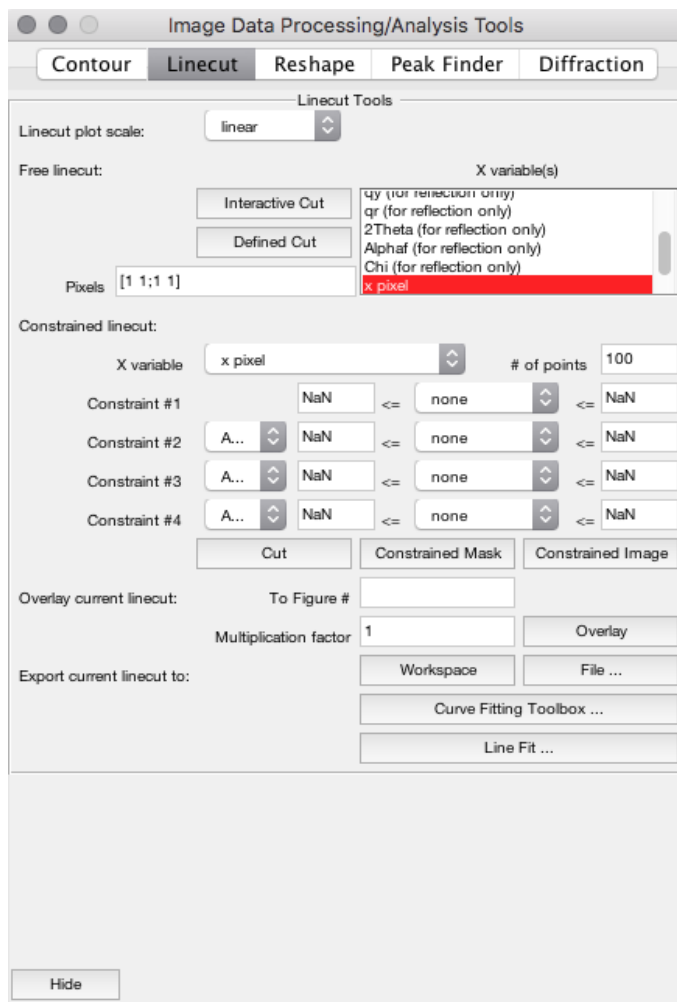


**Figure D4.** Image Processing/Linecut User Interface

2. From the “X variable” drop down menu, select the variable you would like to integrate in
3. For a constrained line cut, use the “Constraint #X” section to set bounds and the connected drop-down menu to select the bound variable
4. For degree of crystallinity measurements, no bounds should be selected. Only the variable of integration (q) should be selected from the aforementioned drop down menu

- Using the “# of points” box, select the number of data points used in the data generation
- Click “Cut.” A linecut such as the one below should appear (Figure D5):

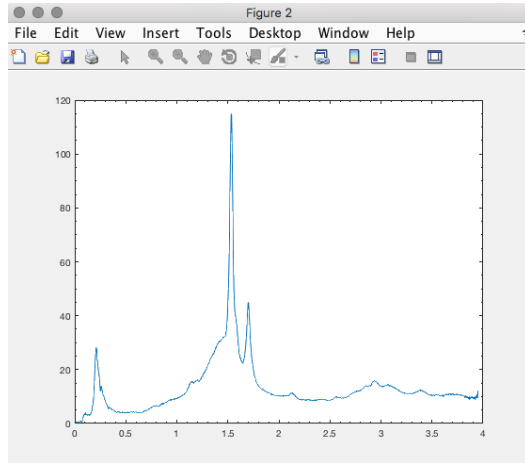


**Figure D5.** Sample 2D linecut

- If the line cut is satisfactory, in the Image Data Processing UI, under the “Export current linecut to” section, click “File ...” and save the file as a .txt file. This file can be used in Excel or the “Linefitgui” program to analyze peak positions, intensities, and other characteristics.

#### Using linefitgui to determine degree of crystallinity

- Once a full-q integration linecut has been saved as a .txt file, in the main MATLAB window, type “linefitgui” and press enter. The following GUI should appear (Figure D6):

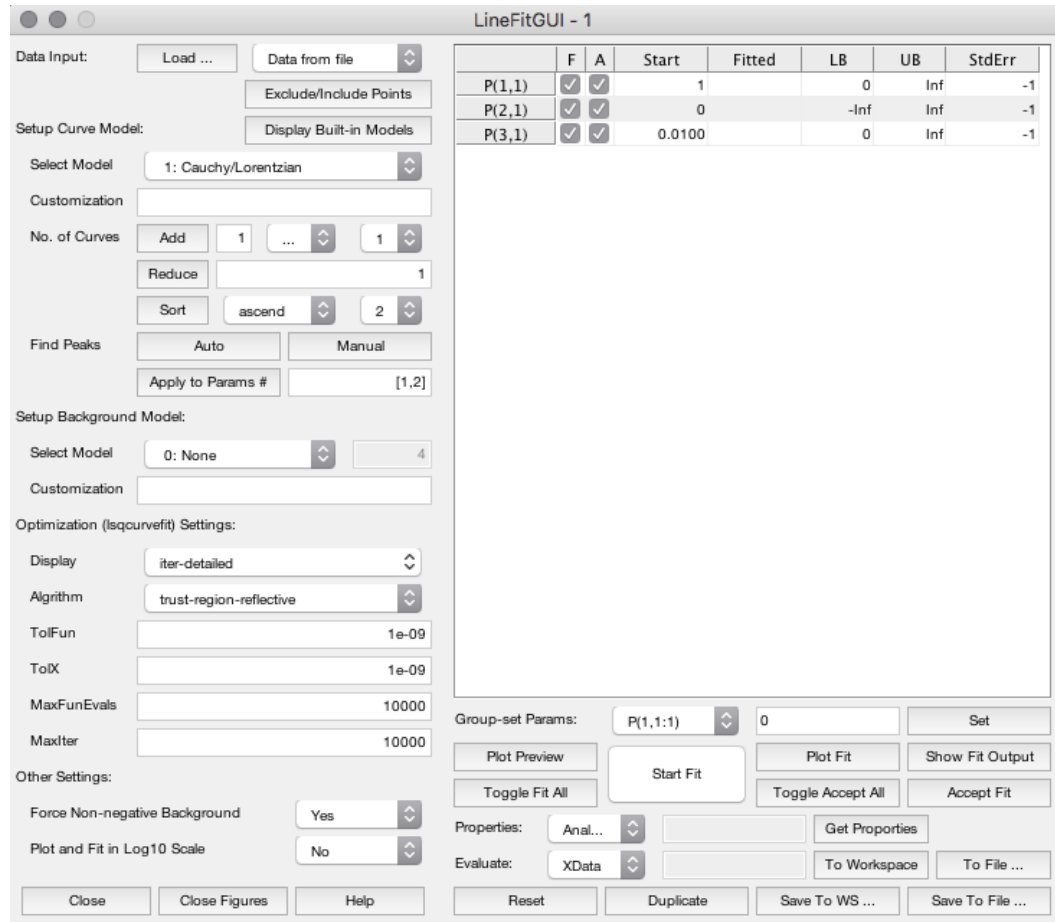


**Figure D6.** Linefitgui User Interface

2. In the linefitgui, under “Data Input” click “Load ...” and select the aforementioned .txt file containing the intensity vs. q linecut.
3. The peaks can be modeled using a variety of models. For degree of crystallinity calculations, we have typically used the Gaussian model, which can be selected from the drop-down menu
4. Under “Find Peaks” click “Manual.” Your line cut should appear as below (Figure D7):

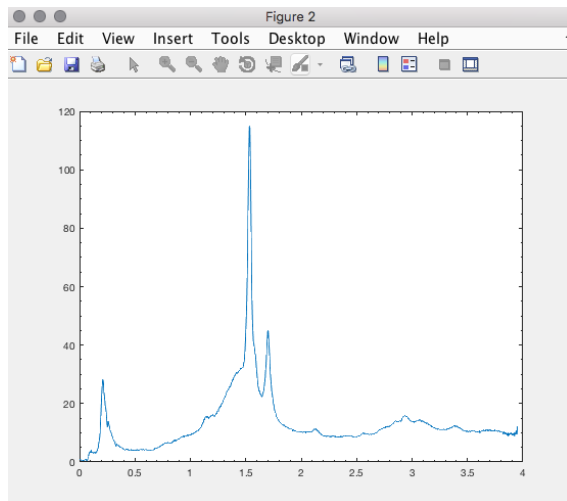


**Figure D7.** Sample linecut

5. Using the mouse and cursor, left-click directly on the peak positions in your spectrum, and then press enter. The GUI will number your peak positions as follows (Figure D8):

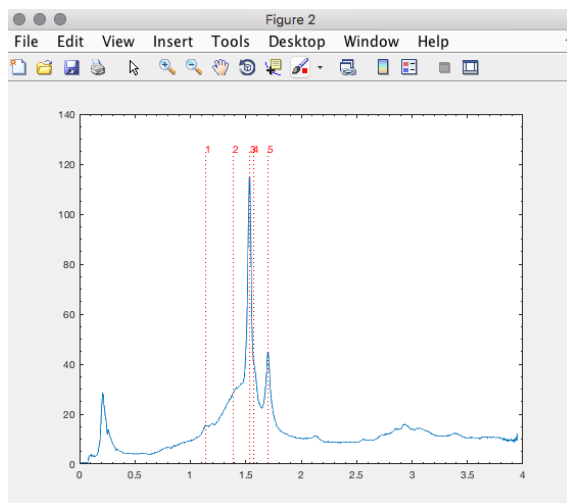


**Figure D8.** Sample linecut with user-chosen peaks to fit

6. In the linefitgui, under “Find Peaks”, click “Apply to Params #”

7. In the linefitgui, under “Setup Background Model” select the desired model for the baseline under “Select Model.” Typically, a Linear baseline model will work for Intensity vs. q linecuts.
8. Click “Start Fit.” MATLAB will run through its calculations, and the model fit with individual peaks modeled along with the raw data will appear as below (Figure D9):

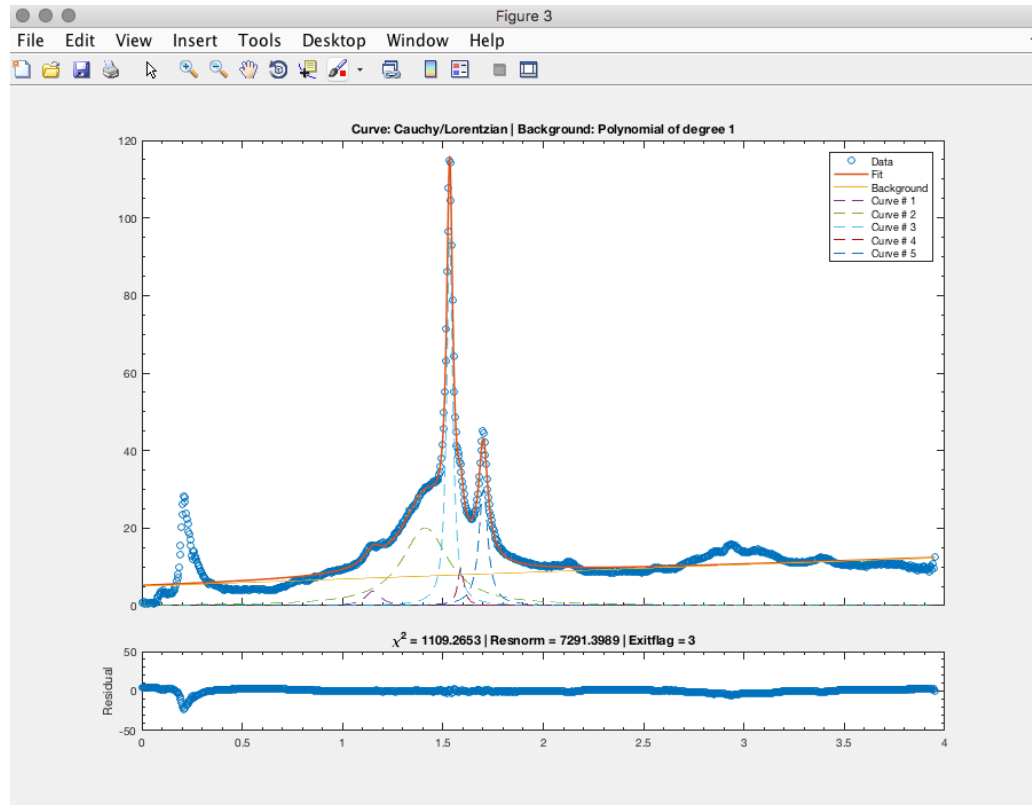


**Figure D9.** Modeled line fits

9. If satisfied with the fit, peak positions, etc., in the linefitgui UI, click “Accept Fit”
10. To export the individual modeled peaks, baseline, etc., click “To File ...” and save as a .txt file. This file can be used for further data analysis.

## Calculating Degree of Crystallinity

Since the degree of crystallinity from GIWAXS is defined as the ratio of the crystalline peak area to the sum of the area of the crystalline and amorphous peak(s), the following steps are taken.

1. Copy and paste the aforementioned .txt file data into an excel file. The data should be arranged in columns as follows:

q	Raw Data Intensity	Peak 1 Intensity	Peak 2 Intensity	Peak X intensity	Baseline Intensity
---	--------------------	------------------	------------------	------------------	--------------------

2. Using a simple trapezoidal rule calculation, the area under each of the curves can be calculated.
3. Once the individual curve areas are calculated, they can be set to a ratio of (area of crystalline peaks/total peak area) x 100, which is equal to the degree of crystallinity in percent.

## LIST OF REFERENCES

- (1) Piorkowska, E.; Rutledge, G. C., *Handbook of Polymer Crystallization*. John Wiley & Sons: New Jersey, 2013.
- (2) Mark, J. E., *Physical Properties of Polymers Handbook*. Springer: 2007; Vol. 1076.
- (3) Brandrup, J.; Immergut, E. H.; Grulke, E. A.; Abe, A.; Bloch, D. R., *Polymer Handbook*. Wiley: New York, 1989; Vol. 7.
- (4) Young, R. J.; Lovell, P. A., *Introduction to polymers*. CRC press: 2011.
- (5) Ketelaars, A.; Papantoniou, Y.; Nakayama, K., Analysis of the density and the enthalpy of poly ( $\epsilon$ -caprolactone)-polycarbonate blends: Amorphous phase compatibility and the effect of secondary crystallization. *J. Appl. Polym. Sci.* **1997**, *66* (5), 921-927.
- (6) Beers, K. L.; Douglas, J. F.; Amis, E. J.; Karim, A., Combinatorial measurements of crystallization growth rate and morphology in thin films of isotactic polystyrene. *Langmuir* **2003**, *19* (9), 3935-3940.
- (7) Córdova, M. E.; Lorenzo, A. T.; Muller, A. J.; Hoskins, J. N.; Grayson, S. M., A Comparative Study On The Crystallization Behavior Of Analogous Linear And Cyclic Poly(caprolactones). *Macromolecules* **2011**, *44* (7), 1742-1746.
- (8) Dargazany, R.; Khiêm, V. N.; Poshtan, E. A.; Itskov, M., Constitutive modeling of strain-induced crystallization in filled rubbers. *Phys Rev E Stat Nonlin Soft Matter Phys* **2014**, *89* (2), 022604.
- (9) Shin, E. J.; Jeong, W.; Brown, H. A.; Koo, B. J.; Hedrick, J. L.; Waymouth, R. M., Crystallization of cyclic polymers: Synthesis and crystallization behavior of high molecular weight cyclic poly ( $\epsilon$ -caprolactone) s. *Macromolecules* **2011**, *44* (8), 2773-2779.

- (10) Mareau, V. H.; Prud'homme, R. E., Crystallization of ultrathin poly( $\epsilon$ -caprolactone) films in the presence of residual solvent, an in situ atomic force microscopy study. *Polymer* **2005**, *46* (18), 7255-7265.
- (11) Ma, M.; He, Z.; Yang, J.; Chen, F.; Wang, K.; Zhang, Q.; Deng, H.; Fu, Q., Effect Of Film Thickness On Morphological Evolution In Dewetting And Crystallization Of Polystyrene/Poly(Epsilon-Caprolactone) Blend Films. *Langmuir* **2011**, *27* (21), 13072-13081.
- (12) Zen, A.; Saphiannikova, M.; Neher, D.; Grenzer, J.; Grigorian, S.; Pietsch, U.; Asawapirom, U.; Janietz, S.; Scherf, U.; Lieberwirth, I.; Wegner, G., Effect of molecular weight on the structure and crystallinity of poly(3-hexylthiophene). *Macromolecules* **2006**, *39* (6), 2162-2171.
- (13) Brinkmann, M.; Rannou, P., Effect of Molecular Weight on the Structure and Morphology of Oriented Thin Films of Regioregular Poly(3-hexylthiophene) Grown by Directional Epitaxial Solidification. *Adv. Funct. Mater.* **2007**, *17* (1), 101-108.
- (14) Vancso, G. J.; Beekmans, L. G. M.; Pearce, R.; Trifonova, D.; Varga, J., From Microns to Nanometers: Morphology Development in Semicrystalline Polymers by Scanning Force Microscopy. *Journal of Macromolecular Science-Physics* **1999**, *B38* (5-6), 491-503.
- (15) Beers, K. L.; Douglas, J. F.; Amis, E. J.; Karim, A., High Throughput Approach To Crystallization In Thin Films Of Isotactic Polystyrene. *Abstracts of Papers of the American Chemical Society* **2001**, *222*, U327-U327.
- (16) Qiu, Z.; Ikehara, T.; Nishi, T., Miscibility and crystallization of poly (ethylene oxide) and poly ( $\epsilon$ -caprolactone) blends. *Polymer* **2003**, *44* (10), 3101-3106.
- (17) Pérez, R.; Córdova, M.; López, J.; Hoskins, J.; Zhang, B.; Grayson, S.; Müller, A., Nucleation, Crystallization, Self-Nucleation And Thermal Fractionation Of Cyclic And Linear Poly ( $\epsilon$ -caprolactone). *React. Funct. Polym.* **2014**, *80*, 71-82.

- (18) Bassett, D.; Hodge, A.; Olley, R. In *On The Morphology Of Melt-Crystallized Polyethylene II. Lamellae And Their Crystallization Conditions*, Proceedings of the Royal Society of London A: Mathematical, Physical and Engineering Sciences, The Royal Society: 1981; pp 39-60.
- (19) Jimenez, G.; Ogata, N.; Kawai, H.; Ogihara, T., Structure and thermal/mechanical properties of poly( $\epsilon$ -caprolactone)-clay blend. *J. Appl. Polym. Sci.* **1997**, *64* (11), 2211-2220.
- (20) Ma, M.; He, Z.; Li, Y.; Chen, F.; Wang, K.; Zhang, Q.; Deng, H.; Fu, Q., Surface Phase Separation, Dewetting Feature Size, And Crystal Morphology In Thin Films Of Polystyrene/Poly(Epsilon-Caprolactone) Blend. *J Colloid Interface Sci* **2012**, *387* (1), 262-269.
- (21) Kelly, G. M.; Albert, J. N. L., Ultrathin film crystallization of poly ( $\epsilon$ -caprolactone) in blends containing styrene-isoprene block copolymers: The nano-rose morphology. *Polymer* **2017**, *117*, 295-305.
- (22) Hay, J.; Mills, P., The use of differential scanning calorimetry to study polymer crystallization kinetics. *Polymer* **1982**, *23* (9), 1380-1384.
- (23) Castillo, R.; Müller, A., Crystallization and Morphology of Biodegradable or Biostable Single and Double Crystalline Block Copolymers. *Prog. Polym. Sci.* **2009**, *34* (6), 516-560.
- (24) Takeshita, H.; Poovarodom, M.; Kiya, T.; Arai, F.; Takenaka, K.; Miya, M.; Shiomi, T., Crystallization behavior and chain folding manner of cyclic, star and linear poly (tetrahydrofuran) s. *Polymer* **2012**, *53* (23), 5375-5384.
- (25) Atanase, L. I.; Glaied, O.; Riess, G., Crystallization Kinetics of PCL Tagged With Well-Defined Positional Triazole Defects Generated By Click Chemistry. *Polymer* **2011**, *52* (14), 3074-3081.
- (26) Schäler, K.; Ostas, E.; Schröter, K.; Thurn-Albrecht, T.; Binder, W. H.; Saalwächter, K., Influence of Chain Topology on Polymer Dynamics and Crystallization. Investigation

of Linear and Cyclic Poly ( $\epsilon$ -caprolactone) s by  $^1\text{H}$  Solid-State NMR Methods. *Macromolecules* **2011**, *44* (8), 2743-2754.

(27) Su, H. H.; Chen, H. L.; Diaz, A.; Casas, M. T.; Puiggali, J.; Hoskins, J. N.; Grayson, S. M.; Perez, R. A.; Muller, A. J., New Insights On The Crystallization And Melting Of Cyclic PCL Chains On The Basis Of A Modified Thomson-Gibbs Equation. *Polymer* **2013**, *54* (2), 846-859.

(28) Du, Z. X.; Xu, J. T.; Fan, Z. Q., Regulation of Micellar Morphology of PCL-b-PEO Block Copolymers by Crystallization Temperature. *Macromol. Rapid Commun.* **2008**, *29* (6), 467-471.

(29) Mareau, V. H.; Prud'Homme, R. E., Growth rates and morphologies of miscible PCL/PVC blend thin and thick films. *Macromolecules* **2003**, *36* (3), 675-684.

(30) Chen, F. C.; Ko, C. J.; Wu, J. L.; Chen, W. C., Morphological study of P3HT:PCBM blend films prepared through solvent annealing for solar cell applications. *Sol. Energy Mater. Sol. Cells* **2010**, *94* (12), 2426-2430.

(31) Mamun, A.; Bazuin, C. G.; Prud'homme, R. E., Morphologies of Various Polycaprolactone/Polymer Blends in Ultrathin Films. *Macromolecules* **2015**, *48* (5), 1412-1417.

(32) DalnokiVeress, K.; Forrest, J. A.; Stevens, J. R.; Dutcher, J. R., Phase Separation Morphology of Thin Films of Polystyrene/Polyisoprene Blends. *Journal of Polymer Science Part B-Polymer Physics* **1996**, *34* (17), 3017-3024.

(33) Ma, M.; He, Z.; Yang, J.; Wang, Q.; Chen, F.; Wang, K.; Zhang, Q.; Deng, H.; Fu, Q., Vertical Phase Separation And Liquid-Liquid Dewetting Of Thin PS/PCL Blend Films During Spin Coating. *Langmuir* **2011**, *27* (3), 1056-1063.

(34) Liu, Y.-X.; Chen, E.-Q., Polymer crystallization of ultrathin films on solid substrates. *Coord. Chem. Rev.* **2010**, *254* (9), 1011-1037.

- (35) Reiter, G.; Hamieh, M.; Damman, P.; Slavovs, S.; Gabriele, S.; Vilmin, T.; Raphael, E., Residual Stresses In Thin Polymer Films Cause Rupture And Dominate Early Stages Of Dewetting. *Nat Mater* **2005**, *4* (10), 754-758.
- (36) González-Viñas, W.; Mancini, H. L., *An introduction to materials science*. Princeton University Press: 2015.
- (37) Flory, P. J.; Yoon, D. Y., MOLECULAR MORPHOLOGY IN SEMI-CRYSTALLINE POLYMERS. *Nature* **1978**, *272* (5650), 226-229.
- (38) Reiter, G.; Strobl, G. R., *Progress in Understanding of Polymer Crystallization*. Springer: Berlin, 2007; Vol. 714.
- (39) Stevens, M. P., *Polymer chemistry: an introduction*. oxford university press New York: 1990.
- (40) De Jeu, W. H., *Basic X-ray scattering for soft matter*. Oxford University Press: 2016.
- (41) Yang, I.; Liu, C. Y., Real-time SAXS and WAXS study of the multiple melting behavior of poly ( $\epsilon$ -caprolactone). *J. Polym. Sci. Pol. Phys.* **2010**, *48* (16), 1777-1785.
- (42) Jiang, Z.; Li, X.; Strzalka, J.; Sprung, M.; Sun, T.; Sandy, A. R.; Narayanan, S.; Lee, D. R.; Wang, J., The dedicated high-resolution grazing-incidence X-ray scattering beamline 8-ID-E at the Advanced Photon Source. *Journal of synchrotron radiation* **2012**, *19* (4), 627-636.
- (43) Freire, E., Differential scanning calorimetry. *Protein Stability and Folding: Theory and Practice* **1995**, 191-218.
- (44) Fava, R., Differential scanning calorimetry of epoxy resins. *Polymer* **1968**, *9*, 137-151.

- (45) Pielichowski, K.; Flejtuch, K., Differential scanning calorimetry studies on poly (ethylene glycol) with different molecular weights for thermal energy storage materials. *Polymers for Advanced Technologies* **2002**, *13* (10-12), 690-696.
- (46) Okazaki, I.; Wunderlich, B., Reversible melting in polymer crystals detected by temperature-modulated differential scanning calorimetry. *Macromolecules* **1997**, *30* (6), 1758-1764.
- (47) Hay, J.; Fitzgerald, P.; Wiles, M., Use of differential scanning calorimetry to study polymer crystallization kinetics. *Polymer* **1976**, *17* (11), 1015-1018.
- (48) Crist, B.; Schultz, J. M., Polymer spherulites: A critical review. *Prog. Polym. Sci.* **2016**, *56*, 1-63.
- (49) Norton, D.; Keller, A., The spherulitic and lamellar morphology of melt-crystallized isotactic polypropylene. *Polymer* **1985**, *26* (5), 704-716.
- (50) Marand, H.; Xu, J.; Srinivas, S., Determination of the equilibrium melting temperature of polymer crystals: linear and nonlinear Hoffman– Weeks extrapolations. *Macromolecules* **1998**, *31* (23), 8219-8229.
- (51) Wunderlich, B., *Macromolecular physics*. Elsevier: 2012; Vol. 2.
- (52) Keith, H. D.; Padden, F. J., Banding in Polyethylene And Other Spherulites. *Macromolecules* **1996**, *29* (24), 7776-7786.
- (53) Keith, H., Banding in Spherulites: Two Recurring Topics. *Polymer* **2001**, *42* (25), 09987-09993.
- (54) Way, J.; Atkinson, J.; Nutting, J., The effect of spherulite size on the fracture morphology of polypropylene. *Journal of Materials Science* **1974**, *9* (2), 293-299.
- (55) Bassett, D.; Hodge, A., On Lamellar Organization in Banded Spherulites of Polyethylene. *Polymer* **1978**, *19* (4), 469-472.

- (56) Schultz, J. M., Self-induced field model for crystal twisting in spherulites. *Polymer* **2003**, *44* (2), 433-441.
- (57) Milner, S. T., Polymer crystal–melt interfaces and nucleation in polyethylene. *Soft Matter* **2011**, *7* (6), 2909-2917.
- (58) Sakai, Y.; Imai, M.; Kaji, K.; Tsuji, M., Growth shape observed in two-dimensional poly (ethylene terephthalate) spherulites. *Macromolecules* **1996**, *29* (27), 8830-8834.
- (59) Yoshioka, T.; Fujimura, T.; Manabe, N.; Yokota, Y.; Tsuji, M., Morphological study on three kinds of two-dimensional spherulites of poly (butylene terephthalate)(PBT). *Polymer* **2007**, *48* (19), 5780-5787.
- (60) Gałęski, A., Computer simulation of two-dimensional spherulite growth. *J. Polym. Sci. Pol. Phys.* **1981**, *19* (5), 721-730.
- (61) Jenkins, M.; Harrison, K., The effect of molecular weight on the crystallization kinetics of polycaprolactone. *Polymers for advanced technologies* **2006**, *17* (6), 474-478.
- (62) Hoffman, J.; Lauritzen, J.; Passaglia, E.; Ross, G.; Frolen, s. L.; Weeks, J., Kinetics of polymer crystallization from solution and the melt. *Kolloid-Zeitschrift und Zeitschrift für Polymere* **1969**, *231* (1-2), 564-592.
- (63) Patel, G.; Patel, R., Growth mechanism of polymer hedrites. *European Polymer Journal* **1970**, *6* (5), 657-662.
- (64) Varga, J.; Ehrenstein, G., High-temperature hedritic crystallization of the  $\beta$ -modification of isotactic polypropylene. *Colloid and Polymer Science* **1997**, *275* (6), 511-519.
- (65) Duan, Y.; Zhang, Y.; Yan, S.; Schultz, J. M., In situ AFM study of the growth of banded hedritic structures in thin films of isotactic polystyrene. *Polymer* **2005**, *46* (21), 9015-9021.

- (66) Reneker, D.; Geil, P., Morphology of polymer single crystals. *J. Appl. Phys.* **1960**, *31* (11), 1916-1925.
- (67) Keller, A., Polymer single crystals. *Polymer* **1962**, *3*, 393-421.
- (68) Peterlin, A., Thickening of polymer single crystals during annealing. *Journal of Polymer Science Part C: Polymer Letters* **1963**, *1* (6), 279-284.
- (69) Qiao, C. D.; Zhao, J. C.; Jiang, S. C.; Ji, X. L.; An, L. J.; Jiang, B. Z., Crystalline morphology evolution in PCL thin films. *Journal of Polymer Science Part B-Polymer Physics* **2005**, *43* (11), 1303-1309.
- (70) Mareau, V. H.; Prud'homme, R. E., Crystallization of ultrathin poly(epsilon-caprolactone) films in the presence of residual solvent, an in situ atomic force microscopy study. *Polymer* **2005**, *46* (18), 7255-7265.
- (71) Mareau, V. H.; Prud'Homme, R. E., In-situ hot stage atomic force microscopy study of poly( $\epsilon$ -caprolactone) crystal growth in ultrathin films. *Macromolecules* **2005**, *38* (2), 398-408.
- (72) Hoffman, J. D.; Davis, G. T.; Lauritzen, J. I., The rate of crystallization of linear polymers with chain folding. In *Treatise on solid state chemistry*, Springer: 1976; pp 497-614.
- (73) Lauritzen Jr, J. I.; Hoffman, J. D., Formation of polymer crystals with folded chains from dilute solution. *J. Chem. Phys.* **1959**, *31* (6), 1680-1681.
- (74) Lauritzen, J. I.; Hoffman, J. D., Extension of theory of growth of chain-folded polymer crystals to large undercoolings. *J. Appl. Phys.* **1973**, *44* (10), 4340-4352.
- (75) Liu, X.-b.; Zhao, Y.-f.; Fan, X.-h.; Chen, E.-q., Crystal orientation and melting behavior of poly( $\epsilon$ -Caprolactone) under one-dimensionally "hard" confined microenvironment. *Chinese Journal of Polymer Science* **2013**, *31* (6), 946-958.

(76) Hu, H.; Dorset, D. L., Crystal Structure of Poly ( $\epsilon$ -caprolactone). *Macromolecules* **1990**, *23* (21), 4604-4607.

(77) Yang, H.; Shin, T. J.; Yang, L.; Cho, K.; Ryu, C. Y.; Bao, Z., Effect of mesoscale crystalline structure on the field-effect mobility of regioregular poly (3-hexyl thiophene) in thin-film transistors. *Adv. Funct. Mater.* **2005**, *15* (4), 671-676.

(78) Kim, D. H.; Park, Y. D.; Jang, Y.; Yang, H.; Kim, Y. H.; Han, J. I.; Moon, D. G.; Park, S.; Chang, T.; Chang, C., Enhancement of field-effect mobility due to surface-mediated molecular ordering in regioregular polythiophene thin film transistors. *Adv. Funct. Mater.* **2005**, *15* (1), 77-82.

(79) Xiao, Z.; Dong, Q.; Bi, C.; Shao, Y.; Yuan, Y.; Huang, J., Solvent Annealing of Perovskite-Induced Crystal Growth for Photovoltaic-Device Efficiency Enhancement. *Adv. Mater.* **2014**, *26* (37), 6503-6509.

(80) Chopra, K.; Paulson, P.; Dutta, V., Thin-film solar cells: an overview. *Progress in Photovoltaics: Research and Applications* **2004**, *12* (2-3), 69-92.

(81) Li, G.; Yao, Y.; Yang, H.; Shrotriya, V.; Yang, G.; Yang, Y., "Solvent annealing" effect in polymer solar cells based on poly (3-hexylthiophene) and methanofullerenes. *Adv. Funct. Mater.* **2007**, *17* (10), 1636-1644.

(82) Zelikin, A. N., Drug releasing polymer thin films: new era of surface-mediated drug delivery. *ACS Nano* **2010**, *4* (5), 2494-2509.

(83) Lu, Y.; Chen, S., Micro and nano-fabrication of biodegradable polymers for drug delivery. *Advanced drug delivery reviews* **2004**, *56* (11), 1621-1633.

(84) Dash, T. K.; Konkimalla, V. B., Poly- $\epsilon$ -caprolactone based formulations for drug delivery and tissue engineering: A review. *J. Control. Release* **2012**, *158* (1), 15-33.

- (85) Balke, S.; Hamielec, A.; LeClair, B.; Pearce, S., Gel permeation chromatography. *Industrial & Engineering Chemistry Product Research and Development* **1969**, 8 (1), 54-57.
- (86) Gellerstedt, G., Gel permeation chromatography. In *Methods in lignin chemistry*, Springer: 1992; pp 487-497.
- (87) Johnson, J.; Porter, R., Gel permeation chromatography. *Prog. Polym. Sci.* **1970**, 2, 201-256.
- (88) Park, T. G., Degradation of Poly(D,L-lactic Acid) Microspheres - Effect of Molecular-Weight. *J. Control. Release* **1994**, 30 (2), 161-173.
- (89) Drott, E.; Mendelson, R., Determination of polymer branching with gel-permeation chromatography. I. Theory. *J. Polym. Sci. Pol. Phys.* **1970**, 8 (8), 1361-1371.
- (90) Casassa, E. F., Comments on exclusion of polymer chains from small pores and its relation to gel permeation chromatography. *Macromolecules* **1976**, 9 (1), 182-185.
- (91) Gewehr, M.; Nakamura, K.; Ise, N.; Kitano, H., Gel permeation chromatography using porous glass beads modified with temperature-responsive polymers. *Die Makromolekulare Chemie* **1992**, 193 (1), 249-256.
- (92) Moore, J., Gel permeation chromatography. I. A new method for molecular weight distribution of high polymers. *J. Polym. Sci. Pol. Chem.* **1964**, 2 (2), 835-843.
- (93) Byrd, H. M.; McEwen, C. N., The limitations of MALDI-TOF mass spectrometry in the analysis of wide polydisperse polymers. *Analytical chemistry* **2000**, 72 (19), 4568-4576.
- (94) Li, Y.; Hoskins, J. N.; Sreerama, S. G.; Grayson, S. M., MALDI-TOF Mass Spectral Characterization of Polymers Containing an Azide Group: Evidence of Metastable Ions. *Macromolecules* **2010**, 43 (14), 6225-6228.

- (95) Raeder, H.; Schrepp, W., MALDI-TOF mass spectrometry in the analysis of synthetic polymers. *Acta Polymerica* **1998**, *49* (6), 272-293.
- (96) Montaudo, G.; Garozzo, D.; Montaudo, M. S.; Puglisi, C.; Samperi, F., Molecular and structural characterization of polydisperse polymers and copolymers by combining MALDI-TOF mass spectrometry with GPC fractionation. *Macromolecules* **1995**, *28* (24), 7983-7989.
- (97) Bednarek, M.; Biedroń, T.; Kubisa, P., Studies of atom transfer radical polymerization (ATRP) of acrylates by MALDI TOF mass spectrometry. *Macromol. Chem. Phys.* **2000**, *201* (1), 58-66.
- (98) Singhal, N.; Kumar, M.; Kanaujia, P. K.; Viridi, J. S., MALDI-TOF mass spectrometry: an emerging technology for microbial identification and diagnosis. *Frontiers in microbiology* **2015**, *6*, 791.
- (99) Miyagi, A.; Wunderlich, B., Superheating and reorganization on melting of poly (ethylene terephthalate). *J. Polym. Sci. Pol. Phys.* **1972**, *10* (7), 1401-1405.
- (100) Richardson, M.-J.; Savill, N., Derivation of accurate glass transition temperatures by differential scanning calorimetry. *Polymer* **1975**, *16* (10), 753-757.
- (101) Fillon, B.; Wittmann, J.; Lotz, B.; Thierry, A., Self-nucleation and recrystallization of isotactic polypropylene ( $\alpha$  phase) investigated by differential scanning calorimetry. *J. Polym. Sci. Pol. Phys.* **1993**, *31* (10), 1383-1393.
- (102) Booth, A.; Hay, J., The use of differential scanning calorimetry to study polymer crystallization kinetics. *Polymer* **1969**, *10*, 95-104.
- (103) Kim, S.; Hewlett, S.; Roth, C.; Torkelson, J., Confinement effects on glass transition temperature, transition breadth, and expansivity: comparison of ellipsometry and fluorescence measurements on polystyrene films. *The European Physical Journal E: Soft Matter and Biological Physics* **2009**, *30* (1), 83-92.

- (104) Franquet, A.; De Laet, J.; Schram, T.; Terryn, H.; Subramanian, V.; Van Ooij, W.; Vereecken, J., Determination of the thickness of thin silane films on aluminium surfaces by means of spectroscopic ellipsometry. *Thin Solid Films* **2001**, *384* (1), 37-45.
- (105) Efremov, M. Y.; Kiyanova, A. V.; Last, J.; Soofi, S. S.; Thode, C.; Nealey, P. F., Glass Transition In Thin Supported Polystyrene Films Probed By Temperature-Modulated Ellipsometry In Vacuum. *Phys. Rev. E* **2012**, *86* (2 Pt 1), 021501.
- (106) Forrest, J. A.; DalnokiVeress, K.; Dutcher, J. R., Interface And Chain Confinement Effects On The Glass Transition Temperature Of Thin Polymer Films. *Phys. Rev. E* **1997**, *56* (5), 5705-5716.
- (107) Fryer, D. S.; Nealey, P. F.; de Pablo, J. J., Thermal probe measurements of the glass transition temperature for ultrathin polymer films as a function of thickness. *Macromolecules* **2000**, *33* (17), 6439-6447.
- (108) Lu, H.; Chen, W.; Russell, T. P., Relaxation of thin films of polystyrene floating on ionic liquid surface. *Macromolecules* **2009**, *42* (22), 9111-9117.
- (109) Chapman, M.; Mullen, M.; Novoa-Ortega, E.; Alhasani, M.; Elman, J. F.; Euler, W. B., Structural evolution of ultrathin films of rhodamine 6G on glass. *The Journal of Physical Chemistry C* **2016**, *120* (15), 8289-8297.
- (110) Qiao, C.-d.; Jiang, S.-c.; Ji, X.-l.; An, L.-j., In situ observation of melting and crystallization behaviors of poly(E  $\epsilon$ -caprolactone) ultra-thin films by AFM technique. *Chinese Journal of Polymer Science* **2013**, *31* (9), 1321-1328.
- (111) Zong, Q.; Li, Z.; Xie, X. M., Inversion of phase morphology in polymer-blend thin films on glass substrates. *Macromol. Chem. Phys.* **2004**, *205* (8), 1116-1124.
- (112) Albert, J. N. L.; Young, W. S.; Lewis III, R. L.; Bogart, T. D.; Smith, J. R.; Epps III, T. H., Systematic Study On The Effect Of Solvent Removal Rate On The Morphology Of Solvent Vapor Annealed ABA Triblock Copolymer Thin Films. *ACS Nano* **2012**, *6* (1), 459-66.

- (113) Cappella, B.; Kaliappan, S.; Sturm, H., Using AFM force-distance curves to study the glass-to-rubber transition of amorphous polymers and their elastic-plastic properties as a function of temperature. *Macromolecules* **2005**, *38* (5), 1874-1881.
- (114) Yoon, D. Y.; Flory, P. J., INTERMEDIATE ANGLE SCATTERING FUNCTIONS AND LOCAL CHAIN CONFIGURATIONS OF SEMI-CRYSTALLINE AND AMORPHOUS POLYMERS. *Polymer Bulletin* **1981**, *4* (12), 693-698.
- (115) Ashraf, A.; Dissanayake, D.; Eisaman, M., The effect of confinement on the crystalline microstructure of polymer: fullerene bulk heterojunctions. *Physical Chemistry Chemical Physics* **2015**, *17* (36), 23326-23331.
- (116) Lawrence, C., The mechanics of spin coating of polymer films. *The Physics of fluids* **1988**, *31* (10), 2786-2795.
- (117) Hall, D. B.; Underhill, P.; Torkelson, J. M., Spin coating of thin and ultrathin polymer films. *Polymer Engineering & Science* **1998**, *38* (12), 2039-2045.
- (118) Norrman, K.; Ghanbari-Siahkali, A.; Larsen, N., 6 Studies of spin-coated polymer films. *Annual Reports Section" C"(Physical Chemistry)* **2005**, *101*, 174-201.
- (119) Davis, R. L.; Jayaraman, S.; Chaikin, P. M.; Register, R. A., Creating Controlled Thickness Gradients in Polymer Thin Films Via Flowcoating. *Langmuir* **2014**, *30* (19), 5637-5644.
- (120) Kim, H. S.; Lee, C. H.; Sudeep, P.; Emrick, T.; Crosby, A. J., Nanoparticle stripes, grids, and ribbons produced by flow coating. *Adv. Mater.* **2010**, *22* (41), 4600-4604.
- (121) Stafford, C. M.; Roskov, K. E.; Epps III, T. H.; Fasolka, M. J., Generating Thickness Gradients of Thin Polymer Films Via Flow Coating. *Rev. Sci. Instrum.* **2006**, *77* (2), 023908.
- (122) Albert, J. N. L.; Baney, M. J.; Stafford, C. M.; Kelly, J. Y.; Epps III, T. H., Generation of Monolayer Gradients in Surface Energy and Surface Chemistry for Block Copolymer Thin Film Studies. *ACS Nano* **2009**, *3* (12), 3977-3986.

- (123) Kelly, J. Y.; Albert, J. N. L.; Howarter, J. A.; Kang, S. H.; Stafford, C. M.; Epps III, T. H.; Fasolka, M. J., Investigation of thermally responsive block copolymer thin film morphologies using gradients. *ACS Appl. Mater. Interfaces* **2010**, 2 (11), 3241-3248.
- (124) Ma, M.; He, Z.; Yang, J.; Chen, F.; Wang, K.; Zhang, Q.; Deng, H.; Fu, Q., Effect of film thickness on morphological evolution in dewetting and crystallization of polystyrene/poly( $\epsilon$ -caprolactone) blend films. *Langmuir* **2011**, 27 (21), 13072-13081.
- (125) Steiner, U.; Klein, J.; Eiser, E.; Budkowski, A.; Fetters, L. J., Complete Wetting From Polymer Mixtures. *Science* **1992**, 258 (5085), 1126-1126.
- (126) Bruder, F.; Brenn, R., Spinodal decomposition in thin films of a polymer blend. *Phys. Rev. Lett.* **1992**, 69 (4), 624.
- (127) Albert, J. N. L.; Epps III, T. H., Self-Assembly of Block Copolymer Thin Films. *Mater. Today* **2010**, 13 (6), 24-33.
- (128) Li, H. Z.; Wu, Y. J.; Sato, H.; Kong, L.; Zhang, C. F.; Huang, K.; Tao, D. L.; Chen, J.; Liu, X. X.; Zhao, Y.; Xu, Y. Z.; Wu, J. G.; Ozaki, Y., A new facile method for preparation of nylon-6 with high crystallinity and special morphology. *Macromolecules* **2009**, 42 (4), 1175-1179.
- (129) Kikkawa, Y.; Abe, H.; Fujita, M.; Iwata, T.; Inoue, Y., Crystal Growth in Poly (L-lactide) Thin Film Revealed by In Situ Atomic Force Microscopy. *Macromol. Chem. Phys.* **2003**, 204 (15), 1822-1831.
- (130) Keith, H. D.; Padden, F. J., Twisting Orientation and the Role of Transient States in Polymer Crystallization. *Polymer* **1984**, 25 (1), 28-42.
- (131) Keith, H. D.; Padden, F. J.; Lotz, B.; Wittmann, J. C., Asymmetries of Habit in Polyethylene Crystals Grown from the Melt. *Macromolecules* **1989**, 22 (5), 2230-2238.
- (132) Lotz, B.; Cheng, S. Z. D., A Critical Assessment of Unbalanced Surface Stresses as the Mechanical Origin of Twisting and Scrolling of Polymer Crystals. *Polymer* **2005**, 46 (3), 577-610.

(133) Bassett, D.; Vaughan, A., Reply to a discussion of spherulitic crystallization and morphology. *Polymer* **1986**, *27* (9), 1472-1476.

(134) Abo el Maaty, M.; Hosier, I.; Bassett, D., A unified context for spherulitic growth in polymers. *Macromolecules* **1998**, *31* (1), 153-157.

(135) Janimak, J.; Bassett, D., On morphological instability in polymeric crystallization. *Polymer* **1999**, *40* (2), 459-468.

(136) Persson, N. E.; McBride, M. A.; Grover, M. A.; Reichmanis, E., Automated Analysis of Orientational Order in Images of Fibrillar Materials. *Chemistry of Materials* **2016**, *29* (1), 3-14.

(137) White, H.; Hosier, I.; Bassett, D., Cylindrical Lamellar Habits in Monodisperse Centrally Branched Alkanes. *Macromolecules* **2002**, *35* (18), 6763-6765.

(138) Vaughan, A., Etching and Morphology of Poly(vinylidene fluoride). *Journal of Materials Science* **1993**, *28* (7), 1805-1813.

(139) Albert, J. N. L.; Bogart, T. D.; Lewis, R. L.; Beers, K. L.; Fasolka, M. J.; Hutchison, J. B.; Vogt, B. D.; Epps III, T. H., Gradient Solvent Vapor Annealing of Block Copolymer Thin Films Using a Microfluidic Mixing Device. *Nano Lett.* **2011**, *11* (3), 1351-1357.

(140) Albert, J. N. L.; Young, W.-S.; Lewis III, R. L.; Bogart, T. D.; Smith, J. R.; Epps III, T. H., Systematic Study on the Effect of Solvent Removal Rate on the Morphology of Solvent Vapor Annealed ABA Triblock Copolymer Thin Films. *ACS Nano* **2011**, *6* (1), 459-466.

(141) Kelly, J. Y.; Albert, J. N.; Howarter, J. A.; Stafford, C. M.; Epps III, T. H.; Fasolka, M. J., Manipulating morphology and orientation in thermally responsive block copolymer thin films. *J. Polym. Sci. Pol. Phys.* **2012**, *50* (4), 263-271.

(142) Stafford, C. M.; Harrison, C.; Beers, K. L.; Karim, A.; Amis, E. J.; VanLandingham, M. R.; Kim, H.-C.; Volksen, W.; Miller, R. D.; Simonyi, E. E., A Buckling-Based

Metrology for Measuring the Elastic Moduli of Polymeric Thin Films. *Nat. Mater.* **2004**, 3 (8), 545-550.

(143) Fasolka, M. J.; Stafford, C. M.; Beers, K. L., Gradient and microfluidic library approaches to polymer interfaces. In *Polymer Libraries*, Springer: 2010; pp 63-105.

(144) Jiang, Z., GIXSGUI: a MATLAB toolbox for grazing-incidence X-ray scattering data visualization and reduction, and indexing of buried three-dimensional periodic nanostructured films. *Journal of Applied Crystallography* **2015**, 48 (3), 917-926.

(145) Richard, A., Interface And Surface Effects On The Glass-Transition Temperature In Thin Polymer Films. *Farad. Discuss.* **1994**, 98, 219-230.

(146) Wang, Y.; Rafailovich, M.; Sokolov, J.; Gersappe, D.; Araki, T.; Zou, Y.; Kilcoyne, A.; Ade, H.; Marom, G.; Lustiger, A., Substrate effect on the melting temperature of thin polyethylene films. *Phys. Rev. Lett.* **2006**, 96 (2), 028303.

(147) Ediger, M. D.; Forrest, J. A., Dynamics near Free Surfaces and the Glass Transition in Thin Polymer Films: A View to the Future. *Macromolecules* **2014**, 47 (2), 471-478.

(148) Bates, F. S., Polymer-Polymer Phase-behavior. *Science* **1991**, 251 (4996), 898-905.

(149) Alward, D. B.; Kinning, D. J.; Thomas, E. L.; Fetters, L. J., Effect of Arm Number and Arm Molecular-Weight on the Solid-State Morphology of Poly(Styrene-Isoprene) Star Block Copolymers. *Macromolecules* **1986**, 19 (1), 215-224.

(150) Adhikari, R.; Michler, G. H., Influence of Molecular Architecture on Morphology and Micromechanical Behavior of Styrene/Butadiene Block Copolymer Systems. *Prog. Polym. Sci.* **2004**, 29 (9), 949-986.

(151) Matsen, M. W., Effect of Architecture on the Phase Behavior of AB-Type Block Copolymer Melts. *Macromolecules* **2012**, 45 (4), 2161-2165.

- (152) Shelton, C. K.; Epps III, T. H., Decoupling Substrate Surface Interactions in Block Polymer Thin Film Self-assembly. *Macromolecules* **2015**, *48* (13), 4572-4580.
- (153) Schultz, J.; Tsutsumi, K.; Donnet, J.-B., Surface Properties of High-energy Solids: II. Determination of the Nondispersive Component of the Surface Free Energy of Mica and its Energy of Adhesion to Polar Liquids. *J. Colloid Interface Sci.* **1977**, *59* (2), 277-282.
- (154) Thornton, J. A.; Hoffman, D., Stress-related effects in thin films. *Thin Solid Films* **1989**, *171* (1), 5-31.
- (155) Reiter, G., Dewetting Of Thin Polymer Films. *Phys Rev Lett* **1992**, *68* (1), 75-78.
- (156) Park, M.; Harrison, C.; Chaikin, P. M.; Register, R. A.; Adamson, D. H., Block Copolymer Lithography: Periodic Arrays Of Similar To 10(11) Holes In 1 Square Centimeter. *Science* **1997**, *276* (5317), 1401-1404.
- (157) Jeong, B. H.; Hoek, E. M. V.; Yan, Y. S.; Subramani, A.; Huang, X. F.; Hurwitz, G.; Ghosh, A. K.; Jawor, A., Interfacial Polymerization Of Thin Film Nanocomposites: A New Concept For Reverse Osmosis Membranes. *J. Membrane Sci.* **2007**, *294*, 1-7.
- (158) Chakrabarty, B.; Ghoshal, A. K.; Purkait, M. K., Effect Of Molecular Weight Of PEG On Membrane Morphology And Transport Properties. *J. Membrane Sci.* **2008**, *309*, 209-221.
- (159) Ioroi, T.; Yasuda, K.; Siroma, Z.; Fujiwara, N.; Miyazaki, Y., Thin film electrocatalyst layer for unitized regenerative polymer electrolyte fuel cells. *Journal of Power sources* **2002**, *112* (2), 583-587.
- (160) Liu, F. Q.; Yi, B. L.; Xing, D. M.; Yu, J. R.; Zhang, H. M., Nafion/PTFE Composite Membranes For Fuel Cell Applications. *J. Membrane Sci.* **2003**, *212*, 213-223.
- (161) Tsai, Y.-C.; Li, S.-C.; Chen, J.-M., Cast thin film biosensor design based on a nafion backbone, a multiwalled carbon nanotube conduit, and a glucose oxidase function. *Langmuir* **2005**, *21* (8), 3653-3658.

- (162) Tiaw, K. S.; Teoh, S. H.; Chen, R.; Hong, M. H., Processing methods of ultrathin poly ( $\epsilon$ -caprolactone) films for tissue engineering applications. *Biomacromolecules* **2007**, *8* (3), 807-816.
- (163) Berry, B. C.; Bosse, A. W.; Douglas, J. F.; Jones, R. L.; Karim, A., Orientational order in block copolymer films zone annealed below the order– disorder transition temperature. *Nano Lett.* **2007**, *7* (9), 2789-2794.
- (164) Seppala, J. E.; Lewis III, R. L.; Epps III, T. H., Spatial and orientation control of cylindrical nanostructures in ABA triblock copolymer thin films by raster solvent vapor annealing. *ACS Nano* **2012**, *6* (11), 9855-9862.
- (165) Van den Mooter, G.; Wuyts, M.; Blaton, N.; Busson, R.; Grobet, P.; Augustijns, P.; Kinget, R., Physical stabilisation of amorphous ketoconazole in solid dispersions with polyvinylpyrrolidone K25. *European journal of pharmaceutical sciences* **2001**, *12* (3), 261-269.
- (166) Ambike, A. A.; Mahadik, K.; Paradkar, A., Spray-dried amorphous solid dispersions of simvastatin, a low T<sub>g</sub> drug: in vitro and in vivo evaluations. *Pharmaceutical research* **2005**, *22* (6), 990-998.
- (167) Vasconcelos, T.; Sarmiento, B.; Costa, P., Solid dispersions as strategy to improve oral bioavailability of poor water soluble drugs. *Drug discovery today* **2007**, *12* (23), 1068-1075.
- (168) Legrand, D., Crazing, yielding, and fracture of polymers. I. Ductile brittle transition in polycarbonate. *J. Appl. Polym. Sci.* **1969**, *13* (10), 2129-2147.
- (169) Aharoni, S. M., Ductile and brittle behavior of amorphous polymers. Relationship with activation energy for glass transition and mechanical fracture. *J. Appl. Polym. Sci.* **1972**, *16* (12), 3275-3284.
- (170) Aharoni, S. M., Correlations between chain parameters and failure characteristics of polymers below their glass transition temperature. *Macromolecules* **1985**, *18* (12), 2624-2630.

(171) Keddie, J. L.; Jones, R. A. L.; Cory, R. A., Size-Dependent Depression of the Glass-Transition Temperature in Polymer-Films. *Europhysics Letters* **1994**, *27* (1), 59-64.

(172) Forrest, J. A.; Dalnoki-Veress, K.; Stevens, J. R.; Dutcher, J. R., Effect of Free Surfaces on the Glass Transition Temperature of Thin Polymer Films. *Phys Rev Lett* **1996**, *77* (10), 2002-2005.

(173) Feng, S.; Li, Z.; Liu, R.; Mai, B.; Wu, Q.; Liang, G.; Gao, H.; Zhu, F., Glass transition of polystyrene nanospheres under different confined environments in aqueous dispersions. *Soft Matter* **2013**, *9* (18), 4614-4620.

(174) Wang, H.; Liu, C.-L.; Wu, G.; Chen, S.-C.; Song, F.; Wang, Y.-Z., Temperature dependent morphological evolution and the formation mechanism of anisotropic nano-aggregates from a crystalline-coil block copolymer of poly (p-dioxanone) and poly (ethylene glycol). *Soft Matter* **2013**, *9* (36), 8712-8722.

(175) Feng, S.; Chen, Y.; Mai, B.; Wei, W.; Zheng, C.; Wu, Q.; Liang, G.; Gao, H.; Zhu, F., Glass transition of poly (methyl methacrylate) nanospheres in aqueous dispersion. *Physical Chemistry Chemical Physics* **2014**, *16* (30), 15941-15947.

(176) Kunugi, S.; Tada, T.; Tanaka, N.; Yamamoto, K.; Akashi, M., Microcalorimetric study of aqueous solution of a thermoresponsive polymer, poly (N-vinylisobutylamide)(PNVIBA). *Polymer journal* **2002**, *34* (5), 383-388.

(177) Balko, J.; Rinscheid, A.; Wurm, A.; Schick, C.; Lohwasser, R. H.; Thelakkat, M.; Thurn-Albrecht, T., Crystallinity of poly (3-hexylthiophene) in thin films determined by fast scanning calorimetry. *J. Polym. Sci. Pol. Phys.* **2016**, *54* (18), 1791-1801.

(178) Tardif, X.; Pignon, B.; Boyard, N.; Schmelzer, J. W.; Sobotka, V.; Delaunay, D.; Schick, C., Experimental study of crystallization of PolyEtherEtherKetone (PEEK) over a large temperature range using a nano-calorimeter. *Polymer Testing* **2014**, *36*, 10-19.

(179) Ellison, C. J.; Ruszkowski, R. L.; Fredin, N. J.; Torkelson, J. M., Dramatic Reduction Of The Effect Of Nanoconfinement On The Glass Transition Of Polymer Films Via Addition Of Small-Molecule Diluent. *Phys. Rev. Lett.* **2004**, *92* (9), 095702.

- (180) Roth, C. B.; McNerny, K. L.; Jager, W. F.; Torkelson, J. M., Eliminating the enhanced mobility at the free surface of polystyrene: fluorescence studies of the glass transition temperature in thin bilayer films of immiscible polymers. *Macromolecules* **2007**, *40* (7), 2568-2574.
- (181) Zhang, L.; Elupula, R.; Grayson, S. M.; Torkelson, J. M., Major impact of cyclic chain topology on the T<sub>g</sub>-confinement effect of supported thin films of polystyrene. *Macromolecules* **2015**, *49* (1), 257-268.
- (182) Zhang, L.; Elupula, R.; Grayson, S. M.; Torkelson, J. M., Suppression of the fragility-confinement effect via low molecular weight cyclic or ring polymer topology. *Macromolecules* **2017**, *50* (3), 1147-1154.
- (183) Kim, J. H.; Jang, J.; Zin, W. C., Thickness dependence of the melting temperature of thin polymer films. *Macromol. Rapid Commun.* **2001**, *22* (6), 386-389.
- (184) Woodruff, M. A.; Hutmacher, D. W., The return of a forgotten polymer—polycaprolactone in the 21st century. *Prog. Polym. Sci.* **2010**, *35* (10), 1217-1256.
- (185) Money, B. K.; Swenson, J., Dynamics of poly (ethylene oxide) around its melting temperature. *Macromolecules* **2013**, *46* (17), 6949-6954.
- (186) Vaselabadi, S. A.; Shakarizaz, D.; Ruchhoeft, P.; Strzalka, J.; Stein, G. E., Radiation damage in polymer films from grazing-incidence X-ray scattering measurements. *J. Polym. Sci. Pol. Phys.* **2016**.
- (187) Sanandaji, N.; Ovaskainen, L.; Gunnewiek, M. K.; Vancso, G. J.; Hedenqvist, M. S.; Yu, S.; Eriksson, L.; Roth, S.; Gedde, U. W., Unusual crystals of poly ( $\epsilon$ -caprolactone) by unusual crystallisation: The effects of rapid cooling and fast solvent loss on the morphology, crystal structure and melting. *Polymer* **2013**, *54* (5), 1497-1503.
- (188) Loiko, V.; Maksimenko, P.; Konkolovich, A., A method for calculating the light extinction coefficients of a polymer layer with small nematic liquid-crystal droplets. *Optics and Spectroscopy* **2008**, *105* (5), 791-797.

- (189) Vezie, M. S.; Few, S.; Meager, I.; Pieridou, G.; Dörling, B.; Ashraf, R. S.; Goñi, A. R.; Bronstein, H.; McCulloch, I.; Hayes, S. C., Exploring the origin of high optical absorption in conjugated polymers. *Nat. Mater.* **2016**.
- (190) Priyadarshi, A.; Shimin, L.; Wong, E.; Rajoo, R.; Mhaisalkar, S.; Kripesh, V., Refractive indices variation with temperature and humidity of optical adhesive. *Journal of electronic materials* **2005**, *34* (11), 1378-1384.
- (191) Moshrefzadeh, R.; Radcliffe, M.; Lee, T.; Mohapatra, S., Temperature dependence of index of refraction of polymeric waveguides. *Journal of lightwave technology* **1992**, *10* (4), 420-425.
- (192) Hoffman, J. D.; Weeks, J. J., Specific volume and degree of crystallinity of semicrystalline polychlorotrifluoroethylene, and estimated specific volumes of the pure amorphous and crystalline phases. *J. Research Natl. Bur. Standards* **1958**, *60*, 465.
- (193) Umemoto, S.; Okui, N., Master curve of crystal growth rate and its corresponding state in polymeric materials. *Polymer* **2002**, *43* (4), 1423-1427.
- (194) Laurent, B. A.; Grayson, S. M., An Efficient Route To Well-Defined Macrocyclic Polymers Via "Click" Cyclization. *J. Am. Chem. Soc.* **2006**, *128* (13), 4238-4239.
- (195) Eugene, D. M.; Grayson, S. M., Efficient Preparation Of Cyclic Poly(Methyl Acrylate)-Block-Poly(Styrene) By Combination Of Atom Transfer Radical Polymerization And Click Cyclization. *Macromolecules* **2008**, *41* (14), 5082-5084.
- (196) Jia, Z. F.; Lonsdale, D. E.; Kulis, J.; Monteiro, M. J., Construction of a 3-Miktoarm Star from Cyclic Polymers. *ACS Macro Lett.* **2012**, *1* (6), 780-783.
- (197) Hossain, M. D.; Jia, Z. F.; Monteiro, M. J., Complex Polymer Topologies Built from Tailored Multifunctional Cyclic Polymers. *Macromolecules* **2014**, *47* (15), 4955-4970.
- (198) Kapnistos, M.; Lang, M.; Vlassopoulos, D.; Pyckhout-Hintzen, W.; Richter, D.; Cho, D.; Chang, T.; Rubinstein, M., Unexpected Power-Law Stress Relaxation Of Entangled Ring Polymers. *Nat. Mater.* **2008**, *7* (12), 997-1002.

- (199) Elupula, R.; Oh, J.; Haque, F. M.; Chang, T.; Grayson, S. M., Determining the Origins of Impurities during Azide-Alkyne Click Cyclization of Polystyrene. *Macromolecules* **2016**, *49* (11), 4369-4372.
- (200) Poelma, J. E.; Ono, K.; Miyajima, D.; Aida, T.; Satoh, K.; Hawker, C. J., Cyclic Block Copolymers For Controlling Feature Sizes In Block Copolymer Lithography. *ACS Nano* **2012**, *6* (12), 10845-10854.
- (201) Jackson, E. A.; Hillmyer, M. A., Nanoporous Membranes Derived From Block Copolymers: From Drug Delivery To Water Filtration. *ACS Nano* **2010**, *4* (7), 3548-3553.
- (202) Phillip, W. A.; O'Neill, B.; Rodwogin, M.; Hillmyer, M. A.; Cussler, E., Self-Assembled Block Copolymer Thin Films As Water Filtration Membranes. *ACS Appl. Mater. Interfaces* **2010**, *2* (3), 847-853.
- (203) Reiter, G., Unstable Thin Polymer Films - Rupture and Dewetting Processes. *Langmuir* **1993**, *9* (5), 1344-1351.
- (204) Henn, G.; Bucknall, D. G.; Stamm, M.; Vanhoorne, P.; Jerome, R., Chain End Effects And Dewetting In Thin Polymer Films. *Macromolecules* **1996**, *29* (12), 4305-4313.
- (205) Xie, R.; Karim, A.; Douglas, J. F.; Han, C. C.; Weiss, R. A., Spinodal Dewetting Of Thin Polymer Films. *Phys. Rev. Lett.* **1998**, *81* (6), 1251-1254.
- (206) Meredith, J. C.; Smith, A. P.; Karim, A.; Amis, E. J., Combinatorial Materials Science For Polymer Thin-Film Dewetting. *Macromolecules* **2000**, *33* (26), 9747-9756.
- (207) Reiter, G.; Khanna, R., Kinetics Of Autophobic Dewetting Of Polymer Films. *Langmuir* **2000**, *16* (15), 6351-6357.
- (208) Matsen, M. W.; Gardiner, J. M., Autophobic Dewetting Of Homopolymer On A Brush And Entropic Attraction Between Opposing Brushes In A Homopolymer Matrix. *J. Chem. Phys* **2001**, *115* (6), 2794-2804.

- (209) Wang, C.; Krausch, G.; Geoghegan, M., Dewetting At A Polymer-Polymer Interface: Film Thickness Dependence. *Langmuir* **2001**, *17* (20), 6269-6274.
- (210) Edgecombe, S. R.; Gardiner, J. M.; Matsen, M. W., Suppressing Autophobic Dewetting By Using A Bimodal Brush. *Macromolecules* **2002**, *35* (16), 6475-6477.
- (211) Waltman, R. J.; Khurshudov, A.; Tyndall, G. W., Autophobic Dewetting Of Perfluoropolyether Films On Amorphous-Nitrogenated Carbon Surfaces. *Tribology Letters* **2002**, *12* (3), 163-169.
- (212) Suh, K. Y.; Park, J.; Lee, H. H., Controlled Polymer Dewetting By Physical Confinement. *J. Chem. Phys* **2002**, *116* (17), 7714-7718.
- (213) Lecommandoux, S.; Borsali, R.; Schappacher, M.; Deffieux, A.; Narayanan, T.; Rochas, C., Microphase Separation of Linear and Cyclic Block Copolymers Poly(styrene-*b*-isoprene): SAXS Experiments. *Macromolecules* **2004**, *37* (5), 1843-1848.
- (214) Zhang, L.; Elupula, R.; Grayson, S. M.; Torkelson, J. M., Major Impact Of Cyclic Chain Topology On The Tg-Confinement Effect Of Supported Thin Films Of Polystyrene. *Macromolecules* **2015**, *49* (1), 257-268.
- (215) Hadziioannou, G.; Cotts, P. M.; Tenbrinke, G.; Han, C. C.; Lutz, P.; Strazielle, C.; Rempp, P.; Kovacs, A. J., Thermodynamic and Hydrodynamic Properties of Dilute-Solutions of Cyclic and Linear Polystyrenes. *Macromolecules* **1987**, *20* (3), 493-497.
- (216) Alberty, K. A.; Hogen-Esch, T. E.; Carlotti, S., Synthesis and Characterization of Macrocyclic Vinyl-Aromatic Polymers. *Macromol. Chem. Phys.* **2005**, *206* (10), 1035-1042.
- (217) Dubois, P.; Barakat, I.; Jerome, R.; Teyssie, P., Macromolecular engineering of polyactones and polyactides. 12. Study of the depolymerization reactions of poly( $\epsilon$ -caprolactone) with functional aluminum alkoxide end groups. *Macromolecules* **1993**, *26* (17), 4407-4412.

- (218) Müller, M.; Wittmer, J.; Cates, M., Topological Effects In Ring Polymers: A Computer Simulation Study. *Phys Rev E Stat Nonlin Soft Matter Phys* **1996**, *53* (5), 5063.
- (219) Roovers, J., Viscoelastic Properties Of Polybutadiene Rings. *Macromolecules* **1988**, *21* (5), 1517-1521.
- (220) Khandwekar, A. P.; Patil, D. P.; Shouche, Y.; Doble, M., Surface Engineering Of Polycaprolactone By Biomacromolecules And Their Blood Compatibility. *Journal of Biomaterials Applications* **2011**, *26* (2), 227-252.
- (221) Xue, L. J.; Han, Y. C., Inhibition Of Dewetting Of Thin Polymer Films. *Progress in Materials Science* **2012**, *57* (6), 947-979.
- (222) Sharma, A.; Reiter, G., Instability Of Thin Polymer Films On Coated Substrates: Rupture, Dewetting, And Drop Formation. *J. Colloid Interface Sci.* **1996**, *178* (2), 383-399.
- (223) Redon, C.; Brochard-Wyart, F.; Rondelez, F., Dynamics Of Dewetting. *Phys Rev Lett* **1991**, *66* (6), 715-718.
- (224) Reiter, G.; Khanna, R., Real-Time Determination Of The Slippage Length In Autophobic Polymer Dewetting. *Phys Rev Lett* **2000**, *85* (13), 2753-2756.
- (225) Hoskins, J. N.; Grayson, S. M., Synthesis and degradation behavior of cyclic poly ( $\epsilon$ -caprolactone). *Macromolecules* **2009**, *42* (17), 6406-6413.
- (226) Kapnistos, M.; Lang, M.; Vlassopoulos, D.; Pyckhout-Hintzen, W.; Richter, D.; Cho, D.; Chang, T.; Rubinstein, M., Unexpected power-law stress relaxation of entangled ring polymers. *Nat. Mater.* **2008**, *7* (12), 997.
- (227) Halverson, J. D.; Grest, G. S.; Grosberg, A. Y.; Kremer, K., Rheology of ring polymer melts: From linear contaminants to ring-linear blends. *Phys. Rev. Lett.* **2012**, *108* (3), 038301.

(228) Zaldua, N.; Liénard, R.; Josse, T.; Zubitur, M.; Mugica, A.; Iturrospe, A.; Arbe, A.; De Winter, J.; Coulembier, O.; Müller, A. J., Influence of Chain Topology (Cyclic versus Linear) on the Nucleation and Isothermal Crystallization of Poly (l-lactide) and Poly (d-lactide). *Macromolecules* **2018**, *51* (5), 1718-1732.

(229) López, J. V.; Pérez-Camargo, R. A.; Zhang, B.; Grayson, S. M.; Müller, A. J., The influence of small amounts of linear polycaprolactone chains on the crystallization of cyclic analogue molecules. *RSC Advances* **2016**, *6* (53), 48049-48063.

(230) van Zanten, J. H.; Wallace, W. E.; Wu, W.-l., Effect of strongly favorable substrate interactions on the thermal properties of ultrathin polymer films. *Phys Rev E Stat Nonlin Soft Matter Phys* **1996**, *53* (3), R2053.

(231) Wang, J.; Li, Z.; Pérez, R. A.; Müller, A. J.; Zhang, B.; Grayson, S. M.; Hu, W., Comparing crystallization rates between linear and cyclic poly (epsilon-caprolactones) via fast-scan chip-calorimeter measurements. *Polymer* **2015**, *63*, 34-40.

## Biography

Giovanni M. Kelly II was born in Manhattan, New York on July 23<sup>rd</sup>, 1991 and grew up in Fleetwood, New York. In 1996, he moved to Las Vegas, Nevada where he developed a love for golf. After finishing 7<sup>th</sup> grade, he moved back to Fleetwood, New York where he attended Iona Preparatory School in New Rochelle, New York. He graduated with honors from Iona in 2009. He then moved on to Manhattan College in Riverdale, New York where he studied Chemical Engineering graduating Magna cum Laude in 2013. At the end of the summer of 2013, he moved down to New Orleans, Louisiana where he started his Ph.D work in Chemical and Biomolecular Engineering at Tulane University.

During his time at Tulane, Giovanni was involved in a wide variety of department, school, and university organizations. He was the President of the Chemical & Biomolecular Engineering Graduate Student Association for two years, Chemical & Biomolecular Engineering department representative for the Graduate Studies Student Association (GSSA) for four years, and a School of Science and Engineering Senator to the Graduate and Professional Students Association (GAPSA) for one year, among other similar roles. He also took an active part in the Tulane Engineering Forum (TEF), serving on its steering committee for three years. He has been awarded the Outstanding Teaching Assistant award, the Outstanding Presenter award at the Chemical & Biomolecular Engineering department's annual 4<sup>th</sup> Year Symposium, as well as the four year Louisiana Board of Regents Graduate Fellowship, which supported his work while at Tulane.

After completing his doctoral work, Giovanni will assume the position of Technology and Applications Consultant for the Reaction Analysis business area of Mettler-Toledo Autochem for the Northeast Region of the United States and Eastern Canada. In this role, he will be responsible for providing elite consulting services to scientists and engineers in many world-class corporations and academic labs to further their research and help them push the boundaries of their scientific study.